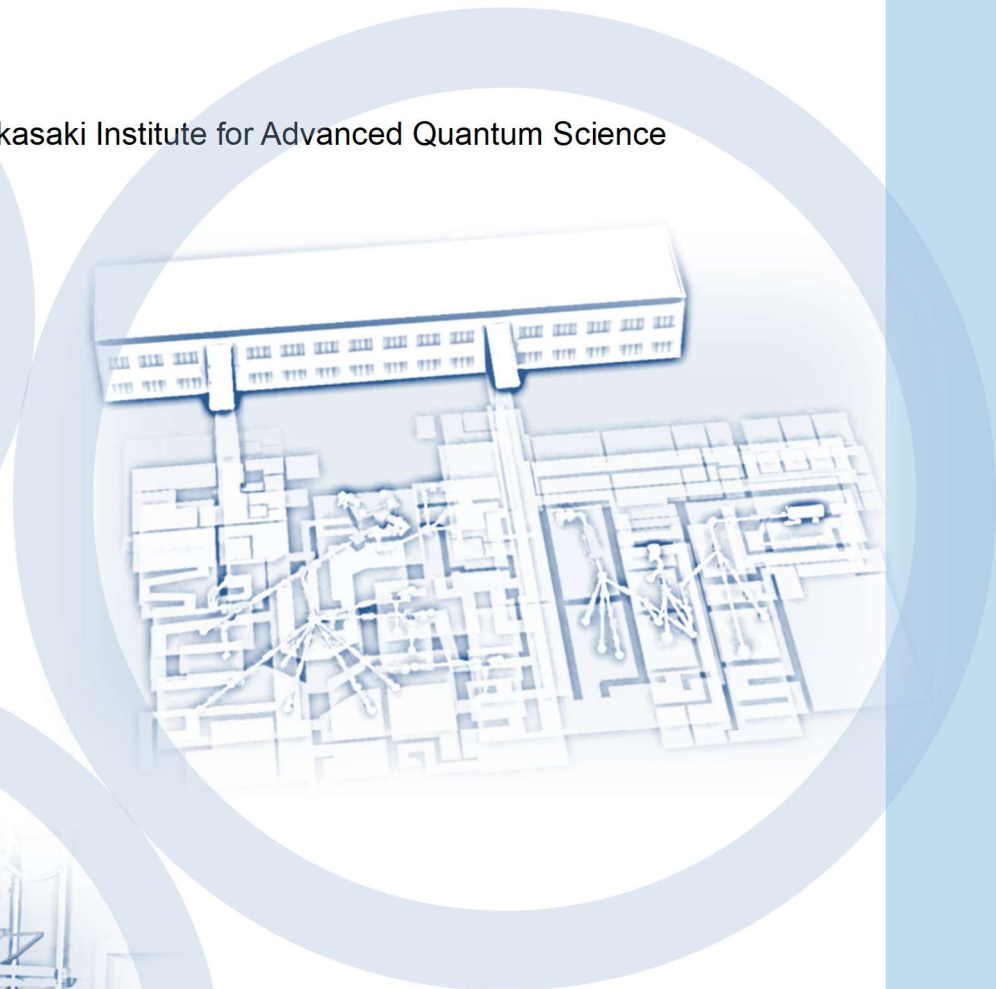


QST Takasaki Annual Report 2023

Takasaki Institute for Advanced Quantum Science



National Institutes for Quantum Science and Technology

Preface



MAEKAWA Yasunari

Director General
Takasaki Institute for Advanced Quantum Science
National Institutes for Quantum Science and Technology (QST)

Takasaki Institute for Advanced Quantum Science is a core R&D site for quantum beam science and technology, which are the main missions of National Institutes for Quantum Science and Technology (QST). We have been conducting innovative researches on radiation/quantum-beam application research for more than 60 years including the predecessor institutes, Takasaki Radiation Chemistry Research Establishment of the Japan Atomic Energy Research Institute (JAERI) and Takasaki Advanced Radiation Research Institute of the Japan Atomic Energy Agency (JAEA). Using advanced beam facilities, we conducted intensive fundamental and applied research in fields such as quantum materials and applications, materials science, life science, and quantum beam technology. The Takasaki Institute manages three main radiation facilities: Takasaki Ion Accelerators for Advanced Radiation Application (TIARA), a 2 MeV electron accelerator, and ^{60}Co gamma-ray irradiation facilities. Since the establishment of QST in 2016, it strongly promotes fundamental research on quantum technology, such as the creation of quantum functional materials that contribute to the realization of quantum sensing and quantum computers. QST has been nominated as one of the Quantum Technology Innovation Hubs (QIH) in Japan. As a QIH activity, we supply high-quality quantum materials to companies and organize the training course for corporate researchers.

At the Takasaki Institute in the fiscal year 2023 (FY2023), we had 15 research projects conducting quantum technology and quantum beam science R&Ds with the aforementioned three main radiation facilities, which contributed to the development of science and technology as well as the promotion of industry. Furthermore, we conduct R&D on advanced ion beam technology at the Beam Engineering Section of the Department of Advanced Quantum Beam Technology. Our beam facilities are available to industry, academia, and governmental research institutes, and beam time is allocated to users based on the evaluation of their R&D programs.

This annual report covers research activities at the Takasaki Institute for FY2023. This report is composed of two parts. Part I describes the recent activities of all research projects. Part II presents recent R&D results obtained using the quantum beam facilities of QST Takasaki. This part contains 49 research papers in the fields of quantum materials and applications, materials science, life science, and advanced quantum beam technology, as well as eight status reports on the operation and maintenance of the quantum beam facilities.

The following topics are the research highlights for FY2023. The first topic is in the field of quantum materials. We developed a novel ferrimagnetic cubic Heusler compound $\text{Mn}_2\text{Fe}_x\text{Ga}$ (MFG) with a half-metallic-like band structure which also exhibits an extremely large perpendicular magnetic anisotropy (PMA) under a tetragonal lattice strain. Synchrotron Mössbauer spectroscopy revealed that these cubic MFG thin films show good chemical ordering close to the X_a -ordered state. First-principles calculations demonstrated that, in X_a -ordered cubic MFG, the characteristic electronic structure of Fe around the Fermi level causes a large uniaxial magnetocrystalline anisotropy under the tetragonal strain consistent with experiment. The ferrimagnetism, large PMA and possibility of high spin polarization in this material make it an ideal candidate for magnetic recording materials such as optical-to-electrical (O-E) conversion non-volatile memory devices used in future all-optical networks. The next topic is in the field of life science. *V. riukiuensis* is one of the salt-tolerant species identified from the genus *Vigna*. We have previously provided that *V. riukiuensis* accumulates a higher amount of sodium in the leaves, whereas *V. nakashimae*, a close relative of *V. riukiuensis*, suppresses sodium allocation to the leaves by autoradiography with radioactive sodium ($^{22}\text{Na}^+$) and Inductively Coupled Plasma Mass Spectrometry. We performed scanning electron microscope-energy dispersive x-ray spectrometry to locate Na in leaf sections and detected Na in chloroplasts of *V. riukiuensis*, especially around the starch granules but not in the middle of. Our results could provide the second evidence of the Na-trapping system by starch granules, following the case of common reed that accumulates starch granule at the shoot base for binding Na.

An azimuthally varying field (AVF) cyclotron and three electrostatic ion beam accelerators at TIARA, as well as a MeV electron accelerator and ^{60}Co gamma-ray irradiation facilities, have been operated continuously and safely. The key components of the accelerator system at TIARA are updated annually to maintain global technological superiority. Recent remarkable study is Ti beam extraction from a laser plasma focused by a magnetic field of a solenoid. The 400-kV ion implanter in TIARA is utilized for implanting ion beams of a wide range of different ion species into various materials. To generate the ion beams of different ion species, a laser ion source (LIS) is developing for the ion implanter. LIS has the advantages of generating plasma from various solid targets and quickly switching the ion species by changing the target. To obtain a higher beam intensity by increasing the number of ions reaching the beam extraction electrode aperture, a plasma transport system with a linear solenoid magnet was installed immediately after the LIS chamber to focus the plasma by a magnetic field. In the Ti plasma focusing experiment using this system, the beam intensity increased up to 6.7 times compared to that of the case without a magnetic field.

Finally, we would like to extend our gratitude to our domestic and foreign colleagues for their cooperation and support in our quantum technology and quantum beam science R&D and the technological advances in the facilities of QST Takasaki.

Quantum Beam Facilities in QST Takasaki

Takasaki Ion Accelerators for Advanced Radiation Application (TIARA) consisting of four ion accelerators, an electron accelerator, and gamma-ray irradiation facilities are available to researchers in QST and other organizations for R&D activities on new functional and environmentally friendly materials, biotechnology, radiation effects of materials, and quantum beam analysis. We are developing various shape area irradiation technique at the cyclotron. In addition, technical developments of elemental map imaging by C₆₀ fullerene microbeam at the electrostatic accelerators are in progress.

Takasaki Ion Accelerators for Advanced Radiation Application: TIARA



TIARA facility



Cyclotron



Tandem accelerator



Single-ended accelerator

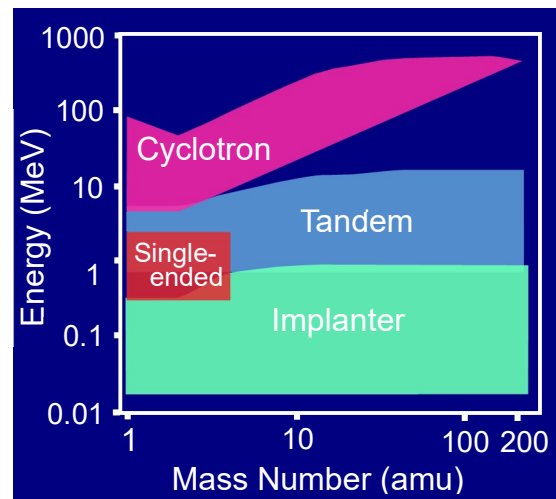


Ion implanter

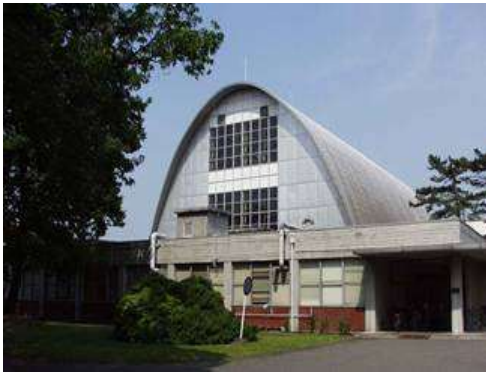
Typical available ions

Accelerator	Ion	Energy (MeV)
AVF Cyclotron (K=110MeV)	H	10~ 80
	He	20~ 107
	C	75~ 320
	Ne	75~ 350
	Ar	150~ 520
	Fe	200~ 400
	Kr	210~ 520
	Xe	324~ 560
	Os	490
Tandem Accelerator (3 MV)	H	0.8~ 6.0
	C	0.8~ 18.0
	Ni	0.8~ 18.0
	Au	0.8~ 18.0
	C ₆₀	0.8~ 9.0
Single-ended Accelerator (3 MV)	H	0.4~ 3.0
	D	0.4~ 3.0
	He	0.4~ 3.0
	e ⁻	0.4~ 3.0
Ion Implanter (400 kV)	H	0.02~ 0.38
	Ar	0.02~ 0.38
	Bi	0.02~ 0.37
	C ₆₀	0.02~ 0.36

Energy-element range covered by the four accelerators



Cobalt-60 gamma-ray and electron beam irradiation facilities



Gamma-ray irradiation facility building



Gamma-rays irradiation room



Electron accelerator
(0.5~2.0 MeV, 0.1~30 mA)



Electron irradiation room with conveyor system

Specification			Apr. 2024
Name of facility	Cobalt-60 activity (PBq)	Number of rooms	Principal utilization
Co No.1 bld.	3.9	3	Radiation-resistance test, radiation effects on materials as polymers, semiconductors, and biological substances as bacteria, cell, plant
Co No.2 bld.	5.7	3	R & D on functional organic materials, inorganic materials and dosimetry

Dose-rate range										Unit : kGy/h
Name of room	10 ⁻⁴	10 ⁻³	10 ⁻²	10 ⁻¹	10 ⁰	10 ¹	10 ²	10 ³	10 ⁴	10 ⁵
Co No.2										
Co No.7										
Co No.3										
EB accel.										

Contents

Part I

1. Quantum Materials and Applications	1
P1-1 Quantum Sensing Project	2
Leader : OHSHIMA Takeshi	
P1-2 Spin-photonics in 2D Materials Project	3
Leader : SAKAI Seiji	
P1-3 Laser-cooled Ion Research Project	4
Leader : NARUMI Kazumasa	
P1-4 Quantum Optical and Spin State Control Project	5
Leader : KOHDA Makoto	
P1-5 Quantum Materials Theory Project	6
Chief : MATSUSHITA Yu-ichiro	
P1-6 Rare-earth Quantum Device Project	7
Chief : SATO Shin-ichiro	
P1-7 Quantum Materials Ultrafine Fabrication Project	8
Chief : YAMAMOTO Hiroki	
2. Materials Science	9
P2-1 Hydrogen Energy Conversion Device Project	10
Leader : SAEKI Morihisa	
P2-2 Nanostructured Polymer Materials Project	11
Leader : ZHAO Yue	
P2-3 Energy Regeneration Materials Project	12
Leader : SEKO Noriaki	
P2-4 Advanced Biodevice Project	13
Leader : TAGUCHI Mitsumasa	
3. Life Science	14
P3-1 Radiotracer Imaging Project	15
Leader : KAWACHI Naok	
P3-2 Environmental-Stress Tolerance Genes Project	16
Leader : HASE Yoshihiro	
P3-3 Medical Radioisotope Application Project	17
Leader : ISHIOKA Noriko S.	
P3-4 Quantum-Applied Biotechnology Project	18
Leader : SUZUKI Michiyo	
4. Quantum-Beam Technology	19
P4-1 Beam Engineering Section	20
Section Manager : ISHII Yasuyuki	

Part II

1. Quantum Materials and Applications	21
1-01 Recovery of the threshold voltage shift of gamma-irradiated 4H-SiC JFET by sub-band gap light illumination	22
1-02 Annealing time dependence on creation of group IV – vacancy centers in diamond by atmospheric annealing	23
1-03 Laser-cooled ion source for an ultrahigh-precision single-ion implanter	24
1-04 Development of selective loading system of Ba isotope using two-step photoionization	25
1-05 Construction of the ion trap system for radioactive Ba ⁺ isotope	26
1-06 Charge state stability of silicon vacancy in silicon carbide	27
1-07 X-ray absorption fine structure analysis of Pr ions implanted in GaN	28
2. Materials Science	29
2-01 Preparation of Pd-doped TiO ₂ films by sputtering deposition on sapphire substrates	31
2-02 Lattice plane spacing change of carbon layer in C-SiC coaxial nanotube by ion irradiation	32
2-03 Superconducting properties of GdBa ₂ Cu ₃ O _y thin films irradiated with 350 keV Ar-ions	33
2-04 Effect of high-dose electron beam irradiation on thermal decomposition behavior of polytetrafluoroethylene (PTFE)	34
2-05 Modification of polymeric materials by quantum beam irradiation (4)	35
2-06 Development of polymeric sealing materials utilizing radiation technique by ion beam irradiation	36
2-07 Machine learning analysis of proton conduction properties of graft-type cation exchange membranes based on various polymers	37
2-08 Preparation of hydrogel/aluminum hydroxide composite adsorbent by in-situ radiation polymerization for lithium recovery from saltlake brine	38
2-09 Measurement method of the degree of grafting by using thermogravimetric analysis	39
2-10 Development of metal adsorbent via radiation-induced graft polymerization and Kabachnik-Fields reaction	40
2-11 The development of environmentally friendly soft contact lenses based on cellulose-derived gels	41

2-12	Irradiation tests of radiation-hard components and materials for ITER blanket remote handling system	42
2-13	Irradiation effects on fiber/matrix interfacial properties of SiC/SiC composites by micro-mechanical testing methods	43
2-14	Study of multi ion-irradiation effects on fusion reactor materials using a micro-tensile testing method	44
2-15	Investigation on tensile properties of single crystal pure tungsten using micro-tensile test methodology	45
2-16	Gamma-ray irradiation experiment for ITER diagnostic systems in JADA VI	46
2-17	Luminescence of samarium complexes in <i>N,N,N',N'</i> -tetraoctyl diglycolamide solvent induced by hydrogen ion beam	47
2-18	Color imaging of carbon ion ($^{15}\text{C}^{+5}$) beam by the carbon tetrachloride gel dosimeter containing the spiropyran-like	48
2-19	γ -ray irradiation effect on ammonia radical derived from hydrothermally altered potassium feldspar: A physical basis for the application to fault dating (II)	49
3.	Life Science	50
3-01	Visualisation of the dynamics of radiocesium after its penetration into a live apple branch using the ^{137}Cs tracer	52
3-02	Visualization of cadmium distribution in roots of oilseed rape plants by in-air micro-PIXE (Particle Induced X-ray Emission) analysis	53
3-03	Simulation study on carbon-ion beam imaging by measuring SEB using an imaging plate	54
3-04	Analysis of DNA rearrangements induced by carbon ion beams in Arabidopsis seeds and seedlings	55
3-05	Resistance of Antarctic yeasts with γ -rays irradiation	56
3-06	Genome-wide detection of low-frequency mutations in plant population mutagenized with gamma ray	57
3-07	Suppression mechanism of DNA damage response protein Ppr1 in <i>Deinococcus radiodurans</i>	58
3-08	Mutation analysis and 3D structure prediction of mutation sites in <i>Rubrobacter radiotolerans</i>	59
3-09	Comparative evaluation of radionuclide therapy using ^{90}Y and ^{177}Lu – dosimetric comparison –	60
3-10	Solvent extraction following oxidation of astatine for the use of a ^{211}Rn – ^{211}At generator	61

3-11	Radioactive metal separation with 3D printed flow device	62
3-12	Effects of γ -irradiation on superoxide dismutase	63
3-13	Olfactory responses in <i>Caenorhabditis elegans</i> are maintained after whole-body carbon ion irradiation	64
4.	Quantum-Beam Technology	65
4-01	Measurement of spin polarization of positrons emitted from ^{44}Sc source generated by nuclear reaction	66
4-02	Beam energy control by the excitation current of the harmonic coil in the AVF cyclotron	67
4-03	Characterization of microfabricated patterns coated with metals using micro-particle induced X-ray emission	68
4-04	Improvements in the beam observation system of hundreds of MeV heavy ion microbeam line in TIARA	69
4-05	Improvement of the heavy-ion microbeam system	70
4-06	Carbon sputtering yield by fullerene-ion bombardment	71
4-07	Study of radiation resistance of Coal Ash Fiber (BASHFIBER®) using Positron Annihilation method, etc.	72
4-08	Electron-stimulated luminescence of liquid water at speeds below the Cherenkov light threshold	73
4-09	ESR measurement of carbonated hydroxyapatite for dosimeter	74
4-10	Effect of polyacrylic acid on remineralization of demineralized dentin	75
5.	Status of Quantum-Beam Facilities	76
5-01	Utilization status at the TIARA facility	77
5-02	Operation of the AVF cyclotron	78
5-03	Operation of electrostatic accelerators in TIARA	79
5-04	Operation, maintenance and utilization status of the gamma-ray irradiation facilities	80
5-05	Operation, maintenance and utilization status of the electron accelerator	81
5-06	Radiation monitoring in QST Takasaki	82

5-07 Radioactive waste management in TIARA 83

5-08 The Shared Use Program of QST facilities in Takasaki..... 84

Appendix

Publication List 85

Part I

Part I

1. Quantum Materials and Applications

P1-1	Quantum Sensing Project	2
	Leader : OHSHIMA Takeshi	
P1-2	Spin-photonics in 2D Materials Project	3
	Leader : SAKAI Seiji	
P1-3	Laser-cooled Ion Research Project	4
	Leader : NARUMI Kazumasa	
P1-4	Quantum Optical and Spin State Control Project	5
	Leader : KOHDA Makoto	
P1-5	Quantum Materials Theory Project	6
	Chief : MATSUSHITA Yu-ichiro	
P1-6	Rare-earth Quantum Device Project	7
	Chief : SATO Shin-ichiro	
P1-7	Quantum Materials Ultrafine Fabrication Project	8
	Chief : YAMAMOTO Hiroki	

P1-1 Quantum Sensing Project

Leader : OHSHIMA Takeshi



For realizing Super Smart Society, it is important to develop quantum technologies such as quantum sensing, quantum information and quantum computing. Therefore, intensive R&D for quantum technologies is carried out all over the world. Quantum Sensing Project studies quantum technologies based on spin defects/single photon emitters in wide bandgap semiconductors such as nitrogen-vacancy (NV) center in diamond and silicon vacancy in silicon carbide (SiC). We introduce such quantum defects in host semiconductors using energetic particle irradiation (both ion and electron beams), and characterize their optical/spin properties to establish the methodologies for the creation of high quality quantum sensors/spin qubits. Besides, we study the radiation effects on semiconductor materials and devices to develop radiation resistant technologies for space and nuclear applications, of which technologies can be applied to quantum devices used in such harsh environments in the future.

Ultralong-term data storage using V_{Si} in SiC

The amounts of data that we need to save dramatically increase in the world because of the exponential growth of the increase in data used on the Internet, social media, and cloud technologies. As a result, the capacity of data storage is urgently needed to increase globally. However, this means that the amounts of electricity increase incredibly, and it is indispensable to develop the non-volatile memories with ultralong term storage capability in order to avoid the increase in electricity consumption. Thus, new solutions should be developed to realize long-term data archiving that goes far beyond traditional magnetic memory, optical disks, and solid-state drives. Here, a concept of energy-efficient, ultralong, high-density data archiving is proposed, based on optically active atomic-size defects such as negatively charged silicon vacancy (V_{Si}) in silicon carbide (SiC) [1]. The information is written in V_{Si} by focused ion beams and read using photoluminescence (PL).

Samples used in this study were a commercially available high-purity semi-insulating (HPSI) 4H-SiC wafer (Norstel). The proton beam writing (PBW) were done to introduce ensemble V_{Si} in SiC at the TIARA, QST Takasaki. The 3MV single-ended particle accelerator was utilized to form a stable focused ion beam with a diameter of 1 μm . The sample holder was equipped with a precision two-axis stage and controlled the position of the SiC wafer accurately. The beam current through the sample holder was monitored during irradiation to register fluctuations and deviations from the intended current and fluence, while precise beam currents were measured before and after each irradiation.

The concept of long-term optical data storage in SiC is

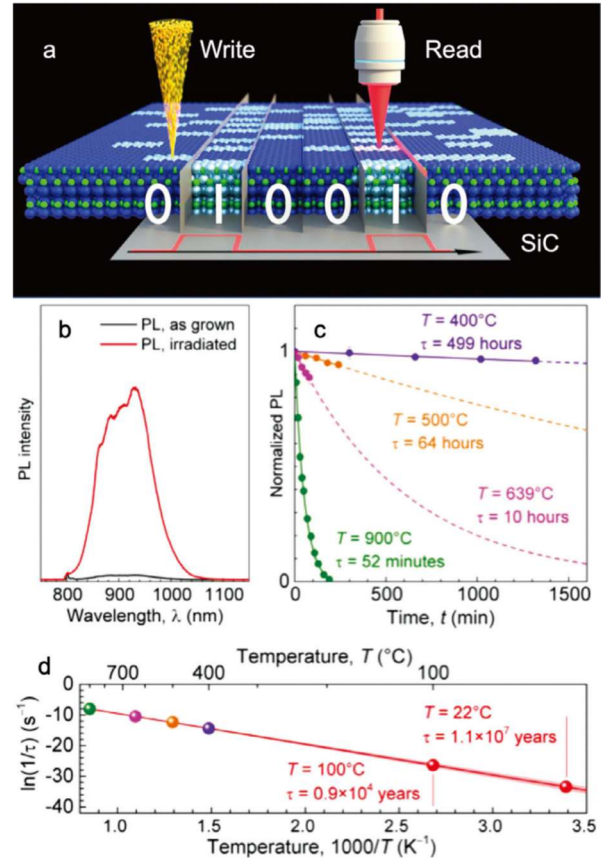


Fig. 1 (a) Concept of this study. (b) Typical PL spectra for V_{Si} . (c) the decay of the intensity of PL for V_{Si} . (d) Arrhenius plot of the PL decay rate $1/\tau$ [2].

shown in Fig. 1 (a). The information is written in V_{Si} s, which are optically active atomic defects, using the PBW technique. Then, the information is retrieved using PL from V_{Si} . PL spectra for V_{Si} for as grown and irradiated 4H-SiC are shown in Fig. 1 (b). The laser with a wavelength of 785 nm is used for excitation. The decay of PL intensity for V_{Si} at different temperatures is shown in Fig. 1 (c). The solid lines are fits to $\exp(-t/\tau)$ and the dashed lines represent extrapolation to longer annealing time t . The Arrhenius plot of the PL decay rate $1/\tau$ is shown in Fig.1 (d). The shaded area around the solid line represents the tolerance of the extrapolated values. At room temperature, the information in V_{Si} can be stored for more than ten million years.

References

- [1] S. Motoki *et al.*, J. Appl. Phys. **133**, 154402 (2023). DOI: 10.1063/5.0139801
- [2] M. Hollenbach *et al.*, Functional Materials 202313413 (2023). DOI: 10.1002/adfm.202313413.

P1-2 Spin-photonics in 2D Materials Project

Leader : SAKAI Seiji



Our project aims to develop novel spin-photonics devices for future information technology applications by taking advantages of the low dimensionality and quantum electronic properties of two-dimensional (2D) materials and related low-dimensional nanostructures. Advanced material techniques available at QST enable us to control and design the local atomic structures and spin-/photon-related properties in low-dimensional systems.

During this fiscal year, we developed a new technique of resistivity-detected electron spin resonance (RDESr) enabling direct observation of spin dynamics in graphene at ultra-high energy resolution ($\sim\mu\text{eV}$) in collaboration with Tohoku University (K. Hashimoto and Y. Hirayama) and demonstrated the introduction of a finite energy gap in monolayer graphene grown on sapphire substrate [1]. This finding serves as a basis for realizing efficient charge and spin transport control in graphene-based nanoelectronics and spin-photonics devices.

Observing Zero-Field Energy Gap in Graphene Grown on Sapphire Substrate

Introducing an energy gap into graphene is a pivotal challenge for the developing graphene-based devices. In this study, we demonstrated the energy gap formation in monolayer graphene, which was grown by chemical vapor deposition (CVD) on a sapphire substrate, using the newly developed resistively-detected electron spin resonance (RDESr) technique [1].

We conducted RDESr measurements by recording the longitudinal resistance ($R_{xx,v}$) under microwave irradiation at a fixed frequency (ν) while sweeping the magnetic field (B) either perpendicular ($\perp B$) or parallel ($\parallel B$) to the sample plane, within a 4 K cryostat.

Initially, the RDESr measurement was performed at $\nu = 27$ GHz. To extract the microwave-induced component, the background resistance ($R_{xx,bg}$) was subtracted from the $R_{xx,v}$, obtaining ΔR_{xx} . Figure 1 shows the ΔR_{xx} curves obtained with $\perp B$ (upper) and $\parallel B$ (lower). Both curves exhibit distinct peaks near $B = \pm 1.0$ T, marked by blue arrowheads. Notably, the ΔR_{xx} curve for $\parallel B$ displays shoulder features on both sides of the main peak, as indicated by red arrowheads.

To further investigate these peak and shoulder features, RDESr measurements under $\parallel B$ were carried out at various frequencies. Figure 2(a) shows a gray-scale map of the derivative of ΔR_{xx} with respect to B ($d(\Delta R_{xx})/dB$) as functions of ν and B . This map reveals that there are three spectral features as evidenced from the three parallel lines. This is supported by the plots the corresponding $\nu - B$ positions in Figure 2(b). A linear fit of the middle line (blue) yielded a slope of 27.9 ± 0.6 GHz/T and verifies that the extrapolated line crosses the origin. This indicates that the

observed peak corresponds to the ESR signal, expected to show simple Zeeman gap in the magnetic field, *i.e.*, $h\nu = g\mu_B B$ (h : Planck's constant, μ_B : Bohr magneton), with a corresponding g -factor of 2.00 ± 0.05 . Conversely, significant deviations from the origin at zero field by 4.6 ± 0.3 GHz (higher) and -5.0 ± 0.6 GHz (lower) were observed for higher and lower red lines, respectively. This deviation shows an energy gap $\Delta \sim 20$ μeV , indicating band splitting in graphene at zero field. The similar splitting has been reported in graphene on hexagonal boron nitride [2, 3], which were attributed to sublattice splitting due to symmetry breaking.

Our findings demonstrate the potential for the substrate-induced band gap tuning and spintronic functionalization of graphene beyond hBN substrates.

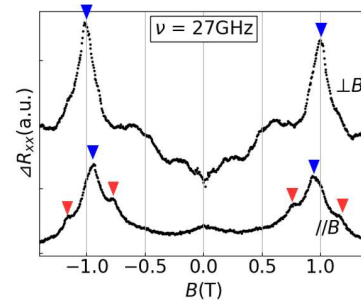


Fig. 1 B -field dependence of ΔR_{xx} ($= R_{xx,v} - R_{xx,bg}$) at $\nu = 27$ GHz. The B -field direction with respect to the sample plane is indicated in the figure. The blue (red) arrowheads indicate main peak (shoulder features).

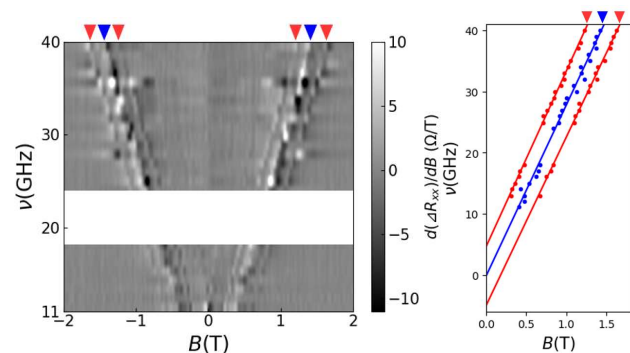


Fig. 2 $\nu - B$ map of ΔR_{xx} signal under $\parallel B$. (a) Gray-scale map of derivative amplitude: $d(\Delta R_{xx})/dB$. (b) Peak positions of ESR signal (blue dots) and satellite signal (red dots) with linear fitting curves. The blue (red) arrowhead indicates main signal (shoulder features).

References

- [1] Y. Hiraga, K. Kaneta, S. Li, Y. Hirayama, S. Sakai, K. Hashimoto, International Conference on the Physics of Semiconductors (ICPS) 2024, Ottawa, Canada, 2024.
- [2] U. R. Singh, *et al.*, Phys. Rev. B. 102, 245134 (2020). DOI: 10.1103/PhysRevB.102.245134
- [3] C. Bray, *et al.*, Phys. Rev. B. 106, 245141 (2022). DOI: 10.1103/PhysRevB.106.245141

P1-3 Laser-cooled Ion Research Project

Leader : NARUMI Kazumasa



We, laser-cooled ion research project, have two objectives: One is to develop an ultrahigh-precision single-ion-implantation system to create any number of nitrogen-vacancy (NV) centers at any place in diamond. The other is to establish fundamental technologies to realize a quantum computer based on ion traps with $^{133}\text{Ba}^+$. The key techniques for both the objectives are trapping ions and laser cooling.

Design of an apertureless two-stage acceleration lens for a single-ion implantation system [1]

NV centers are one of the key quantum bits (qubits) for quantum information technologies. In order to make the best use of them, it is required to create any number of NV centers at any place with precision of a few tens of nanometers. Our ultrahigh-precision single-ion-implantation system consists of a linear Paul trap and an electrostatic focusing lens. A linear Paul trap as an ion source can provide us with a single ion almost at rest; such an ion makes it possible to conduct deterministic implantation with precision of a few tens of nanometers.

As a focusing lens, a two-stage acceleration lens has been selected. We designed it by performing numerical simulations to obtain parameters determining lens characteristics: especially, the second-stage lens. In the design, we based the new acceleration lens on our previously developed two-stage acceleration lens. In addition, the new acceleration lens must be without an aperture and with a magnification of $\ll 1$ to realize the deterministic implantation.

The total magnification of the new two-stage acceleration lens was numerically obtained as 0.006. The calculation demonstrated that the beam width for a 14-keV single nitrogen ion was 4.5 nm including intrinsic aberrations at full width at half maximum and that the working distance, the distance between the second-stage lens and a sample, was 9.3 nm. Specifications of the new two-stage acceleration lens are summarized in Table 1.

Trapping-ion experiment using non-RI Ba ions

The use of trapped ions for storing and manipulating

quantum information has attracted attention for its high fidelities compared to other physical layer implementations such as superconductor. In particular, the ions having the lowest non-zero nuclear spin $I = 1/2$ are known to have many advantages [2] over those having other nuclear spin values $I \neq 1/2$ because of their simple hyperfine structure and their ease of quantum state manipulation. Among such a few ions capable of laser cooling, e.g. $^{111}\text{Cd}^+$, $^{171}\text{Yb}^+$, we have selected a long-lifetime (10.6 yr) radioactive $^{133}\text{Ba}^+$ [3] as the quantum information carrier and started constructing an experimental system for this isotope. Despite its difficulty in treating the radioactive isotope (RI), the Ba^+ have main transitions in the visible spectral range and have metastable D states, appropriate for a high-fidelity scalable information processing system.

The trapping and cooling experiment using our first trap system, "Trap-I (Hiroshima-type)" was conducted with non-RI Ba. In the experiment, neutral Ba atoms provided via Ohmic heating of an oven were ionized with an electron beam. The ions inside the trap, if present, were subsequently extracted, detected by a channel electron multiplier, and analyzed with a time-of-flight method. By appropriately choosing the amplitude and frequency of the radio frequency (RF) voltage applied onto the trap electrodes, we confirmed that Ba ions were successfully loaded and trapped in the trap.

Next, we tried laser cooling and observing the fluorescence from the trapped Ba^+ . No fluorescence signals, however, have been observed so far for some reason. Possible reasons for this are insufficient densities of Ba vapor and of electrons, presence of undesired ion species other than Ba^+ , and insufficient cooling in the radial direction.

References

- [1] Y. Ishii *et al.*, Nucl. Instrum. Methods B 541, 200 (2023). DOI: 10.1016/j.nimb.2023.05.021
- [2] S. Olmschenk *et al.*, Phys. Rev. A 76, 052314 (2007). DOI: 10.1103/PhysRevA.76.052314
- [3] J.E. Christensen *et al.*, npj Quantum Inf 6, 35 (2020). DOI: 10.1038/s41534-020-0265-5

Table 1 Specifications of the new two-stage acceleration lens.

Ion source	Beam width (μm)	0.54
	Divergence angle (rad)	3.55×10^{-5}
First acceleration lens	Incident beam energy (keV)	0.5
	Applied voltage (V1) (kV)	2.35
Second acceleration lens	Incident beam energy (keV)	2.85
	Applied voltage (V2) (kV)	11.15
Total magnification		0.006
Intrinsic aberrations	Spherical (nm)	1.45
	Chromatic (nm) [†]	0.13
Beam width with aberration (FWHM) (nm)		4.5
Working distance (mm)		9.3

P1-4 Quantum Optical and Spin State Control Project

Leader : KOHDA Makoto



The goal of the Quantum Optical and Spin State Control Project is to bridge the gap between quantum and classical technologies necessary for the future quantum information society. We focus on the precise control of quantum states of single electron spins by exploiting defects in wide-gap semiconductors such as diamond and SiC. We are also working on the precise control of spin and magnetic structures for parallel computing and efficient magnetization reversal based on electron spin waves. Our research interests range from the creation of two-dimensional materials to the optical and electrical control of spin defects, as well as quantum device applications utilizing the spin degrees of freedom of semiconductors.

Highly sensitive temperature measurement by SiC-based spin defects

Quantum sensing using optically addressable defects in wide-band-gap materials, *i.e.*, spin defects, is a promising technique because it can measure various physical quantities. In quantum sensors using silicon vacancy in silicon carbide (SiC), it has been challenging to realize highly sensitive temperature detection because of the no temperature sensitivity for the ground state (GS). In addition, the excited state (ES) only shows weak temperature dependence in the optically detected magnetic resonance (ODMR). We propose and demonstrate a new temperature sensing method, namely simultaneously resonated ODMR (SRODMR), which can measure temperature with higher signal intensity than the conventional ES ODMR. As shown in Fig. 1(a), conventional ODMR contrast is shown as blue circle, while the proposed SRODMR enhances the signal contrast. Such a large enhancement of the ODMR contrast is based on the phenomenon that the GS ODMR contrast is modified under simultaneous resonance of GS and ES. We demonstrate that SRODMR improves signal intensity by 1 order of magnitude compared with ES ODMR, which leads

to higher-precision temperature measurements. Figure 1(b) shows the temperature measurement by zero-field splitting in SRODMR. We enlarge the temperature region to measure by spin defects in SiC based on our proposed technique.

Deterministic current-induced perpendicular switching in epitaxial Co/Pt layers without an external field

Current-induced spin-orbit torques (SOTs) have emerged as an important technique for precisely controlling the magnetic orientation and magnetic textures. SOT-induced magnetization switching with perpendicular magnetic anisotropy is required for the future memory technology. However, it generally requires an external field to break the rotational symmetry for the deterministic switching. Here, we propose and demonstrate new mechanisms to eliminate the external magnetic field. Figure 2(a) shows the device structure for magnetization switching. We show current-induced external field-free switching of an epitaxial MgO/Pt/Co trilayer with an extremely large perpendicular anisotropy in excess of 3 Tesla. Figure 2(b) compares the epitaxial and polycrystalline Co/Pt for the switching property. It is found that field free switching occurs only for epitaxial films due to the interplay of strong SOTs, local anisotropy fluctuations, and the Dzyaloshinskii-Moriya interaction. Since Co/Pt systems is well known for the field free switching by optical excitation, it would be promising for integrating the photonic and electronic circuits with non-volatile memory technology proposed here.

References

- [1] Y. Yamazaki, *et al.*, Physical Review Applied **20**, L031001 (2023). DOI: 10.1103/PhysRevApplied.20.L031001
- [2] J. Ryu, *et al.*, Advanced Functional Materials 2209693 (2023). DOI: <https://doi.org/10.1002/adfm.202209693>

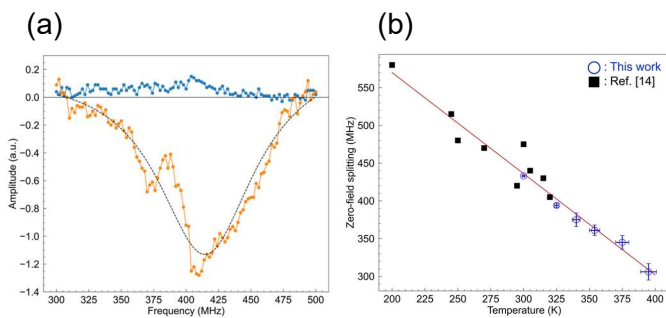


Fig. 1 (a) ODMR contrast in spin defect in SiC for conventional ODMR method (blue circles) and SRODMR method (orange circles). (b) Temperature measurement based on the zero-field splitting in SRODMR method.

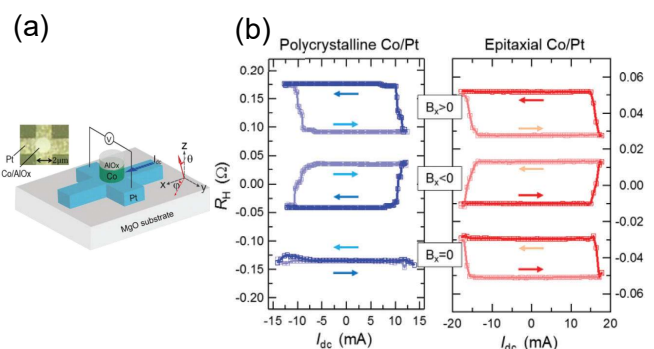


Fig. 2 (a) Schematic view of an epitaxial Co/Pt structure for magnetization switching. (b) Current induced magnetization switching for polycrystalline and epitaxial Co/Pt films

P1-5 Quantum Materials Theory Project

Chief : MATSUSHITA Yu-ichiro



To further accelerate the adoption of quantum devices, the challenge is to understand and improve device properties in detail and to reduce noise under real-world conditions. The Quantum Materials Theory Project will analyze the fundamental properties of quantum devices, search for new materials for quantum devices, and develop protocols for noise reduction under real-world conditions from an approach based on theoretical simulations in collaboration with the experimental groups at the Quantum Materials and Applications Research Center (QUARC).

Advancing Fault-Tolerant Quantum Computing: A Breakthrough in Quantum Chemistry Calculations

Recent advances in quantum computing, particularly in hardware and error correction technologies, have accelerated the development of quantum algorithms. While research has primarily focused on Noisy Intermediate-Scale Quantum (NISQ) devices, the goal of achieving Fault-Tolerant Quantum Computing (FTQC) is becoming a reality, with global roadmaps emerging. Among FTQC applications, quantum chemical calculations are considered a promising area for commercial viability, as these calculations are inherently governed by quantum mechanics.

In our research, we used a hybrid approach, combining a quantum computer with the supercomputer "ohtaka" at the University of Tokyo to perform quantum chemical calculations. First, we performed coarse computations on a 300-atom system using density functional theory (DFT) and applied the downfolding method to reduce problem size without sacrificing accuracy. We then executed FTQC algorithms on the Quantinuum H1-1 ion-trap quantum computer, using a quantum error detection (QED) code called Iceberg to mitigate quantum noise and enable high-precision FTQC execution.

This marked the world's first successful execution of FTQC combined with QED on a real quantum computer. Using the Probabilistic Imaginary Time Evolution (PITE) method, developed by our group, we achieved high-precision calculations of complex defects' ground and excited states. Our results showed that even with current quantum hardware, we achieved 98% accuracy compared to an ideal FTQC machine, a significant milestone toward practical quantum computing.

This research, published in *Physical Review Applied*, demonstrates the growing potential of quantum computing hardware and marks a major step in the application of FTQC algorithms in real-world problems.

Qubit Encoding: Generative AI-designed Quantum Circuits

Recent advancements in quantum computing emphasize the need for efficient qubit encoding to improve computational accuracy and reduce errors. Before executing simulations, data must be encoded into the quantum system, a step that poses challenges without improved efficiency. Traditional methods of designing quantum circuits for encoding are complex and computationally expensive as the number of qubits increases. However, generative AI now offers a solution to automate and enhance this process, enabling more efficient and scalable quantum circuit designs.

In this study, we created a custom database of one million entries containing quantum circuits and data sets for encoding. We trained a transformer-based AI model to generate novel qubit encoding circuits, which were simulated and benchmarked against traditional designs. The results show that generative AI successfully generates quantum circuits, with 10% of circuits produced by the AI being shallower than traditional methods. These shallower circuits offer better fidelity due to increased robustness against noise.

This research marks a significant step in automating and optimizing quantum circuit design. As quantum hardware improves, integrating AI-driven methodologies could lead to breakthroughs in fault-tolerant quantum computing and scalable applications, paving the way for practical quantum computing solutions.

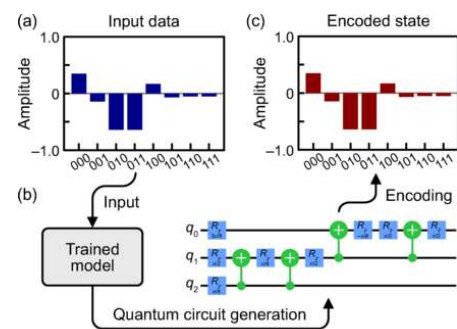


Fig.1 Schematic of flow of quantum circuit generation by generative AI.

References

- [1] H. Nishi *et al.*, *Phys. Rev. Applied*. **23**, 034016(2025). DOI: 10.1103/PhysRevApplied.23.034016
- [2] S. Daimon and Y. Matsushita, *Phys. Rev. Applied* **22**, L041001 (2024). DOI: 10.1103/PhysRevApplied.22.L041001

P1-6 Rare-earth Quantum Device Project

Chief : SATO Shin-ichiro



Rare-Earth Quantum Device Project aims to develop quantum devices based on gallium nitride (GaN), which has high quality and advanced microfabrication and device technologies, and rare-earth ions (RE³⁺), which have excellent characteristics as qubits and single photon sources. RE:GaN quantum devices have the potential to realize "electrically controlled single photon sources (SPSs) in the optical communication wavelength band at room temperature," "on-chip quantum entangled light sources," and "real-time diagnostics inside GaN devices by quantum sensing," which have not been achieved to date. Currently, our project studies ion implantation and post thermal annealing for high efficiency optical activation of implanted RE ions in GaN, local atomic structure of implanted RE ions, development of quantum sensing using RE ions in GaN, and enhancement of spontaneous emission of implanted RE ions in GaN by coupling to photonic crystal.

Purcell Enhancement of ${}^4F_{3/2} - {}^4I_{9/2}$ Emissions of Nd³⁺ in GaN Photonic Crystal L3 Cavity

Neodymium (Nd)-doped GaN (GaN:Nd) exhibits near-infrared (NIR) emission from the 4f-4f transition that is temperature insensitive, sharp, and stable. The photon emission is electrically controllable, and the well-developed GaN platform allows integration into more complex devices. These superior optical and optoelectronic properties are suitable for SPSs. To realize GaN:Nd SPS, our project investigates the photon emission rate enhancement of Nd ions in GaN coupled to a photonic crystal (PhC) cavity.

Nd ions were implanted in the center of the GaN PhC-L3 cavity, as shown in the inset of Fig. 1(a), using a resist film with 400 nm diameter holes. Post-implantation thermal annealing was performed at 1200 °C for 2 min in N₂ atmosphere to optically activate the Nd ions. The optimal design parameters (hole spacing a , and hole radius r) were determined by FDTD simulation. Time-resolved photoluminescence was characterized at room temperature to investigate the change in luminescence lifetime of Nd³⁺ ions due to the coupling of the PhC-L3 cavity.

Figure 1(a) shows the representative PL decay curves of the ${}^4F_{3/2} - {}^4I_{9/2}$ transition of Nd³⁺ ions with and without PhC-L3 cavity. The luminescence transition lifetime, which was derived by the single exponential function fitting, showed shorter values for Nd-PhC than that for Nd without PhC. The lifetimes of twelve Nd-PhCs are shown in Fig. 4(b). While the lifetimes of Nd without PhC were almost unchanged (127 μ s), a large variation in lifetime was found for the twelve Nd-PhCs. The reduction ratio of the transition lifetime due to the Purcell effect is linearly related to the Q-value. Figure 1(b) shows a positive correlation between the Q-value and the ratio of T_{noPhC} to T_{PhC} , where T_{noPhC} and T_{PhC} represent the transition lifetimes of Nd without PhC and Nd-

PhC, respectively. This result strongly indicates that the decrease in lifetime was caused by an increase in the spontaneous emission rate of the implanted Nd ions, resulting in an increase in PL intensity. This is attributed to the Purcell effect based on the optical coupling of Nd³⁺ ions to the PhC-L3 cavity [1].

This work was supported by JST FOREST Program (Grant No. JPMJFR203G, Japan), JSPS KAKENHI (Grant Nos. JP18H01483; JP22H03880, Japan), and the Foundation for Promotion of Material Science and Technology of Japan. Part of this study was conducted at the NIMS Nanofabrication Platform, supported by "Advanced Research Infrastructure for Materials and Nanotechnology in Japan (ARIM)" of the Ministry of Education, Culture, Sports, Science and Technology (MEXT), Proposal No. JPMXP1223NM0008.

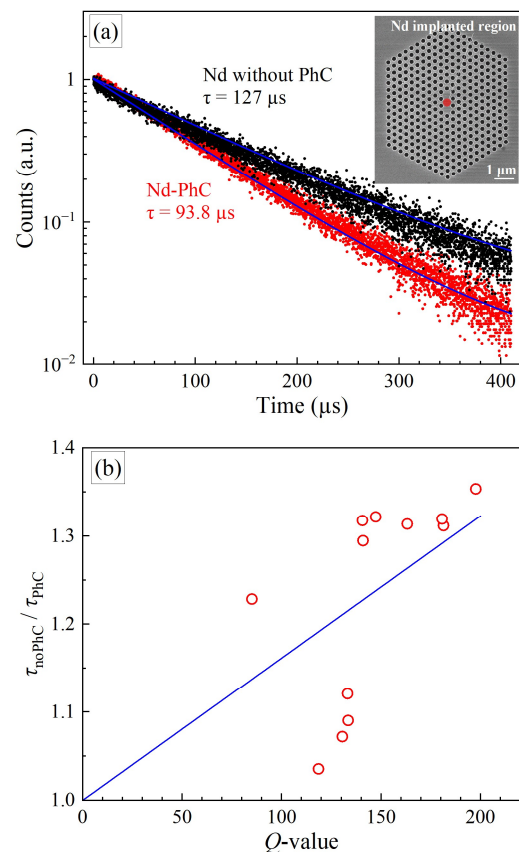


Fig. 1 (a) PL decay curves of a Nd implanted region without the PhC-L3 cavity (black) and a Nd-PhC (red). The blue lines show the single exponential fit and the inset illustrates the typical SEM image of Nd-PhC. (b) Ratio of transition lifetime of the Nd implanted region without PhC (T_{noPhC}) to the Nd-PhC (T_{PhC}) as a function of Q-value. The blue line represents the linear fit with an intercept of 1.

Reference

- [1] S.-I. Sato, T. Oto, Appl. Phys. Express **17**, 072001 (2024). DOI: 10.35848/1882-0786/ad5bbd

P1-7 Quantum Materials Ultrafine Fabrication Project

Chief : YAMAMOTO Hiroki



Project “EUV Ultra-fine Fabrication” has been developing the functional polymer materials such as high-performance resist materials for extreme ultraviolet (EUV) and next generation EUV lithography. We have investigated dependence of dissolution kinetics of main-chain scission type resists on molecular weight and transient swelling during development of resist materials such as poly(methyl methacrylate) resist by using quantum beams such EUV and electron beam (EB). We aim to develop resist materials for EUV lithography and conduct fusion between top-down and bottom-up nanofabrication for next generation EUV lithography. We report herein two recent study: study on resist performance of inorganic-organic resist materials for EUV and EB lithography and competitive coexistence of ferromagnetism and metal-insulator transition of VO₂ nanoparticles.

Study on resist performance of inorganic-organic resist materials for EUV and EB lithography [1]

In the realization of further miniaturization at scales of 10 nm and below in semiconductor devices, it is essential to get the new resist design such as hybrid inorganic-organic resist materials for ionizing radiation to clarify the effect of metal resist structure on resist performances.

In this study, some hybrid inorganic-organic resist materials known as metal-oxo clusters were synthesized and their lithographic characteristics were investigated to clarify relationship between resist performance such as sensitivity and resolution and their absorption coefficient or cross-section and their density of elements by using EUV and EB exposure. Fig.1 shows SEM micrographs of line & space patterns delineated on (a) Ti-based and (b) Zr-based oxo clusters films. In the case of all hybrid inorganic-organic oxo clusters, the phenomena induced by EB account for a negative tone resist because the exposed areas undergo a crosslinking reaction. Although the exposure dose was not optimized, the patterns of Ti-based and Zr-based oxo clusters showed a 100 and 50 nm line and space patterns, respectively. They were obtained at the dose of 250 and 80 $\mu\text{C}/\text{cm}^2$, respectively. Our results indicated that the sensitivity in Zr-based oxo clusters was higher than those of Ti-based oxo clusters in both EB and EUV exposure. We clarified that it is very important for the new resist design such as hybrid inorganic-organic resist to increase photo-absorption cross section and density of elements for EUV and EB without degradation of film quality. Also, the size and homogeneity of building block and film quality is very important for resist performance of hybrid inorganic-organic resist materials. Furthermore, it is clarified that the etch durability of metal oxo clusters is higher than conventional resist materials and they are much more increased by annealing them at 800 °C.

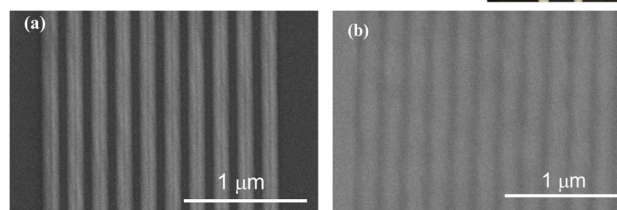


Fig. 1 SEM micrographs of line & space patterns delineated on (a) Ti-based and (b) Zr-based oxo clusters using EB.

Competitive coexistence of ferromagnetism and metal-insulator transition of VO₂ nanoparticles [2]

One simple way to observe the metal-insulator transition (MIT) of VO₂ nanoparticles is to measure the variations of electric resistance values. However, measuring electric resistance by attaching electrodes to VO₂ nanoparticles is difficult. Therefore, there have been no experimental results that measure both the magnetic and electric properties of VO₂ nanoparticles.

In this study, we prepared VO₂ nanoparticles by milling VO₂ powder, and VO₂ samples were fabricated by bridging between submicron-sized nanogap electrodes with the VO₂ nanoparticles. Nanogap electrodes with Ti and Au were created on substrates using 100 kV electron beam

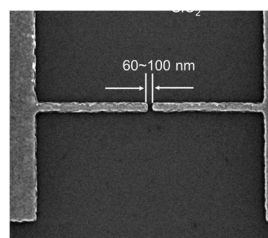


Fig. 2 SEM image of nanogap electrodes.

lithography and a metal evaporator. Fig. 2 shows the SEM image of typical nanogap electrodes. The distances between the two electrodes were 60 – 100 nm. Then, the prepared VO₂ nanoparticles were dissolved in ethanol by stirring with ultrasonic waves, and a VO₂ solution was created. Next, the VO₂ solution was sprayed onto the SiO₂, where the nanogap electrodes were located and VO₂ transistors were fabricated. Then, the temperature dependence of the resistance of the VO₂ samples was measured. Although MIT was also obtained in the temperature dependence of the resistance of the VO₂ transistors, it was exhibited over a wider temperature range than that of bulk VO₂. This wider hysteresis of MIT was because the VO₂ particles had not only nanometer sizes but also dispersed sizes due to aggregation.

References

- [1] H. Yamamoto *et al.*, *Jpn. J. Appl. Phys.* **64** 04SP87 (2024). DOI: 10.35848/1347-4065/ad38c5
- [2] T. Hatano *et al.*, *Jpn. J. Appl. Phys.* **63** 04SP07 (2024). DOI: 10.35848/1347-4065/ad2d04

Part I

2. Materials Science

P2-1	Hydrogen Energy Conversion Device Project	10
	Leader : SAEKI Morihisa	
P2-2	Nanostructured Polymer Materials Project	11
	Leader : ZHAO Yue	
P2-3	Energy Regeneration Materials Project	12
	Leader : SEKO Noriaki	
P2-4	Advanced Biodevice Project	13
	Leader : TAGUCHI Mitsumasa	

P2-1 Hydrogen Energy Conversion Device Project

Leader : SAEKI Morihisa



The Green Growth Strategy has proposed the realization of carbon neutrality by 2050, and the hydrogen energy market has been expanding rapidly. To meet these demands our project develops materials that are useful for hydrogen production, hydrogen storage and hydrogen fuel cells and proposes new devices incorporating the developed materials. One of our targets is development of electrocatalysts, which plays a crucial role in oxygen reduction reaction (ORR) in the hydrogen fuel cell (Fig. 1). Presently, a platinum (Pt) supported carbon catalyst shows high performance in ORR and is mainly used in the hydrogen fuel cell. The Pt-supported carbon, however, is expected to be replaced by more available materials because its price drastically depends on world situation. Thus, we plan to create ceramic catalysts (oxide, carbide, etc.) activated by quantum beam functionalization (ion, electron and laser beam irradiation) and decrease the usage of Pt in the fuel cell.

There is not much information about the effect of the quantum beam functionalization on the ceramic materials. In the first step, we studied the effect of the ion beam irradiation on the carbon in the Pt-supported catalyst and obtained fundamental information on the quantum beam functionalization in the ceramics, as described below.

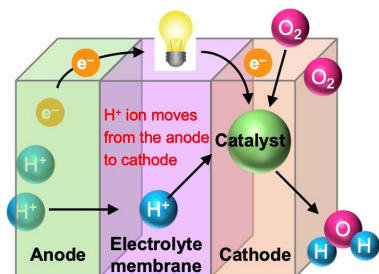


Fig. 1 The Schematic drawing of fuel cell. Electricity is generated by ORR ($O_2 + 4H^+ + 4e^- \rightarrow 2H_2O$) on the catalyst.

Effect of ion irradiation after platinum nanoparticles deposition onto glassy carbon substrates

In the Pt-supported carbon catalyst, we studied the effect of Ar^+ -irradiation after the deposition of platinum nanoparticles (PtNPs) onto glassy carbon (GC) substrates [1]. The relationship between the microstructural evolution and the ORR activities was investigated by transmission electron microscopy (TEM) and X-ray photoelectron spectroscopy (XPS). The TEM image showed that the average size of PtNPs on GC substrate slightly increased after the irradiation up to 1.0×10^{15} ions/cm² and decreased afterwards. The XPS measurement, which is surface sensitive measurement, exhibited that the amount ratio of Pt to carbon (C) decreased proportionally with increasing the Ar^+ fluence. It suggests that a part of PtNPs and/or small PtNPs (<1 nm) might be buried in carbon substrates. Figure

2 shows relationship of the reduction rate of Pt/C with the reduction rate of the electrochemical active surface area (ECSA). The slope=1 means that the reduction rate of ECSA is equal to the reduction rate of amount ratio of Pt to carbon. Although the reduction rate of Pt/C decreased proportionally with increasing the Ar fluence, the ECSA values did not change up to the reduction rate of Pt/C=38% (1.0×10^{15} ions/cm²). We assume that interaction between Pt and C in the Pt/GC interface is enhanced by the ion irradiation up to the fluence of 1.0×10^{15} ions/cm². It means that the ion irradiation improves the ORR activities below the fluence of 1.0×10^{15} ions/cm².

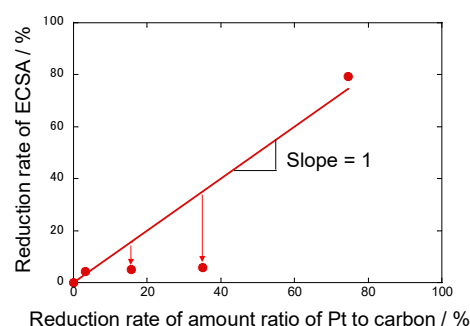


Fig. 2 The relationship between the reduction rate of ECSA and amount ratio of Pt to carbon evaluated from XPS spectra.

Weakened Oxygen Adsorbing Pt-O Bond of Pt Catalyst Induced by Vacancy Introduction into Carbon Support

A Pt-supported carbon catalyst, which is prepared by deposition of PtNPs on Ar^+ -irradiated GC substrate, shows the increase of ORR activity [2]. It is attributed to the introduction of vacancies in the GC substrate by the Ar^+ irradiation. In this work, to obtain the information on the oxygen adsorption states in the catalyst, which are the first step in the ORR process, we performed *in situ* X-ray absorption fine structure (XAFS) measurement [3]. The XAFS spectra of the Pt L_3 edge shows a decrease in the Pt-O antibonding level by the ion irradiation. This suggested that the introduction of vacancies in the carbon support would result in weak Pt-O bonds assumable through the stronger Pt-C interaction, which was considered to enhance the ORR activity of the deposited PtNPs. Our results suggest that the introduction of vacancies in the support is a useful way to improve the ORR activity.

References

- [1] T. Taguchi *et al.*, Nucl. Inst. Methods Phys. Res. B **549**, 165286 (2024). DOI: 10.1016/nimb.2024.165286
- [2] T. Kimata *et al.*, Phys. Rev. Mater. **6**, 035801 (2022). DOI: 10.1103/PhysRevMaterials.6.035801
- [3] H. Okazaki *et al.*, J. Phys. Chem. C **127**, 23628 (2023). DOI: 10.1021/acs.jpcc.3c04117

P2-2 Nanostructured Polymer Materials Project

Leader: ZHAO Yue

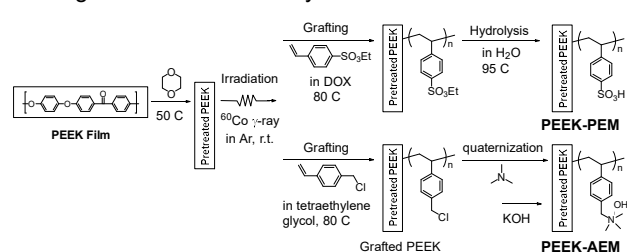


Nanostructured Polymer Materials Project is developing advanced functional polymer materials, such as polymer electrolyte membrane, separation membranes and ionomers for energy devices such as fuel cells, electrolyser and metal-air batteries, by quantum beam technologies. We have synthesized the proton- and anion-conducting electrolyte membranes (PEMs and AEMs) and the hydrogen permselective membranes using γ -rays and electron beams, and characterized their nanostructures using scattering, imaging and simulation techniques. We report herein our latest research progress on the development of advanced polymer membranes through a deep understanding of structure-property correlations.

Development of advanced poly (ether ether ketone)-based polymer electrolyte membrane using radiation-induced graft polymerization (RGP)¹

Using RGP technique, for the first-time we successfully synthesized both PEM and AEM using poly (ether ether ketone) (PEEK) as a base polymer, which is regarded as the most promising aromatic hydrocarbon material for the long life-time device operation due to its excellent mechanical stability and high gas barrier property at high temperature.

The PEEK base films were first immersed in 1, 4-dioxane (DOX) at 50°C for 18 hours, and then pre-irradiated with ⁶⁰Co γ -ray at Takasaki Institute for Advanced Quantum Science, QST, at room temperature in argon atmosphere with a total dose of 160 kGy. Next, the pre-irradiated PEEK films were immersed in the monomer solution for graft polymerization, followed by hydrolysis or quaternization to make PEMs or AEMs, respectively, as shown in Scheme 1. The grafted-PEEK membrane shows a grafting degree (GD) up to 150%, and the corresponding PEMs and AEMs were found to possess high ion conductivity >100 mS/cm, and high mechanical stability.



Scheme 1 Synthesis route of PEEK-based PEM and AEM.

Effects of functional graft polymers on phase separation and ion-channel structures in AEMs analyzed by SANS partial scattering function²

The partial scattering function (PSF) analysis through the contrast variation small-angle neutron scattering (CV-SANS) technique is applied to characterize structures of

radiation-grafted AEMs, prepared by graft copolymerization of 2-methyl-*N*-vinylimidazolium (Im) and styrene (St) monomers with Im/St ratios of 62/38 and 26/74 (denoted as AEM_IS64 and AEM_IS37), on the poly(ethylene-co-tetrafluoroethylene) (ETFE) base polymer (BP).

The PSF self-terms can be expressed by the combination of mass fractal, Teubner-Strey, Guinier-Exponential, and Hard-Sphere structural models to give precise structures such as shape, size and distribution of individual domains of hydrophobic BP, hydrophilic graft-polymer (GP) and water (W). For AEM_IS64, ion-channels made of GP/W domains show coexistence of bicontinuous and isolated spheres with a mean separation distance of 33-34 nm and a radius of 4.0 nm, respectively, as shown in Figure 1. Furthermore, in a low q -region, slightly larger fractal dimension for GP (~1.6) than those of BP and W (~1.1) strongly supports the previously proposed “conducting and non-conducting two-phase structure” because only GP distributes in both phases. In AEM_IS37, GP/W and BP domains show the ion-channel network structure with random particles having an average radius of gyration of ~10.0 nm, and hard-sphere model fitting in the high- q region confirms the formation of nanophase separated water-rich puddles in ion-channels with a size of ~3.8 nm in that accelerating alkaline degradation.

This work certifies the unique capability of PSF analysis over the conventional intensity analysis to visualize the entire structure of individual components in the graft-type AEMs and provide mechanistic insights into the effects of functional graft polymers on phase separation and ion-channel structures. This in turn can help in the design of high-performing AEMs for a wide range of energy conversion applications.

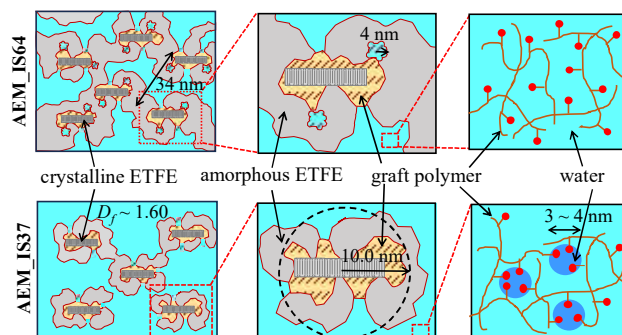


Figure 1 Schematic of the hierarchical structure of BP, GP, and W domains in the hydrated AEM_IS64 and AEM_IS37 at (a) large-scale; (b) middle-scale; and (c) small-scale.

References

- [1] S. Hasegawa et al., Japanese Patent Application No. 2023-161783 (2023).
- [2] K. Yoshimura et al., *Macromolecules* **57**, 1998 (2024). DOI: 10.1021/acs.macromol.3c01897.

P2-3 Energy Regeneration Materials Project

Leader : SEKO Noriaki



In our Project “Energy Regenerative Materials”, we are developing high-performance energy regenerative materials by radiation graft polymerization using electron beams and gamma rays. To accelerate this research, we used the state-of-the-art CREST (Conformer-Rotamer Ensemble Sampling Tool) software package at the GFN-xTB level to calculate the structure, vibrational frequency, and non-covalent interactions in the molecular system. By providing explanatory variables for radiation graft polymerization under emulsion conditions, we aimed to obtain the target properties of the grafted materials. We also modified natural abaca fibers by radiation graft polymerization to develop high-strength unsaturated polyester resin (UPR)/abaca fiber composites.

Comprehensive understanding of emulsion radiation graft polymerization through GFN-xTB-based calculations [1]

Using the state-of-the-art CREST software package, we can deeply understand the emulsion radiation graft polymerization by calculating the molecular properties of the monomer solution primarily at the semi-empirical GFN-xTB level. As a result, we obtained the effective reactivity predictions by establishing machine learning models and revealed the important factors of the radiation graft polymerization in a chemically interpretable form.

As shown in Figure 1, insights into the monomers used for radiation graft polymerization were gained by calculating explanatory variables (solvation free energies of the monomer in water and in hexane, radius, dipole moments, and conformational entropy of the monomer) at the GFN2-xTB level using the CREST software package. When methacrylate monomers were used in radiation graft polymerization, the above parameters provided the dynamic properties of the monomer considering the grafting conditions using the CREST software package. In this way, a predictive model for the grafting of methacrylate monomers was established. In addition to predicting the grafting degree, the important factors in the grafting processes could be quantified as explanatory variables in the machine learning model, making them easily interpretable by chemists. This revealed that the size and rigidity of the monomer are crucial for monomer design in radiation graft polymerization. It is expected that the next generation of material sciences could be driven by machine learning models, allowing chemists to avoid blind experiments.

Development of high-strength UPR/abaca fiber composites by radiation graft polymerization [2]

To enhance the interface of UPR/abaca fiber composite, the abaca fiber surface was modified by radiation grafting of glycidyl methacrylate (GMA). Furthermore, the molecular weight of the graft chains was controlled by reversible addition-fragmentation chain transfer (RAFT)-mediated polymerization. The surface was also functionalized by reacting the grafted chains with 1-vinylimidazole. The effects of these modified abaca fibers as reinforcements on the thermal stability, moisture resistance, and mechanical properties of the composites were evaluated.

The results demonstrated that the prepared composites exhibited significant improvements in tensile and flexural strengths, with at least 23% improvement in tensile strength and 59% improvement in flexural strength, compared to the composites reinforced with untreated fibers. As shown in Figure 2, the most substantial improvements were achieved for abaca fibers modified by the RAFT-mediated grafting mechanism (R6 and R12 composites). In addition, shorter graft chains on the abaca fibers resulted in a greater improvement in mechanical strength (R6 composite). The modified composites exhibited improved thermal stability and moisture resistance. These enhancements could be attributed to improved interfacial adhesion between the modified abaca fibers and the UPR matrix, which was confirmed by scanning electron microscope (SEM) analysis. Overall, these results highlight the potential of this approach as a surface modification technique to enhance the applicability of natural fibers in the composites industry.

References

- [1] K. Matsubara *et al.*, ChemPlusChem. **89**(4), e202300480 (2023).
- [2] B. Jeremiah, *et al.*, Polym. J. **56**(2), 97 (2023).

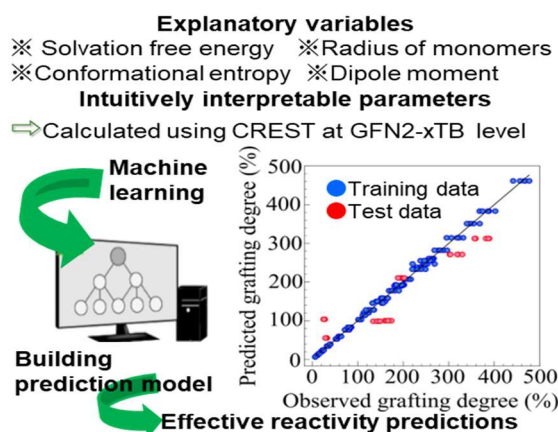


Fig. 1 Schematic diagram of the machine-learning model and the predicted degree of grafting for different monomer combination.

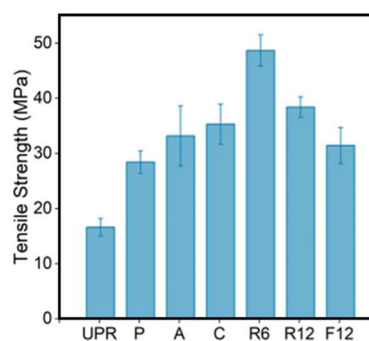


Fig. 2 Tensile strength of neat resin of UPR and UPR/abaca fabric composites (P~F12). P, pristine fabric; A, alkali-treated fabric; C, conventional grafted fabric; R6, RAFT-grafted fabric with low molecular weight; R12, RAFT-grafted fabric with high molecular weight; F12, functionalized with 1-vinylimidazole.



Advanced Biodevice Project has been developing innovative functional biodevices through the advanced use of quantum beam crosslinking and oxidation reactions. The developed biodevices are expected to be applied in a wide range of medical fields, from diagnosis to therapy, drug discovery, and even regenerative medicine.

Protein nanogels for pancreatic cancer diagnosis

Pancreatic cancer is a serious issue among the leading causes of death in Japan. The five-year survival rate for pancreatic cancer patients is very grim, at less than 10%, which further increases the importance of early diagnosis of pancreatic cancer. However, it is very difficult to detect pancreatic cancer early and efficiently with currently available imaging probes. The purpose of this study is to develop a novel imaging agent for the diagnosis of pancreatic cancer using positron emission tomography (PET). [1]

Low- and high-molecular-weight gelatins (gelatin 1: $M_w = 5.0 \times 10^3 \text{ g mol}^{-1}$ and gelatin 2: $M_w = 1.5 \times 10^5 \text{ g mol}^{-1}$) were prepared and dissolved in Millipore Milli-Q water to prepare a 0.1 wt.% gelatin solution, respectively. The sample solutions were irradiated with γ rays from a ^{60}Co γ -ray source at the Takasaki Institute for Advanced Quantum Science, National Institutes for Quantum Science and Technology (QST) at 25°C in the dose range 0.5 to 10 kGy ($\text{Gy} = \text{J kg}^{-1}$) and dose rate 5 kGy h^{-1} . Isotopically enriched ^{64}NiO targets were irradiated with a 5 μA 11 MeV proton beam induced from the AVF cyclotron of the Takasaki Ion Accelerator for Advanced Radiation Application (TIARA) at QST to produce carrier-free ^{64}Cu by the $^{64}\text{Ni}(p,n)^{64}\text{Cu}$ reaction. High-purity $^{64}\text{CuCl}_2$ was isolated from the irradiated target by a chemical separation method using chelate exchange resin.

Nanoparticles were produced by γ -ray irradiation of the aqueous gelatin solutions. Nanoparticle size increased with absorbed dose, reaching 20 nm after 5 kGy of irradiation. The obtained gelatin nanoparticles of 5, 13, and 20 nm (Fig. 1) were used in subsequent experiments. The nanoparticles retained their stability over time in water and the biodegradability of gelatin. The fluorescently labeled nanoparticles has a negative surface charge, which is considered to enhance accumulation in pancreatic cancer [2]. When the nanoparticles were cultured with PANC-1 pancreatic cancer cells, they accumulated intracellularly as shown in Fig. 2. No morphological changes in the cells were observed, indicating that the nanoparticles have low toxicity.

The amino groups of the nanoparticles were then labeled with radioactive Cu using the chelating agent DOTA (1,4,7,10-tetraazacyclododecane-1,4,7,10-tetraacetic acid) and injected into the tail vein of cancer-bearing mice. The ^{64}Cu -labeled DOTA used as a control was immediately

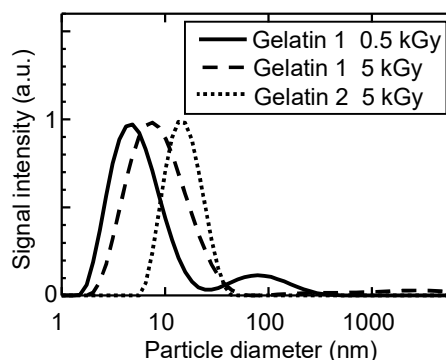


Fig. 1 Light scattering intensity of 0.1 wt.% aqueous gelatin 1 solution at 0.5 kGy (line), 0.1 wt.% aqueous gelatin 1 solution at 5 kGy (dashed line), and 0.1 wt.% aqueous gelatin 2 solution at 5 kGy (dotted line) as a function of particle diameter.

excreted in the urine without accumulation in the organs. On the other hand, ^{64}Cu -labeled nanoparticles were distributed in body organs such as liver and kidney. The smaller nanoparticles accumulated in the kidneys after a short metabolic period, while the larger nanoparticles tended to accumulate in the spleen, lungs, and intestine owing to drug metabolism, given that nanoparticle-based drugs are easily taken up by the reticuloendothelial system [3]. ^{64}Cu -labeled gelatin nanoparticles accumulated in the tumor, with an accumulation rate of about 3% of the injected dose.

Although there are still issues to be addressed in the accumulation of the nanoparticles developed in this study into tumors and healthy organs, modification of the nanoparticles with cell-adhesive sequences and other elements may increase the rate of accumulation in pancreatic cancer.

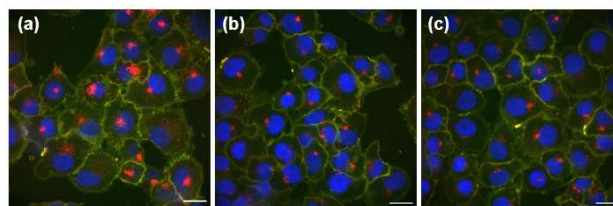


Fig. 2 Confocal images of red fluorescent gelatin nanoparticles with sizes of (a) 5 nm, (b) 13 nm, and (c) 20 nm in PANC-1 cells after incubation for 1 day. Blue: nuclei; Green: cell membranes; red: nanoparticles. Scale bars, 20 μm .

References

- [1] Y. Sugo *et al.*, *Radiochimica Acta*, in press.
- [2] H. Cabral *et al.*, *Nat. Nanotechnol* **6**, 815-823 (2011). DOI: 10.1038/nano.2011.166
- [3] C. Pérez-Campaña *et al.*, *ACS Nano* **7**, 3498-3505 (2013). DOI: 10.1021/nn400450p

Part I

3. Life Science

P3-1	Radiotracer Imaging Project	15
	Leader : KAWACHI Naok	
P3-2	Environmental-Stress Tolerance Genes Project	16
	Leader : HASE Yoshihiro	
P3-3	Medical Radioisotope Application Project	17
	Leader : ISHIOKA Noriko S.	
P3-4	Quantum-Applied Biotechnology Project	18
	Leader : SUZUKI Michiyo	



The aim of the Radiotracer Imaging Project is to quantitatively measure and visualize radiation sources, as well as to characterize biological processes and functions using radioisotopes and imaging devices such as PETIS, PET, and Gamma Camera. We aim to establish a systematized set of the most advanced techniques for live imaging with radiotracers, including production methods, nuclear imaging apparatus, imaging techniques specific to each device, and kinetic analytical methods. These techniques will be applied to understand the transport functions of elements and molecules related to agriculture, environmental issues, and medicine within living systems.

Diversity of Na⁺ allocation in salt-tolerant species of the genus *Vigna*

Salt tolerance is an important issue given more and more arable lands are degraded by soil salinity. Wild species in the genus *Vigna* are a great resource of tolerance to various stresses including salinity. We have previously screened the genetic resources of the genus *Vigna* and identified several accessions that have independently evolved salt tolerance. However, many aspects of such tolerance have remained unknown. Thus, we used autoradiography with radioactive sodium (²²Na⁺) and Inductively Coupled Plasma Mass Spectrometry (ICP-MS) to visualize and compare Na⁺ allocation in *Vigna angularis* (Willd.) Ohwi & H. Ohashi (azuki bean), *Vigna nakashimae* (Ohwi) Ohwi & H. Ohashi, *Vigna riukiensis* (Ohwi) Ohwi & H. Ohashi, *Vigna luteola* (Jacq.) Benth. and *Vigna marina* (Burm.) Merr. (Fig. 1). The results indicated: 1) Tolerant accessions suppress Na⁺ accumulation compared to azuki bean. 2) *V. nakashimae* and *V. marina* does so by accumulating higher amount of K⁺, whereas *V. riukiensis* and *V. luteola* does so by other mechanisms. 3) *V. luteola* avoids salt-shedding by allocating excess Na⁺ to newly expanded leaves. As the mechanisms of the tolerant species were different, they could be piled up in a single crop via classical breeding or by genetic engineering or genome editing.

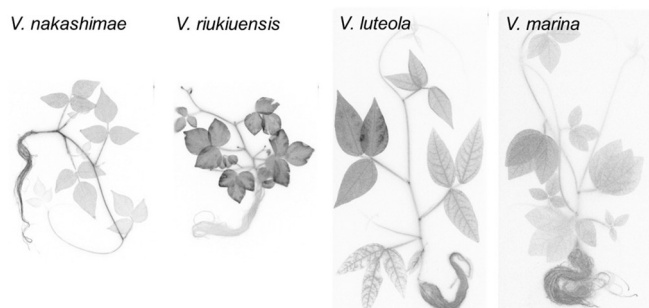


Fig. 1 Visualization of ²²Na distribution by autoradiography in four different genus *Vigna*. Color change from blue to red indicates ²²Na accumulation.

Starch-dependent sodium accumulation in the leaves of *Vigna riukiensis*

This research provides insight into a unique salt tolerance mechanism of *Vigna riukiensis*. We have previously reported that *V. riukiensis* accumulates a higher amount of sodium in the leaves, whereas *V. nakashimae*, a close relative of *V. riukiensis*, suppresses sodium allocation to the leaves (Fig. 1). We first suspected that *V. riukiensis* would have developed vacuoles for sodium sequestration, but there were no differences compared to a salt-sensitive species *V. angularis*. However, many starch granules were observed in the chloroplasts of *V. riukiensis*. In addition, forced degradation of leaf starch by shading treatment resulted in no radio-Na (²²Na) accumulation in the leaves (Fig. 2A). We performed SEM–EDX to locate Na in leaf sections and detected Na in chloroplasts of *V. riukiensis*, especially around the starch granules but not in the middle of (Fig. 2B). Our results could provide the second evidence of the Na-trapping system by starch granules, following the case of common reed that accumulates starch granule at the shoot base for binding Na.

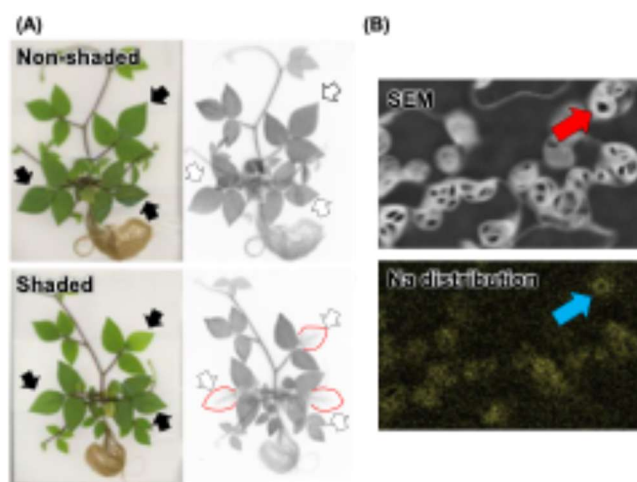


Fig. 2 (A) ²²Na accumulation in shaded and non-shaded leaves of *V. riukiensis*. Black and white arrows indicate leaves that were wrapped with cling film (non-shaded) or foil. (B) Electron microscopy (SEM) and Na distribution of leaf cells. In the SEM images, the white structures in the cells are chloroplasts and the black objects inside are starch granules. The red arrow indicates the starch granules and the blue Na signal surrounds the starch.

References

- [1] Y. Noda, *et al.*, *Breed. Sci.* **Vol 72** (4), 326-331 (2022). DOI: 10.1270/jsbbs.22012
- [2] Y. Noda, *et al.*, *J. Plant Res.* **Vol 136**, 705-714 (2023). DOI: 10.1007/s10265-023-01470-8

P3-2 Environmental-Stress Tolerance Genes Project

Leader : HASE Yoshihiro



Our project aims to create novel genetic information that can be utilized to confer environmental-stress tolerances in crops and microorganisms in order to contribute to the sustainable agriculture. In particular, our project focuses on the experimental evolution combined with mutagenesis using quantum beams, because appropriately increased mutation frequency is expected to accelerate the adaptation to stress environment and also stimulate the accumulation of beneficial mutations. Here we report our recent achievements regarding the characterization of mutations induced by quantum beams.

Overall picture of the induced mutation in relation to the linear energy transfer (LET) values

Quantum beam is a powerful tool as a mutagen to develop new crops and industrial bacteria. However, mutagenesis in the practical mutation program still largely depends on the experience and intuition. This is partly because few studies have characterized the mutations induced by different radiation qualities with the same analysis method. This makes it difficult to obtain an overall picture of the induced mutations. Therefore, in the last several years, we performed whole genome sequencing analysis to elucidate the characteristics of induced mutations using *Arabidopsis thaliana* and *Bacillus subtilis* as a model organism of plants and bacteria with the same mutation detection method.

Arabidopsis dry seeds and seedlings were irradiated with gamma rays (LET: ~ 0.2 keV/ μ m) and carbon ions (107 keV/ μ m). Whole genome sequencing analysis was performed in the following generation to detect induced mutations. Mutation frequency at the equivalent dose for survival reduction was higher with gamma rays than with carbon ions, and was higher with dry-seed irradiation than with seedling irradiation. Carbon ions induced a higher frequency of deletions (2–99 bp) than gamma rays in the case of dry-seed irradiation, but this difference was less evident in the case of seedling irradiation. This result supported the inference that dry-seed irradiation under a lower water content more clearly reflects the difference in radiation quality. However, the ratio of rearrangements (inversions, translocations, and deletions larger than 100 bp), which are considered to be derived from the rejoining of two distantly located DNA breaks, was significantly higher with carbon ions than gamma rays irrespective of the irradiated material. This finding suggested that high-linear energy transfer radiation induced closely located DNA damage, irrespective of the water content of the material, that could lead to the generation of rearrangements [1].

Freeze-dried spores of *B. subtilis* were irradiated with gamma rays and six kinds of ion beams with the LET in the range of 24 to 2214 keV/ μ m (48 MeV He (24 keV/ μ m), 311 MeV C (111), 208 MeV C (156), 177 MeV C (179), 316 MeV Ne (468), and 310 MeV Ar (2214)). Whole genome sequencing analysis was performed using the colonies at a dose resulting in a survival fraction of around 1% for each radiation. The radiations with lower LET showed low lethality and high mutation frequency, resulting in the major induction of single-base substitutions. Whereas radiations with higher LET showed high lethality and low mutation frequency, resulting in the preferential induction of deletion mutations. Carbon ions with intermediate LET (111 keV/ μ m) likely possess characteristics of both low- and high-LET radiations simultaneously [2].

Taken together, these results provide an overall picture of the induced mutation in relation to the LET values (Fig. 1). Particularly, our results suggest that ion beams with an intermediate LET around 110 keV/ μ m can induce the most diverse types of mutations in both plants and bacteria. In case of plants, seed irradiation is preferable than seedling irradiation, because higher mutation frequency and higher ratio of deletions are expected. These results are useful for selection of a suitable radiation treatment for mutagenesis.

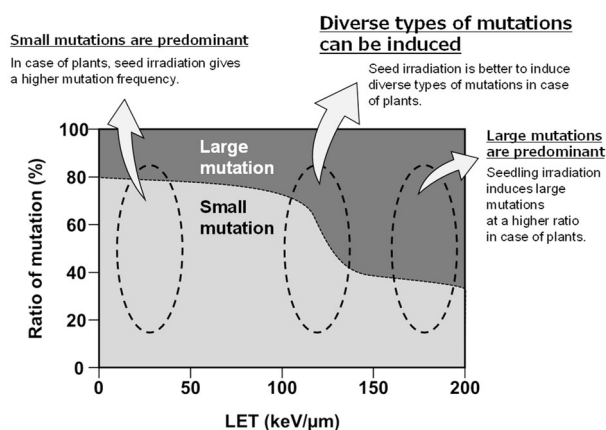


Fig. 1 Schematic representation of the relationship between LET and types of mutation.

References

- [1] Y. Hase *et al.*, *Front. Plant Sci.* **14**, 1149083 (2023). DOI: 10.3389/fpls.2023.1149083
- [2] K. Satoh *et al.*, *Mut. Res. Fund. Mol. Mech. Mut.* **827**, 111835 (2023). DOI: 10.1016/j.mrfmmm.2023.111835

P3-3 Medical Radioisotope Application Project

Leader : ISHIOKA Noriko S.



Based on various RI manufacturing technologies using quantum beams, we develop basic technologies that contribute to the development of radiopharmaceuticals useful for the diagnosis and treatment of diseases. In particular, our research focuses on the elucidation of the key mechanisms that maximize the therapeutic effect of radiation and the development of new RI compounds that enhances the cell-killing effect by simultaneously irradiating multiple targets.

Development of precursor containing highly storable Cdf ester for radiohalogenation [1]

Radiotheranostics combines internal radiation therapy with diagnostics based on molecular imaging and provides a potent yet non-invasive method for cancer therapy. Radiohalogens have a variety of useful radionuclides for diagnostic and therapy, which means suitable for application in radiotheranostics. Chemical properties between each halogen element are similar. However, *in vivo* stability of radiohalogenated compounds is often different. For example, ^{211}At -labeled compounds more readily undergo dehalogenation *in vivo* than radioiodinated compounds. ^{211}At released from its labeled compounds reduces accumulation rate of astatine in targeted cancer cells, resulting in causes unnecessary radiation exposure. We found that carbon–halogen bond in a neopentyl group (Figure 1) exhibited high *in vivo* stability, and significantly resisted dehalogenation even in ^{211}At -labeled compounds [2]. Radiohalogenated compounds **2** with the neopentyl group are prepared by nucleophilic substitution of a radiohalide using a leaving group such as sulfonyl ester. At first, compound **1a** with a triflate (CF_3SO_3^-) group was used as the precursor for radiohalogenation under mild heating conditions. Although the triflate group is highly reactive and useful as the leaving group, long-term storage of precursors is difficult because the triflate group is unstable. To streamline the development of radiopharmaceuticals using the neopentyl group, it is necessary to develop highly reactive and storable precursors. In this study, a 1-(*N,N*-di-*n*-octylcarbamoyl)-1,1-difluoromethanesulfonyl (Cdf) ester **1b** was developed as a stable precursor for radiohalogenation via the neopentyl group.

The Cdf ester has a *N,N*-di-*n*-octylcarbamoyl ($(\text{C}_8\text{H}_{17})_2\text{N}(\text{CO})^-$) group replaced by one of the fluorine atoms of the triflate group. Although it is likely that the carbamoyl group reduce reactivity of nucleophilic substitution due to its weaker electron-withdrawing effect than that of fluorine, it is also expected to enhance the chemical stability of the sulfonyl ester. We initially evaluated stability of the precursors containing triflate group **1a** or Cdf ester **1b**. A solution of **1a** and **1b** in acetonitrile- d_3 were quantitatively analyzed using ^1H -NMR spectroscopy after 1

or 30 days. As a result, **1a** completely decomposed after 1 day. In contrast, no significant degradation of **1b** was observed after 30 days. Next, we evaluated the radiobromination, radioiodination, and astatination of precursor **3** containing Cdf ester and naphthyl group (Table 1). The solutions of ^{77}Br , ^{125}I , and ^{211}At were reacted with **3** in acetonitrile at 70°C for 10 min to synthesize **4a**, **4b**, and **4c**, respectively. Radiochemical conversion (RCC) values of **4a** and **4b** were 80% and 83%, respectively. In contrast, this reaction provided only a trace amount of ^{211}At -labeled compound **4c**. We thought that the significant decrease in RCC value of **4c** occurred because astatine forms a neutral chemical species in the prepared solution. Therefore, we hypothesized that a base would improve the nucleophilicity of astatine species, which led us to investigate astatination of **3** in the presence of K_2CO_3 . As a result, RCC values of **4c** were dramatically improved (95 and 90%) by addition of K_2CO_3 .

In conclusion, Cdf ester exhibited superior stability compared to triflate group. We also found reaction conditions that obtained high RCC values for radiohalogenation using **1b**. Therefore, precursor containing Cdf ester is expected to contribute to the efficient development of radiopharmaceuticals with radiohalogen.

References

- [1] I. Sasaki *et al.*, *Org. Biomol. Chem.* **21**, 7467 (2023). DOI: 10.1039/D3OB00944K
 [2] H. Suzuki *et al.*, *J. Med. Chem.* **64**, 15846 (2021). DOI: 10.1021/acs.jmedchem.1c01147

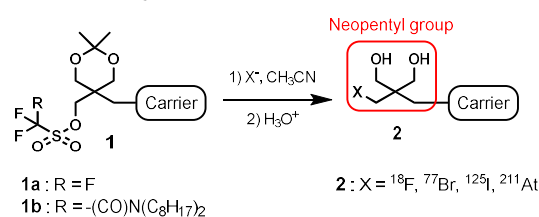
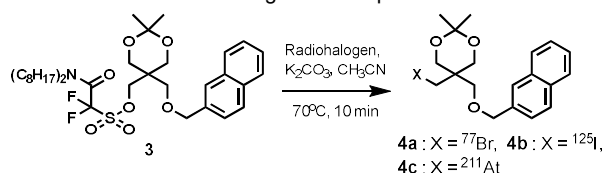


Fig. 1 Preparation of radiohalogenated compounds with neopentyl group using different sulfonated ester precursors

Table 1

RCC values in the radiohalogenation of precursor **3**



Entry	Radiohalogen	K_2CO_3	Product 4	RCC (%)
1	^{77}Br	—	4a	80
2	$\text{Na}[^{125}\text{I}]$	—	4b	83
3	^{211}At	—	4c	9
4	^{211}At	O	4c	95 and 90

P3-4 Quantum-Applied Biotechnology Project

Leader : SUZUKI Michiyo



The "Quantum-Applied Biotechnology Project" is working on research and development of quantum biotechnology, which will form the basis of biotechnology, using the quantum beam facilities of TIAQS, based on the results of the previous "Microbeam Radiation Biology Project". In particular, we are focusing on incubation to refine the numerous quantum biotechnology seeds created in life science research using quantum beams, especially for the nematode *Caenorhabditis elegans*, into truly "usable" technology. We are conducting the following three research lines: 1. Development of technology to control plant-damaging nematodes using quantum beams (agricultural field), 2. Elucidation and application of biological functions of animals and plants (basic science field), 3. High-precision inspection of samples using nematode sensors (medical and environmental field). Through research and development of quantum biotechnology, we aim to contribute to solving problems in various fields.

This report highlights our recent studies in radiation technology [1] and radiation biology research [2].

A method to locally irradiate specific organ in model organisms using a focused heavy-ion microbeam [1]

Localized irradiation with heavy ion microbeams, which inactivate only a portion of the constituent cells without destroying the physical intercellular connections of the organ/tissue, is a practical approach to elucidating tissue function. However, conventional collimated microbeams are limited in the shape of the area that can be irradiated.

Therefore, using a focused heavy-ion microbeam at the HX1 port of the TIARA [3], which produces a highly precise beam spot, we developed a technology to uniformly irradiate specific organs of an organism with a defined dose, which cannot be achieved by conventional methods. We evaluated the performance of the developed method to locally irradiate specific organ with a focused heavy-ion microbeam by irradiating the CR-39 ion track detector and confirmed that the technology enables the area to be uniformly irradiated with a specified dose. As an example, Figure 1(a) shows the irradiation plan to target the gonad

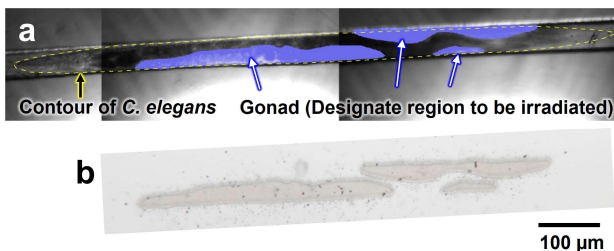


Fig.1 Local irradiation of specific organ in *C. elegans*. (a) The gonads of *C. elegans* are marked in blue for tissue shape irradiation using self-developed software. (b) Etch pits of carbon ions passed through CR-39 film placed under the *C. elegans*.

area (blue) of *C. elegans*, and Fig. 1(b) shows the carbon ion (C^{6+} , 320 MeV) passed through the CR-39 film placed under *C. elegans*. This indicates that the irradiation of the gonad only was successful. Organ specific irradiation will elucidate biological mechanisms that are difficult to analyze with conventional collimated microbeam irradiation. We are developing a technique for radiation sterilization of plant-parasitic nematodes, which can cause significant damage in agriculture and forestry, and using this organ-shape irradiation technique, we can study the differences in the effects of sterilizing nematodes by gonadal irradiation and whole-body irradiation.

Short-term γ -ray irradiation with hyperoxia induces lifespan extension in *C. elegans* [2]

Before extravehicular activities in interplanetary space, astronauts are required to repeat exposure to 100% oxygen several times a week. Thus, astronauts are simultaneously exposed to two stresses that have different biological effects on cells: cosmic radiation and high oxygen. The effects of simultaneous exposure to both on aging and lifespan control remain unknown.

Therefore, we sought to evaluate the interaction between the two on lifespan using *C. elegans* exposed to short-term ^{60}Co γ -ray irradiation under high oxygen (95% oxygen) conditions. As a result, the lifespan of the group exposed to both γ -rays and high oxygen was extended by 10-15% compared to the group exposed to γ -rays alone (21% oxygen). In addition, we found that the interaction of γ -rays and high oxygen induced the expression of antioxidant genes via the insulin/IGF-1 pathway, a decrease in mitochondrial reactive oxygen species, and the induction of DNA damage repair systems and gene activation. Short-term exposure to low LET (linear energy transfer) radiation, including γ -rays and X-rays, temporarily inactivates the transcription of most genes, but under high-oxygen conditions, gene expression levels are at least partially restored. This suggests that the interaction between low-LET radiation and high oxygen promotes longevity by affecting gene transcription and mitochondrial dynamics, and will be of great help in the search for new intracellular molecular targets that contribute to the protection of astronauts.

References

- [1] T. Funayama *et al.*, *Biology* **12**, 1524 (2023). DOI: 10.3390/biology12121524
- [2] S. Yanase *et al.*, *Biological Sciences in Space* **37**, 12 (2023). DOI: <https://doi.org/10.2187/bss.37.12>
- [3] T. Funayama *et al.*, *Nuclear Instruments and Methods in Physics Research B* **465**, 101 (2020). DOI: 10.1016/j.nimb.2019.12.028

Part I

4. Quantum-Beam Technology

P4-1 Beam Engineering Section..... 20
Section Manager : ISHII Yasuyuki

P4-1 Beam Engineering Section

Section Manager : ISHII Yasuyuki



The research objectives in our section are the development of various accelerator-related techniques including beam-irradiation-techniques and beam-analyses. Each member has been engaged in individual research more than one. Recent remarkable study is “Ti beam extraction from a laser plasma focused by a magnetic field of a solenoid”.

Ti beam extraction from a laser plasma focused by a magnetic field of a solenoid [1]

The 400-kV ion implanter in TIARA is utilized for implanting ion beams of a wide range of different ion species into various materials. To generate the ion beams of different ion species, a laser ion source (LIS) is developing for the ion implanter. It has the potential to implant ion beams of different ion species with a quick-change procedure. In addition, an average current of more than 1 μA is required at the implanter. Hence, the plasma pulse of the LIS must be continuously generated at a high frequency to achieve the required average beam current.

In a LIS, the plasma generated at the laser irradiation point on the target diffuses in three dimensions with a wide angular distribution, and only a small fraction of the ions that reach the beam extraction aperture are extracted as a beam. Hence, we conducted research to enhance the number of plasma ions transformed into a beam by focusing the generated plasma toward the beam extraction aperture with a magnetic field generated by a solenoid magnet. This study aims to increase the beam intensity by focusing the laser plasma with a relatively low plasma density generated by a low energy laser of the order of 10 mJ or less using a solenoid magnet to develop a LIS for the ion implanter.

Figure 1 shows the apparatus used in the experiments. A laser beam emitted from a laser system placed on an optical table near the LIS vacuum chamber was guided by mirrors and focused by a lens ($f = 750$ mm) onto a flat target in the chamber. The laser energy can be changed without changing the pulse width by a combination of a wavelength plate and polarizing beam splitter. The angle of incidence of the laser on the target is 25 degrees. The LIS chamber consisted of a double structure, in which a high-voltage chamber was placed inside a vacuum chamber at ground potential. This arrangement prevents exposure to high voltage charged conductors outside the vacuum chamber. A solenoid magnet was installed downstream of the chamber, and it had a double structure with a plasma transport tube at the same potential as the inner chamber of the ion source. A beam extraction aperture 10 mm in diameter was located at the end of the plasma transport tube. The distance from the target surface to the aperture

is 800 mm. The solenoid magnet consists of hollow conductors for water cooling wound around a vacuum pipe with flanges. The pipe length and inner diameter were 500 and 60.5 mm, respectively. The magnetic field at the center of the magnet per excitation current was 6.97 G/A, and a maximum magnetic field of 1184 G was generated using a 170-A power supply.

Plasma was generated from the target material by a laser focused on the target. The plasma was laterally focused by the magnetic field generated by the solenoid magnet, resulting in a higher fraction reaching the extraction aperture than that in free expansion. An ion beam was extracted from the plasma by the electric field between the plasma transport tube and the extraction electrode with a 10-mm aperture, which was positioned 40 mm downstream from the extraction aperture of the plasma transportation tube. The time-of-flight (TOF) signal of the beam intensity was measured as a voltage signal using an oscilloscope at a Faraday cup with an inner diameter of 50 mm installed downstream of the solenoid magnet. The high-voltage chamber was grounded to measure the ion current in the plasma without extracting the beam. In this case, ions in the plasma were extracted in the Faraday cup by applying -2 kV to the suppressor electrode.

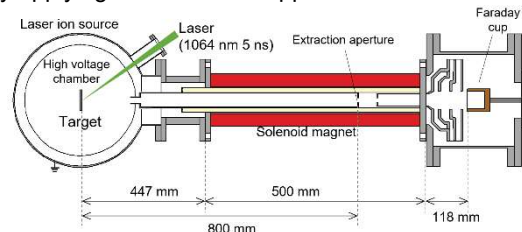


Fig. 1 Experimental setup comprising a laser ion source, a solenoid magnet, and a Faraday cup.

The results of estimating were the average current of the $^{48}\text{Ti}^{1+}$ beam when beams are generated at a repetition rate of 1 kHz, which was one-tenth of the maximum plasma repetition frequency of 10 kHz obtained in the carbon plasma experiment. The ion charges in Figure 2 include not only Ti^{1+} but also other charge states. In addition, the beam contains stable isotopes with mass numbers from 46 to 50. Thus, the average current of the most abundant $^{48}\text{Ti}^{1+}$ was calculated by multiplying the ratio of Ti^{1+} measured in another experiment and abundance ratio. The results show that the laser energies of 12.5 and 5.9 mJ provide a beam on the order of microamperes required for the TIARA ion implanter and a beam current close to 1 μA even at the lowest energy of 2.5 mJ.

Reference

- [1] H. Kashiwagi *et al.*, J. Phys. Conf. Ser 2743, 012062 (2024). DOI: 10.1088/1742-6596/2743/1/012062

Part II

Part II

1. Quantum Materials and Applications

1-01	Recovery of the threshold voltage shift of gamma-irradiated 4H-SiC JFET by sub-band gap light illumination.....	22
	A. Takeyama, T. Makino, Y. Tanaka, S-I. Kuroki and T. Ohshima	
1-02	Annealing time dependence on creation of group IV – vacancy centers in diamond by atmospheric annealing	23
	T. Baba, M. Iizawa, K. Takenaka, K. Kimura, A. Kawasaki, T. Taniguchi, M. Miyakawa, H. Okazaki, O. Hanaizumi and S. Onoda	
1-03	Laser-cooled ion source for an ultrahigh-precision single-ion implanter	24
	K. Hosaka, Y. Yuri, S. Hosoya, M. Iizawa, H. Kashiwagi, N. Miyawaki, Y. Ishii, H. Shimada, R. Yamagata, S. Onoda, K. Narumi, K. Muroo, K. Ito and H. Okamoto	
1-04	Development of selective loading system of Ba isotope using two-step photoionization.....	25
	K. Tamura	
1-05	Construction of the ion trap system for radioactive Ba ⁺ isotope.....	26
	H. Shimada, K. Hosaka, H. Kashiwagi, S. Hosoya, Y. Yuri, R. Nakanishi, K. Tamura, K. Ogura, H. Ohba and K. Narumi	
1-06	Charge state stability of silicon vacancy in silicon carbide.....	27
	Y. Yamazaki, R. Akashi, M. Hanawa, K. Murata, S.-I. Sato, N. Miyawaki, S. Entani, Y. Masuyama, Y. Nishiya, Y. Matsushita, H. Tsuchida, M. Kohda and T. Ohshima	
1-07	X-ray absorption fine structure analysis of Pr ions implanted in GaN	28
	E. Yokozuka, T. Tsuji, D. Matsumura, M. Deki, H. Watanabe, S. Nitta, Y. Honda, H. Amano, N. Nagasawa, H. Saitoh and S.-I. Sato	

Recovery of the threshold voltage shift of gamma-irradiated 4H-SiC JFET by sub-band gap light illumination

A. Takeyama ^{a)}, T. Makino ^{a)}, Y. Tanaka ^{b)}, S-I. Kuroki ^{c)} and T. Ohshima ^{a)}

^{a)} Quantum Materials and Applications Research Center, QST

^{b)} Advanced Power Electronics Research Center, AIST

^{c)} Research Institute for Semiconductor Engineering, Hiroshima University

Introduction

Silicon carbide (SiC) junction field-effect transistor (JFET) is a promising device working in high-temperature and/or high-radiation conditions. It consists of p-n junctions and does not include the gate oxide which is positively charged by gamma-rays irradiation. Accordingly, higher radiation tolerance relative to a common metal-oxide-semiconductor (MOSFET) is expected. We previously showed threshold voltage (V_{th} , the gate voltage for device turn-on) of SiC JFET shifted less than 1 V even after 17 MGy irradiation, which is much smaller than several V reported for MOSFET [1]. The V_{th} shift might be caused by some traps formed in the device, hence energy levels of the traps (defects) are investigated in this study. Using light illumination prevents irreversible and additional degradation of irradiated devices. Through estimating the V_{th} from the current-voltage characteristics, approximate energy levels of the defects were explored.

Experimental

Figure.1 is a cross sectional view of 4H-SiC JFET. Several JFETs were irradiated with gamma-rays at room temperature up to 17 MGy (H_2O) at QST Takasaki. Dose rate was 9-10 kGy/h. Light-emitting diodes (LEDs) with a center wavelength from 745 (1.67 eV) to 1545 nm (0.80 eV) were employed as the light sources. As the light energies were located approximately below a half of the 4H-SiC bandgap, 3.26 eV, the defects formed in the upper/bottom half of the bandgap were mainly excited during the illumination. The averaged intensity of the focused light onto the device was $15 \mu W/mm^2$. The drain current-gate voltage (I_D-V_G) curves were measured illuminating the devices.

Results and Discussion

The I_D-V_G curves shown in Figure 2 (a) moved positively after irradiation (dashed lines). In figure 2 (b), V_{th} shift from non-irradiated one increased up to about 0.6 V. Based on simple theoretical calculation, the shift is interpreted as positive charging of the region around p-type gate.

Figure 3 shows V_{th} shift from the irradiated device during illumination. V_{th} shifted negatively with increasing light energy. A little steep slope above 1.2-1.3 eV and a slight gap were observed at 1.4 eV. As the V_{th} shifted when the LED spectra passed the trap energy level, it indicates positive charges of traps were neutralized by photo-excited electrons from the valence band [2]. These traps can be

assigned to deep hole traps as HK3 ($E_v + 1.24$ eV, E_v : the valence band top energy) and HK4 ($E_v + 1.44$ eV) [3]. They were formed around the gate by displacement damage.

Acknowledgments

This research was partially funded by MEXT the Initiative to Establish the Next-Generation Novel Integrated Circuits Centers (X-NICS), grant number JPJ011438, and JSPS KAKENHI grant number JP20H00252 and JP21K04955.

References

- [1] A. Takeyama *et al.*, J. Appl. Phys. **131**, 244503-1 (2022). DOI: 10.1063/5.0095841
- [2] A. Takeyama *et al.*, Quantum Beam Sci. **7**, 31-1 (2023). DOI:10.3390/qubs7040031.
- [3] T. Kimoto, Jpn. J. App. Phys. **54**, 040103 (2015). DOI: 10.7567/JJAP.54.040103.

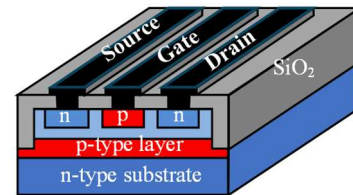


Fig. 1 Cross sectional view of SiC JFET.

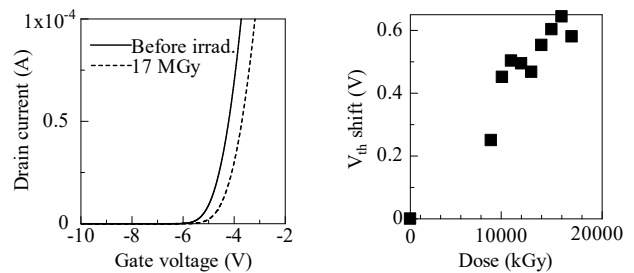


Fig. 2 (a) I_D-V_G curve shift by irradiation. (b) V_{th} shift from non-irradiated device.

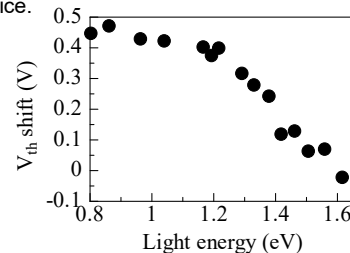


Fig. 3 Recovery of V_{th} shift of 17 MGy irradiated JFET as a function of illuminating light energy.

1 - 02 Annealing time dependence on creation of group IV – vacancy centers in diamond by atmospheric annealing

T. Baba ^{a,b)}, M. Iizawa ^{a)}, K. Takenaka ^{a)}, K. Kimura ^{a,b)}, A. Kawasaki ^{b)}, T. Taniguchi ^{c)}, M. Miyakawa ^{c)}, H. Okazaki ^{d)}, O. Hanaizumi ^{b)} and S. Onoda ^{a)}

^{a)} Quantum Materials and Applications Research Center, QST

^{b)} Faculty of Science and Technology, Gunma University

^{c)} National Institute for Materials Science

^{d)} Department of Advanced Functional Materials Research, QST

Introduction

The group IV-V centers, including SiV, GeV, SnV, and PbV centers, are the leading candidates for next-generation quantum devices. The properties of the strong photon emission into zero phonon line (ZPL), tolerance to disturbances from external noise due to the no permanent electric-dipole moment, and low inhomogeneous spectral distribution outperform other solid-state quantum systems. There are two main methods of creating group IV-V centers. One is the doping of group IV atoms during diamond synthesis. The second method is to implant with group IV ion beams. In the case of implantation method, an annealing process is indispensable after implantation due to the bonding of implanted atoms and vacancies. The annealing process impacts not only the amount of Group IV-V centers created but also the increase or decrease of various defects affecting the spin relaxation time. Usually high-pressure high-temperature annealing is utilized for this purpose. Conversely, high-pressure annealing cannot be performed in a vacuum or under inert gas, which would degrade the surface of the diamond sample. In this report, we discuss the forming group IV-V centers by atmospheric pressure annealing at 1800 °C with argon flow to suppress the surface degradation.

Experimental

The ion implantation was carried out by a tandem accelerator at TIARA. The diamond samples were implanted by silicon-28, germanium-74, and tin-120 ions accelerated to 18 MeV at room temperature. The implantation fluences were 6.80×10^{12} ions·cm⁻², 1.53×10^{13} ions·cm⁻², and 1.68×10^{13} ions·cm⁻², respectively, which corresponds to the volume density of 10 ppm for all cases.

The annealing process was performed using an infrared heating furnace, Thermo Riko's ultra-high temperature rapid thermal annealing (RTA) system SR1800G with argon gas flowing. The temperature was ramped up to 300 °C in 1 minute and held at 300 °C for 10 minutes before every annealing process. To avoid temperature overshooting, the temperature was increased to 50 °C below the target temperature of 1800 °C in the first 30 seconds and then increased to the target temperature in the next 30 seconds. After annealing, every sample was treated with hot mixed acid.

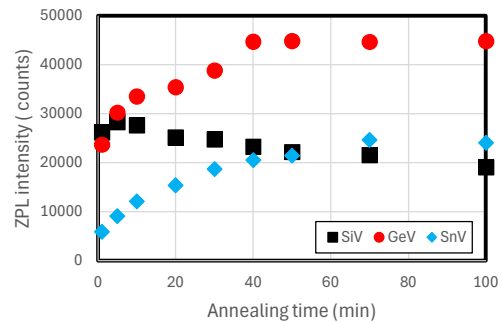


Fig. 1. ZPL intensity as a function of annealing time.

For estimating the density of group IV-V centers, photoluminescence (PL) spectra were obtained using a confocal Raman microscope LabRAM HR Evolution manufactured by Horiba Scientific. We confirmed that the ZPL intensity of the group IV-V centers linearly correlated with the power of the 532 nm excitation light in the order of 1–10 mW, and then the PL intensities were normalized by the obtained laser power before every PL measurement. The exposure time was set to 5 seconds with 1% ND filter for Si samples and 0.1% ND filter for Ge and Pb samples.

Results and Discussion

The time dependence of ZPL intensity is shown in Fig. 1. We found that the creation of SiV, GeV, and SnV are presented by the atmospheric annealing in the argon flow. Compared to high-pressure annealing, in which gas cannot flow, atmospheric annealing with an inert gas flow not only causes less degradation of the sample surface but also has the advantage of reducing equipment cost and preparation time. Excessive annealing time has been shown to reduce the amount of centers created. As shown in Fig. 1, it is clear that there is an optimal annealing time and that longer is not better; that is, not only the formation process of group IV-V centers but also the dissociation process must be considered.

Acknowledgments

This work was supported by JST moonshot R&D Grant Number JPMJMS2062.

Reference

[1] T. Baba *et al.*, Phys. Status. Solidi. (a). 2400303 (2024). DOI: 10.1002/pssa.202400303

K. Hosaka^{a)}, Y. Yuri^{a)}, S. Hosoya^{a)}, M. Iizawa^{a)}, H. Kashiwagi^{a)}, N. Miyawaki^{a)}, Y. Ishij^{a)}, H. Shimada^{a)}, R. Yamagata^{a)}, S. Onoda^{a)}, K. Narumi^{a)}, K. Muroo^{b)}, K. Ito^{b)} and H. Okamoto^{b)}

^{a)}Quantum Materials and Applications Research Center, QST

^{b)}Graduate School of Advanced Science and Engineering, Hiroshima University

Introduction

Deterministic ion implantation and color-center creation methods on a nanometer scale provide a route towards scalable quantum information processing [1-3]. For this purpose, we have developed an inherently deterministic single-ion implantation method based on a linear Paul trap (LPT) as a single-ion source since the laser-cooling technique can be applied to the trap system to obtain ultralow-emittance ions and manipulate single ions one by one [2,3].

Experimental

The schematic view of a laser-cooled ion source constructed at QST for 100 keV nitrogen ion implantation is depicted in Fig. 1. Doubly charged nitrogen ions (N^{2+}) produced in a sputter ion source is introduced into the LPT and sympathetically cooled with laser-cooled calcium ions (Ca^+). Both the sputter ion source and the LPT chamber are elevated to +50 kV for the 100 keV-implantation of doubly charged single ions into a grounded diamond crystal.

The LPT consists of four cylindrical rods and seven gate electrodes A–F, where Ca^+ are laser-cooled between gates A and B. The distance from the trap center axis to the

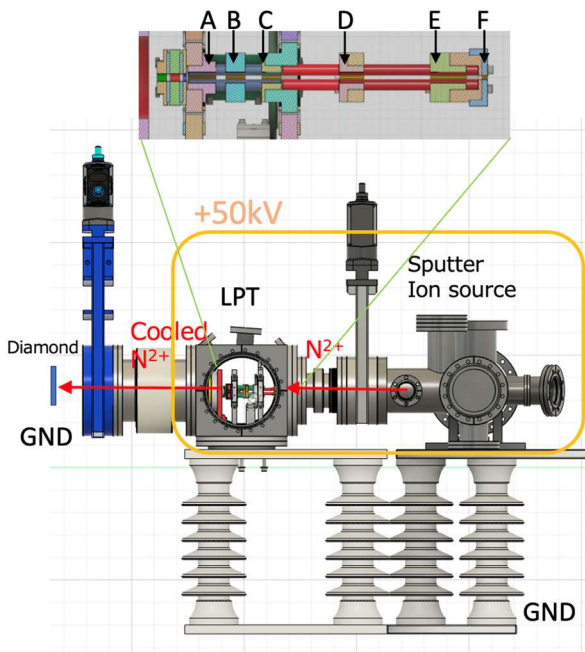


Fig. 1 Schematic of the laser-cooled ion source.

surface of the rod electrodes is 3.0 mm and the distance between the gate electrodes A and B is 6.0 mm. Neutral Ca gases were photo-ionized by two lasers (423 nm and 390 nm). The LPT utilizes an rf quadrupole field to confine charged particles transversely. The rf frequency and amplitude were 1.9 MHz and 20 V, respectively. The axial ion confinement was achieved by applying DC voltages to the two gates A and B ($V_A = V_B = +1.0$ V). The trapped $^{40}Ca^+$ were Doppler cooled with cooling (397 nm) and repumping (866 nm) lasers. Laser-induced fluorescence (LIF) photons were detected with a CCD camera.

Results

Figure 2 shows an example of LIF images obtained with the CCD camera, where each spot represents a single $^{40}Ca^+$. This crystal-like structure is called a “Coulomb crystal”, where the translational motion of ions is negligibly small, and each ion stays at its own position as the result of the balance between Coulomb repulsion and trapping electric field.

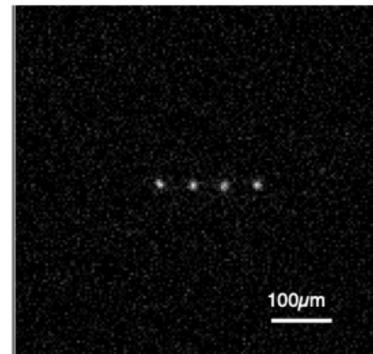


Fig. 2 An example of LIF image of a string Coulomb crystal of Ca^+ .

Acknowledgments

This work was supported in part by a JSPS KAKENHI Grant No. JP20H00145 and by a JST Moonshot R&D Grant No. JPMJMS2062.

References

- [1] K. Groot-Berning, *et al.*, Phys. Rev. Lett. **123**, 106802 (2019). DOI: 10.1103/PhysRevLett.123.106802
- [2] K. Iizawa *et al.*, J. Phys. Soc. Jpn. **79**, 124502 (2010). DOI: 10.1143/JPSJ.79.124502
- [3] K. Muroo *et al.*, PTEP, **2023**, 063G01 (2023). DOI: 10.1093/ptep/ptad071

1 - 04 Development of selective loading system of Ba isotope using two-step photoionization

K. Tamura

Quantum Materials and Applications Research Center, QST

Introduction

Cooling and trapping ion system is considered as a promising candidate for quantum information processor. Especially, by manipulating $^{133}\text{Ba}^+$ ion, improved fidelity of qubit operation is expected [1], where selective ^{133}Ba isotope introduction to the ion trap is required. In this report, development of isotope selective loading system of Ba ion for the ion trap using the two-step laser photoionization is considered.

Development of excitation laser

Figure 1(a) shows the Ba photoionization scheme based on the two-step photoionization. For excitation step, target isotope atom (^{133}Ba) is selectively photo-excited among other Ba isotopes ($^{130-140}\text{Ba}$) based on their isotope shift. The selected excitation scheme needs to have high efficiency leading to high loading rate, where factors such as transition probability and available laser output power are important. A tunable laser with laser wavelength corresponding to the transition is required. The laser needs to have narrow spectral line width compared with adjacent Ba isotope shift. In this study, two types of transition from ground state were considered, and consequently, two types of lasers (791 nm and 553 nm) corresponding to each scheme were under development.

For the first excitation step (791 nm), laser based on the external cavity diode laser (ECDL) was developed (Fig.1(b)). Output from a diode laser controlled with a LD driver was collimated with a lens and was introduced to a diffraction grating. The grating was moved with a piezo actuator. Output power of more than 70 mW was obtained, which was sufficient for excitation of the Ba atomic beam. The longitudinal mode was monitored with an air-spaced etalon, and the single-longitudinal-mode operation was confirmed. Mode-hop-free (MHF) scan required for selective excitation was achieved by simultaneous extension of the piezo actuator and reduction of the LD current (feed forward; FF). By the FF, MHF scan range of 10-18 GHz was achieved, which is considered to be well applicable to the selective tuning to the Ba isotopes.

For the second step (553 nm), a fiber coupled distributed-feedback laser (Fig. 1(c)) at the wavelength of 1107nm is prepared with output power of more than 45mW and beam profile shown in Fig1(c). The output is converted to 553nm using a periodically poled lithium niobate (PPLN) with ridge structure waveguide.

Development of photoionization system

For second ionization step, a pulsed N_2 laser (SRS-NL100, 337.1 nm, pulse width 3.3 ns, pulse energy 130 μs)

was used. Both laser beams were combined using a mirror, focused with a lens, and introduced into a spherical octagon vacuum chamber. The focused beams irradiate the atomic beam at the right angle from a Ba source produced by resistive heating, and generated ions are measured with a channeltron detector and a mass filter.

Optimal ionization process for Ba loading would be compared between schemes using the developing excitation lasers and the developing photoionization system.

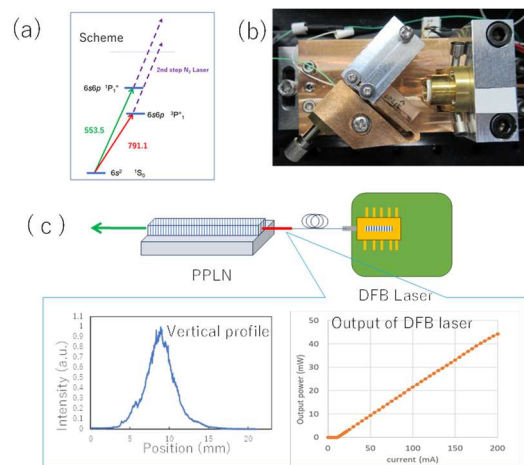


Fig. 1 Excitation scheme (a), and excitation lasers 791 nm (b), 553 nm (c).

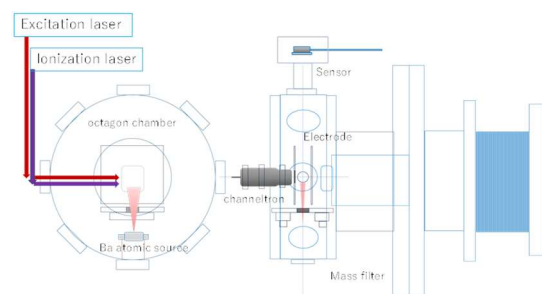


Fig. 1 Experimental setup of isotope selective loading of Barium ion by two-step photoionization.

Acknowledgments

This research is supported the JST Moonshot R&D Grant Number JPMJMS2063, and QST President's Strategic Grant QST Advanced Study Laboratory.

Reference

- [1] J.E. Christensen *et al.*, npj Quantum Inf **6**, 35 (2020). DOI: <https://doi.org/10.1038/s41534-020-0265-5>.

Construction of the ion trap system for radioactive Ba⁺ isotope

H. Shimada^{a)}, K. Hosaka^{a)}, H. Kashiwagi^{a)}, S. Hosoya^{a)}, Y. Yuri^{a)}, R. Nakanishi^{a)},
K. Tamura^{a)}, K. Ogura^{a)}, H. Ohba^{b)} and K. Narumi^{a)}

^{a)} Quantum Materials and Applications Research Center, QST

^{b)} Collaborative Laboratories for Advanced Decommissioning Science, JAEA

Introduction

The use of trapped ions for storing and manipulating quantum information has attracted attention for its high fidelities compared to other physical layer implementations such as superconductor. In particular, the ions having the lowest non-zero nuclear spin $I = 1/2$ are known to have many advantages [1] over those having other nuclear spin values $I \neq 1/2$ because of their simple hyperfine structure and their ease of quantum state manipulation. Among a few such ions capable of laser cooling, e.g. ¹¹¹Cd⁺, ¹⁷¹Yb⁺, we have chosen a long-lifetime (10.6 yr) radioactive ¹³³Ba⁺ [2] as the quantum information carrier and started constructing an experimental system for this isotope. Despite its difficulty in treating the radioactive isotope (RI), the Ba⁺ ions have main transitions in the visible spectral range and have metastable *D* states, appropriate for a high-fidelity scalable information processing system.

Trap experiment using non-RI Ba

We have tried the trapping and cooling experiment using our first trap system, "Trap-I (Hiroshima-type)" with non-RI Ba. In this experiment, vapor of neutral Ba atoms is provided via Ohmic heating of an oven and is ionized with an electron beam. The ions inside the trap, if present, are subsequently extracted and analyzed by using a channel electron multiplier and a time-of-flight method. By appropriately choosing the amplitude and frequency of the radio frequency (RF) voltage applied onto the trap electrodes, we have confirmed that Ba⁺ ions have been successfully loaded and trapped in this trap.

Next, we have tried the laser cooling and observing the fluorescence from the trapped Ba⁺ ions. For some reason, however, no fluorescence signals have been observed so far. Possible reasons for this are insufficient densities of Ba vapor and of electrons, presence of undesired ion species other than Ba⁺, and insufficient cooling in the radial direction.

In order to overcome these problems, the second trap system, "Trap-II (NICT-type)" is under construction. In this system, the Ba vapor is supplied using pulsed laser ablation instead of an oven and is ionized using resonant photoionization. With this technique, higher instantaneous density of Ba and lower contamination of ions other than Ba⁺ are expected. We are preparing a new laser system for this resonant photoionization. As the first step of the photoionization, the brightest transition of Ba is resonantly excited with this laser. An advantage of using this transition is that a quantitative evaluation of Ba vapor density will be

possible by observing the bright fluorescence from the excited Ba.

Having smaller size and enclosed in a smaller chamber, this "Trap-II" also provides easier optical access compared to that of "Trap-I", allowing off-axis incidence of laser beams and the cooling of Ba⁺ ions in the radial direction. Our next goal is to trap and cool the non-RI Ba⁺ ions using this "Trap-II." After confirming the proper operation, the system will be set up in the RI-controlled area for the ¹³³Ba⁺ experiment.

Preparation for RI experiment

For loading, trapping and cooling the radioactive ¹³³Ba⁺, the trap itself and its vacuum chamber, the peripheral optics and electronics need to be located inside the RI-controlled area. For this purpose, not only the trap system "Trap-II" as described above but also its peripheral apparatus are newly designed. These include the optical laser light delivery system using long fiber cables connecting laser located at the non-RI experimental room and the experimental chamber located at the RI-controlled area, the power and frequency control system of the delivered light, the synchronization system between lasers for ablation and resonant photoionization, the microscope system for observation of the trapped and cooled ion, and the low-noise DC and RF voltage sources for driving trap electrodes. These apparatuses are now under construction.

Acknowledgments

This work was supported by the JST Moonshot R&D Grant Number JPMJMS2063.

References

- [1] S. Olmschenk et al., Phys. Rev. A 76, 052314 (2007).
DOI: 10.1103/PhysRevA.76.052314
- [2] J.E. Christensen et al., npj Quantum Inf 6, 35 (2020).
DOI: 10.1038/s41534-020-0265-5

Y. Yamazaki^{a)}, R. Akashi^{a)}, M. Hanawa^{b)}, K. Murata^{b)}, S.-I. Sato^{a)}, N. Miyawaki^{a)}, S. Entani^{a)}, Y. Masuyama^{a)}, Y. Nishiya^{c,d)}, Y. Matsushita^{a,c,d)}, H. Tsuchida^{b)}, M. Kohda^{a,e)} and T. Ohshima^{a,e)}

^{a)} Quantum Materials and Applications Research Center, QST

^{b)} Central Research Institute of Electric Power Industry

^{c)} Quemix Inc.

^{d)} Department of Physics, The University of Tokyo

^{e)} Department of Materials Science, Tohoku University

Introduction

Spin defects, such as nitrogen-vacancy complex defects in diamond (known as NV centers), have been intensively studied for their potential applications in single-photon sources and quantum sensors. For all spin defects, a specific charge state must be present to allow for spin manipulation and readout. For example, silicon vacancies (V_{Si}) [1] in silicon carbide (SiC) must be single-negatively charged (V_{Si}^-).

Direct measurement inside a SiC power semiconductor device using V_{Si} -based quantum sensors is a promising application. Because a device structure consists of layers with various doping characteristics such as type and concentration, the charge state stability in each layer is an important factor in determining sensor availability.

In this study, we investigated the charge state stability of V_{Si} using high quality epitaxial films with fewer defects other than V_{Si} fabricated under a wide range of doping conditions.

Experimental

We used 6 μm -thick p- (dopant: aluminum) and n-type (nitrogen) epitaxial layers (p- and n-layer) on a n-type SiC substrate ($\sim 6 \times 10^{18} \text{ cm}^{-3}$) with different doping concentrations ranging from 1×10^{15} to $1 \times 10^{19} \text{ cm}^{-3}$ for each doping type. As a pseudo-intrinsic layer (hereafter referred to as the i-layer), a depletion layer formed between the p-type epitaxial layer with the lowest doping concentration and the n-type substrate was utilized. The V_{Si} ensemble was generated into samples by particle beam writing (PBW) using a focused He ion beam with a diameter of $\sim 1 \mu\text{m}$. The ion energies were set to 0.5 and 2.5 MeV for p- and n-layers, and the i-layer, respectively. The fluence was changed from 3×10^3 to $3 \times 10^6 \text{ He}^+/\text{spot}$ ($= 3 \times 10^{11} \sim 3 \times 10^{14} \text{ cm}^{-2}$) for all samples. Samples were annealed at $600 \text{ }^\circ\text{C}$ to improve the optical and spin properties of V_{Si}^- by removing unwanted defects with low thermal stability. A home-built confocal microscope was used for photoluminescence (PL) and optically detected magnetic resonance (ODMR) measurements. All measurements were performed at room temperature.

Results and Discussion

Figure 1 shows the saturated PL counts (I_{max}) under all conditions. The I_{max} values were obtained from the saturation curves: $I(P) = I_{\text{max}}/(1+P_0/P)$, where P and P_0 are

the laser and saturated laser powers, respectively. The PL originating from V_{Si}^- was confirmed in 76 out of 98 conditions. This result shows that V_{Si}^- is stable over a wide range of doping concentration for both p- and n-type, although optimization of V_{Si} density is necessary. Under optimized condition leading the maximum charge state stability, a maximum ODMR contrast of 1.2% was achieved, which was the highest value achieved, except for the specific cases [2,3]. In conclusion, the finding is important for designing V_{Si} -based quantum sensors to realize direct measurement inside a SiC power semiconductor device.

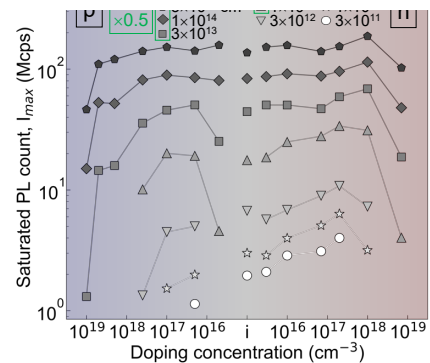


Fig. 1 Dependence of saturated PL count (I_{max}) on doping condition and fluence. Data below the detection limit are not plotted. For the i-layer, the data was normalized ($\times 0.5$) to account for the difference in V_{Si} generation rate between 0.5 and 2.5 MeV. The data for fluences above $1 \times 10^{13} \text{ cm}^{-2}$ are multiplied by 0.5.

Acknowledgments

This study was partially supported by JSPS KAKENHI 21H04553 and 20H00355, MEXT Quantum Leap Flagship Program (MEXT Q-LEAP) Grant Number JPMXS0118067395, Innovative Science and Technology Initiative for Security Grant Number JPJ004596, ATLA, Japan, and the Center of Innovations for Sustainable Quantum AI (JST Grant Number JPMJPF2221).

References

- [1] N. Mizuochi et al., Phys. Rev. B **66**, 235202 (2002).
- [2] J. B. S. Abraham et al., Phys. Rev. Appl. **15**, 064022 (2021).
- [3] H. Singh et al., Phys. Rev. B **107**, 134117 (2023).

X-ray absorption fine structure analysis of Pr ions implanted in GaN

E. Yokozuka ^{a)}, T. Tsuji ^{b)}, D. Matsumura ^{b)}, M. Deki ^{c)}, H. Watanabe ^{d)}, S. Nitta ^{d)}, Y. Honda ^{d)}, H. Amano ^{d)}, N. Nagasawa ^{a)}, H. Saitoh ^{e)} and S.-I. Sato ^{a)}

^{a)} Quantum Materials and Applications Research Center, QST

^{b)} Materials Sciences Research Center, JAEA

^{c)} Deep Tech Serial Innovation Center, Nagoya University

^{d)} Institute of Materials and Systems for Sustainability, Nagoya University

^{e)} Synchrotron Radiation Research Center, QST

Introduction

In recent years, quantum technologies such as quantum computing, quantum communication, and quantum sensing have been attracted attention. The development of single-photon sources that generate a single photon at any time is crucial to the realization of quantum technologies. Lanthanide (Ln) ions in gallium nitride (GaN) are expected to be used for novel single-photon sources, since they exhibit stable photon emission with a narrow linewidth at room temperature [1]. To be used as the single-photon sources, isolated Ln ions must be placed in a specific position, and ion implantation is one of the most effective methods to realize the deterministic placement of isolated Ln ions. It is generally understood that trivalent Ln ions (*i.e.* Ln³⁺), which substitute the Ga site in GaN, act as the stable luminescent center [2]. However, the local structures and electronic states of the implanted Ln ions in GaN are less well understood, as only a few experimental studies on the local structures of implanted Ln ions in GaN have been performed [3]. In this study, praseodymium (Pr) ions, which is one of Ln ions emitting red light, were implanted in GaN and their electronic state was investigated by X-ray absorption fine structure (XAFS) using synchrotron radiation at SPring-8. The change in electronic state due to thermal annealing was also analyzed.

Experimental

N-type (Si-doped) GaN epi-layers grown on GaN (0001) substrate were implanted with 100, 200, 350, and 700 keV Pr ions at the doses of 1.3×10^{14} cm⁻², 1.7×10^{14} cm⁻², 3.2×10^{14} cm⁻², and 1.1×10^{15} cm⁻², respectively to obtain a uniform Pr concentration of 10^{20} cm⁻³ within a depth of 150 nm from the surface. The Pr implantation profile was calculated using the Monte Carlo simulation code, TRIM. The Pr ion implantation was performed at the Takasaki Ion Accelerators for Advanced Radiation Application (TIARA), QST. The Pr-implanted GaN samples were then thermally annealed at 1200°C for 2 min in a N₂ atmosphere to restore the implantation damage and to activate the Pr ions as luminescence centers.

The XAFS measurements were performed at the beamline BL14B1 at SPring-8 with a Si(111) double-crystal monochromator. The XAFS spectra for the Pr-implanted GaN were measured in the fluorescence detection mode

with a 36-element Ge detector. All the measurements were performed at room temperature. The XAFS spectra were analyzed using the ATHENA and ARTEMIS XAFS analysis packages.

Results

Figure 1 shows the Pr L_{III}-edge X-ray Absorption Near Edge Structure (XANES) spectra of Pr-implanted GaN before and after annealing. The XANES spectrum of Pr₂O₃ is also shown as a reference for Pr³⁺. The peak energy of Pr-implanted GaN is in good agreement with that of Pr₂O₃ regardless of thermal annealing, indicating that the valence state of the implanted Pr ions is +3. However, the spectral intensity increases and the peak line width decreases after annealing. This spectral change is thought to be caused by the recovery of the GaN lattice from implantation damage, resulting in the improvement of symmetry of local structure around the implanted Pr ions.

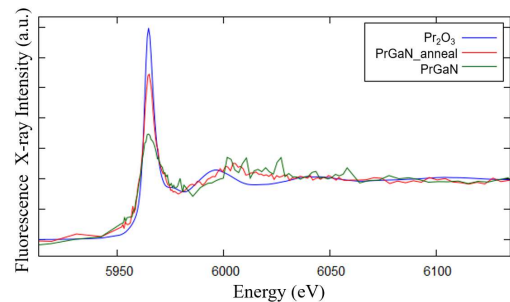


Fig. 1 Pr L_{III}-edge XANES spectra of Pr-implanted GaN before annealing (green), after annealing (red), and Pr₂O₃ (blue).

Acknowledgments

This work was supported by JST FOREST Program (Grant No. JPMJFR203G, Japan) and partially carried out by the joint research program of the Institute of Materials and Systems for Sustainability (IMaSS), Nagoya University.

References

- [1] R. Birkhahn *et al.*, Appl. Phys. Lett. **74**, 2161 (1999). DOI: 10.1063/1.123787
- [2] K. P. O' Donnell *et al.*, Springer, Netherlands, vol. 124 (2010).
- [3] U. Wahl, *et al.*, Nucl. Instrum. Meth. B **267**, 1340-1344 (2009). DOI: 10.1016/j.nimb.2009.01.043

Part II

2. Materials Science

2-01	Preparation of Pd-doped TiO ₂ films by sputtering deposition on sapphire substrates	31
	S. Yamamoto, A. Idesaki, T. Taguchi and M. Saeki	
2-02	Lattice plane spacing change of carbon layer in C-SiC coaxial nanotube by ion irradiation	32
	T. Taguchi, S. Yamamoto and M. Saeki	
2-03	Superconducting properties of GdBa ₂ Cu ₃ O _y thin films irradiated with 350 keV Ar-ions	33
	T. Ozaki, H. Okazaki, H. Koshikawa, S. Yamamoto and M. Saeki	
2-04	Effect of high-dose electron beam irradiation on thermal decomposition behavior of polytetrafluoroethylene (PTFE)	34
	H. Yu, A. Idesaki, A. Hiroki, S. Hasegawa, K. Hirota and Y. Maekawa	
2-05	Modification of polymeric materials by quantum beam irradiation (4)	35
	A. Idesaki, A. Hiroki, S. Hasegawa and Y. Maekawa	
2-06	Development of polymeric sealing materials utilizing radiation technique by ion beam irradiation	36
	A. Idesaki, S. Hasegawa, K. Yoshimura, A. Hiroki and Y. Maekawa	
2-07	Machine learning analysis of proton conduction properties of graft-type cation exchange membranes based on various polymers	37
	S. Sawada, Y. Sakamoto, K. Funatsu and Y. Maekawa	
2-08	Preparation of hydrogel/aluminum hydroxide composite adsorbent by in-situ radiation polymerization for lithium recovery from saltlake brine	38
	J. Chen and N. Seko	
2-09	Measurement method of the degree of grafting by using thermogravimetric analysis	39
	M. Omichi, H. Hoshina, H. Morishima, K. Ohshima and N. Seko	
2-10	Development of metal adsorbent via radiation-induced graft polymerization and Kabachnik-Fields reaction	40
	M. Kuroiwa, K. Matsubara, M. Omichi, H. Hoshina, N. Seko and R. Kakuchi	
2-11	The development of environmentally friendly soft contact lenses based on cellulose-derived gels	41
	A. Hiroki, A. Kimura and M. Taguchi	
2-12	Irradiation tests of radiation-hard components and materials for ITER blanket remote handling system	42
	M. Saito, Y. Kawai, K. Nakata, T. Ito, T. Fujiwara, H. Seki, Y. Noguchi and N. Takeda	
2-13	Irradiation effects on fiber/matrix interfacial properties of SiC/SiC composites by micro-mechanical testing methods	43
	T. Nozawa and M. Ando	

2-14	Study of multi ion-irradiation effects on fusion reactor materials using a micro-tensile testing method.....	44
	M. Ando and T. Nozawa	
2-15	Investigation on tensile properties of single crystal pure tungsten using micro-tensile test methodology	45
	D. Hamaguchi, Ju-Hyeon Yu M. Ando and H. Kurotaki	
2-16	Gamma-ray irradiation experiment for ITER diagnostic systems in JADA VI.....	46
	S. Kitazawa, Y. Nunoya, M. Ishikawa, R. Imazawa, E. Yatsuka, K. Nojiri, T. Ushiki, H. Natsume, S. Kono, K. Torimoto, M. Inamine, Y. Nemoto, T. Kikuchi, T. Yokozuka, H. Murakami, K. Shimizu and T. Sugie	
2-17	Luminescence of samarium complexes in <i>N,N,N',N'</i> -tetraoctyl diglycolamide solvent induced by hydrogen ion beam	47
	M. Nakahara, Y. Ishii, R. Yamagata, N. Yamada and M. Koka	
2-18	Color imaging of carbon ion ($^{15}\text{C}^{+5}$) beam by the carbon tetrachloride gel dosimeter containing the spiropyran-like	48
	T. Tachikawa and C. Koizumi	
2-19	γ -ray irradiation effect on ammonia radical derived from hydrothermally altered potassium feldspar: A physical basis for the application to fault dating (II)	49
	T. Fukuchi	

Preparation of Pd-doped TiO₂ films by sputtering deposition on sapphire substrates

S. Yamamoto, A. Idesaki, T. Taguchi and M. Saeki

Department of Advanced Functional Materials Research, QST

Introduction

Polymer Electrode Membrane Fuel Cells (PEMFCs) have attracted attention for their higher energy densities and lack of pollutant emissions. The current operating temperature of PEMFCs is approximately 80°C. Operation at 130°C is required for the next generation of PEMFCs to increase the efficiency of power generation. Carbon supported platinum (Pt) nanoparticles are the most attractive catalysts for an oxygen reduction reaction (ORR) at present. However, carbon supported Pt nanoparticles are not durable in operation above 100°C. Therefore, there is a need to develop electrode materials with high durability and high activity for the ORR above 100°C. One promising electrode material is based on the metal-doped TiO₂. In this work, we investigated the effect of the post-annealing on the microstructure of Pd-doped TiO₂ films prepared by simultaneous deposition.

Experimental

The Pd-doped TiO₂ films were grown by rf magnetron sputtering, which was performed using metallic Ti and Pd targets in an Ar and O₂ gas mixture. The single crystal sapphire substrates (α -Al₂O₃) of c-plane were used. Simultaneous deposition was performed at a substrate temperature of 500°C and sputtering power of 50 W for Ti and 2 W for Pd, respectively. The post-annealing treatment was carried out at 800°C for 1 h in air using an electric furnace. The crystallographic structure of the films was determined by XRD. The composition and crystallinity of the films were determined by RBS/channeling measurements carried out using a 2.0 MeV ⁴He⁺ beam from a 3 MV single-stage accelerator at QST/Takasaki. The microstructure of films was characterized by transmission electron microscope (TEM) operating at 200 kV. Cross-sectional TEM samples were prepared with ion slicer (IB-

090600CIS, JEOL) using Ar ion.

Results and Discussion

The results of XRD measurements indicated that rutile-type (100) oriented TiO₂ films were grown on c-plane sapphire substrates both the as-deposited and the post-annealed films. Figure 1 shows the RBS spectra of the Pd-doped TiO₂ (100) films on the c-plane sapphire substrates (a) as-deposited at 500°C and (b) post-annealed at 800°C taken under the random and the TiO₂<100> aligned conditions. The peaks at 1.72, 1.44 and 1.11 MeV correspond to the Pd and Ti components in the Pd-doped TiO₂ film and the Al component in the sapphire substrate, respectively. The atomic ratio of Pd to Ti was 0.01 as determined by RBS. The reduction of the normalized yields of Ti and Al in the aligned conditions reveal the TiO₂ <100> crystallographic axis is parallel to the sapphire <0001> axis. However, the yields of Pd were almost the same taken under the random and the TiO₂<100> aligned conditions. This indicates that the doped Pd atoms were not substituted into the TiO₂ lattice sites. Figure 2 shows a cross-sectional TEM image of the Pd-doped TiO₂ film grown on the c-plane sapphire substrate (post-annealed at 800°C). As can be seen, the nanoparticles of Pd or Pd oxide are present in the TiO₂ layer. Preliminary results indicate that the Pd-doped TiO₂ prepared by simultaneous deposition and post-annealing shows the formation of nanoparticles of Pd or Pd oxide. We suggest that non-equilibrium processes, such as high-temperature ion implantation and pulsed laser annealing, can provide atomically doping in TiO₂.

Acknowledgments

The authors thank Ms. C. Suzuki for her help with the TEM observations.

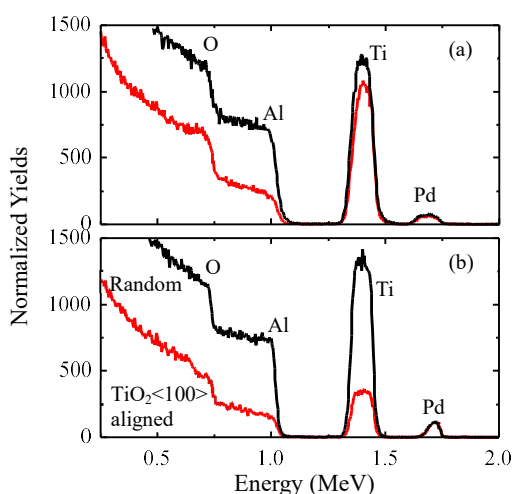


Fig. 1 RBS/channeling spectra of a Pd-doped TiO₂ film on c-plane sapphire substrate (a) as-deposited at 500°C and (b) post-annealed at 800°C for 1 h in air.

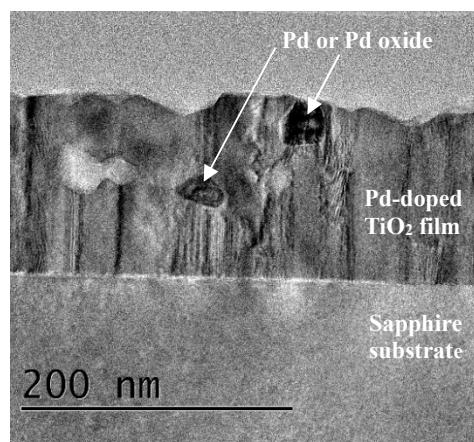


Fig. 2 Cross-sectional TEM image of a Pd-doped TiO₂ film grown on the c-plane sapphire substrate with post-annealed at 800°C for 1 h in air.

2 - 02 Lattice plane spacing change of carbon layer in C-SiC coaxial nanotube by ion irradiation

T. Taguchi, S. Yamamoto and M. Saeki

Department of Advanced Functional Materials Research, QST

Introduction

Silicon carbide (SiC) has been reported to be utilized as wide-band-gap semiconducting and structural materials for high temperatures. On the other hand, it is well known that one-dimensional nanomaterials, such as nanowires, nanorods and nanotubes possess new properties different from those of their bulk materials. So far, we have succeeded in synthesizing polycrystalline single-phase SiC nanotubes and C-SiC coaxial nanotubes, in which multi-walled carbon nanotubes (MWCNTs) were sheathed with a SiC layer [1, 2]. Furthermore, we reported that a successful synthesis of a new structured hybrid carbon nanomaterials was achieved for the first time, which consisted of one-dimensionally stacked graphene nano-disks with diameter less than 50 nm, and cylindrical multi-walled carbon nanotubes (MWCNTs), inside an amorphous SiC nanotube by the ion irradiation of C-SiC coaxial nanotubes [3]. However, the carbon layer structure change in the C-SiC coaxial nanotubes during the ion irradiation has not been particularly investigated. In this study, we reported the lattice plane spacing changes of the carbon layer in C-SiC coaxial nanotubes under the ion irradiation using in-situ TEM observation techniques.

Experimental

MWCNTs (GSI Creos Corporation, Tokyo, Japan) were used as the template. The C-SiC coaxial nanotubes were synthesized by heating MWCNTs with Si powder (The Nilaco Corporation, Tokyo, Japan) at 1,200 °C for 100 h in a vacuum. The samples heated at the above conditions included many unreacted MWCNTs besides the C-SiC coaxial nanotubes. Therefore, the samples were then heated at 700 °C for 2 h in air in order to remove unreacted MWCNTs. The molybdenum grid holder, which deposited the C-SiC coaxial nanotubes, were irradiated with 200 keV Si⁺ ions from 400 kV ion implanter at room temperature in TEM (Model JEM-4000FX, JEOL Ltd., Japan). In-situ TEM observation of C-SiC coaxial nanotube under Si⁺ ions irradiation was carried out. The maximum irradiation damages for the SiC and carbon layer in C-SiC coaxial nanotubes were calculated by SRIM 2008 to be 46.8 and 43.9 dpa respectively.

Results and Discussion

TEM observations revealed that the SiC crystals in the C-SiC coaxial nanotubes were completely amorphized by the ion irradiation at room temperature. On the other hand, the carbon layer in the C-SiC coaxial nanotube was confirmed to have remained crystalline, even after the

irradiation dose exceeded 40 dpa. Therefore, the carbon layer possessed better resistance against amorphization after ion irradiation, compared with the SiC layer in the C-SiC coaxial nanotube, because the sputtering of C atoms is restrained on the outer surface of the carbon layer and due to the compression stress, attributed to the SiC layer undergoing configurational change during irradiation.

The lattice plane spacing of basal planes in the carbon layer increased up to the point of irradiation damage demonstrated by the complete amorphization of SiC crystals; afterwards it started to decrease. Our previous study reported that new graphitic shells perpendicular to the nanotube length direction suddenly emerged after ion irradiation in the C-SiC coaxial nanotube [3]. Figure 1 shows the effect of original thickness of carbon layer parallel to nanotube length on narrowest lattice plane spacing of carbon layer after ion irradiation. From this result, both the narrowest lattice spacing of carbon layer parallel and perpendicular to the nanotube length decreased with increasing the original carbon layer in the C-SiC nanotube. The reason is considered that the configuration change ratio such as inner, outer diameter and length of C-SiC coaxial nanotube increased with increasing the original carbon layer.

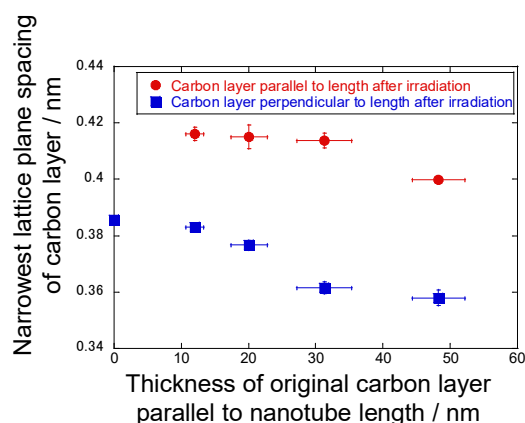


Fig. 1 Effect of original thickness of carbon layer parallel to nanotube length on narrowest lattice plane spacing of carbon layer after ion irradiation.

References

- [1] T. Taguchi *et al.*, J. Am. Ceram. Soc. **88**, 459 (2005). DOI: 10.1111/j.1551-2916.2005.00066.x
- [2] T. Taguchi *et al.*, Physica E **28**, 431 (2005). DOI: 10.1016/j.physe.2005.05.048
- [3] T. Taguchi *et al.*, Acta Materialia **173**, 153 (2019). DOI: 10.1016/j.actamat.2019.05.007

2 - 03 Superconducting properties of $\text{GdBa}_2\text{Cu}_3\text{O}_y$ thin films irradiated with 350 keV Ar-ions

T. Ozaki^{a)}, H. Okazaki^{b)}, H. Koshikawa^{b)}, S. Yamamoto^{b)} and M. Saeki^{b)}

^{a)}School of Engineering, Kwansei Gakuin University,

^{b)}Department of Advanced Functional Materials Research, QST

Introduction

High in-field critical current properties in $\text{REBa}_2\text{Cu}_3\text{O}_y$ (REBCO, RE: Y and rare earth) superconducting films are very important for high magnetic field applications. The practical critical current density J_c is governed by the vortex pinning strength. The Vortex pinning, which is determined by the ability of defects in superconducting materials, is the key to increase J_c in magnetic fields. The desirable pinning structures could be provided by ion irradiation, which can enable the creation of a variety of defects, such as points, clusters and tracks, by choosing appropriate ion species and energy. Therefore, ion irradiation would be a promising approach to realize high performance REBCO films. In this work, we present superconducting properties in GdBCO thin films irradiated with 350 keV Ar-ions.

Experimental

The samples were 0.4 μm thick GdBCO superconducting layers on clad-type textured metal substrates deposited by a pulsed laser deposition (PLD) process. The irradiation experiment was carried out using 400 kV ion implanter at TIARA. A beam of 350 keV Ar-ions was directed to the film surface at normal incidence with $4.8 \times 10^{11} - 6.9 \times 10^{13}$ ions/cm² dose. The superconducting properties were measured using a Quantum Design superconducting quantum interference device (SQUID) magnetometer.

Results and Discussion

Fig. 1 shows superconducting transition temperature T_c obtained from magnetization measurement as a function of fluence in GdBCO films irradiated with 350 keV Ar-ions. We found that the T_c 's of the irradiated GdBCO thin films decreased gradually with increasing fluence up to around 1.0×10^{13} ions/cm² and then significantly started to drop.

Fig. 2 shows critical current density J_c as a function of the magnetic field for pristine and the irradiated films at different doses. The J_c enhancement as a function of magnetic field are displayed in the inset, where J_c enhancement is defined as $(J_c \text{ of irradiated film} - J_c \text{ of pristine film}) / J_c \text{ of pristine film}$. We found that the 350 keV Ar-ion irradiation yielded up to over 50% J_c enhancement in the magnetic field over 4 T. These results indicate that 350 keV Ar-ions irradiation is effective to provide strong pinning defects in high- T_c GdBCO superconducting films.

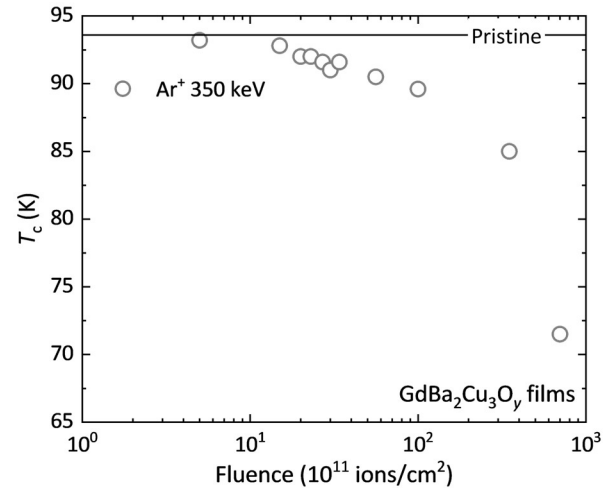


Fig. 1 Superconducting transition temperature T_c as a function of fluence for GdBCO films irradiated with 350 keV Ar-ions.

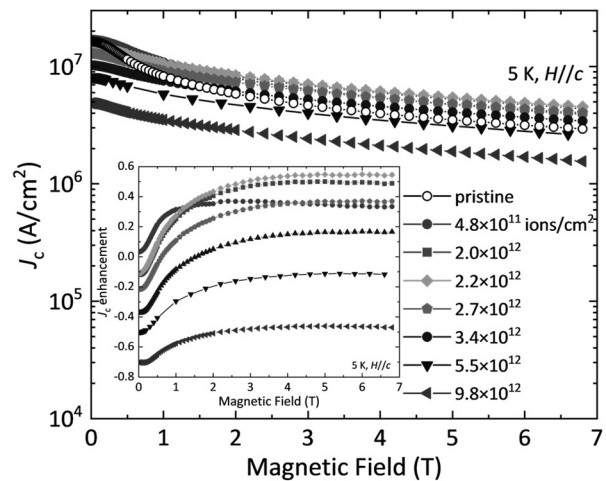


Fig. 2 Critical current density J_c as a function of magnetic field for a pristine (prior to irradiation) GdBCO film and films irradiated with 350 keV Ar-ions at 5 K. The inset shows calculated J_c enhancement.

References

- [1] M. A. Kirk *et al.*, *Micron* 30, 507–526 (1999). DOI: 10.1016/S0968-4328(99)00051-7
- [2] W. K. Kwok *et al.*, *Rep. Prog. Phys.* 79, 116501 (2016). DOI: 10.1088/0034-4885/79/11/116501
- [3] T. Ozaki *et al.*, *Supercond. Sci. Technol.*, 33, 094008 (2020). DOI: 10.1088/1361-6668/ab9f66

2 - 04 Effect of high-dose electron beam irradiation on thermal decomposition behavior of polytetrafluoroethylene (PTFE)

H. Yu, A. Idesaki, A. Hiroki, S. Hasegawa, K. Hirota and Y. Maekawa

Department of Advanced Functional Materials Research, QST

Introduction

Fluoropolymers such as polytetrafluoroethylene (PTFE) is high-performance plastics widely used in various industries, including automation, electronics, and medicine. Their excellent thermal and chemical stability continues to improve year by year. However, this exceptional heat resistance hinders recycling and reuse, as these plastics require substantial energy for pyrolysis. Consequently, there is an urgent need to develop highly efficient recovery and recycling technologies for high-performance plastics to build a carbon-neutral society. Quantum beams, such as electron beams, could potentially enhance fluorocarbon decomposition and modification due to their ability to ionize or excite the polymer molecules, which can result in the easy cleavage of the most stable C-F bonds. However, the full effects of radiation on these materials and the decomposition mechanisms remain unclear. In this report, we explore the impact of electron beams and additives on reducing the decomposition temperature of PTFE powder.

Experimental

PTFE (Mw = 5,000–20,000) micropowder was purchased from FUJIFILM Wako Pure Chemical Corporation (Osaka, Japan) and used as received. The PTFE powder samples were placed on sample holders and irradiated with electron beams with a voltage of 2.0 MeV and a current of 0.5 mA by using the electron beam irradiation facility at the Takasaki Institute for Advanced Quantum Science (TIAQ), The National Institutes for Quantum Science and Technology (QST). The dose rate was 0.40–0.92 kGy/s, as measured via cellulose triacetate film dosimetry. The maximum absorbed dose was 15.0 MGy. Samples were irradiated at room temperature in the presence of oxygen.

We measured weight changes and analyzed chemical structures of PTFE residues after irradiation and thermal treatment as well as the outgas components during thermal treatment using differential thermogravimetric analyzer (TG-DTA), chromatography-mass spectrometry (GC-MS), and Fourier transform infrared (FT-IR) spectroscopy.

Results and Discussion [1, 2]

Thermogravimetric analyses indicated that the residual PTFE powder irradiated with 15 MGy exhibited an initial decomposition (5% weight loss) at 159 °C, which is 365 °C lower than that of the original unirradiated sample, as shown in Figure 1. The initial decomposition temperature decreased at up to 5 MGy and gradually leveled off at above 140 °C. FT-IR spectroscopy analyses of the residual

PTFE powders indicated that the contents of thermal decomposition at lower temperature ranges were qualitatively related to the extent of the formation of oxidizable PTFE components, such as carbonyl groups. The formation of these components increased as the absorbed doses increased. The oxidized components gradually decreased with increasing thermal treatment temperature and tended to disappear at 470 °C. This demonstrated the effect of the oxidized compounds in the irradiated PTFE on lower temperature decomposition.

The analysis of the gas components of the PTFE residuals revealed more detailed chemical information concerning the oxidative components of the irradiated PTFE. At temperatures below 420 °C, ~30% of the PTFE residue underwent pyrolysis to yield oxidized fluorocarbon products (C_xF_yO_z) and decomposed products (CO₂). The remaining 70% of the residue thermally decomposed at temperatures above 420 °C, yielding monomer-related products such as C₂F₄, C₃F₆, and C₄F₈, which are identical to the gas products from the thermal degradation of the original PTFE in the same temperature range.

These results are indicative of the possibility of recycling and reusing fluorocarbons during irradiation.

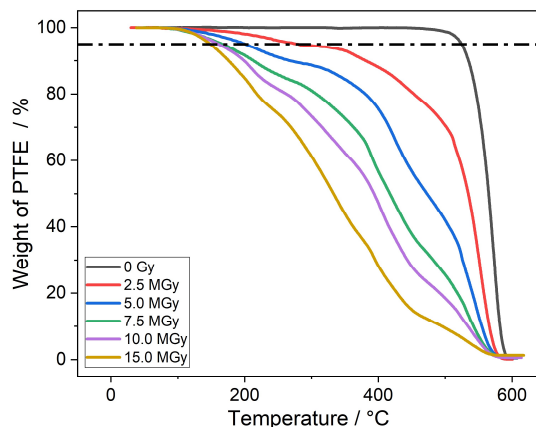


Fig. 1 Thermogravimetric curves of PTFE powder with absorbed doses of 1-15 MGy.

Acknowledgments

This work was supported by JST, CREST (JPMJCR21L1), Japan.

References

- [1] H. Yu et al. Radiation Physics and Chemistry, 216, 111435, (2024). DOI:10.1016/j.radphyschem.2023.111435.
- [2] Y. Maekawa et al., Japanese Patent Application No. 2023-117122, (2023).

2 - 05 Modification of polymeric materials by quantum beam irradiation (4)

A. Idesaki, A. Hiroki, S. Hasegawa and Y. Maekawa

Department of Advanced Functional Materials Research, QST

According to the Basic Hydrogen Strategy, revised in June 2023, efforts for popularization of fuel cell vehicles (FCVs) and hydrogen refueling stations (HRSs) are positioned as one of the most important issues in the field of mobilities. Especially, the costs of FCVs should be reduced to realize the popularization. For example, the cost of current high pressure-hydrogen tank for the FCVs is ¥700,000; the cost is required to be reduced to around ¥300,000. The common high pressure-hydrogen tank for FCVs, type IV tank, is composed of plastic liners and carbon fiber reinforced plastics (CFRPs). It is effective to reduce the amount of expensive carbon fiber to realize the low cost-tank, therefore, novel high performance-polymeric materials which can be alternative to the CFRPs have been strongly desired.

The materials in the type IV tank are exposed repeatedly to severe conditions such as high pressure of 70 MPa, wide temperature range of -40°C to 85°C . Especially, the materials must retain sufficient durability against the high pressure-hydrogen; the materials with low hydrogen gas permeability and high mechanical properties are desirable as shown as "TARGET ZONE" in Figure 1. Referring to the Fig. 1, we have been examined radiation crosslinking of polymeric materials such as polyethylene (PE), polyamides (PA), and lately, polymer blends [1-3]. In this work, effect of compatibilizer on radiation crosslinking of PA/PE blend (80/20 in weight). The compatibilizer is effective to form fine dispersion of PE domain in the PA matrix. The samples composed of PA/PE blend with compatibilizer (0-10 phr) were irradiated by gamma-rays with dose of 70 kGy under vacuum at room temperature. Figure 2 shows gel fraction of samples after the gamma-ray irradiation. The gel fractions for pure PA and pure PE after the irradiation were 0% and 6.5%, respectively. According to these values, the

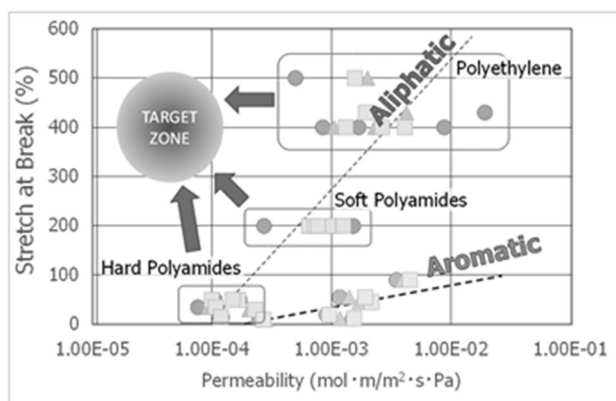


Fig. 1 Relationship between H_2 permeability and tensile property for various polymeric materials presented by Prof. Nishimura at Kyushu University.

gel fraction for PA/PE (80/20) without compatibilizer can be calculated to be 1.3% if no reaction occurs between PA and PE. However, the gel fraction for PA/PE (80/20) with 0 phr was 8.5%. This result suggests that crosslinking reaction occurs at the interface of PA matrix and PE domain. On the other hand, the PA/PE with 5 and 10 phr showed the gel fraction of 13.0% and 15.6%, showing that the gel fraction after the irradiation much increased by the addition of compatibilizers of more than 5 phr. Sufficient compatibilizer forms fine dispersion of PE domain which leads larger area at the interface of PA and PE. It was found that it is useful to increase the area at the interface by adding the compatibilizer for effective radiation crosslinking of PA/PE blend.

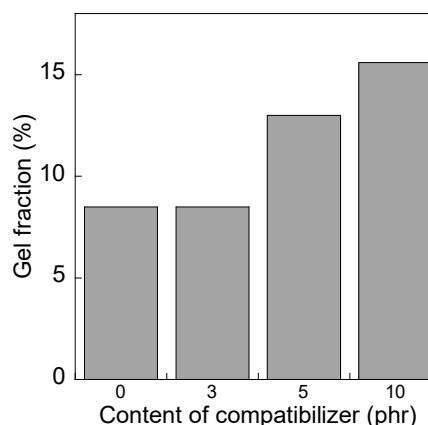


Fig. 2 Gel fraction of PA/PE (80/20) blends with compatibilizer after gamma-ray irradiation.

Acknowledgments

This work is based on results obtained from a project, JPNP20003, commissioned by the New Energy and Industrial Technology Development Organization (NEDO). This is a collaboration work with Prof. Shin Nishimura at Kyushu University and Prof. Katsuhisa Tokumitsu at The University of Shiga Prefecture.

References

- [1] A. Idesaki *et al.*, QST Takasaki Annu. Rep. 2020, **QST-M-33** 27 (2021).
- [2] A. Idesaki *et al.*, QST Takasaki Annu. Rep. 2021, **QST-M-39** 34 (2022).
- [3] A. Idesaki *et al.*, QST Takasaki Annu. Rep. 2022, **QST-M-47** 42 (2023).

A. Idesaki, S. Hasegawa, K. Yoshimura, A. Hiroki and Y. Maekawa

Department of Advanced Functional Materials Research, QST

Utilization of hydrogen is one of the most promising solutions to realize the carbon neutrality. So far, manufacture and sales of fuel cell vehicles (FCVs) and construction of hydrogen refueling stations (HRSs) have been strongly progressing in Japan: number of FCVs sold is about 7,700 and number of HRSs installed is about 180, as of February 2023. The number of installations of HRSs in one of the most important issues; it should be increased to promote the popularization of FCVs.

On the other hand, application of fuel cells for heavy duty vehicles (HDVs) such as trucks, trains, ships, and so on, has been considered recently. Since the instruments and specifications of current HRSs are for light duty vehicles (LDVs), it is necessary to develop HRSs with updated specifications for the HDVs. For example, mounting amount of hydrogen for HDVs is expected to be 400 kg, although the mounting amount of hydrogen for LDVs is about 6 kg. It would be indispensable to greatly increase the flow rate of hydrogen for refilling the tank in reasonably short time. To achieve such specifications, instruments of compressors and accumulators with high performance should be developed. These instruments include some parts made of polymeric materials as hoses, sealings, and so on. We aim at the development of sealing parts with high performance through modification of polymeric materials utilizing radiation technique.

The polymeric materials are used as dynamic sealings in the compressors and accumulators, therefore, the properties of sliding property, airtightness for hydrogen and abrasion resistance are required. The abrasion resistance relates closely to surface hardness of materials; the abrasion resistance generally become high as the surface hardness is high. Then, change of surface hardness of high-density polyethylene (HDPE), as a model material, by gamma-ray irradiation was investigated.

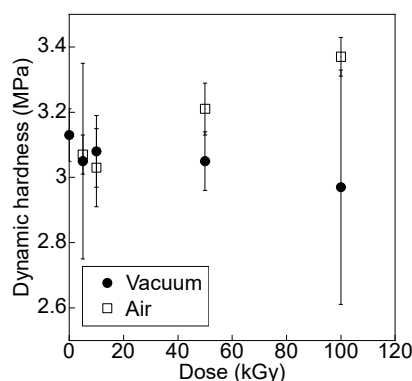


Fig. 1. Change of surface hardness of HDPE after gamma-ray irradiation.

HDPE sheets were irradiated by gamma-rays up to the dose of 100 kGy under vacuum or air atmosphere at room temperature. After the irradiation, surface hardness was measured by a dynamic micro-hardness tester. The hardness was measured at 10 different points and the values were averaged (Fig. 1). The dynamic hardness of unirradiated HDPE was 3.13 MPa. In the case of irradiation under vacuum, the hardness decreased slightly to 2.97 MPa at 100 kGy. On the contrary, the hardness started to increase above 10 kGy, and finally reached 3.37 MPa at 100 kGy. Similar result was obtained in the measurement of density after the irradiation (Fig. 2). The density was measured by Archimedes method using ethanol as a buoyant. In the case of irradiation in air, the density started to increase above 10 kGy and reached 0.9450 g/cm³ which is higher than that of vacuum (0.9439 g/cm³). The difference was not large, but the increasing in the density in the case of irradiation in air was caused by weight gain by oxidation and volume shrinkage by molecular-chain scission. This suggests that increasing in the density led to increasing in the surface hardness.

According to the obtained results, gamma-ray irradiation is useful for modification of surface hardness of HDPE. It is expected that the abrasion resistance of HDPE is also modified by the irradiation.

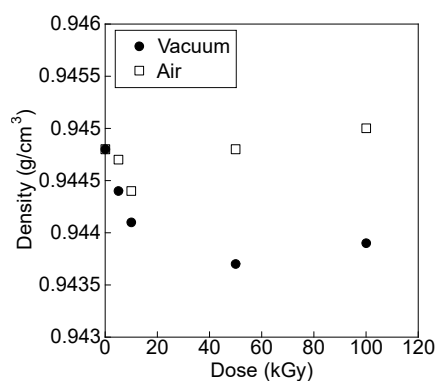


Fig. 2 Change of density of HDPE after gamma-ray irradiation.

Acknowledgments

This work is based on results obtained from a project, JPNP23004, commissioned by the New Energy and Industrial Technology Development Organization (NEDO).

Machine learning analysis of proton conduction properties of graft-type cation exchange membranes based on various polymers

S. Sawada^{a)}, Y. Sakamoto^{a)}, K. Funatsu^{b)} and Y. Maekawa^{a)}

^{a)} Takasaki Institute for Advanced Quantum Science, QST

^{b)} Graduate School of Engineering, University of Tokyo

Introduction

Proton conductivity (σ) and hydration number (λ) are important characteristics of cation exchange membranes (CEMs) used for fuel cells. A high σ yields high output power, while low λ improves the dimensional stability to achieve the long-term stable operation. Accordingly, σ/λ is the crucial characteristics because it reflects how efficiently protons can conduct at low water content.

The radiation grafting method is promising to develop the CEMs. This method introduces the cation exchange graft chains such as poly(styrene sulfonic acid) into the base polymer film. The characteristics of the obtained CEMs are greatly influenced by the type of base polymers, but this influence mechanism has not been fully understood.

In this study, the σ/λ data of the graft-type CEMs based on various polymers was analyzed by machine learning. This analysis revealed the specific properties of the base polymers that affected the σ/λ .

Data collection and ML analysis^[1]

Fig. 1 shows the σ/λ of the CEMs based on 10 different polymers as a function of the volume-normalized ion exchange capacity (IECv). The σ/λ significantly changed depending on the base polymers in spite of the same IECv.

As the explanatory variables, the following 20 properties of the base polymers were selected: density, molecular weight, van der Waals volume, formation energy, crystallinity (ϕ_c), glass transition temperature, melting point (MP), solubility parameter, HOMO and LUMO energy, band gap, ionization energy, electron affinity, dipole moment, electronegativity, polarizability, relative permittivity, tensile strength and elongation at break, and Young's modulus. The values of the above variables were obtained from the literature, experiments, quantum chemical calculation, and descriptor generators.

The relationship between the objective variable, σ/λ , and explanatory variables was modeled by random forest (RF) regression, which was performed using the scikit-learn module in Python. To evaluate the model prediction accuracy, the coefficient of determination (R^2) was calculated.

Results and Discussion^[1]

93 datasets were collected and randomly divided into 65 training datasets and 28 test datasets. Firstly, the RF model was constructed using the training datasets. From the grid search, the hyperparameters were determined as follows:

the number of trees was 200; the number of variables in one tree was 11; and the number of leaf nodes was 20. The σ/λ was predicted from the explanatory variables using the RF model. Fig. 2 shows the RF-predicted σ/λ as a function of the measured σ/λ for the training and test datasets. The R^2 values were enough high for both cases (0.98 and 0.89), indicating a high prediction accuracy of this model.

Based on the RF model, the relative importance of the explanatory variables was calculated using Gini impurity. Consequently, the low ϕ_c and high MP of the base polymers were found to enhance the σ/λ of the CEMs. In these CEMs, the ion channels should have good connectivity throughout the CEM to efficiently transport protons. Actually, PEEK has the low ϕ_c and high MP, and the PEEK-based CEMs showed high σ/λ to achieve a high output power in fuel cells^[2]. A future work is to search for more suitable base polymers to prepare the high σ/λ CEMs.

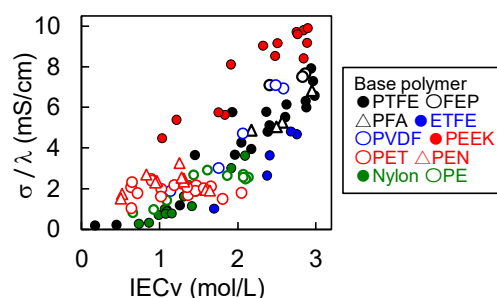


Fig. 1 The σ/λ as a function of the IECv of the graft-type CEMs based on 10 different polymers.

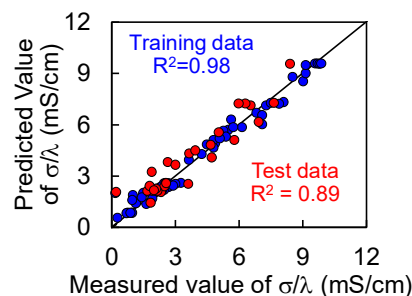


Fig. 2 The relationship between the RF-predicted and measured values of σ/λ .

References

- [1] S. Sawada *et al.*, J. Membr. Sci. **692**, 122169 (2024). DOI: 10.1016/j.memsci.2023.122169
- [2] T. Hamada *et al.*, J Mater. Chem. A **3**, 20983 (2015). DOI: 10.1039/c5ta05567a

2 - 08 Preparation of hydrogel/aluminum hydroxide composite adsorbent by in-situ radiation polymerization for lithium recovery from saltlake brine

J. Chen and N. Seko

Department of Advanced Functional Materials Research, QST

Recently, the rapid increase in the production and use of electric vehicles using lithium-ion batteries has led to a surge in the price of lithium prices due to the limited supply. To date, there are only about 20 million tons of minable lithium resources, which is insufficient to meet the needs of future electric vehicle. Despite this, low-grade lithium resources such as seawater and saltlake brine contain a large amount of lithium.

In this study, we developed a hydrogel composite adsorbent for lithium recovery from aqueous solutions with low lithium concentration. That is, a hydrogel composite adsorbent containing aluminum hydroxide and poly(N-isopropylacrylamide) (Poly(NiPAAm)) was synthesized under gamma-ray irradiation.

Figure 1 shows the preparation process of the hydrogel/aluminum hydroxide composite adsorbent. Here, aluminum chloride (0.1 mol) and lithium hydroxide (0.1 mol) were dissolved in water in a glass bottle, and 1 mol of urea was added. The bottle was controlled at 80 °C under magnetic stirring. Thus, $\text{LiAl}_2(\text{OH})_6\text{Cl}$ precipitate was formed. The precipitate was filtered and washed with water to remove unreacted urea and lithium chloride, and then dried at 60 °C for 24 h. Subsequently, powdered $\text{Al}_2(\text{OH})_6\text{Cl}$ was dispersed in 20 % NiPAAm aqueous solution by magnetic stirring. The resulting dispersion was irradiated with gamma-rays at ice water temperature. The total irradiation dose was 80 kGy, and the irradiation rate was 5 kGy/h. During the irradiation, the NiPAAm aqueous solution underwent radiation polymerization and cross-linking reactions, resulting in the formation of hydrogel/aluminum hydroxide composite adsorbent. Thus, the aluminum hydroxide, which has a bilayer structure capable of binding lithium ions, was immobilized in a hydrophilic hydrogel.

The test solution was a simulated solution containing mixed cations of lithium, sodium, potassium, magnesium, calcium and chloride ions. The prepared hydrogel adsorbent (2.0 g) was immersed in 200 ml of the test solution for batch adsorption under magnetic stirring at room temperature for 16 h. The lithium-adsorbed hydrogel adsorbent was washed with 20 ml of water for 5 min to remove surface ions, and then desorbed with 200 ml of water for 16 h. After desorption, the ion concentrations (C_w) in the desorption solution (recovered solution) were detected by ion chromatograph, and the ion recovery (%) was calculated as follows: $C_w/C_o \times 100$. The initial ion concentrations (C_o) of the test solution and the ion concentrations in the recovered solution (C_w) as well as the ion recovery rate (%) were summarized in Table 1.

Figure 2 illustrates the results of ion chromatography analysis of (a) the test solution and (b) the recovered solution. As shown in Figure 2(b), the peak for the lithium ion was significantly higher than that of other cations, indicating that the lithium ions in the test solution was selectively adsorbed by the hydrogel adsorbent and desorbed with distilled water without any additional environmental burden. Hence, this new adsorbent is expected to facilitate lithium recovery from low-grade sources such as seawater and saltlake brine.

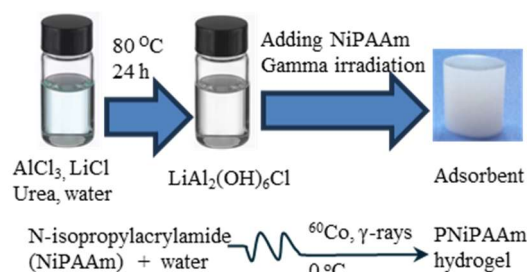


Figure 1 Preparation process of hydrogel/aluminum hydroxide composite adsorbent. Aluminum chloride, lithium chloride and urea were weighed and dissolved in water, stirred at 80 °C for 24 h until aluminum hydroxide colloid was formed, and then NiPAAm was added for γ -irradiation polymerization.

Table 1 Ion concentrations in the test solution and recovered solution, and the calculate ion recovery rate.

Metal ions	Li	Na	K	Mg	Ca
C_o (ppm)	65	224	232	101	212
C_w (ppm)	33	43	31	14	28
Recovery%	51	19	13	14	13

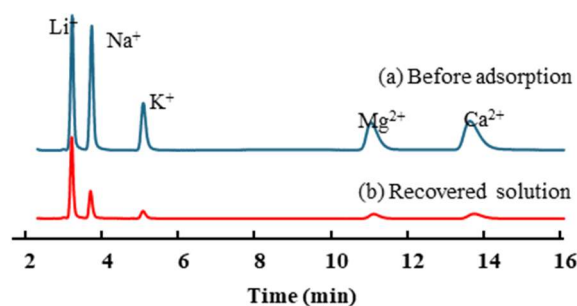


Figure 2 Ion chromatography analysis of (a) the test solution before adsorption and (b) the recovered solution after the desorption.

2 - 09 Measurement method of the degree of grafting by using thermogravimetric analysis

M. Omichi ^{a)}, H. Hoshina ^{a)}, H. Morishima ^{b)}, K. Ohshima ^{b)} and N. Seko ^{a)}

^{a)} Department of Advanced Functional Materials Research, QST

^{b)} Technical Research Laboratory, Kurabo Industries Ltd.

Introduction

Radiation-induced graft polymerization (RIGP) is widely used to develop various functional polymer materials and is applicable to various polymer substrate. The functions of grafted materials depend on a degree of grafting (DG), which is the weight ratio of the grafted chains to the polymer substrate. Thus, the DG is an essential indicator for evaluating the performance of a grafted material. However, when a portion of the grafted material is extracted, its performance does not necessarily match the performance predicted from the DG. This is because heterogeneous RIGP is likely to occur due to various factors. In conventional gravimetric measurement, it is not possible to determine the DG in the spot area, because it is necessary to measure the weight before the graft reaction in the spot area. Thus, accurate measurement of the DG excluding gravimetric measurement requires in production site.

In this study, we developed a method for accurately measuring the DG by combining thermogravimetric analysis (TGA) with cryo-milling. Similar components exhibit similar pyrolysis behavior, which implies that a grafted material exhibits a specific pyrolysis behavior depending on its structure, including the DG. Therefore, the DG can be predicted by measuring the pyrolysis behavior of a test sample and comparing it to the pyrolysis behavior of a reference sample with a known DG. Cryo-milling involves grinding samples into a powder form at cryogenic temperatures, which homogenizes them and reduces differences in the DG according to the sampling point due to heterogeneous RIGP to negligible levels. Together, TGA and cryo-milling should address the two main problems with spot DG measurements: low measurement accuracy and difficulty in preparing reference samples with a known DG. We conducted experiments to evaluate the performance of our proposed method.

Experimental

Cotton fibers were irradiated with an electron beam of 250 keV energy for a total dose of 40 kGy. The graft reaction was carried out by reacting 0.5-4.0 wt% acrylic acid monomer solution and the cotton-*g*-acrylic acid fibers with various DG (1.9-107.0%) were prepared. The cotton-*g*-acrylic acid fibers were cut into smaller pieces of less than 5 mm using scissors. A cryo-milling treatment was carried out on these samples for 5 min and then the cotton-*g*-acrylic acid powder was prepared. TGA of cotton-*g*-acrylic acid powder was performed at a heating rate of 20 °C/min under nitrogen flow (100 mL/min).

Results and Discussion

Fig. 1(a) shows derivative thermogravimetry (DTG) curves of the reference samples with varying DG (0%–107.0%). DTG varied continuously with the DG, which confirmed that reference samples with similar DGs exhibited similar TG properties. The DTG measurements indicated that three peaks at 250°C, 325°C, and 415°C varied with the DG. These three peaks were attributed to the dehydration condensation reaction of the grafted chains (acrylic acid), degradation of the cotton fiber (cellulose) substrate, and degradation of the grafted chains, respectively. We focused on these three DTG peaks to evaluate the DG values. Fig. 1(b) shows the correlations between the DG and DTG values at 250°C, 325°C, and 415°C. The DTG value increased with the DG at both 250°C and 415°C, which indicated a positive correlation. The sharp increase in the DG below 5% is because the degradation peak of the cotton fiber substrate shifted to a lower temperature (Fig. 1(a)). Therefore, this peak is not suitable for evaluating low DGs. However, it had the largest change in the DTG value with the DG among the three DTG peaks. Therefore, this peak should be useful for evaluating high DGs of over 90%.

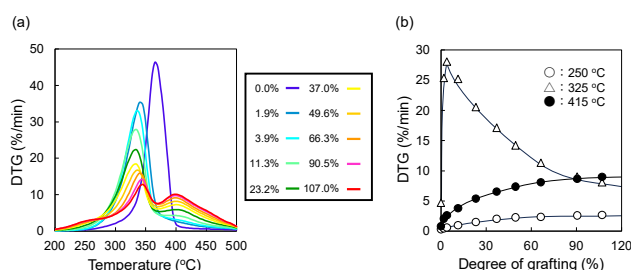


Fig 1. (a) DTG curves of cotton-*g*-acrylic acid powders with varying DGs (0%–107.0%). (b) Correlations between DG and DTG values at 250, 325, and 415°C.

From these results, there is a high correlation between DG and DTG, and DG can be obtained by evaluating DTG. The pyrolysis behavior of polymer substrates and grafted chains is never exactly the same. Therefore, the proposed method should be applicable to various combinations of polymer substrates and monomers in addition to the cotton fibers and acrylic acid monomer tested in this study. The proposed method is expected to help improve the quality control of grafted materials in the production site by providing a simple way to evaluate the DG.

2 - 10 Development of metal adsorbent via radiation-induced graft polymerization and Kabachnik-Fields reaction

M. Kuroiwa ^{a)}, K. Matsubara ^{a)}, M. Omichi ^{b)}, H. Hoshina ^{b)}, N. Seko ^{b)} and R. Kakuchi ^{a)}

^{a)} Division of Molecular Science, Faculty of Science and Technology, Gunma University

^{b)} Department of Advanced Functional Materials Research, QST

Introduction

Rare metals, which include elements used in magnetic materials, rechargeable batteries, and optical discs, are important components in various advanced technologies. However, the rare metal production is difficult, and their supply remains unstable, thereby making the recycling of these materials a critical issue. One promising approach for recycling rare metals involves recovering them from industrial wastewater. Unfortunately, it is difficult to separate only target rare metals from wastewater because of the presence of co-existing multiple metals. Furthermore, the concentration of rare metals in wastewater is typically much lower compared to more common metals such as iron and sodium. Considering this background, there is a pressing need for materials that can efficiently and selectively recover low concentrations of rare metals from solutions containing multiple metal ions.

In this study, we attempted to synthesize a new metal adsorbent with α -aminophosphate that shows coordination to metal elements. Specifically, poly (methacrylated vanillin) (PMV) was first introduced onto non-woven polyethylene/polypropylene fabrics (PE/PP) by radiation-induced graft polymerization (RIGP) of methacrylated vanillin (MV). After RIGP, surface modification using the Kabachnik-Fields reaction (KF-3CR), one of the multi-component reactions, was performed to synthesize fiber materials decorated with α -aminophosphate groups. [1] Furthermore, the metal adsorption capacity of the synthesized fiber materials was evaluated.

Experimental

As described above, we firstly introduced α -aminophosphate groups onto PE/PP. (Fig. 1) PE/PP was irradiated with an electron beam at 200 kGy to initiate the graft polymerization of MV, resulting in PE/PP grafted with PMV segments (PE/PP-g-PMV). The PE/PP-g-PMV was then reacted with excess *N,N*-dimethyl-1,4-phenylenediamine and diethyl phosphite to install polymeric α -aminophosphate groups on the fiber surface to obtain the final product (PE/PP-PAP). Next, we evaluated the metal adsorption capacity of PE/PP-PAP. The adsorption capacity and selectivity of PE/PP-PAP were evaluated by immersing PE/PP-PAP in 50 mL of a mixed solution containing 31 metal ions prepared at a concentration of 50 ppb ($\mu\text{g/L}$) for 2 hours at 25°C with stirring at 150 rpm. Following this step, PE/PP-PAP was removed from the solution, and the adsorbed metal was quantified using inductively coupled plasma mass

spectrometry (ICP-MS).

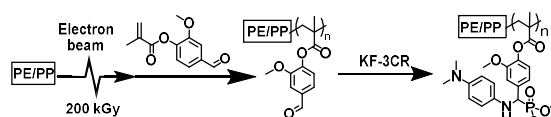


Fig. 1 Introduction of α -aminophosphate groups into PE/PP fabrics via radiation-induced graft polymerization and KF-3CR.

Results and Discussion

The synthesized fiber material was evaluated by Fourier transform infrared spectroscopy (FT-IR), and a new phosphate-derived peak appeared at 928 cm^{-1} , confirming the progress of KF-3CR. Next, the metal adsorption capacity of the synthesized fiber materials was evaluated by ICP-MS. Fig. 2 shows the adsorption results of the top 10 elements with the highest adsorption rates among the 31 metal elements measured. The results show that the synthesized fiber material exhibits higher adsorption behavior for bismuth (Bi) than other metal elements. To summarize, in this study, we have succeeded in synthesizing a new metal adsorbent with α -aminophosphate groups on the fiber surface that exhibits coordination ability for metal ions.

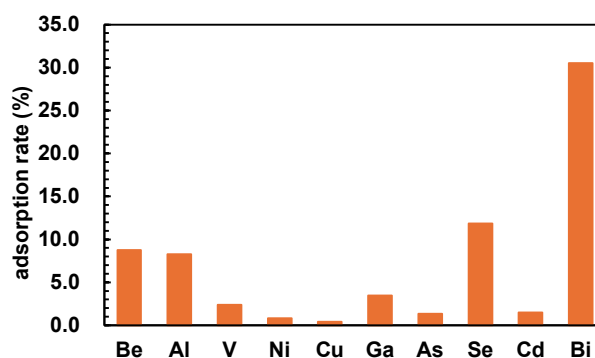


Fig. 2 Metal adsorption capacity of synthesized PE/PP-PAP.

Acknowledgments

R. K. gratefully acknowledges the S-Membrane Project at Gunma University for the financial support.

References

[1] R. Kakuchi *et al.*, *ACS Sustainable Chem. Eng.* **7**, 7795-7805 (2019).

2 - 11 The development of environmentally friendly soft contact lenses based on cellulose-derived gels

A. Hiroki, A. Kimura and M. Taguchi

Department of Advanced Functional Materials Research, QST

Introduction

Recently, environmental pollution caused by disposed soft contact lenses (SCLs) has been worried [1]. To reduce the environmental burden, the replacement with biodegradable materials is required. However, there are no reports about SCL materials containing environmental-friendly cellulose derivatives as the main component because of issues such as their mechanical properties. In this work, we aimed the development of hydrogels for environmental-friendly SCL by using radiation polymerization and crosslinking techniques [2].

Experimental

Aqueous solutions containing hydroxypropyl cellulose (HPC) and methacrylate monomers were prepared, in which the monomers used here were 2-hydroxyethyl methacrylate (HEMA), methyl methacrylate (MMA), and tricosaeethylene glycol dimethacrylate (23G), and the contents of HPC, HEMA (or MMA), and 23G were 20 wt.%, 2.0 wt.%, and 0.2 wt.%, respectively. The aqueous solution as a paste-state was sandwiched by polyethylene terephthalate films of 25 μm thickness and pressed to form a 150 mm long \times 150 mm wide \times 0.1 mm thick shape, and then sealed in polyethylene-nylon package after degassing. The samples were irradiated to a dose of max 50 kGy to obtain HPC-based gels. The irradiations were carried out using Cock-croft Walton type electron beam accelerator (2 MeV, 2 mA) at the Takasaki Institute for Advanced Quantum Science, QST. The gel properties required for soft contact lens materials, such as transparency, oxygen permeability, mechanical strength, protein adsorption, and biodegradability, were evaluated.

Results and Discussion

The gel fraction of the HPC-based gels increased with increasing dose, reaching a maximum of 95% at 50 kGy. On the other hand, the swelling decreased with increasing dose, reaching approximately 10. The obtained HPC-based gels with the thickness of about 0.2 mm were highly transparent and exhibited more than 96% transmittance in the visible light region. The HPC gel prepared without monomer had a low breaking strength of 0.1 MPa and an elongation ratio of 70%. However, the HPC-based gel prepared with monomer had an increased breaking strength and was less likely to break. Among them, the gel prepared with MMA exhibited the most balanced and highest values of breaking strength of 0.23 MPa and an elongation ratio of 80%. The mechanical strength of the HPC-based gels would be improved because a monomer-derived network structure was formed within the HPC network structure, and further the HPC and the resulting

polymer partially chemically bonded to each other. The oxygen diffusion rate of the HPC-based gel prepared with HEMA and MMA was 4.0×10^{-2} and $5.8 \times 10^{-2} \text{ mg L}^{-1} \text{ min}^{-1}$, at 25 $^{\circ}\text{C}$, respectively. The oxygen diffusion rates would be close to the migration rate of oxygen molecules in water, because the water contents of HPC-based gels are more than 90%. The adsorption amount of lysozyme as a protein which is present in large amounts in tear fluid was approximately $55 \mu\text{g cm}^{-2}$ for the HPC-based gel measured at 6 days. The degradation rate of HPC-based gel prepared with MMA increased with increasing cellulase treatment time, reaching approximately 14% after 7 days, as shown in Fig.1. Therefore, the transparency, oxygen permeability, mechanical strength, and protein adsorption of the HPC-based gels were comparable to those of commercially available polyHEMA-based SCL material. Furthermore, it was confirmed that HPC-based gels were degraded by cellulases as an enzyme present in the soil.

Thus, biodegradable cellulose-derived hydrogels for SCLs were produced by the radiation crosslinking technique. This technique could be applied to the fabrication of environmentally friendly SCLs to achieve sustainable development goals.

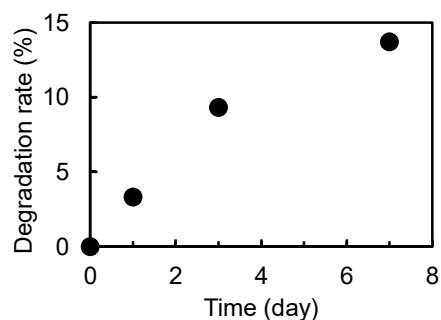


Fig. 1 Time dependence of the biodegradability of the HPC-based gel prepared with MMA. The HPC-based gel was immersed in 0.1 g L^{-1} of cellulase solution at 37 $^{\circ}\text{C}$.

Acknowledgments

This work was partially supported by the Japan Society for the Promotion of Science Grants-in-Aid for Scientific Research (KAKENHI) [grant number 17K05134], and Innovative Science and Technology Initiative for Security Grant Number JPJ004596, ATLA, Japan.

References

- [1] C. Rolsky *et al.*, *Environ. Sci. Technol.* **54**, 12102 (2020). DOI: 10.1021/acs.est.0c03121
- [2] A. Hiroki *et al.*, *Radiat. Phys. Chem.* **213**, 111257 (2023). DOI: 10.1016/j.radphyschem.2023.111257

2 - 12 Irradiation tests of radiation-hard components and materials for ITER blanket remote handling system

M. Saito, Y. Kawai, K. Nakata, T. Ito, T. Fujiwara, H. Seki, Y. Noguchi and N. Takeda

Department of ITER Project, Naka Institute for Fusion Science and Technology, QST

Introduction

The ITER blanket remote handling system (BRHS) will replace the first walls in a γ -ray radiation environment having a dose rate of 250 Gy/h to 500 Gy/h. We set a radiation hardness target value of 3 MGy to increase the availability of the system. This report shows the irradiation test results of the pneumatic components of the BRHS. Since the BRHS will replace the blanket modules by using various tools, a tool changer will be used in the BRHS design. Pneumatic components, such as pumps and tanks, will supply the tool changer with compressed air as its power source. In this study, we irradiated a metal bellows pump and 3-port solenoid valves by using γ -rays. After irradiation, the functions of these components were confirmed.

Irradiation tests

The samples were irradiated at a γ -ray irradiation facility using the conditions shown in Table 1. After irradiation, the samples underwent testing, the test items of which are shown in Table 2 for the metal bellows pump and Table 3 for the 3-port solenoid valves. The samples were also disassembled to check their individual parts.

Table 1

Irradiation conditions for each sample

Component	Dose rate [Gy/h]	Total [MGy]
Metal bellows pump	1100	2 (N=1)
3-port solenoid valve	1000–1500	1, 2, 3, 4 (N=1)

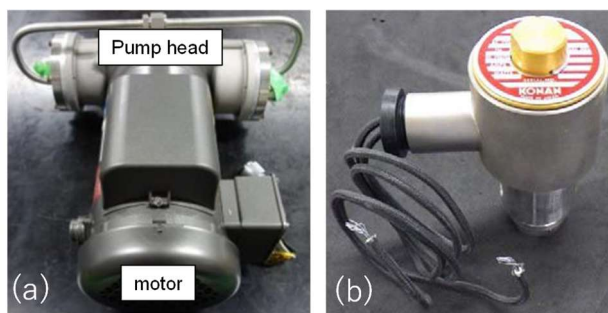


Fig. 1 (a) Metal bellows pump and (b) 3-port solenoid valve

Results and Discussion

The metal bellows pump was irradiated up to 2 MGy. After irradiation, its functions were tested, the results of which are shown in Table 2. The values of insulation resistance and current did not meet the acceptance criteria. Upon disassembling the metal bellows pump, we discovered that some components had degraded, e.g., corrosion of fastening screws, cracks in the external fan,

Table 2

Test items for metal bellows pump

Test item	Result
Pump performance	Pass
Flow rate	Pass
Pressure	Pass
Degree of vacuum	Pass
He leak	Pass
Insulation resistance test	Fail
Current value	Fail

Table 3

Test items for 3-port solenoid valves

Test item	Result
Performance test	Pass
Voltage tolerance test	Pass
Insulation resistance test	Pass
Leak test	Slight leakage

capacitor malfunction, and damage to protective sponge of the capacitor. Since the motor degraded significantly, we determined that the motor needed to be improved, such as changing to a three-phase power supply, removing the capacitor, and changing the cooling method to totally enclosed fan-cooled.

The 3-port solenoid valves (four samples in total) were individually irradiated up to 1 MGy, 2 MGy, 3 MGy, or 4 MGy. After irradiation, the samples underwent testing, the test items of which are shown in Table 3. No leakages occurred before irradiation, however, after irradiation, slight leakages (within acceptance criteria) were discovered in all samples. These leakages were most likely caused by a loss of elasticity in its rubber components induced by the γ -ray irradiation. We are planning to improve the valves by reducing the area of the rubber sheet disc that receives pressure by using smaller port openings (orifices), which should reduce the forces on the surface of the sheet and be more resilient against dents.

Acknowledgments

The authors would like to acknowledge Beam Operation Co., Ltd. and the Takasaki Institute for Advanced Quantum Science's Irradiation Facilities Section who supported these irradiation experiments.

2 - 13 Irradiation effects on fiber/matrix interfacial properties of SiC/SiC composites by micro-mechanical testing methods

T. Nozawa and M. Ando

Rokkasho Institute for Fusion Energy, QST

Introduction

SiC's excellent heat resistance is offset by its brittleness, limiting its structural use. To address this, SiC is used as a composite with SiC fibers to enhance ductility. However, understanding damage accumulation from the onset of fractures is crucial for assessing structural integrity and lifespan. Key factors include evaluating crack propagation at the fiber/matrix (F/M) interface and the impact of irradiation on interface strength [1]. This study used micro tensile [2] and micro pillar [3] tests to assess the strength of SiC/SiC composite interfaces and their response to ion beam irradiation. These methods enable precise evaluation of material and interface strength in thin-film structure and have been more attracted in recent years.

Experimental

The specimens were SiC/SiC composites fabricated by chemical vapor infiltration using Tyranno-SA3 as the reinforcing fiber, with 150 nm-thick pyrolytic carbon (PyC) at the F/M interface formed by chemical vapor deposition.

Ion ($^{28}\text{Si}^{2+}$: 6.0 MeV) beam irradiation test was performed using the 3MV tandem accelerator at TIARA. In this experiment, the irradiation dose was 2-3 dpa at the test section. The irradiation temperature was 345°C.

Micro tensile tests perpendicular and 45-deg. offset to the F/M interface were conducted to evaluate the interfacial detachment strength (τ_{detach}) and interfacial shear strength (τ_{debond}), respectively, using a Hitachi High-Tech FB2100 FIB system. The load was estimated from the deflection of a SiC micro beam with 1 μm -wide notches and a 0.8 μm thickness. The test area was prepared by depositing W on the irradiated surface to set a damage zone at around 2 dpa, though with a gradient (Fig. 1). Micro pillar tests were also conducted to evaluate the interfacial shear fracture behavior by an Ernix ENT1100a nanoindenter with a 10 μm -diameter flat punch indenter tip. The test measured indentation depth with a maximum load of 100 mN, using 300 steps with 200 ms intervals. The micropillars were 2 μm in diameter, and the evaluation area was estimated to have about 3 dpa of irradiation damage (Fig. 2). Note that both tests were conducted at room-temperature.

Results and Discussion

Weibull statistics of micro tensile tests were summarized in Fig. 1. Both τ_{detach} and τ_{debond} increased by irradiation. By contrast, the Weibull modulus for τ_{debond} contrarily remained nearly the same or increased slightly compared to the non-irradiated condition, while the Weibull modulus for τ_{detach} decreased significantly. This indicates that irradiation does

not significantly reduce interfacial strength but increases uncertainty, in particular for τ_{detach} . But remember that τ_{detach} was not dominant in interfacial fracture because of quite higher strength than τ_{debond} before and after irradiation.

The resolved shear stress (τ_{critical}), which composes τ_{debond} and interfacial friction, was measured from the applied load during the sliding process of the micro pillar tests (Fig. 2). The test results revealed that both τ_{critical} and the Weibull modulus increased with irradiation. This is very consistent with τ_{debond} obtained by micro tensile tests.

In conclusion, the above results by different approaches demonstrate a good applicability of ion irradiation to micro tests, enabling to clarify some of the effects of irradiation on the F/M interface of composites.

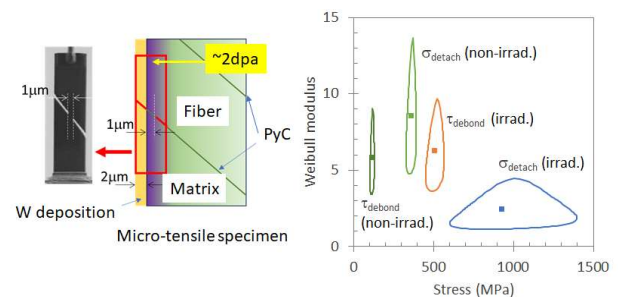


Fig. 1 Micro-tensile tests for ion-irradiated composites.

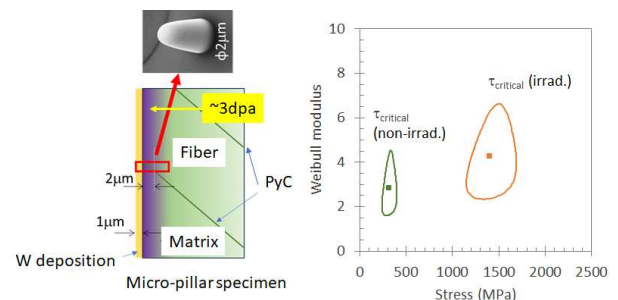


Fig. 2 Micro-pillar tests for ion-irradiated composites.

Acknowledgments

This work was supported by METI Technical Development for Improving Nuclear Safety Program Grant Number JPMT003830.

References

- [1] T. Nozawa *et al.*, J. Nucl. Mater. **566**, 153787 (2022). DOI: 10.1016/j.jnucmat.2022.153787
- [2] M. Ando *et al.*, Nucl. Mater. Energy **16**, 258 (2018). DOI: 10.1016/j.nme.2018.07.008
- [3] O. Karakoc *et al.*, Compos. B **224**, 109189 (2021). DOI: 10.1016/j.compositesb.2021.109189

2 - 14 Study of multi ion-irradiation effects on fusion reactor materials using a micro-tensile testing method

M. Ando and T. Nozawa

Department of Fusion Reactor Materials Research, RFI, QST

Introduction

Reduced activation ferritic/martensitic steels (RAFM) such as F82H and EUROFER97 are candidates for DEMO blanket structural materials. Many reactor irradiation studies have shown possible neutron irradiation effects on RAFM, however, the details of the 14 MeV fusion neutron effect are still unknown since a fusion neutron irradiation facility is currently unavailable. Instead, several simulated fusion neutron irradiation damage experiments are used to understand their effects. For instance, ion irradiation experiments using multiple accelerators can partially simulate the characteristics of fusion neutron irradiation, i.e., displacement damage and helium production at a certain rate, however unfortunately the evaluation volume is very small and only limited evaluation methods can be applied.

In the past, as ion irradiation experiments and post-irradiation examinations, evaluation of void swelling (mainly cavity microstructure analysis) has been conducted mainly by electron microscope observation, and strength for irradiated materials (irradiation hardening/softening) has been conducted by micro-hardness tests. In particular, the effect of helium on swelling is significant and contributes to the judgment (critical point) of how far the fission reactor irradiation data (almost no helium) can be used. In terms of strength, there is concern that helium accelerates embrittlement, and more information on fracture characteristics is needed. To obtain such fracture-related information from ion-irradiated materials, the micro tensile test method has been improved, and we have successfully applied it to evaluate fracture strength as a new indicator. In this study, we used the same method to compare and evaluate the deformation in ion-irradiated F82H block sections.

Experimental

The materials used in this study were F82H IEA. The irradiations were carried out with 10.5 MeV Fe³⁺ ions and 1.05 MeV He⁺ ions. In multi-ion irradiation, He implantation rate was fixed to be 15 appm/dpa. The irradiation dose was up to 80 dpa. A micro tensile specimen has notches in the middle gauge section.

It is considered that a kind of fracture stress (μ -FS) for a single-block F82H can be obtained by using μ -tensile specimens with notches because the local deformation constraint occurs around notches. The micro tensile tests were performed in a focused ion beam (FIB) processing device. Each micro tensile specimen was prepared and fixed to the micro-probe attached to the FIB device, and micro tensile tests were performed. The test load was estimated from the deflection of the SiC micro-beam to

which the specimen was fixed. In the previous year, the indicator of fracture strength was reported as the maximum stress just before fracture [1], but this year, the deformation is obtained by $k = L/\sqrt{W} \cdot t$ shown in Figure 1 and the deformation change is compared.

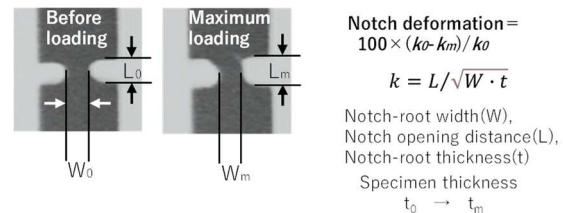


Figure 1 Calculation of deformation from notched tensile specimen.

Results and Discussion

Figure 2 shows the results of the deformation evaluated by the notched micro tensile test. It was confirmed that the 470°C irradiated F82H showed a very large deformation exceeding that of the unirradiated F82H despite the high irradiation dose. This is consistent with the fact that the 470°C irradiated F82H did not show irradiation hardening. On the other hand, the irradiated F82H at 300°C, which exhibited significant irradiation hardening, showed a large decrease in deformation with irradiation dose, but in the irradiation temperature above 400°C, the results were generally similar to those of the unirradiated F82H. These trends are consistent with the behavior expected from the results of micro-hardness tests. As described above, we have obtained a prospect to systematically evaluate the micro tensile deformation behavior of F82H irradiated with single and/or dual ions, which has been difficult to evaluate so far. The narrowing down of the helium effect for each indicator considering the critical point will be continued, and the methodology for scaling up for macro-strength prediction to irradiated materials will be discussed.

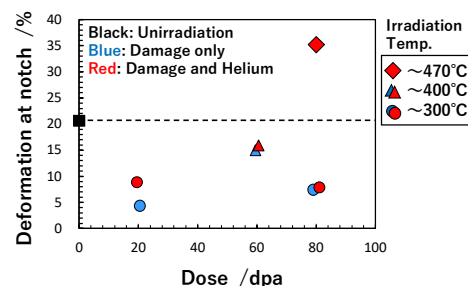


Figure 2 Dependence of notch deformation on dose for each irradiated F82H.

Reference

[1] M. Ando *et al.*, QST Takasaki Annu. Rep. 2022, **QST-M-47 58** (2024).

2 - 15 Investigation on tensile properties of single crystal pure tungsten using micro-tensile test methodology

D. Hamaguchi ^{a)}, Ju-Hyeon Yu ^{b)} M. Ando ^{a)} and H. Kurotaki ^{c)}

^{a)}Rokkasho Institute for Fusion Energy, QST

^{b)}current Hanhwa Aerospace, former QST researcher (till 2023)

^{c)} former QST technical staff

Tungsten is a promising candidate material for the plasma-facing component (PFC) of the DEMO divertor. The design of the DEMO divertor follows the concept of the ITER divertor, with the major difference being that the neutron irradiation effects must be taken into account. Therefore, we are now working on obtaining irradiation data of tungsten that will contribute to the design. Many neutron irradiation tests are being conducted so far using existing fission reactors to investigate the effects of neutron irradiation, however, the issue is the effect of transmutation. The transmutation rate of products such as Re, which affect the conductivity and mechanical properties, is significantly different between the fission reactor neutron spectrum and that in fusion reactors, and consequently, it is difficult to judge at the moment whether the properties evaluated there are realistic or not. Therefore, an attempt is being made to evaluate the basic irradiation effects of tungsten using ion irradiation, in which defects can be introduced without such transmutation effects. However, the main drawback of ion irradiation is that the area where damage can be introduced is limited to a very shallow and narrow area from the surface, and therefore it is difficult to derive mechanical properties from these specimens so far. As a solution to this problem, we have developed a mechanical testing technique using a micro-level tensile specimen mainly for steels (micro-tensile test hereafter) and we have applied this technique to evaluate the irradiation effects of tungsten using ion irradiations.

Fig. 1 (a) shows the irradiation hardening trend of pure tungsten irradiated up to 18 dpa, as reported in the annual report 2021, using micro tensile specimens. The results are in good agreement with the trends obtained by nanoindentation, indicating that the micro-tensile test is useful for evaluating irradiation hardening behaviors. However, Fig. 1 (b) shows the total elongation results from the same test, which showed that the elongation data scattered widely. This scattering in the data is a common trend in tungsten, even when macro specimens are used, and is considered to be a characteristic of tungsten, which is brittle at room temperature. One possible cause of this is the effect of grain anisotropy. As tungsten plates are usually manufactured by powder sintering, the influence of grain boundary strength is also considered, but as is also reported in the 2021 annual report, the presence or absence of grain boundaries has little effect on both tensile strength and the scattering of elongation, and therefore grain anisotropy is considered to be more effective. Based on this assumption, the effect of crystalline orientation on

tensile behaviors was investigated in the present study using a single crystal with micro-tensile specimens.

In this test, tensile tests were carried out in the vertical direction on three different single crystals with (100), (110), and (111) planes. Fig. 2 is a plot showing the relationship between elongation and tensile strength of the tensile tests to each crystal orientation. As a result, although the difference in strength between the planes was small, the elongation in the [110] orientation was approximately three times larger than that in the other planes. The result suggests that the brittle behavior of polycrystalline tungsten at room temperature does not reflect the intrinsic strength properties of tungsten and that the variation in ductility data is in part dependent on the orientation of the crystalline grains. Our future goal is to determine critical resolved shear stress for representative crystalline orientations through such tests and to improve the simulation precision of the deformation behavior of polycrystals and the irradiation effects on them.

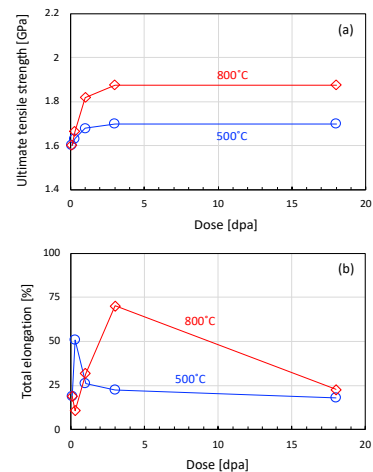


Fig. 1. (a) Ultimate tensile strength and (b) total elongation of pure tungsten irradiated up to 18dpa with 18MeV W^{6+} ion.

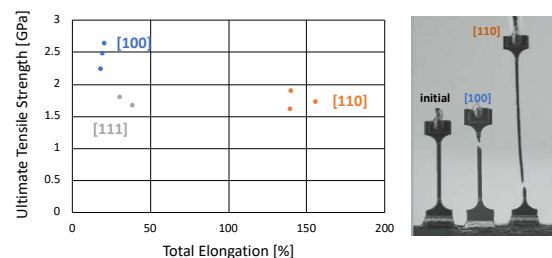


Fig. 2. Relationship between elongation and tensile strength in three different crystal orientation.

2 - 16 Gamma-ray irradiation experiment for ITER diagnostic systems in JADA VI

S. Kitazawa, Y. Nunoya, M. Ishikawa, R. Imazawa, E. Yatsuka, K. Nojiri, T. Ushiki, H. Natsume[#], S. Kono, K. Torimoto, M. Inamine, Y. Nemoto, T. Kikuchi, T. Yokozuka, H. Murakami, K. Shimizu and T. Sugie

Department of ITER Project, NFI, QST

[#]Current affiliation: Global Research Institute of Nuclear Energy (GRINE), Tokai University

JADA (ITER project Japan Domestic Agency) is developing to procure five diagnostic systems, microfission chamber (MFC), poloidal polarimeter (PoPola), Edge Thomson Scattering (ETS), divertor impurity monitor (DIM) and divertor infrared thermography (IRTh).

The reliability under the ITER radiation conditions of relevant equipment to be installed in the vacuum vessel, in the interspaces (IS) between the vacuum boundary and the biological shield and in the port cells (PC) outside the biological shields should be evaluated. The maximum doses evaluated are estimated as acceptance values to be 10 MGy for IS and 200 kGy for PC. In this project, we launched gamma-ray irradiation experiments in QST TARRI from 2018. The experimental results are being used as important evidence in the design review of each diagnostic system to confirm that the components can maintain their performance in the ITER radiation environment.

The gamma-ray irradiation experiments on optical components for plasma diagnostics have mainly been conducted by measuring optical density or reflectance before and after irradiations [1, 2]. Regarding electronic equipment for diagnostic systems, we have conducted gamma-ray irradiation durability tests on piezo elements and electrical equipment, observing their characteristics before and after irradiation [3]. As the ITER construction procurement activities progressed and the designs have been finalized, implementation verification became necessary, it became necessary to verify the actual installation, and so in-situ experiments were conducted in which gamma-rays were irradiated with electric current.

For MFC, changes were observed in the frequency characteristics of the preamplifier during irradiation tests last year, but measures to prevent oscillation were subsequently implemented and improvements were confirmed in irradiation tests. Neutron monitoring experiments on the related preamplifier were carried out at National Institute for Fusion Science (NIFS) and its applicability was confirmed [4].

For ETS, gamma-ray irradiation tests were conducted on optical fiber up to 10 MGy. Low-OH UVWFS fiber manufactured by CeramOptec with and without hydrogen loading on the core. Comparing the spectral transmittance after irradiation, the hydrogen loaded samples showed 20-30% decrease in transmittance compared to before irradiation, while the non-hydrogen loaded sample showed a decrease of about 50% in visible light.

For DIM, gamma-ray irradiation tests were conducted to

select optical elements to be used in the PC. To select lens materials for the UV spectrometer, two types of highly homogeneous optical glasses (OHARA PBL1Y, PBL6Y) for i-line (365 nm) were irradiated and the change in spectral transmittance was observed. At 1 kGy irradiation, much lower than expected in the PC, these specimens showed a significant decrease below 450 nm, indicating that they were not suitable for use in the spectrometer and that glass materials other than i-line glass should be considered. To select the optical fiber, we conducted in-situ testing on multiple fiber products by CeramOptec. For the transmittance at wavelengths around 400 nm, the candidate fiber for visible light had a significant decrease compared to previous ex-situ experiments. This may be due to transmittance recovering during the waiting period in previous ex-situ experiments.

For IRTh, the gamma-ray irradiation test on the ultrasonic motor used to drive the steering mirror placed in the IS has been conducted. This test confirmed that there was no significant deterioration in the torque vs. rotational speed characteristics of the ultrasonic motor, even under irradiation up to 1.6 MGy.

Irradiation experiments were also carried out on equipment common to multiple diagnostic systems. Pressure gauge candidates for PCSS were tested to ensure durability. Irradiation tests up to 300 kGy were conducted on three types of pressure gauges for use in the gas compression system for the shutter mechanism. One was found to be durable, but other two became unusable at 5 kGy. Solenoid valves for PCSS were tested to ensure durability. In irradiation experiments with three types of solenoid valves, it was confirmed that they could function up to 300 kGy.

Acknowledgments

We would like to thank Naotsugu Nagasawa, Hajime Seito, Yuuto Nagao, Eri Yokozuka, Hiroyuki Okazaki, Shunya Yamamoto and Hiroshi Koshikawa (TARRI) for their cooperation in irradiation and observation.

References

- [1] S. Kitazawa *et al.*, J. Plasma Fusion Res., **14** 3405089 (2019).
- [2] T. Ushiki *et al.*, J. Nuclear Materials, **595** 155047 (2024).
- [3] S. Kitazawa *et al.*, Plasma Fusion Res., **18** 2405014 (2023).
- [4] S. Kono *et al.*, Plasma Fusion Res., **19** 1405015 (2024).

2 - 17 Luminescence of samarium complexes in *N,N,N',N'*-tetraoctyl diglycolamide solvent induced by hydrogen ion beam

M. Nakahara ^{a)}, Y. Ishii ^{b)}, R. Yamagata ^{b)}, N. Yamada ^{c)} and M. Koka ^{c)}

^{a)} Nuclear Fuel Cycle Engineering Laboratories, JAEA

^{b)} Takasaki Institute for Advanced Quantum Science, QST

^{c)} Beam Operation Co., Ltd.

Introduction

An extractant and a separation process are developed for recovering trivalent minor actinides (MAs) such as Am and Cm from high-level radioactive liquid waste generated during nuclear fuel reprocessing [1]. MAs are proposed to be reused as components of nuclear fuel alongside U and Pu in fast reactor fuel cycle systems. Therefore, MAs should be efficiently recovered from high-level radioactive liquid waste. Stabilization of MA complexes is one of the important factors in recovering MAs from loaded solvent; hence, the structures of these complexes should be determined. Therefore, the structures of MA complexes were investigated herein using ion beam induced luminescence (IBIL). In particular, Sm complexes in an organic solvent were irradiated with an H⁺ ion beam, and the IBIL spectra of the complexes were obtained to examine their structures in the Takasaki Ion Accelerators for Advanced Radiation Application.

Experimental

Nonradioactive Sm was used as a simulated MA because MAs are generally radioactive and their handling requires special equipment. The extraction behavior of Sm is similar to that of trivalent MAs. Sm exhibits luminescence through the transition of 4f electrons under ion beam irradiation [2]. Herein, Sm(NO₃)₃·6H₂O powder was dissolved in a HNO₃ solution. *N,N,N',N'*-tetraoctyl diglycolamide (TODGA) was used as an extractant for the MA [3]. The prepared Sm nitrate solution was mixed with TODGA for 180 min to extract Sm into the organic solvent. Subsequently, the organic phase was separated from the aqueous phase.

The organic solvents were put in a Kapton® case and placed on a revolving sample stage. A 3-MeV H⁺ ion beam was generated using the light-ion microbeam line connected to a 3-MV single-ended accelerator. The luminescence of Sm complexes was measured using ultraviolet–visible spectrophotometry. The exposure time was 6.5 s, and the IBIL spectra were obtained 10 times at intervals of 5 s. The particle induced X-ray emission (PIXE) of the samples was obtained simultaneously with the IBIL spectra. The PIXE spectrum confirmed the extraction of Sm into TODGA.

Results and Discussion

Fig. 1 shows the first, fifth, and tenth IBIL spectra of the

Sm complexes extracted into TODGA [4]. The ⁴G_{5/2} → ⁶H_{5/2} transition at 567 nm is observed. The dominant peak is the ⁴G_{5/2} → ⁶H_{7/2} transition. The peak at 643 nm is attributed to the ⁴G_{5/2} → ⁶H_{9/2} transition. The broad peak of the ⁴G_{5/2} → ⁶H_{11/2} transition is observed at approximately 710 nm.

The peak intensity of the ⁴G_{5/2} → ⁶H_{7/2} transition in the tenth spectrum is lower than that in the first spectrum. It is reported that He⁺ radiation damaged the polymer film and decreased the intensity of the IBIL spectra of the polymer [5]. Therefore, the chemical bonds in TODGA were broken by the ion beam. The IBIL peaks of the ⁴G_{5/2} → ⁶H_{7/2} and ⁴G_{5/2} → ⁶H_{9/2} transitions contributed to the symmetric properties of the Sm complexes in TODGA. Further investigation should be performed using various MA extractants to elucidate the correlation between IBIL spectra and complex structures.

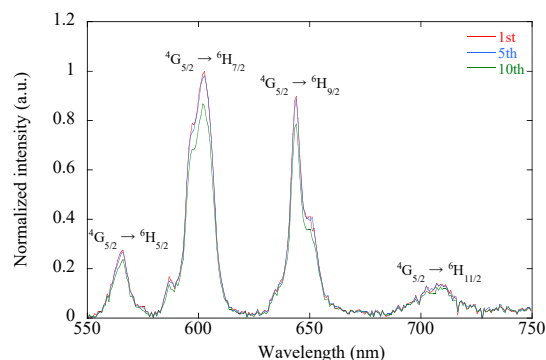


Fig. 1 IBIL spectra of Sm complexes in TODGA.

References

- [1] P. Baron *et al.*, Prog. Nucl. Energy **117**, 103091 (2019). DOI: 10.1016/j.pnucene.2019.103091
- [2] K. Zhang *et al.*, ACS Omega **4**, 18334 (2019). DOI: 10.1021/acsomega.9b02576
- [3] S.A. Ansari *et al.*, Solvent Extr. Ion Exch. **23**, 463 (2005). DOI: 10.1081/SEI-200066296
- [4] M. Nakahara *et al.*, Nucl. Instrum. Methods Phys. Res. B **554**, 165449 (2024). DOI: 10.1016/j.nimb.2024.165449
- [5] A. Quaranta *et al.*, Nucl. Instrum. Methods Phys. Res. B **191**, 680 (2002). DOI: 10.1016/S0168-583X(02)00632-8

2 - 18 Color imaging of carbon ion ($^{15}\text{C}^{+5}$) beam by the carbon tetrachloride gel dosimeter containing the spiropyran-like color former

T. Tachikawa and C. Koizumi

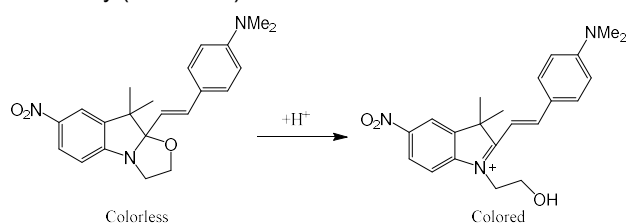
Faculty of Engineering, Graduate School of Science and Engineering, Saitama University

Introduction

The color formers have been developed to detect radiations by visual observation in our laboratory [1-3]. The radiation detection using gel dosimeters is useful method for the area radiations with heavy particle beams [4,5].

When halogenated solvents are irradiated, chlorine radicals are formed, and the chlorine radical draw a hydrogen from the surroundings to form a hydrogen chloride. In carbon tetrachloride, hydrogen chloride is not produced because there is no hydrogen in the surroundings to be drawn off by the chlorine radicals.

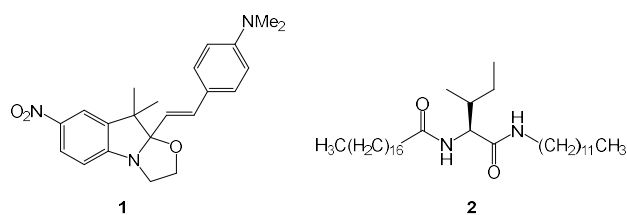
The application of the acid-induced color former to γ -ray detection using gel dosimeters has been studied in our laboratory (scheme 1).



Scheme 1. Color formation of spiropyran-like color former.

The color former does not develop color when irradiated in carbon tetrachloride. However, in the case of carbon tetrachloride gel dosimeters, hydrogen chloride is generated due to the withdrawal of hydrogen from the gelling agent, and the coloration of the gel dosimeter will be caused. Carbon tetrachloride is a more convenient for the preparation of dye gel dosimeters than methylene chloride, which has a low boiling point, or chloroform, which is susceptible to degradation by light and other substances.

This report presents the coloration of carbon tetrachloride gel dosimeters prepared using a spiropyran-like color former **1**, which develops color in the presence of acid, and a low-molecular-weight organogelator **2**, which can form a organogel in carbon tetrachloride (Scheme 2).



Scheme 2. Color former **1** and organogelator **2**

Experimental

The carbon tetrachloride gel dosimeters were prepared as follows. The suspension of the color former **1** and the organogelator **2** in carbon tetrachloride was prepared so that the concentrations were [1] = 13 mM and [2] = 71 mM, respectively. Then, the suspension was heated until the **2** was dissolved and cooled to prepare the dye gel dosimeter.

Irradiation of carbon ion beam to the dye gel dosimeter was carried out at TIARA. 220 MeV carbon ions ($^{12}\text{C}^{+5}$) were irradiated to the dosimeters at 4 nA for the exposure time of 30 s and 60 s, or at 2 nA for 120 s with scanning the beam over the area of 7.5 cm x 7.5 cm under normal temperature and ambient pressure.

Results and Discussion

The image of the carbon tetrachloride dye dosimeters are shown in Fig. 1. The coloration of blue color was recognized by naked eyes. The difference in the color of the gel between the areas irradiated with and without heavy particle radiation was clearly visible.

The colored gel dosimeters after irradiation were dissolved in carbon tetrachloride and UV-VIS spectra of the solutions were measured. An increase in absorbance at the absorption maxima of the dye (592 nm) was observed between 30- and 60-second irradiations.

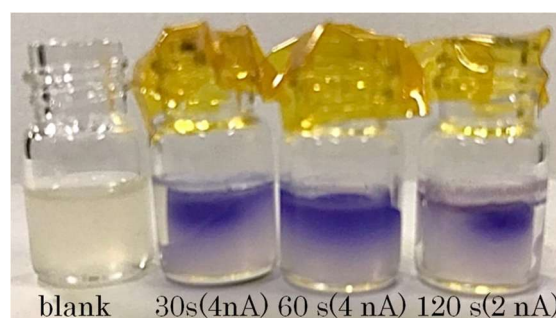


Fig. 1. Color changes of **1** to give colored form **1-H⁺** by $^{12}\text{C}^{5+}$ beam irradiation in carbon tetrachloride gel of **2** ([1]₀ = 0.13 mM, [2]₀ = 71 mM).

References

- [1] T. Tachikawa, *et al.*, *Isotope News*, **731**, 7(2015).
- [2] T. Tachikawa and S. Ishibashi, *QST Takasaki Annu. Rep.* 2019, **1-48** 76 (2020).
- [3] T. Tachikawa and M. Yoshioka, *QST Takasaki Annu. Rep.* 2021, **2-27** 67 (2021).
- [4] H. Itoi, *et al.*, *Chem. Lett.*, **38**, 1002 (2009). DOI: 10.1246/cl.2009.1002.
- [5] T. Tachikawa and K. Yamada, *QST Takasaki Annu. Rep.* 2022, **1-39** 66 (20213).

2 - 19 γ -ray irradiation effect on ammonia radical derived from hydrothermally altered potassium feldspar: A physical basis for the application to fault dating (II)

T. Fukuchi

Faculty of Education, Graduate Faculty of interdisciplinary Research, University of Yamanashi

Introduction

For the assessment of fault activity of unrecognized active faults during the Quaternary period, it is important to determine their absolute ages using an available dating technique. The ESR (electron spin resonance) dating method is applicable to radical centers detected from fault rocks subjected to frictional heating at the time of fault movement [1]. Previous studies showed that the Mo quartet signals with the signal intensity ratio of 1:3:3:1, the intrinsic g-values and the hyperfine splitting parameter of $A=2.4\text{mT}$, which were originally detected from natural montmorillonite in fault rocks, are available to fault dating [2]. Recent studies revealed that the Mo quartet signals are detected also from the hydrothermally altered potash feldspar (orthoclase) in natural fractured granite and attributed to the ammonia ($\cdot\text{NH}_3^+$) radicals as a result of ESR analyses [3].

Experimental

I carried out hydrothermal reaction experiments (for 2 weeks at 250°C) under pure water (H_2O) and an aqueous solution of $10\%\text{NH}_4\text{Cl}$ using the GSJ standard geochemical sample JF-1 (powder K-feldspar), and then investigated γ -ray irradiation effect on radical centers detected from the original standard and hydrothermal reaction samples using ESR. The γ -ray irradiation was carried out with a ^{60}Co source in the γ -ray irradiation facility (No.1 bld., No.1 cell) at Takasaki Advanced Radiation Research Institute, QST. The ESR measurements were done with an X-Band ESR spectrometer (JEOL RE-3X) at the University of Yamanashi.

Results and Discussion

Although the original standard sample before γ -ray irradiation has very weak quartet signals, these signals hardly increase by γ -ray irradiation (Fig.1A). On the other hand, the hydrothermally altered samples under pure water and an aqueous solution of $10\%\text{NH}_4\text{Cl}$ have no signal before γ -ray irradiation, but quartet signals emerge after γ -ray irradiation and increase with radiation dose (Figs.1B and 1C). ESR analyses indicate that these quartet signals are attributed to $\cdot\text{NH}_3^+$ radicals on the basis of the signal intensity ratio, the intrinsic g-values and the hyperfine splitting parameter. A remarkable point is the fact that $\cdot\text{NH}_3^+$ radicals are formed even under pure hot water without the addition of NH_4^+ ions as precursors of $\cdot\text{NH}_3^+$ radicals, implying that NH_4^+ ions eluted from K-feldspar were replaced with K^+ ions in K-feldspar during the hydrothermal reaction. This suggests that $\cdot\text{NH}_3^+$ radicals begin to emerge by fracturing and subsequent hydrothermal reaction in a fault zone and are applicable to the absolute dating of fault movement.

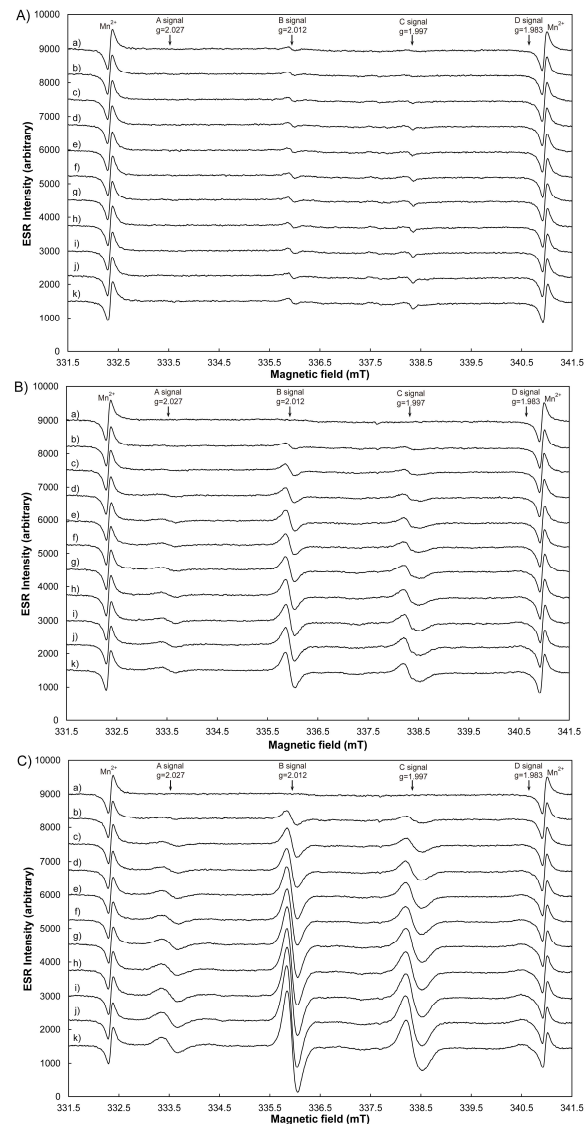


Fig. 1 γ -ray irradiation effect on radical centers detected from the standard and hydrothermal reaction samples. A) GSJ standard K-feldspar, B) hydrothermal reaction sample under pure H_2O , C) hydrothermal reaction sample under an aqueous solution of $10\%\text{NH}_4\text{Cl}$. ESR spectra were measured at a microwave power of 1 mW at room temperature (20°C). The irradiation dose rate is 281.9 Gy/h (A) and 274.5 Gy/h (B&C). Irradiation time: a) 0h, b) 1h, c) 2h, d) 3h, e) 4h, f) 5h, g) 6h, h) 7h, i) 8h, j) 9h, k) 10h.

References

- [1] T. Fukuchi, *Radioisotopes*, **70**, 131 (2021). Doi: 10.3769/radioisotopes.70.131
- [2] T. Fukuchi, *Jpn. J. Appl. Phys.*, **35**, 1977 (1996).
- [3] T. Fukuchi, QST Takasaki Annual Report 2022, **2-26**, 66 (2024).

Part II

3. Life Science

3-01	Visualisation of the dynamics of radiocesium after its penetration into a live apple branch using the ^{127}Cs tracer.....	52
	Y. Noda, T. Yoshihara, N. Suzui, Y.-G. Yin, Y. Miyoshi, K. Enomoto and N. Kawachi	
3-02	Visualization of cadmium distribution in roots of oilseed rape plants by in-air micro-PIXE (Particle Induced X-ray Emission) analysis.....	53
	S. Nakamura, T. Yuzawa, A. Kijima, A. Shinozawa, K. Sato-Izawa, R. Yamagata, Y. Ishii, T. Satoh, Y. Noda, Y. Miyoshi, K. Enomoto, Y.-G. Yin, N. Suzui and N. Kawachi	
3-03	Simulation study on carbon-ion beam imaging by measuring SEB using an imaging plate	54
	M. Tsuda, M. Yamaguchi, W. Kada, T. Kamiya, M. Sakai, H. Watabe, Y. Nagao, T. Yabe and N. Kawachi	
3-04	Analysis of DNA rearrangements induced by carbon ion beams in Arabidopsis seeds and seedlings.....	55
	S. Kitamura, K. Satoh, Y. Hase, R. Yoshihara, Y. Oono and N. Shikazono	
3-05	Resistance of Antarctic yeasts with γ -rays irradiation.....	56
	M. Tsuji, S. Kudoh, K. Satoh and Y. Hase	
3-06	Genome-wide detection of low-frequency mutations in plant population mutagenized with gamma ray.....	57
	Y. Hase, K. Satoh and S. Kitamura	
3-07	Suppression mechanism of DNA damage response protein Ppr1 in <i>Deinococcus radiodurans</i>	58
	K. Satoh, Y. Hase and I. Narumi	
3-08	Mutation analysis and 3D structure prediction of mutation sites in <i>Rubrobacter radiotolerans</i>	59
	I. Kawasaki, A. Kubo, K. Satoh and I. Narumi	
3-09	Comparative evaluation of radionuclide therapy using ^{90}Y and ^{177}Lu – dosimetric comparison –.....	60
	H. Hanaoka, K. Hashimoto, S. Watanabe, S. Matsumoto, T. Sakashita, S. Watanabe, N. S. Ishioka and K. Endo	
3-10	Solvent extraction following oxidation of astatine for the use of a ^{211}Rn – ^{211}At generator.....	61
	Y. Shin, S. Maruyama, K. Kawasaki, K. Aoi, K. Washiyama, I. Nishinaka, S. Yano, H. Haba and A. Yokoyama	
3-11	Radioactive metal separation with 3D printed flow device.....	62
	S. Obata, G. Kagawa, Y. Sugo, H. Manabe, Y. Arima, K. Toda, N. S. Ishioka, M. Mori and S. Ohira	
3-12	Effects of γ -irradiation on superoxide dismutase.....	63
	M. Kikuchi	

3-13	Olfactory responses in <i>Caenorhabditis elegans</i> are maintained after whole-body carbon ion irradiation	64
	M. Suzuki and T. Funayama	

3 - 01 Visualisation of the dynamics of radiocesium after its penetration into a live apple branch using the ^{127}Cs tracer

Y. Noda ^{a)}, T. Yoshihara ^{b)}, N. Suzui ^{a)}, Y.-G. Yin ^{a)},
Y. Miyoshi ^{a)}, K. Enomoto ^{a)} and N. Kawachi ^{a)}

^{a)} Department of Quantum-Applied Biosciences, QST

^{b)} Faculty of Bioscience and Applied Chemistry, Hosei University

Introduction

The Fukushima Dai-ichi nuclear power plant accident caused extensive radiocesium (rCs) contamination in fruit trees, raising concerns about long-term ecological effects. Understanding the translocation of rCs within trees after bark penetration is crucial for identifying organs that accumulate rCs, developing effective pruning methods to reduce rCs, and predicting its dynamics within trees and their environments. However, due to the large size of trees, the translocation of rCs has mainly been estimated based on field surveys, model analyses, and studies using small trees (Noda, *et al.*, 2016), and the exact translocation patterns remain unclear. In this study, we aimed to obtain detailed rCs distribution in living apple trees using positron-emitting Cs-127, which allows observation via gamma-ray detection despite its short half-life.

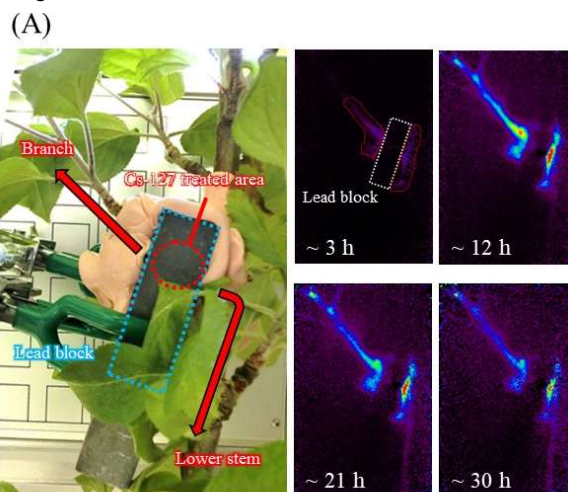
Experimental

For our observations of rCs dynamics, we mainly used the positron-emitting tracer imaging system (PETIS), which detects the gamma-ray annihilation generated by the β^+ decay of positron-emitting radionuclides and allows continuous, non-contact, non-destructive imaging of the distribution of elements within living plants. We used apple trees (*Malus purunifolia*), and the ^{127}Cs was produced and purified according to the method of Suzui *et al.* (2020) using the AVF cyclotron (55 MeV $^4\text{He}^{2+}$) of the Takasaki Ion Accelerators for Advanced Radiation Application (TIARA). Before supplying the purified ^{127}Cs solution, the bark was removed from both the front and back sides of the branch and paper was wrapped around the debarked area. Then, 150 μL (10 MBq) of the purified solution was applied to the paper. The treated area was shielded with lead and clay. Afterward, the branch and main stem were then placed in the PETIS field of view, and the translocation of ^{127}Cs was imaged continuously for 36 hours under spring growth conditions.

Results and Discussion

We could visualize ^{127}Cs translocation from the branches to the young shoot tip and the main stem under controlled spring growing conditions (Fig. 1A). About 6 h later, rCs reached the young shoot, and about 12 h later, rCs signals were clearly observed at the nodes of the young shoot. On the other hand, rCs transported to the main stem were directed both upward and downward from the branch node, with downward transport being favored. We made a similar observation in individuals with fruits, but there was

no ^{127}Cs signal in the fruits. The transport velocity of rCs within the branches was faster than that within the main stem. Using PETIS data, ^{127}Cs transport velocities were estimated, showing faster transport in the branch (4.3 cm/h and 17.1 cm/h) than in the main stem (1.4 cm/h and 6.0 cm/h). The transport velocity in the branch was 3.0 and 2.8 times higher than that in the main stem, respectively, indicating a relative tendency for faster ^{127}Cs transport within the branch (Fig. 1B). This supports the idea that the method is useful for predicting rCs dynamics and identifying organs that rapidly translocate rCs after similar accidents, aiding in the development of effective decontamination strategies.



(B)

	^{127}Cs transport velocity (cm h ⁻¹)		
	Branch	Stem	Branch / Stem
Plant 1	4.3	1.4	3.0 times
Plant 2	17.1	6.0	2.8 times

Figure 1. Observation of ^{127}Cs dynamics in the branch and main stem by PETIS imaging.

(A) Montage of images of ^{127}Cs distribution in the branch and main stem acquired by PETIS imaging. (B) Cs-127 transport velocity (cm h⁻¹) in the branch and stem of two individual plants, and the ratio of the velocity of the branch to that of the stem.

References

- [1] Y. Noda *et al.*, *Sci Rep.* **Vol 6**, 38360 (2016). DOI: 10.1038/srep38360
- [2] N. Suzui *et al.*, *Sci Rep.* **Vol 10**, 16155 (2020). DOI: 10.1038/s41598-020-73351-2
- [3] Y. Noda *et al.*, *Appl Radiat Isot.* **Vol 198**, 110859 (2023). DOI: 10.1016/j.apradiso.2023.110859

3 - 02 Visualization of cadmium distribution in roots of oilseed rape plants by in-air micro-PIXE (Particle Induced X-ray Emission) analysis

S. Nakamura^{a)}, T. Yuzawa^{a)}, A. Kijima^{a)}, A. Shinozawa^{a)}, K. Sato-Izawa^{a)}, R. Yamagata^{b)}, Y. Ishii^{b)}, T. Satoh^{b)}, Y. Noda^{c)}, Y. Miyoshi^{c)}, K. Enomoto^{c)}, Y.-G. Yin^{c)}, N. Suzui^{c)} and N. Kawachi^{c)}

^{a)}Department of Bioscience, Faculty of Life Sciences, Tokyo University of Agriculture

^{b)}Department of Advanced Quantum Beam Technology, QST

^{c)}Department of Quantum-Applied Biosciences, QST

Introduction

Cadmium (Cd) is one of the toxic heavy metal elements. The accumulation of Cd in agricultural crops is harmful to our health. So, the establishment of cultivation technology for safe agricultural crops with low cadmium accumulation is an urgent issue. To establish this technology, control of Cd behaviors in roots of crop plants is necessary. However, the control mechanisms of Cd behaviors in roots of these plants, especially field crops, has not been fully elucidated. The elucidation of the tissue distribution of Cd in plant roots is expected to lead to that of these molecular mechanisms. In-air micro-PIXE (Particle-Induced X-ray Emission) analysis enables us to visualize the tissue distribution of various element of interest in samples [1, 2]. Therefore, we attempted to visualize the tissue distribution of Cd in roots of oilseed rape plants by in-air micro-PIXE analysis.

Experimental

Oilseed rape (*Brassica napus* L. var. Westar) plants were grown hydroponically under fully controlled conditions [3]. In the present study, 100 μM CdCl₂ were given to test plants for 2 days prior to harvest to visualize tissue distribution of Cd in roots. Harvested plant roots were embedded immediately in a clear resin (Cryomatrix, Eprexia) for frozen section preparation and stored at -80°C. Cross sections were prepared for micro-PIXE analysis using a sectioning device (CM1520, Leica Biosystems). After slicing (thickness 60 μm), the cut-out sections were heated immediately on a hot plate (NHP-45N, NISSIN) to remove excessive moisture in them. Microscopic observations were made to determine the samples to be used for in-air micro-PIXE analysis.

In-air micro-PIXE analysis was performed at TIARA in Takasaki Institute for Advanced Quantum Science. Prepared section samples were irradiated with a 3 MeV proton beam for 60 min. The specific X-rays generated by irradiated proton beam were detected. The distribution and intensity of several elements including Cd were determined from the monitored X-ray.

Results and Discussion

Figure 1 indicates a microscopic observation of the prepared sections and the tissue distribution of Cd, potassium (K) and sulfur (S). In this study, we were able to

visualize distribution of Cd in the roots of oilseed rape plants (Fig.1B). Cd, K and S were similarly distributed in roots of oilseed rape plants (Fig1. B, C and D). S is an element in the thiol group. Our previous study demonstrated glutathione with a thiol group in its molecule has effects on Cd behaviors in plant roots [4]. These results suggest that in-air micro-PIXE can be a powerful tool for elucidating the mechanisms that are controlling Cd behaviors in plant roots.

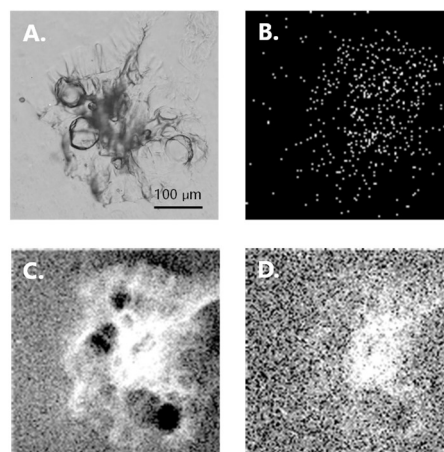


Fig. 1 In-air micro-PIXE analysis in root cross sections prepared from roots of oilseed rape plants treated with 100 μM Cd for 2 days. (A) Microscopic observation, Tissue distribution of cadmium (B), potassium (C) and sulfur (D).

Acknowledgments

This study was supported in part by JSPS KAKENHI Grant Number JP22H02480) to S.N.

References

- [1] T. Sakai et al., Nucl. Instrum. Methods Phys. Res. B. 190, 271-275 (2002). DOI:10.1016/S0168-583X(02)00469-X
- [2] P.M. Kopittke et al., Plant Physiol. 182, 1869-1882 (2020). DOI:10.1104/pp.19.01306
- [3] S. Nakamura et al., Plant Sci. **283**, 424-434 (2019). DOI: 10.1016/j.plantsci.2018.10.018
- [4] S. Nakamura et al., J Exp Bot **64**, 1073-1081 (2013). DOI: 10.1093/jxb/ers388

Simulation study on carbon-ion beam imaging by measuring SEB using an imaging plate

M. Tsuda ^{a, b)}, M. Yamaguchi ^{a)}, W. Kada ^{c)}, T. Kamiya ^{a)}, M. Sakai ^{d)}, H. Watabe ^{b)},
Y. Nagao ^{a)}, T. Yabe ^{a)} and N. Kawachi ^{a)}

^{a)} Department of Quantum-Applied Biosciences, QST

^{b)} Graduate School of Biomedical Engineering, Tohoku University

^{c)} Graduate School of Engineering, Tohoku University

^{d)} Gunma University Heavy Ion Medical Center (GHMC), Gunma University

Introduction

Beam imaging techniques in particle therapy are important for verifying irradiation deviations and improving treatment outcomes. We recently introduced a beam imaging method that measures secondary electron bremsstrahlung (SEB) [1] using an imaging plate (IP) and demonstrated that high-resolution carbon-ion beam images can be achieved with a system combining an IP and a pinhole-type tungsten collimator [2]. The range estimation accuracy for carbon ions could reach a standard deviation of 2.5 mm and may be further enhanced by reducing prompt gamma rays emitted from the particle beam trajectory from entering the IP.

This study evaluates the effect of a lead radiation shield on this imaging system. Removing the lead shield reduces the device's weight; however, it may increase contamination by non-SEB photons, which is called the background (BG) component. Monte Carlo simulations were conducted to investigate the effect of the lead shield on the imaging results [3].

Material and method

The simulations were performed using PHITS version 3.24 [4]. Figure 1 shows the geometry of the simulations. A ^{12}C ion beam was irradiated an acrylic target (6 cm × 6 cm × 12 cm). The beam energy was set to 243.7 MeV/u. A tungsten pinhole collimator with a diameter of 1 cm was placed 31.2 cm from the beam axis. A 6 cm thick lead radiation shield was placed on the side of the collimator. The IP (4 cm × 4 cm × 0.01 cm) material was defined as barium fluoride bromide (BaFBr) and placed 7.5 cm below the collimator. Beam images were obtained by calculating energy deposition to the IP. The IP was divided into 200 × 200 pixels (each pixel size was 0.2 mm × 0.2 mm), giving a magnification of 4.2 and making one pixel correspond to 0.8 mm at the beam position. To evaluate the effect of the lead shield on the BG component, simulations were also conducted with and without the shield, using ^{12}C ions as source particles and restricting secondary electron production. SEB components were calculated using the SEB-source subprogram [1].

Results and Discussion

Figure 2 shows the profiles along the beam direction for SEB and BG. These profiles were generated by projecting the data along the perpendicular axis onto the beam axis.

The results show that the distribution of BG is almost the same with and without the lead radiation shield. They indicate that existence of the lead radiation shield does not contribute to the reduction of BG in the beam images.

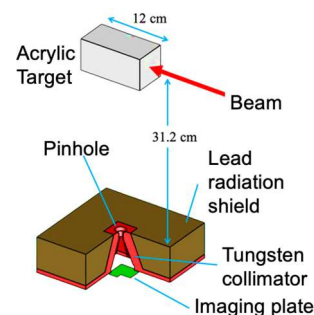


Fig. 1 A 3-dimensional view of the simulation geometry.

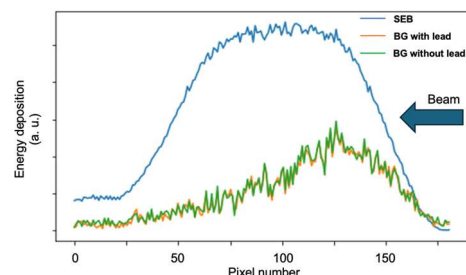


Fig. 2 Profiles of beam images along the beam direction. The blue curve represents the profile of the SEB image. The orange and green curves represent the profiles of the BG images with and without the lead radiation shield, respectively.

Acknowledgments

The authors thank the GHMC staff for supporting our experiment and maintaining the accelerators, the Center for Computational Science, e-Systems, and JAEA staff for supercomputer maintenance. The authors acknowledge funding from TERUMO LIFE SCIENCE FOUNDATION.

References

- [1] M. Yamaguchi et al., *Phys. Med. Biol.* 63, 045016 (2018). DOI: 10.1088/1361-6560/aaa17c
- [2] M. Tsuda et al., *Radioisotopes* 71, 109 (2021). DOI: 10.3769/radioisotopes.71.109
- [3] M. Tsuda et al., *J. Instrum.* 18, C01071 (2023). DOI: 10.1088/1748-0221/18/01/C01071
- [4] T. Sato et al., *J. Nucl. Sci. Technol.*, 61, 127-135 (2024). DOI: 10.1080/00223131.2023.2275736

3 - 04 Analysis of DNA rearrangements induced by carbon ion beams in Arabidopsis seeds and seedlings

S. Kitamura^{a)}, K. Satoh^{a)}, Y. Hase^{a)}, R. Yoshihara^{b)}, Y. Oono^{a)} and N. Shikazono^{c)}

^{a)} Department of Quantum-Applied Biosciences, QST

^{b)} Department of Regulatory Biology, Saitama University

^{c)} Institute for Quantum Life Science, QST

Among several types of genomic alterations, DNA rearrangements, such as structural variations (SVs; i.e., inversions and translocations) and large insertions and/or deletions (indels), have been the most impactful mutations because they may involve the simultaneous modification of multiple genes within and adjacent to the rearranged DNA fragments. The DNA rearrangements can be induced more frequently by ion beams than other mutagens, but molecular mechanisms by which the DNA rearrangements occur are less understood. In the present study, we examined how the DNA rearrangements are formed in Arabidopsis plants, after irradiation with ion beams at dry seed and seedling stages.

A triple Arabidopsis mutant harboring *tt4*, *tt3*, and *tt18* was crossed with the wild-type plant to obtain F1 hybrid seeds with a triple heterozygous genotype (*TT4/tt4 TT3/tt3 TT18/tt18*). Dry seeds or germinated seedlings of the triple heterozygous Arabidopsis were irradiated with 17.3 MeV/u ¹²C⁵⁺ (LET = 107 keV/μm) accelerated by the AVF cyclotron at TIARA, QST. The irradiation doses were 100 Gy for seeds and 15 or 20 Gy for seedlings. The irradiated seeds and seedlings were grown in a growth chamber, to isolate anthocyanin-less sectors in vegetative tissues as described previously [1]. DNA extracted from the anthocyanin-less sectors was used to prepare the next-generation sequencing (NGS) libraries. The libraries were sequenced on the Illumina NGS systems, and the raw NGS reads were analyzed by our standard bioinformatics workflow [1].

After irradiation of 160 seeds and 253 seedlings, 12 and 17 plants produced anthocyanin-less sectors in their vegetative tissues, respectively. Seven and 13 anthocyanin-less sectors derived from the seed- and seedling-irradiation, respectively, were analyzed by whole-genome sequencing analysis. In total, 348 and 355 mutations were identified in the seed- and seedling-irradiated plants, respectively. Of the mutations in the seed-irradiated and seedling-irradiated plants, 9.5% and 10.7% were DNA rearrangements, which were approximately 2-times higher than the corresponding proportions in a recent analysis of the M2 generation [2].

For the seed- and seedling-irradiated plants, 16 and 13 SVs were identified, respectively. Determination of junction sequences at breakage sites of the SVs indicated that deletions at the breakage sites were significantly larger in the seedling-irradiated plants than the seed-irradiated plants (Fig. 1A). The rejoined patterns were also determined for the SVs and >100 bp deletions. A proportion

of rejoined sites harboring inserted nucleotides was significantly higher in the seedling-irradiated plants than the seed-irradiated plants ($p = 0.001$). Additionally, lengths of the inserted nucleotides were significantly larger in the seedling-irradiated plants than the seed-irradiated plants (Fig. 1B). Together with the significant difference in deletion sizes at the breakage sites (Fig. 1A), our data suggest that the breakage/rejoined sites of the DNA rearrangements were more extensively processed in seedlings than in seeds, indicative of the diversity in the main DSB repair mechanisms following the carbon ion irradiation of the seeds and seedlings [3].

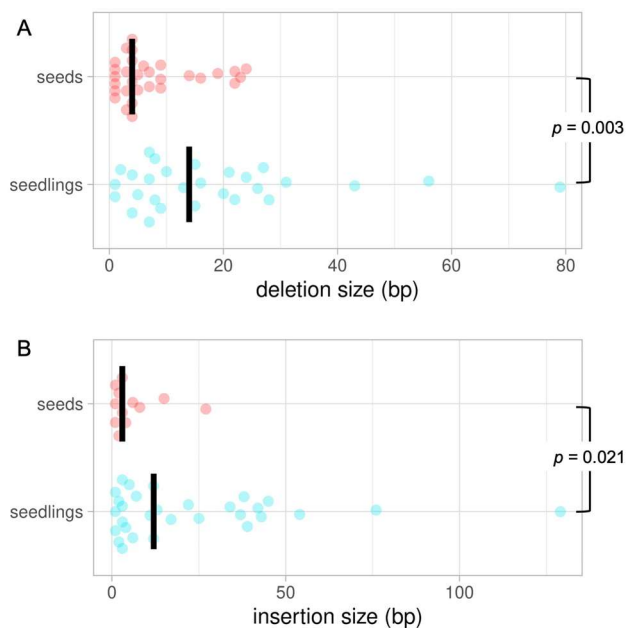


Fig. 1 Junction analysis at breakage sites of SVs (A) and rejoined sites of DNA rearrangements (B) in seed- and seedling-irradiated plants. Vertical lines indicate median lengths.

Acknowledgments

This work was partially supported by JSPS KAKENIH 19K12333 and 16H06279.

References

- [1] S. Kitamura *et al.*, PLoS Genet. **18**, e1009979 (2022). DOI: 10.1371/journal.pgen.1009979
- [2] Y. Hase *et al.*, Front. Plant Sci. **14**, 1149083 (2023). DOI: 10.3389/fpls.2023.1149083
- [3] S. Kitamura *et al.*, Plant J., in press (2024). DOI: 10.1111/tpj.16955

3 - 05 Resistance of Antarctic yeasts with γ -rays irradiation

M. Tsuji^{a, b)}, S. Kudoh^{b)}, K. Satoh^{c)} and Y. Hase^{c)}

^{a)} Department of Material Science, NIT Asahikawa College

^{b)} Bioscience Group, NIPR

^{c)} Department of Quantum-Applied Biosciences, QST

Introduction

Antarctica, the southernmost landmass on Earth, covers an area of approximately 14 million km², making it the fifth largest continent in the world. It is subjected to extremely cold and dry conditions, with the lowest recorded temperature being -90°C . Approximately 98% of Antarctica is covered by ice and snow, with coastal temperatures typically ranging from 5°C to -35°C . Ice- and snow-free areas, present during the austral summer, are located around the continent's coast. Most life forms in continental Antarctica are known to inhabit these ice-free and snow-free areas [1].

Some Antarctic fungi, such as *Cryomyces antarcticus*, require radiation doses of 50 kGy or more to reduce cell survival rates below 10% [2]. However, radioresistance studies have not been conducted on *Mrakia blollopis* and *Cyatobasidium ongulense*, which are dominant species near the Syowa Station, East Antarctica [3]. Therefore, in this study, we decided to investigate the γ -rays resistance of *M. blollopis* and *C. ongulense*.

Experimental

Mrakia blollopis and *Cyatobasidium ongulense* cells were cultured in YPD liquid medium (2% glucose, 1% peptone and 2% yeast extract) at 10°C , 120 rpm, $1 \times \text{g}$ for one week. After one week, 10^6 cells were collected from each species and washed twice with sterile distilled water. Samples were irradiated with 0 to 1,000 Gy of γ -rays in the ⁶⁰Co irradiation facility at TIAQ, QST. Cells after γ -ray irradiation were incubated on PDA agar plate (Potato dextrose agar, Difco, Japan) at 10°C for 2 weeks, and the number of colony forming unit (CFU) that emerged was counted to determine viability.

Results and Discussion

The survival curves of *M. blollopis* and *C. ongulense* obtained in these experiments are indicated as Fig. 1.

The 10% survival dose (D_{10}) for *M. blollopis* was 0.48 kGy and 1.1 kGy for *C. ongulense* (Table 1).

Next, we plan to select mutant strains from γ -rays and carbon ion beams irradiated *M. blollopis* and *C. ongulense* to improve their lipolytic activity and lipid production capacity.

To elucidate the tolerance of Antarctic yeast to extreme environments, the mutant strains should be used in above experiments.

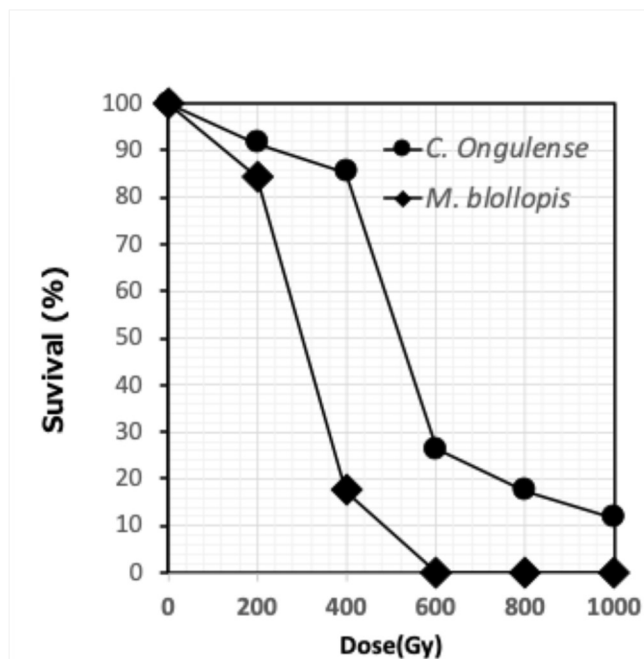


Fig. 1. Survival curves of Antarctic yeasts, *Mrakia blollopis* and *Cyatobasidium Ongulense* with γ -rays irradiation

Table 1. D_{10} of *Mrakia blollopis* and *Cyatobasidium Ongulense*

Species	D_{10}
<i>Mrakia blollopis</i>	0.48 kGy
<i>Cyatobasidium ongulense</i>	1.1 kGy

References

- [1] M. Tsuji, Mycoscience **59**, 319 (2018). DOI: 10.1016/j.myc.2017.08.007
- [2] L. Selbmann *et al.*, Fungal Biol. **122**, 546 (2023). DOI: 10.1016/j.funbio.2017.10.012
- [3] M. Tsuji, Climate, **11**, 195 (2023). DOI: 10.3390/cli11090195

3 - 06

Genome-wide detection of low-frequency mutations in plant population mutagenized with gamma ray

Y. Hase, K. Satoh and S. Kitamura

Department of Quantum-Applied Biosciences, QST

We are investigating the genomic changes in plant and bacterial population grown under stress conditions, in order to detect useful gene mutations that can be utilized to develop stress-tolerant crops and industrial bacteria. To this end, we need to establish a genome-wide detection method for mutations contained in a small number of cells or plants in the population, i.e., low-frequency mutations. Here, we considered the genome-wide detection method of low-frequency mutations using artificially prepared DNA samples using Arabidopsis mutation accumulation lines (MA lines) prepared in our previous study [1].

Fig. 1 shows the outline of the experiment. The MA lines were prepared by growing Arabidopsis plants under 500 or 100 mGy/h gamma rays in five successive generations. The accumulated mutations have already been detected by a whole-genome sequencing (WGS) analysis using randomly chosen sixth-generation plants (M_6 plants) grown under normal conditions. In this study, randomly chosen M_7 plant obtained by a self-pollination of the M_6 plant of the eight independent MA lines were used. The genomic DNA isolated from M_7 plant was mixed with wild-type DNA so that the proportion of the known mutation to be five percent of total. The eight independent mixed DNA samples were designated as sample A to H and subjected to a WGS analysis. Total number of known mutations in the M_6 plants of MA lines used for preparing sample A to G was 227 ~ 322 including both homozygous and heterozygous mutations. The MA line used for sample H contains lesser number of mutations than the others (52 mutations), because this line was prepared under 100 mGy/h gamma rays. Theoretically, M_7 plants contain all homozygous mutations detected in the parental M_6 plant and the expected allele frequency (AF) of them is 0.050. The heterozygous mutations in M_6 plants are partially transmitted to M_7 plants according to the Mendelian segregation, and the expected AF is either 0.050 or 0.025.

In order to detect low-frequency mutations, 50 ~ 80 Gb of short-read sequence data was obtained for each artificially prepared DNA sample. The mean depth of coverage was in the range of 270 to 421 at this point. Variant call was performed by VarDict program [2], and then filtering of false positives was performed. The called variants detected in two or more samples were removed as false positives. The called variants were also removed as false positives, if two or more different mutant allele were called at the same position in a single sample. To ensure data reliability, the called variants with the altered sequence length < 100 bp were selected. Furthermore, the called variants with the variant depth ≥ 4 and the AF ≥ 0.040 were

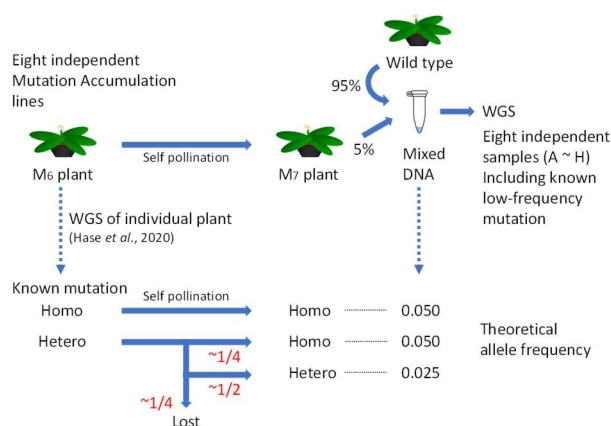


Fig. 1 Schematic representation of mutation detection experiment performed in this study.

selected. The number of selected called variants was in the range of 178 ~ 504 and the mean depth of coverage was in the range of 192 ~ 319.

Furthermore, all of the selected called variants were verified with the Integrative Genomics Viewer. In this step, the called variants were regarded as false positives if any other sample had the same mutation with the AF > 0.010. Finally, the number of reliable variants detected by our mutation detection method was in the range of 136 ~ 160 for sample A to G and 35 for sample H. Of those, only two and four mutations in sample C and G were regarded as unknown mutations, and all of the others were identical with known mutations. These results suggests that the overall accuracy of the verified mutations with the AF ≥ 0.040 was close to 100%. Although the detection rate of known mutations and also the dependency on the types of mutations should be further examined, we believe this mutation detection method can be used to detect beneficial mutations for the growth under stress conditions.

Acknowledgments

This study was partially supported by The Canon Foundation.

References

- [1] Y. Hase *et al.*, *Front. Plant Sci.*, **11**, 336 (2020). DOI: 10.3389/fpls.2020.00336
- [2] Z. Lai *et al.*, *Nucleic Acid Res.* **44**, e108 (2016). DOI: 10.1093/nar/gkw227

K. Satoh^{a)}, Y. Hase^{a)} and I. Narumi^{b)}

^{a)} Department of Quantum-Applied Biosciences, QST

^{b)} Faculty of Life Sciences, Toyo University

Introduction

The radiation resistance of *Deinococcus radiodurans* has been attributed to its highly efficient capacity for DNA repair. The previous studies revealed that the expression of a unique DNA repair-related protein, PprA, was up-regulated by a regulatory protein, PprI, following DNA damage in *D. radiodurans* [1]. The comparative genome analysis of *Deinococcus* has been revealed the radiation/desiccation response (RDR) motif in the upstream regions of the radiation-inducible genes (RDR regulons) [2]. The RDR motif is an operator sequence in the unique DNA repair response system [3]. The PprI consists of three domains, namely metalloprotease, DNA binding, and GAF-like domains. Unlike the RDR regulons, the *pprI* gene is constitutively expressed, suggesting that PprI is post-translationally activated following DNA damage. *In vitro*, the PprI has been shown to have metalloprotease activity by coordinating bonds of manganese (Mn) ions [4]. *In vivo*, the functional complementation studies have shown that the metalloprotease activity is crucial for the DNA damage response mechanism [5]. Recently, it has been shown that the GAF-like domain of PprI is critical for metalloprotease activation by single-stranded DNA (ssDNA) binding [6]. In other bacteria, the GAF-like domains bind cyclic nucleotides such as cAMP and cGMP, and act as receptors for signal transduction [7]. Thus, cyclic nucleotides may regulate the PprI activation through GAF-like domain interactions. In this study, we investigated the relationship between PprI activation and cyclic nucleotides by performing a reporter assay following gamma irradiation in the presence or absence of cGMP.

Experimental

The site-directed mutagenesis was performed to introduce the following mutations (E119Q and E149Q in the metalloprotease domain, Y196A in the DNA binding domain, and H260L in the GAF-like domain) into the wild-type *pprI* expression plasmid. The wild-type and mutated *pprI* expression plasmids were introduced into the *pprI*-deleted luciferase reporter strain XDAP (designated DAW, DAM119, DAM149, DAM196, and DAM260). These reporter strains were incubated in TGY broth with and without 5 μ M cGMP at 30 °C for 24 h with agitation. Cells were harvested, washed, and irradiated at room temperature with 2 kGy of ⁶⁰Co gamma rays at the Gamma-ray Irradiation Facility, QST. After irradiation, the cells were resuspended in the same broth and incubated at 30 °C for 2 h with agitation. After incubation, the cells were subjected to the luciferase

reporter assay [5].

Results and Discussion

The changes in the intracellular level of PprI activation with cGMP following irradiation were compared between the *pprI* mutant and wild-type strains using the luciferase reporter assay (Fig. 1). Under the presence of cGMP, wild-type, DAW, DAM196 and DAM260 exhibited decreased luciferase activity after gamma irradiation and post-irradiation incubation. On the other hand, XDAP, DAM119 and DAM149 could not induce the luciferase activity. These results indicate that the binding of cGMP to the GAF-like domain has a significant impact on the suppression of the PprI protein. Furthermore, the GAF-like domain interacting with cGMP would be also involved in the activation of the PprI protein by Mn ions and ssDNA.

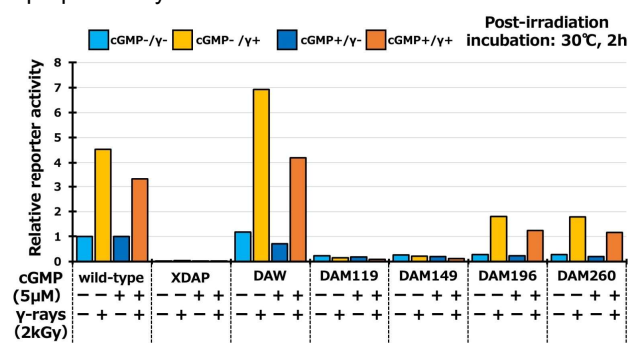


Fig. 1 Changes in the intracellular level of PprI activation with cGMP following irradiation.

Acknowledgments

This work was supported by JSPS KAKENHI Grant Number JP21K05356 to K. Satoh.

References

- [1] Y. Hua *et al.*, *Biochem. Biophys. Res. Commun.* **306**, 354 (2003). DOI: 10.1016/s0006-291x(03)00965-3
- [2] K.S. Makarova *et al.*, *PLoS ONE* **2**, e955 (2007). DOI: 10.1371/journal.pone.0000955
- [3] M. Ludanyi *et al.*, *Mol. Microbiol.* **94**, 434 (2014). DOI: 10.1111/mmi.12774
- [4] Y. Wang *et al.*, *PLoS ONE* **10**, e0122071 (2015). DOI: 10.1371/journal.pone.0122071
- [5] K. Satoh *et al.*, *QST Takasaki Annu. Rep.* 2020, **QST-M-33**, 85 (2022).
- [6] H. Lu *et al.*, *Nature Commun.* **15**, 1892 (2024). DOI: 10.1038/s41467-024-46208-9
- [7] C.C. Heikaus, *et al.*, *Structure* **17**, 1551 (2009). DOI: 10.1016/j.str.2009.07.019

Mutation analysis and 3D structure prediction of mutation sites in *Rubrobacter radiotolerans*

I. Kawasaki ^{a)}, A. Kubo ^{b)}, K. Satoh ^{c)} and I. Narumi ^{a,b)}

^{a)} Graduate School of Life Sciences, Toyo University

^{b)} Faculty of Life Sciences, Toyo University

^{c)} Department of Quantum-Applied Biosciences, QST

Introduction

Rubrobacter radiotolerans is a Gram-positive, rod-shaped bacterium that belongs to the phylum Actinobacteria. It has an optimum growth temperature of 45°C and was originally isolated from the biofilms of a hot spring in Japan in 1973 [1]. This bacterium is known for having the highest radioresistance among all identified bacteria. However, the molecular mechanisms underlying this radioresistance have not been fully understood. This study aims to clarify the radioresistance mechanism by analyzing the DNA repair mechanism and investigating the increased mutation rate induced by DNA damage stress. The study includes determining the background spontaneous mutation rate and analyzing the mutation spectrum through DNA sequencing.

Experimental

The spontaneous mutation rate was calculated based on the number of rifampicin-resistant mutants to the total viable cells, and then using Drake's formula ($\mu = f / \ln(N\mu)$, where μ is the mutation rate, f is the mutant frequency, N is the total viable count) to determine the mutation rate [2,3]. Additionally, we collected the rifampicin-resistant mutants and extracted their genomic DNA using a FastDNA SPIN Kit. The mutation sites were identified by PCR amplification and DNA sequencing analysis of the *rpoB* gene from the genomic DNA of rifampicin-resistant mutants. Furthermore, we utilized a molecular dynamics method to predict a 3D structural model of the RpoB protein in this bacterium and analyze its interaction with rifampicin.

Results and Discussion

When the concentration of rifampicin was varied (0.05 µg/mL, 0.5 µg/mL, and 5.0 µg/mL), the respective mutation rates were 7.71×10^{-8} , 5.66×10^{-8} , and 5.61×10^{-8} , suggesting that the mutation rate increased with decreasing rifampicin concentration.

The mutation rates of *Escherichia coli* (with rifampicin at 100 µg/mL) and the radioresistant bacterium *Deinococcus radiodurans* (50 µg/mL) were found to be 4.1×10^{-10} and 7.7×10^{-9} , respectively [5,6]. This indicates that *R. radiotolerans* had a higher mutation rate than these bacteria. The mutation rate is expected to increase with the number of genome copies, and indeed, *E. coli* has a haploid genome, while *D. radiodurans* has an oligoploid genome with 4–10 copies. It is suggested that *R. radiotolerans* may have a multiploidy genome, possessing even more genome copies than *D. radiodurans*.

Moreover, after sequencing the *rpoB* gene from 150

rifampicin-resistant mutants, it was found that mutations were focused in 15 specific locations. These mutations included a 9-base deletion, hotspots with high substitution rates, and mutations that were only present when low concentrations of rifampicin were used (Fig. 1). Additionally, the 3D structural prediction indicated that the identified mutations were clustered at the rifampicin-binding sites (Fig. 2).

In the future, we will use gamma radiation to induce random mutagenesis and obtain DNA repair-deficient mutants. Subsequently, we will identify the mutation sites.

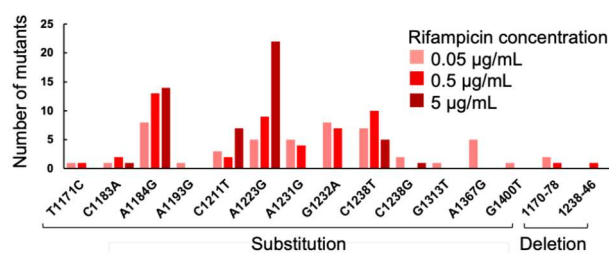


Fig. 1 Mutation spectrum of *rpoB* gene.

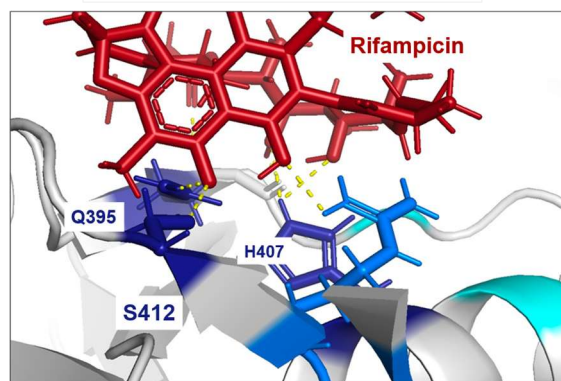


Fig. 2 The 3D structural prediction of the RpoB protein.

References

- [1] T. Yoshinaka *et al.*, *Agr. Biol. Chem.* **37**, 2269 (1973). DOI: 10.1080/00021369.1973.10861003
- [2] J. W. Drake, *Proc. Natl. Acad. Sci. USA* **88**, 7160 (1991). DOI: 10.1073/pnas.88.16.7160
- [3] I. Kawasaki *et al.*, *QST Takasaki Annu. Rep.* 2022, **QST-M-47**, 83 (2024).
- [4] J. Jee *et al.*, *Nature*, **534**, 693 (2016). DOI: 10.1038/nature18313
- [5] M. Kim *et al.*, *Genetics*, **166**, 661 (2004). DOI: 10.1534/genetics.166.2.661

Comparative evaluation of radionuclide therapy using ^{90}Y and ^{177}Lu – dosimetric comparison –

H. Hanaoka ^{a)}, K. Hashimoto ^{b)}, S. Watanabe ^{c)}, S. Matsumoto ^{c)}, T. Sakashita ^{c)},
S. Watanabe ^{c)}, N. S. Ishioka ^{c)} and K. Endo ^{a)}

^{a)} Graduate School of Medicine, Gunma University

^{b)} Quantum Beam Science Center, JAEA

^{c)} Department of Quantum-Applied Biosciences, QST

Introduction

Both ^{90}Y (half-life 64 hours) and ^{177}Lu (half-life 6.7 days) are attractive β -emitters for radionuclide therapy and have been used in clinical practice. Nevertheless, comparative evaluation between ^{90}Y - and ^{177}Lu -labeled molecules has not been fully conducted. Thus, in this study, the features of ^{90}Y and ^{177}Lu for radionuclide therapy were assessed in tumor-bearing mice. Here, we report on the dosimetry aspects of the comparative evaluation.

Methods

Biodistribution studies of ^{177}Lu -labeled antibodies (^{177}Lu -Abs) were conducted in each tumor-bearing mouse model. Abs of NuB2 with affinity for the CD20 antigen and trastuzumab that specifically binds to HER2 proteins were used. Subsequently, the therapeutic effects of ^{90}Y - and ^{177}Lu - Ab were assessed in tumor-bearing mice. The absorbed radiation dose for the tumor was estimated using the three-dimensional radiation transport code PHITS developed by the Japan Atomic Energy Agency [1], assuming that the Abs labeled with ^{177}Lu or ^{90}Y were distributed uniformly in the tumor tissue.

Results and Discussion

Using the results of biodistribution experiments, we estimated the tumor tissue total doses. As shown in Table 1, tumor tissue doses were comparable between ^{90}Y -NuB2 (3.7 MBq) and ^{177}Lu -NuB2 (14.8 MBq), and ^{90}Y -trastuzumab (3.7 MBq) and ^{177}Lu -trastuzumab (11.1 MBq).

Table. 1 Injected dose (MBq) and tumor tissue dose (Gy) of each ^{90}Y - or ^{177}Lu -Ab.

Nuclide	^{90}Y		^{177}Lu	
	NuB2	Trastuzumab	NuB2	Trastuzumab
Injected dose (MBq)	3.7	7.4	14.8	11.1
Tumor tissue dose (Gy)	13.9	27.8	14.4	73.0

Regarding therapeutic effects, the relative tumor size two weeks after administration was in the following order: ^{90}Y -NuB2 (7.4 MBq) < ^{177}Lu -NuB2 (14.8 MBq) < ^{90}Y -trastuzumab (3.7 MBq). On the other hand, when tumor-bearing mice generated from HER2-positive cells NCI-H2170 were administered a drug consisting of trastuzumab labeled with ^{90}Y or ^{177}Lu , the relative size of the tumor approximately seven weeks after administration was in the order of ^{177}Lu -

trastuzumab (11.1 MBq) < ^{90}Y -trastuzumab (3.7 MBq). These results suggest that ^{177}Lu has a stronger antitumor effect than ^{90}Y at comparable total doses.

To understand the differences in dosimetry characteristics between ^{177}Lu and ^{90}Y , we investigated the dose rates and dose distributions of both nuclides. The analysis of the time changes in dose rate showed that the Ab labeled with ^{177}Lu was able to deliver a dose over a longer period than that labeled with ^{90}Y at the same dose (Fig. 1a). In addition, the analysis of the dose distribution showed that the Ab labeled with ^{177}Lu was able to deliver a dose almost uniformly to the periphery of the tumor tissue compared with ^{90}Y (Fig. 1b). These results suggest that the time change in tumor tissue dose (dose rate) and the dose distribution may contribute to the greater antitumor effect of the Ab labeled with ^{177}Lu than that of the Ab labeled with ^{90}Y when the tumor total doses are comparable.

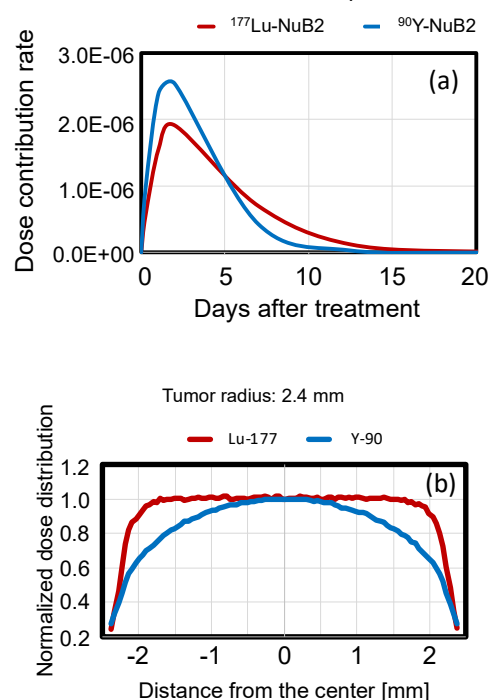


Fig. 1 (a) Dose contribution rate (s^{-1}) for 20 days after treatment and (b) normalized dose distribution for spherical tumors.

Reference

[1] T. Sato *et al.*, J. Nucl. Sci. Technol. **61**, 127 (2024). DOI: 10.1080/00223131.2023.2275736

3 - 10 Solvent extraction following oxidation of astatine for the use of a ^{211}Rn – ^{211}At generator

Y. Shin ^{a)}, S. Maruyama ^{a)}, K. Kawasaki ^{a)}, K. Aoi ^{a)}, K. Washiyama ^{b)}, I. Nishinaka ^{c)}, S. Yano ^{d)}, H. Haba ^{d)} and A. Yokoyama ^{e)}

^{a)} Graduate School of Natural Science and Technology, Kanazawa University

^{b)} Advanced Clinical Research Center, Fukushima Medical University

^{c)} Department of Quantum-Applied Biosciences, QST

^{d)} Nishina Center for Accelerator-Based Science, RIKEN

^{e)} Institute of Science and Engineering, Kanazawa University

Introduction

Targeted α -therapy is increasingly used for the treatment of various types of tumors. One of the most promising nuclides among various α -emitters is astatine-211 (^{211}At) owing to its suitable half-life ($t_{1/2}$) of 7.2 h and high probability of α emission.

To improve the availability of ^{211}At , we are developing a ^{211}Rn – ^{211}At generator that may provide nuclides to locations distant from accelerator facilities where they are produced. The production of ^{211}Rn in the $^{209}\text{Bi}(^7\text{Li},5n)^{211}\text{Rn}$ nuclear reaction had been studied; wet chemical processes were used for efficient collection of Rn in dodecane following the dissolution of the irradiated target with nitric acid (HNO_3) [1].

In this study [2], the separation of ^{211}At via a decay of ^{211}Rn in dodecane has been studied to optimize the conditions for the back-extraction of ^{211}At into ethanol aqueous solution with oxidizing agents from dodecane.

Experimental

^{211}At was produced via either the $^{209}\text{Bi}(\alpha,2n)$ reaction at AVF cyclotron of the Research Center for Nuclear Physics, Osaka University, the RIKEN AVF cyclotron, and a CYPRIS MP-30 cyclotron in the Advanced Clinical Research Center at Fukushima Medical University, or by milking of the ^{211}Rn produced in the $^{209}\text{Bi}(^7\text{Li},5n)$ reaction at the JAEA tandem accelerator. ^{211}At tracers were prepared by dissolving the irradiated targets with HNO_3 and extracting into dodecane.

^{211}At was back extracted from 3 mL of dodecane to 3 mL of aqueous ethanol solutions after the addition of N-chlorosuccinimide (NCS), N-bromosuccinimide (NBS), N-iodosuccinimide (NIS), Br_2 water, or HBr at several concentrations. Radioactivity of ^{211}At was measured with liquid scintillation counter; samples were prepared by mixing 0.1 mL each of dodecane and ethanol phase after back-extraction with 0.9 mL of Ultima Gold AB cocktail.

Results and Discussion

As shown in Fig.1, back-extraction rates decrease with time due to the deactivation time of NBS and Br_2 . Effects of both NBS and Br_2 are lost over time. This shows that NBS is relatively slow to deactivate because it generally generates Br_2 while decomposing in aqueous ethanol solution, whereas Br_2 water deactivates quickly because the Br_2 concentration decreases from its initial value.

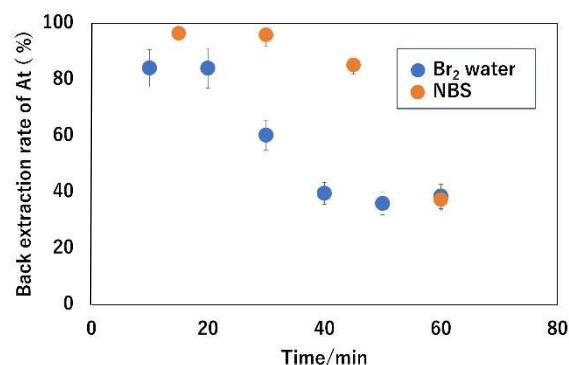


Fig. 1 ^{211}At back-extraction rates as a function of time elapsed from the addition of Br_2 water or NBS.

The ^{211}At back-extraction rates for different concentrations of NCS, NBS, and NIS are shown in Fig. 2. The rate decreased in the order NBS > NCS > NIS. No clear correlation was found between the NCS, NBS, and NIS concentrations and the ^{211}At back-extraction rate.

We conclude that Br_2 produced from NBS increased the ^{211}At back-extraction rate and NBS has strongest effect on the rate among NCS, NBS, and NIS. Some ^{211}At species, which are more easily oxidized than other halogen species, contribute to the increase of the back-extraction rate.

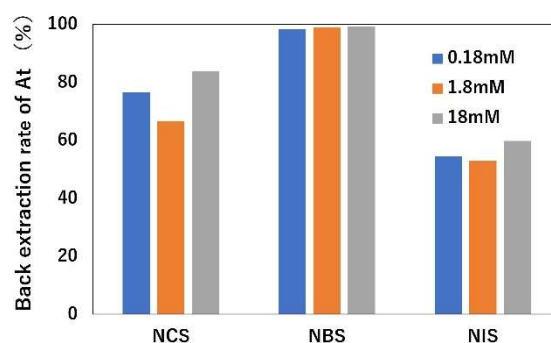


Fig. 2 ^{211}At back-extraction rates as the addition of NCS, NBS, and NIS.

References

- [1] E. Maeda *et al.*, J. Radioanal. Nucl. Chem. 303, 1465 (2015). DOI: 10.1007/s10967-014-3586-z
- [2] Y. Shin *et al.*, J. Radioanal. Nucl. Chem. 333, 403 (2024). DOI: 10.1007/s10967-023-09282-9

3 - 11 Radioactive metal separation with 3D printed flow device

S. Obata^{a)}, G. Kagawa^{a)}, Y. Sugo^{b)}, H. Manabe^{c)}, Y. Arima^{a)},
K. Toda^{a)}, N. S. Ishioka^{b)}, M. Mori^{c)} and S. Ohira^{a)}

^{a)}Department of Chemistry, Kumamoto University

^{b)}Department of Quantum-Applied Biosciences, QST

^{c)}Faculty of Science and Technology, Kochi University

Introduction

Radioactive Ga can be produced from the source Zn by irradiation with proton beam using cyclotrons. For clinical usage, radioisotopes need to be rapidly and efficiently separated from a large amount of the source metals. Previously, we have developed a flow-based system with a parallel plate type cation-trapping device followed by a UV reactor [1].

In this study, a new automated separation system including the 3D printed flow-based device was designed and fabricated. The separation performance was optimized and evaluated with cold and hot tests [2].

Experimental

Details of the 3D printed separation device are shown in Fig. 1. The device was integrated using high resolution inkjet 3D printer (KEYENCE AGILISTA series) with the acrylic resins. All of the solution channels were coated by fluoropolymer to avoid undesired adsorption. Five three-way solenoid valves (SV) were mounted on the 3D printed flow device. A solution channel gasket was prepared with PTFE film (2 mm thickness, channel volume ~3.2 cm³). A pen shape UV mercury lamp was used for ozone generation. A column (5 mm diameter, 38 mm length) incorporated into the device was filled with cation exchange resin (Dowex 50W×8, 100~200 mesh). The flow lines were switched with programmable relays.

A solid target ^{nat}ZnO was irradiated with an 18 MeV

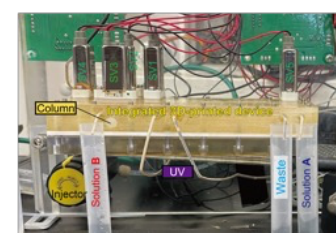
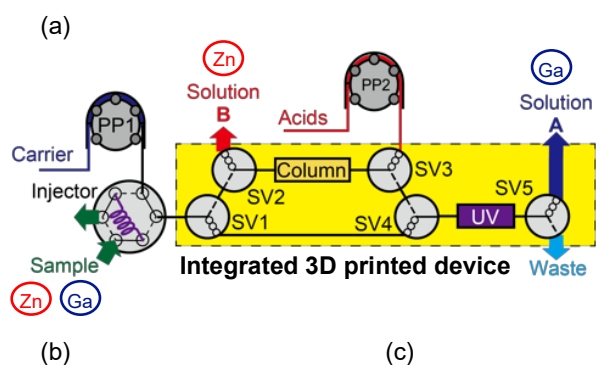


Fig. 1 Flow diagram (a), photograph (b), and schematic drawing (c) of the whole system of the 3D printed separation device.

proton beam at a current of 5 μ A using the AVF cyclotron of TIARA. Radioactive nuclides such as ⁶⁷Ga (half-life of 3.26 d) and ⁶⁵Zn (243.7 d) were simultaneously produced by nuclear reactions of ⁶⁸Zn(*p,2n*)⁶⁷Ga and ⁶⁶Zn(*p,pn*)⁶⁵Zn, respectively. These nuclides were used as tracers for the evaluation of Ga/Zn separation performance. The irradiated target was dissolved in HNO₃. The solution matrices were adjusted to 1 mmol L⁻¹ ethylenediaminetetraacetic acid (EDTA) in 30 mmol L⁻¹ HNO₃ (pH 1.5).

Results and Discussion

The sample containing ⁶⁷Ga and ⁶⁵Zn tracers with 100 mg L⁻¹ ^{nat}Zn was introduced into the developed system and automatically separated. The fractions were collected every one min and measured with NaI (TI) scintillation counter. The separation based on the selective chelate formation and UV radiation for chelate decomposition were achieved within 14 min. The recovery of Ga and Zn in each fraction is illustrated in Fig. 2. Ga was quantitatively recovered in the solution A within 5 min, and Zn was collected in the solution B within 14 min. The total recoveries of ⁶⁷Ga and ⁶⁵Zn were 97% and 100%, respectively. Furthermore, the recovery of free ⁶⁷Ga³⁺ ions from ⁶⁷Ga-EDTA complex by UV radiation was also effective, 87%.

In conclusion, the system was successfully applied to separate the radioactive Ga selectively, rapidly, and effectively from the dissolved solution containing larger amounts of source material Zn. This method and system can be applied to other radioactive metals from the target metals.

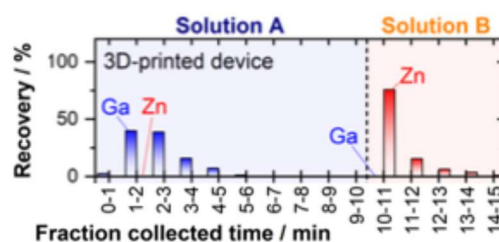


Fig. 2 Separation of Ga from Zn using the developed system.

Acknowledgments

This work was supported by JSPS KAKENHI Grant Number JP 21H02870.

References

- [1] Y. Sugo *et al.*, QST Takasaki Annu. Rep. 2021, **QST-M-39** 89 (2023).
- [2] S. Obata *et al.*, *Anal. Sci.* **39**, 671 (2023). DOI: 10.1007/s44211-022-00254-9

M. Kikuchi

Department of Quantum-Applied Biosciences, QST

Introduction

Ionizing radiations induce various radicals such as hydroxyl radical ($\cdot\text{OH}$), hydrated electron (e_{aq}^-) in cells. Some of them are changed to H_2O_2 that are called as reactive oxygen species (ROS), which is degraded by catalase or peroxidase. However, metal ions of Fe^{2+} may react with H_2O_2 to generate $\cdot\text{OH}$ again (Fenton reaction). In the biological cells, a decoupled electron is often changed to a self-inducing radical that comes from the process of the respiration and that can be vanished through same system for radiation-inducing radicals. Especially when an e_{aq}^- reacts with an O_2 molecule, they change to a superoxide anion radical ($\cdot\text{O}_2^-$). The $\cdot\text{O}_2^-$ radical is disproportionated into O_2 and H_2O_2 by superoxide dismutase (SOD) [1]. It means that SOD should increase radiation resistance for the cell, because of continuously decreasing DNA lesions. Therefore, the effect of ionizing radiation on the enzyme activity was investigated in this research.

Experimental

Since SOD has one of transition metals (Mn, Fe, Cu/Zn), electron spin resonance spectroscopy (ESR) can show indicatable signals according to unpaired electrons. Especially in case of Mn^{2+} , the spectrum indicates an electron in strong ligand field, or 5 electrons in weak ligand field. Thereby, the Mn amount in cell must be estimated from peak number and its intensity by ESR.

At first, SOD activity was measured using enzyme-substrate system, indicated in product description of chemical supplier. For instance, xanthine oxidase (XO) produces $\cdot\text{O}_2^-$ from xanthine, then the radical changes from oxidative form of cytochrome C (CytC) to reductive form (A_{550} , that is, absorbance at 550 nm). By contrast, SOD degrades $\cdot\text{O}_2^-$ radical, causing less A_{550} increase. In the experiments, 100 μM Xanthine, 16 μM CytC, 0.5 U XO, and 6 U SOD were reacted in cuvettes of 0.5 mL buffer at 33°C.

To know effects of γ -irradiation on SOD, it was irradiated at ambient temperature using Co-60 facility in TIAQ.

Results and Discussion

Figure 1 showed $\cdot\text{O}_2^-$ degradation. In more than 1 μL SOD, A_{550} increase were highly inhibited. The absorbance gradually increased according to less SOD volume, up to maximum reductive CytC by XO alone.

Concerning the irradiation effects of γ -rays, SOD (6 U) was almost inactivated after 0.5 kGy-irradiation (Fig. 2).

The bacterium, *Escherichia coli*, was cultivated in 0.2 mM MnCl_2 -supplemented LB-Broth (Lennox), recovered and washed in phosphate buffer. Then, the aliquots of bacterium were irradiated for cell surviving test. The result showed that radiation resistance of both cultures with and without Mn was no difference (Fig. 3). To estimate Mn content, medium before and after culture, and bacterial

cells were measured with ESR. Compared with peak intensities, the Mn content in medium was half decreased after cultivation. Mn content missing in medium was not found in bacterial cells, though the cells were applied in a 1000-fold higher sensitivity than medium (data not shown).

Therefore, the cell survivals may come from that SOD is easy deactivated by γ -irradiation, or existence of SOD is far limited in cells.

Acknowledgment

This work was carried out in part of JSPS KAKENHI (JP19K15781).

Reference

[1] J.M. McCord, I. Fridovich, J. Biol. Chem. **244**, 6049 (1969).

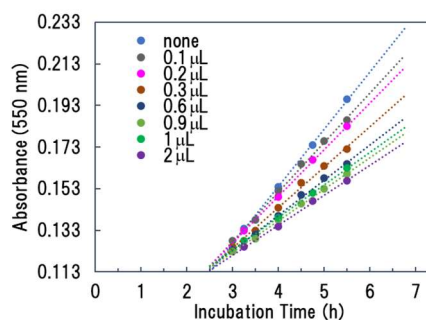


Fig. 1 Effects of SOD volume for changing its activity against superoxide anion radicals.

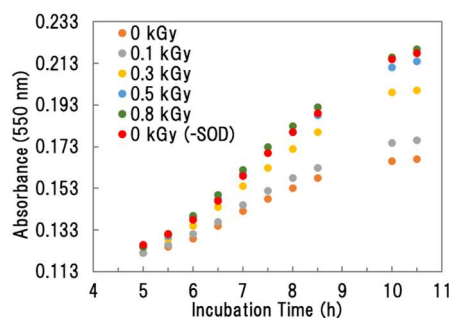


Fig. 2 Effects of γ -irradiation on the activities of SOD enzyme.

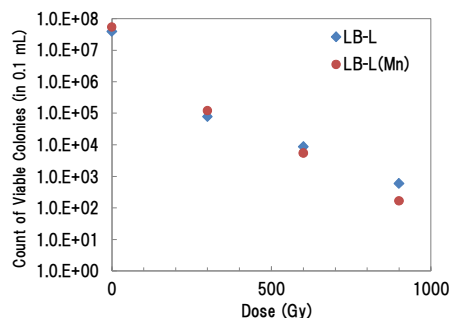


Fig. 3 Preliminary result on effects of growth medium, LB-broth (Lennox), containing Mn on cell survivals after γ -irradiation.

3 - 13

Olfactory responses in *Caenorhabditis elegans* are maintained after whole-body carbon ion irradiation

M. Suzuki and T. Funayama

Department of Quantum-Applied Biosciences, QST

Introduction

We have studied the effects of carbon ion irradiation on muscular movement and lifespan in the nematode *Caenorhabditis elegans*. On the other hand, it has been difficult to detect stimulation responses, especially olfactory responses to low concentrations of odorants in *C. elegans* due to problems with the experimental methods themselves. We have developed a new assay method, named "the pond assay for the sensory system (PASS)" [1] that overcomes this problem, and it has become possible to accurately detect the response of *C. elegans* to low concentrations of odorants. Therefore, the aim of this study was to investigate whether whole body carbon ion irradiation affects the sensitivity of the *C. elegans* olfactory system.

Experiments

(1) Strains and cultures

The nematode *Caenorhabditis elegans* hermaphrodites of wild-type strain N2 were grown at 20°C on an agar plate with bacterial lawn as a food source. Age-synchronized and well-fed young adults were used for all experiments.

(2) Carbon ion Irradiation at TIARA

Animals on an agar plate with bacterial lawn were irradiated with a carbon-ion (C^{6+} , 320 MeV) broad beam at the HY1 port of TIARA. Four doses, 100 Gy, 500 Gy, 1,000 Gy, and 0 Gy as a control, were irradiated independently.

(3) Olfactory experiments by using a PASS method

The PASS method involves creating a pond by filling the holes on either side of an agar plate with the odorant solution to be tested and the target ultrapure water, then releasing a large number of nematodes into the center of the plate to see which side they gravitate to (see Fig.1)[1]. After one hour, almost all of the animals will have fallen into one of the ponds, so by counting the number of animals that have fallen into each pond, it is possible to quantify the group response. After carbon ion irradiation, the olfactory response of animals to diacetyl solution diluted by 0 to 1000000 were examined.

(4) Evaluation of olfactory response of *C. elegans*

Approximately 1 h after starting the assay, an image of each pond was captured with a digital camera mounted on a microscope. Animals in the image were counted manually. For the evaluation of chemotaxis to odorants, the chemotaxis index (C.I.) was calculated based on the number of animals in the ponds as follows:

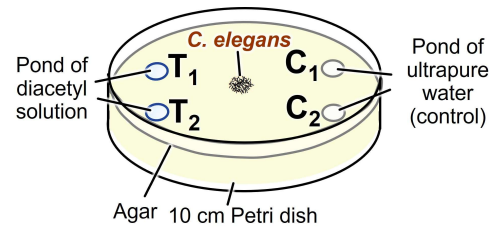
$$C.I. = \frac{\text{number of animals trapped in two ponds } (T_1+T_2) - \text{number of animals trapped in two control ponds } (C_1+C_2)}{T_1+T_2+C_1+C_2}$$


Fig.1 Schematic of a PASS plate to examine chemotaxis of *C. elegans* group to diacetyl.

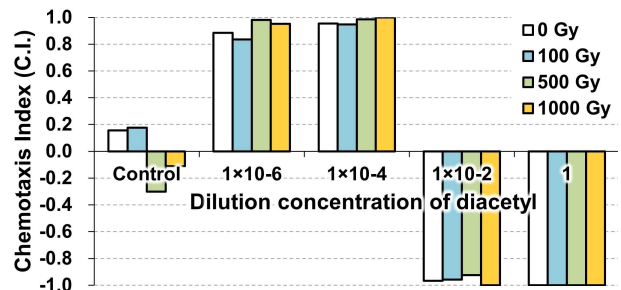


Fig.2 Chemotaxis (olfactory response) of the carbon-ion irradiated *C. elegans* to diacetyl solution.

Results

The results of an investigation of the olfactory response of nematodes exposed to whole body carbon ion irradiation to diacetyl are shown in Fig. 2. The 100 Gy (light blue), 500 Gy (yellow-green), and 1,000 Gy (yellow) irradiation groups all showed an avoidance response to the undiluted diacetyl solution and the 100-fold diluted solution, and an attraction response to the 10000-fold diluted solution and the 1000000-fold diluted solution. The C.I. values of all irradiated groups were equivalent to those of the non-irradiated group (white). These results suggest that, although preliminary, whole-body carbon ion irradiation of 1,000 Gy or less does not affect the olfactory responses to diacetyl at concentrations of 1,000,000 times or less. In the future, we will clarify the effects of whole body carbon ion irradiation at higher doses and responses to odorants at lower concentrations.

Acknowledgments

We thank the *Caenorhabditis* Genetic Center (CGC) of the University of Minnesota, which is funded by the NIH Office of Research Infrastructure Programs (P40 OD010440), for providing strains of *C. elegans* and *E. coli*.

Reference

[1] M. Suzuki *et al.*, *Biology*. **11**, 335 (2022).

DOI: <https://doi.org/10.3390/biology11020335>

Part II

4. Quantum Beam Technology

4-01	Measurement of spin polarization of positrons emitted from ^{44}Sc source generated by nuclear reaction	66
	M. Maekawa and A. Kawasuso	
4-02	Beam energy control by the excitation current of the harmonic coil in the AVF cyclotron	67
	N. Miyawaki, H. Kashiwagi, S. Watanabe, N. S. Ishioka and S. Kurashima	
4-03	Characterization of microfabricated patterns coated with metals using micro-particle induced X-ray emission	68
	S. Sada, R. Ishida, K. Kosumsupamala, N. Puttaraksa, Y. Ishii and H. Nishikawa	
4-04	Improvements in the beam observation system of hundreds of MeV heavy ion microbeam line in TIARA	69
	H. Kashiwagi, R. Yamagata, N. Yamada and N. Miyawaki	
4-05	Improvement of the heavy-ion microbeam system	70
	Y. Ishii, R. Yamagata, T. Satoh, S. Matsuyama, S. Onoda and Y. Saitoh	
4-06	Carbon sputtering yield by fullerene-ion bombardment	71
	K. Narumi, K. Yamada, Y. Hirano, A. Chiba and Y. Saitoh	
4-07	Study of radiation resistance of Coal Ash Fiber (BASHFIBER®) using Positron Annihilation method, etc.	72
	Y. Murakami, K. Sekine, H. Fukazawa, M. Maekawa and A. Kawasuso	
4-08	Electron-stimulated luminescence of liquid water at speeds below the Cherenkov light threshold	73
	K. Enomoto, Y. Nagao, T. Yabe, M. Tsuda, M. Yamaguchi, S. Yamasaki, S. Kano, N. Nagasawa and N. Kawachi	
4-09	ESR measurement of carbonated hydroxyapatite for dosimeter	74
	H. Seito, E. Yokozuka, T. Oka, Y. Kitatsuji and N. Nagasawa	
4-10	Effect of polyacrylic acid on remineralization of demineralized dentin	75
	Y. Matsuda, K. Okuyama, H. Yamamoto, M. Sakurai, K. Naito, H. Kanda, T. Saito, M. Hayashi, Y. Tamaki, T. Sato, N. Yamada and R. Yamagata	

4 - 01

Measurement of spin polarization of positrons emitted from ^{44}Sc source generated by nuclear reaction

M. Maekawa and A. Kawasuso

Department of Advanced Quantum Beam Technology, QST

Introduction

We have developed several spin-polarized positron beam apparatuses that are equipped with commercial ^{22}Na radioisotopes. The spin polarization and beam intensity are typically $\sim 30\%$ and $\sim 10^4$ e $^+$ /s respectively. However, both performances should be improved for further advanced applications, such as the surface positronium (Ps) spectroscopy or the Ps Bose-Einstein Condensation (BEC).

To obtain highly spin-polarized positrons, β^+ decay sources emitting high energy positrons should be used [1]. If a large amount of such nuclides could be produced by nuclear reactions of the high-energy ion beam from the accelerator, a high-intensity spin-polarized positron beam can be obtained. In this study, we focus on ^{44}Sc , which is easily produced by the $^{45}\text{Sc}(p, pn)^{44}\text{Sc}$ reaction. The maximum spin polarization of the emitted positron is predicted to be 85 %. The aim of this paper is to measure the actual spin polarization of positrons from the ^{44}Sc source generated by the TIARA cyclotron.

Experimental

A metal Sc target (250 μm x 6 stacked plates) was enclosed in a carbon capsule and irradiated with 20 MeV protons at 2.4 μAh on a water-cooled irradiation stage installed at the LX1 port of the TIARA cyclotron [2]. The irradiated area covered an aperture of 8 mm ϕ . Subsequently, the spin polarization of the emitted positrons was determined by measuring the magnetic dependence of the S parameter in SiO_2 . [1,3,4]. Figure 1 shows the schematic of the measurement system. The irradiated Sc target and the SiO_2 sample (with dimensions of 20 mm x 20 mm) were positioned 3 mm apart in the electromagnet. Using a lead slit with a width of 1mm, only the annihilation gamma rays originating from the SiO_2 sample were measured.

Results and Discussion

The measured S parameters are shown in Fig. 2. The spin polarization reflects the asymmetry of the S parameter in positive and negative magnetic fields. From the fitting by equations described in Ref.1, the spin polarization was determined to be $P = 52\%$.

The average spin polarization $\langle P \rangle$ of positrons emitted from the source into an open angle θ is given by

$$\langle P \rangle = \frac{\langle v \rangle}{c} \frac{1 + \cos \theta}{2},$$

where $\langle v \rangle$ is the average velocity of the emitted positrons and c is the speed of light. The average energy of the positron emission from the ^{44}Sc source is 0.45 MeV (with a velocity parameter $\langle v \rangle/c = 0.85$). The maximum spin polarization, as aforementioned, occurs when the open

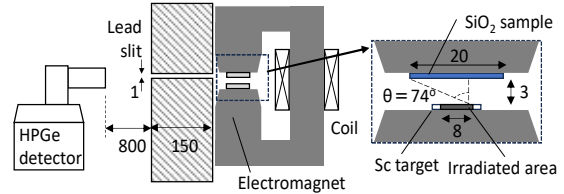


Fig. 1 Schematics of the polarization measurement system. The irradiated Sc target and SiO_2 sample are installed during the pole piece of the electromagnet. Only the annihilation gamma rays from SiO_2 sample are measured by the HPGe detector by using the lead slit.

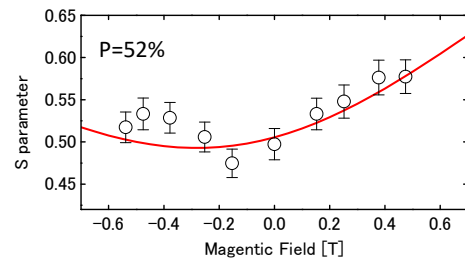


Fig. 2 Magnetic field dependences of S parameters of SiO_2 obtained using ^{44}Sc source. The solid line denotes the fitting curves calculated from the equations in Ref.1.

angle is $\theta = 0$. As shown in Fig.1, the open angle in this measurement is $\theta = 74^\circ$. In this case the predicted polarization is $P = 54\%$, which is consistent with our experimental result.

Although the ^{44}Sc source has the disadvantage of a short half-life (4 hours), its high production rate (230 MBq/ $\mu\text{A}/\text{h}$) and high melting point (1500°) allow mass production by high current ion beam irradiation. The ^{44}Sc source produced by ion beam irradiation can be used for experiments such as the Ps-BEC experiment, which require ultra-high intensity spin-polarized positrons even in a short time.

Acknowledgments

This work was supported by JSPS KAKENHI Grant No. 23H05462.

References

- [1] M. Maekawa et al., Nucl. Instr. Methods B308(2013)9. DOI: 10.1016/j.nimb.2013.04.015
- [2] M. Maekawa et al., QST Takasaki Annu. Rep. 2022, QST-M-47 98 (2023).
- [3] Y. Nagai et al., Nucl. Instr. Methods B171(2000)199. DOI: 10.1016/S0168-583X(00)00044-6
- [4] M. Maekawa et al., Nucl. Inter. Methods B480(2020)49. DOI: 10.1016/j.nimb.2020.08.001

4 - 02 Beam energy control by the excitation current of the harmonic coil in the AVF cyclotron

N. Miyawaki ^{a)}, H. Kashiwagi ^{a)}, S. Watanabe ^{b)}, N. S. Ishioka ^{b)} and S. Kurashima ^{a)}

^{a)} Department of Advanced Quantum Beam Technology, QST

^{b)} Department of Quantum-Applied Biosciences, QST

Introduction

The beam energy control technology in the TIARA AVF cyclotron has been developed mainly for the production of ²¹¹At. The production rate of ²¹¹At increases with the energy of the He beam used to produce it, but at beam energy above 29 MeV, the isotope ²¹⁰At is produced and decays to the highly toxic nuclide ²¹⁰Po. Therefore, to maintain the high production rate of ²¹¹At without producing ²¹⁰Po, the energy of the beam accelerated by the cyclotron is required to be precisely controlled [1]. The adjustment of excitation current of harmonic coils in the injection region was the best method for controlling the beam energy because it could change the widest range of energy with the small reduction of beam intensity [2]. However, it was not clear why changes in beam energy occur due to the excitation current of the harmonic coils. Therefore, the correlation between the excitation current of the harmonic coil and the beam energy was investigated in this study.

Experiments and Calculations

As shown in Fig. 1, the harmonic coils are located in the valleys of the spiral sectors in the injection (CHI1-4) region and that of the extraction (CHE1-4) one, respectively. By exciting a set of two harmonic coils symmetrical to the cyclotron center, e.g., CHI1 and CHI3 (CHI13) in the injection region, with the opposite polarities of each other, the beam orbit center can be shifted perpendicularly to the direction of the CHI13 line. Combining this set with another set of CHI24 coils with the difference of 90-degree, the beam orbit center can be controlled in the beam rotation plane. The CHE13 and CHE24 coils in the extraction region can make the beam orbit center controlled similarly. The displacement and direction for the beam orbit center is controlled corresponding to the intensity and direction of the first harmonic magnetic field produced by the harmonic coil, respectively. The intensity and direction of the first harmonic magnetic field generated by the harmonic coils were calculated from the excitation current of the coils.

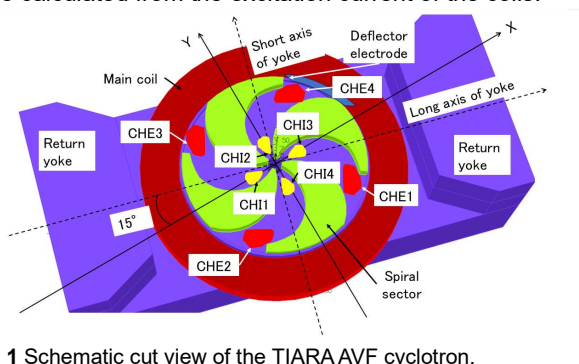


Fig. 1 Schematic cut view of the TIARA AVF cyclotron.

To extract the beam from the cyclotron, two sets of harmonic coils are usually adjusted for the injection region and the extraction region, respectively. The combination pattern of excitation currents of the harmonic coils that can extract the beam is approximately fixed, and the beam energy was measured at each combination.

Results and Discussion

Fig. 2 shows the intensity and direction of the first harmonic magnetic field calculated from the excitation current of the harmonic coils for each measured beam energy. The 0-degree direction in Figure 2 expressed in polar coordinates corresponds to the positive X-axis in Fig. 1, and the first harmonic magnetic field of 0 corresponds to the cyclotron center. From this figure, the correlation shows that the beam energy increases with decreasing intensity of the first harmonic magnetic field and increasing azimuthal angle for both the injection and the extraction region harmonic coils. The beam energy was increased by changing the intensity and direction of the first harmonic magnetic field away from the deflection electrodes. Previous studies have shown that the amount of change in the intensity of the first harmonic magnetic field corresponds to the displacement of the beam orbit center, and their directions also match. Therefore, the beam orbit center moves away from the deflector electrode as the beam energy increases. As the beam orbit center moves away from the deflector electrode, the number of turns to extraction increases and the number of beam accelerations increases, resulting in an increase in beam energy.

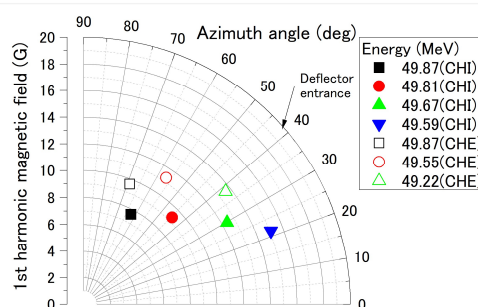


Fig. 2 Relationship between the first harmonic magnetic field intensity and its azimuth angle by the excitation current of the harmonic coil in the injection and extraction region for each measured beam energy.

References

- [1] Yutian Feng *et al.*, Nuclear Medicine and Biology 100-101, 12 (2021). DOI: 10.1016/j.nucmedbio.2021.05.007
- [2] N. Miyawaki *et al.*, QST Takasaki Annu. Rep. 2022, QST-M-47 97 (2023).

4 - 03 Characterization of microfabricated patterns coated with metals using micro-particle induced X-ray emission

S. Sada^{a)}, R. Ishida^{b)}, K. Kosumsupamala^{a)}, N. Puttaraksa^{b)}, Y. Ishii^{c)} and H. Nishikawa^{b)}

^{a)}Graduate School of Engineering and Science, Shibaura Institute of Technology,

^{b)}College of Engineering, Shibaura Institute of Technology

^{c)}Department of Advanced Quantum Beam Technology, QST

Introduction

Micro-particle induced X-ray emission (micro-PIXE) is an ion beam analysis technique to characterize the composition of samples chemically and spatially at the same time [1]. The different emitted X-ray energies from different elements lead to the fingerprint energy spectrum that allows us to identify its composition and map its microscopic location, namely elemental mapping. One of the most challenging global issues is the distribution of microplastics in our oceans. Naturally, it degrades and absorbs biotas and/or metals, making the investigation of microplastics' constituents more complicated. To approach this long-run problem systematically, a standard sample mimicking microplastics must be created and its contamination should be well-controllable. Hence, we investigated the fabrication of metal-coated microfabricated patterns with different methods and used the micro-PIXE system at TIARA for characterization.

Experimental

In this experiment, we developed two different metal deposition techniques on microfabricated patterns as artificial microplastics produced by proton beam writing (PBW) at Shibaura Institute of Technology (SIT). Firstly, the SU-8 resist was selected and fabricated by 1-MeV focused protons at SIT to be cylinder-shaped artificial microplastics. The SU-8 was spin-coated to a thickness $\sim 18 \mu\text{m}$ on silicon (Si) wafers before being irradiated by PBW at a fluence of 100 nC/mm^2 with the design of $25 \mu\text{m}$ diameter microcylinder arrays.

To represent the metal adsorption on the environmental microplastics, the irradiated SU-8 samples were subsequently coated with metals. In the first deposition technique, the magnetron sputtering was used to create a 150 nm Au layer on the samples after the development process. For the second deposition technique, the irradiated SU-8 samples were coated by the thermal evaporation of aluminum (Al) before the development process to obtain an Al thickness of 139 nm.

The micro-PIXE measurements were executed at TIARA with the proton energy of 1 MeV to obtain elemental mapping of the samples.

Results and Discussion

Figure 1 (a) illustrates the micro-PIXE spectrum of the Au sample and (b) elemental mapping of the Au $M\alpha$ signals. While Fig1. (a) the Au $M\alpha$ peaks can be significantly observed, Fig1.(b) shows that Au is distributed over the

whole area, this result is consistent with SEM observations. Accordingly, the areal density of metal (Au) may not be determined accurately for quantitative PIXE analysis.

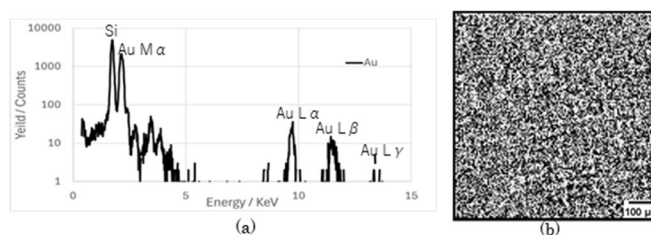


Fig. 1 (a) PIXE spectrum and (b) $800 \mu\text{m} \times 800 \mu\text{m}$ Au $M\alpha$ elemental map of Au sample

Figure 2 (a) illustrates the micro-PIXE spectrum of the Al sample. In Fig.2 (a) the Al $K\alpha$ peak is less significant and in the proximity of the Si $K\alpha$ peaks. Hence the mapping of Al is hard, and Si $K\alpha$ map was taken instead in Fig.2 (b) where the dark spots are created by the microfabricated SU-8 patterns that block the Si $K\alpha$ signal. From SEM observation, Al is coated only on the surface of the pattern.

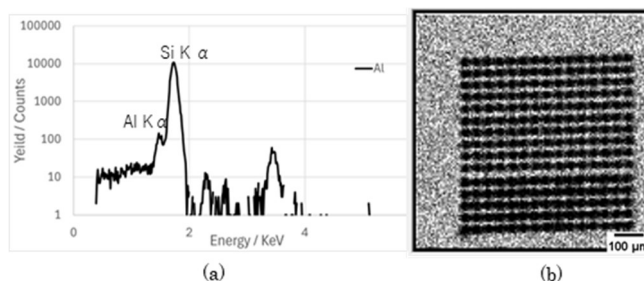


Fig. 2 (a) PIXE spectrum and (b) $800 \mu\text{m} \times 800 \mu\text{m}$ Si $K\alpha$ elemental map of Al samples

From Fig.1 (a) and Fig.2 (a), the statistic of the Au $M\alpha$ signal for 150 nm Au layer is better than the Al $K\alpha$ signal for 139 nm Al layer. However, Fig.1 (b) shows that the first deposition method cannot define the areal density of metals on the pattern. Nevertheless, SEM observation shows that the second method can define areal density of metals on the patterns. This proves the potential applications of this method to create standard samples for PIXE measurements of metal-adsorbed microplastics in the future.

Reference

- [1] K. Ishii, PIXE and Its Applications to Elemental Analysis. *Quantum Beam Sci.* **3**, 12 (2019). DOI: 10.3390/qbs3020012

4 - 04

Improvements in the beam observation system of hundreds of MeV heavy ion microbeam line in TIARA

H. Kashiwagi ^{a)}, R. Yamagata ^{a)}, N. Yamada ^{b)} and N. Miyawaki ^{a)}

^{a)} Department of Advanced Quantum Beam Technology, QST

^{b)} Beam Operation Co., Ltd.

Introduction

At the TIARA AVF cyclotron, high-energy heavy ion microbeams of several hundred MeV [1] have been utilized for the study of irradiation effects in microscopic regions in biological research and semiconductor research. The formation of microbeams requires precise control, involving the positioning, shaping, and focusing of beams from an initial size in the centimeter range down to several microns. The formation process often took over 5 to 7 hours, depending on the beam characteristics. However, since the daily operation of the cyclotron started in 2021, it has become crucial to complete the microbeam formation and provide beams to users within 8-hour operation hours. Therefore, we have been working on reducing the time required for microbeam formation by improving the equipment and software. Among various modifications, this paper focuses on the improvements in the beam observation system.

Microbeam line

Figure 1 shows the microbeam system installed in the HX beamline. A few hundred MeV heavy ion beam extracted from the cyclotron is transported through a horizontal beamline and directed into the vertical HX beamline by a bending magnet. A beam with a tiny emittance is precisely shaped through the object slits and the divergence-defining slits that restrict the beam position and the divergence angle, respectively. This beam is then focused to the micron order by a quadruplet of quadrupole magnets. A beam shifter is installed before the object slit to align the beam axis with the magnetic center axis of the quadruplet of quadrupole magnets.

Improvements to the beam observation system

In the microbeam formation tuning, it is necessary to maximize the intensity of the beam shaped by the object slits and the divergence-defining slits. The tuning was performed by observing the fluorescence from the scintillator (CaF₂(EU)) installed just under each slit using composite video cameras. This process required visual assessment of the approximate beam position and intensity by viewing the images on the monitor. Additionally, after the divergence-defining slit, the beam often passes outside the scintillator, resulting in significant time required to adjust its position with the beam shifter due to the unclear beam position. To address these issues, the scintillators and their holders were replaced with new ones, expanding the effective areas of the scintillators from 8 mm square to 28 mm square, thereby increasing the beam detection areas by more than ten times. The cameras were replaced with

CMOS models to capture the beam position and intensity as digital data.

Furthermore, to observe the scintillators under the object slits, where beam position is particularly important, a telecentric lens was used with the camera to minimize image distortion (Fig. 2). A camera tilt mechanism was adopted to adjust the angle of the camera's image plane relative to the lens optical axis, ensuring the entire scintillator surface is in focus even when observed obliquely at a 45-degree angle, based on the Scheimpflug principle. Additionally, a measurement program for the digital camera images was developed to represent beam intensity variations with color changes and to acquire and save the beam's central coordinates. As a result, beam alignment upstream of the quadrupole magnets has been achieved with simple adjustments to match the beam center coordinates to the pre-recorded coordinates, reducing the adjustment time by approximately one hour.

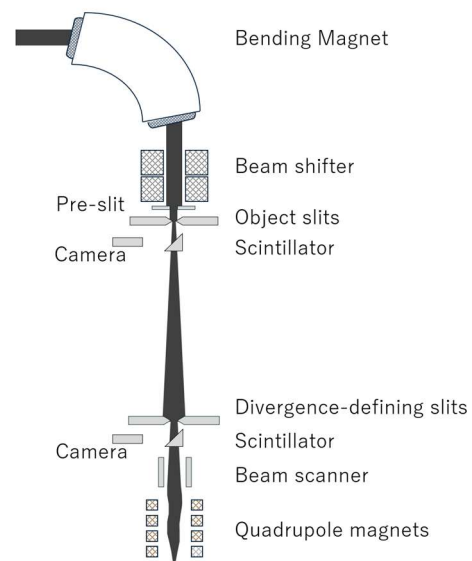


Fig. 1 HX beamline with the microbeam system



Fig. 2 Telecentric lens (left) and camera tilt unit (right)

Reference

- [1] M. Oikawa *et al.*, Nuclear Instruments and Methods in Physics Research B 260 (2007) 85–90. DOI: 10.1016/j.nimb.2007.01.280

4 - 05 Improvement of the heavy-ion microbeam system

Y. Ishii^{a)}, R. Yamagata^{a)}, T. Satoh^{a)}, S. Matsuyama^{b)}, S. Onoda^{c)} and Y. Saitoh^{a)}

^{a)}Quantum Materials and Applications Research Center, QST

^{b)}Department of Physics, Osaka University

1. Introduction

The heavy-ion microbeam system linked to the tandem accelerator at TIARA was improved last fiscal year in order to produce a submicron ion beam, whose system is hereinafter referred to “improved H-MB”. The previous H-MB[1] was used for many studies and made a lot of excellent results[2][3]. However, the demagnification of previous H-MB was insufficient to produce submicron ion beams. In addition, many components of the previous H-MB worked insufficiently because of aging. Therefore, the H-MB was almost totally improved with new developed 4 quadrupole magnets. In this paper, the brief overview of the improvement was reported with the beam size simulated using two quadrupole magnets (doublet).

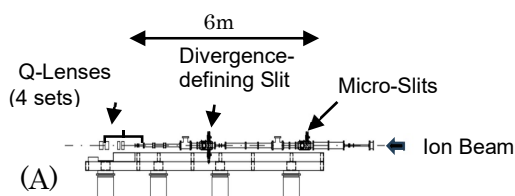


Fig. 1 Schematic of the new H-MB

2. The improved H-MB

The schematic view of the improved H-MB (A) and the photograph (B) are shown in Fig.1. The main improvement of the improved H-MB was carried out as follows:

- The length of the H-MB was lengthened from about 4 m to 6 m.
- The quadrupole magnets, placed on a linear guideway, were redeveloped, whose number was increased from 2 to 4.

The length and the magnets lead to the larger demagnification and the flexible magnet combination, respectively. Specifically, in the later, the configuration of magnets can be changed with doublet, triplet and two-stage doublets. In the current configuration, the doublet is used for a preliminary microbeam formation with the adjustment of the magnets easy.

The polarity change switches for the quadrupole magnets were installed in the system to make the alignment of the

quadruple magnets easy. In addition, the auto beam focusing system using a PC code was also installed in the system to form a microbeam in a short time.

3. Simulation result of beam size based on the improvement

The simulation result of the improvement is shown Tabel 2 as well as Tabel 1 of the previous H-MB. The demagnifications of X and Y are increased from 4.6 and 28 to 53 and 19, respectively. Therefore, beam size is reduced from $1 \times 1 \mu\text{m}^2$ to $0.44 \times 0.49 \mu\text{m}^2$, respectively, when a 15 MeV Ni ion beam was provide to the system from the Tandem accelerator. The beam size is satisfied to form the submicron beam using the double in the preliminary study. In the future, the magnet configuration can be changed with the triplet or the two-stage double to form mare small beam size.

Table1 The specification of the previous H-MB

Previous System			
Direction	Beam Energy (MeV)	Demagnification	Calculated Beam Size (μm)
X	15 (Ni)	$\langle x x_0 \rangle = 4.6$	1.0
Y		$\langle y y_0 \rangle = 28$	1.0

Table 2 The specifications of the improved H-MB

Improved system (Doublet)				
Beam Energy (MeV)	Object Size (μm)	Demagnification	Divergence Defining Slit (μm)	Calculated Bam Size (μm)
15	25	$\langle x x_0 \rangle = 53.19$	$dx = 250$	0.4
	10	$\langle y y_0 \rangle = 19.23$	$dy = 100$	0.5

The formation of ion microbeam has been performed with 15 MeV Si^{3+} ion beam since last fiscal year.

Acknowledgments

Thanks are extended to N. Yamada and M. Koka from Beam Operation Co. Ltd for their extensive technical support.

References

- [1] R. Tanaka, etl all, Nucl. Instr. Meth. Sect. B 79 432 (1993).
- [2] T. Kamiya, et. all. Nucl. Instr. Meth. Sect. B 158 1 (1999)
- [3] J.S. Laird, et all. Nucl. Instr. Meth. Sect. B 181 87 (2001)

4 - 06 Carbon sputtering yield by fullerene-ion bombardment

K. Narumi^{a)}, K. Yamada^{a)}, Y. Hirano^{a)}, A. Chiba^{a)} and Y. Saitoh^{b)}

^{a)}Department of Advanced Quantum Beam Technology, QST

^{b)}Department of Innovation Strategy, QST

Introduction

When a solid target is bombarded with a C_{60} ion, its constituent ions or atoms simultaneously collide with many target atoms in a small space. This induces a lot of phenomena characteristic of C_{60} -ion bombardment: It is well known that huge sputtering is one of such phenomena. In our previous report [1], we reported carbon sputtering yields induced by 0.03-to-6-MeV C_{60} -ion bombardment due to two objectives: systematic measurement of sputtering yields by C_{60} ions and evaluation of nonlinear effect on sputtering yields. For the former, practical data on fundamental processes relating to ion stopping in solid are indispensable for application use of C_{60} -ion beams; however, there are not enough data on C_{60} ions up to the present. Sputtering is closely related to C_{60} -ion stopping in solid. Thus, we have been focusing on sputtering by C_{60} ions and measured sputtering yields systematically [2, 3]. Concerning the latter, on the other hand, it is well known that nonlinear effect on sputtering by cluster/molecular-ion bombardment is observed [4], *i.e.*, the sputtering yield is not proportional to the number of the constitutional atoms. We have observed the effect on the Au sputtering yield by C_{60} - and C_{70} -ion bombardment [3].

In the present report, we add data by 0.07-to-7-MeV C_{70} -ion bombardment to the previous ones and discuss the whole results again.

Experimental

Carbon sputtering yields were measured with a quartz-crystal microbalance technique. A target carbon film was deposited on an Au electrode of a quartz crystal with resistive heating. The film was conductive and 300-nm thick. C_{60} and C_{70} ions were accelerated to 0.03 to 1.08 MeV and to 1.08 to 7 MeV with the 400-kV ion implanter and the 3-MV tandem accelerator of TIARA, respectively [5]. Sputtering yields by 18-to-100-keV C^+ ions were also measured for comparison.

Results and Discussion

Measured carbon sputtering yields are shown in Fig. 1. It should be noted that the abscissa and ordinate represent ion energy per atom and the sputtering yield per atom, respectively. As obvious in the figure, dependence of the sputtering yield per atom on the energy per atom is almost the same for C, C_{60} and C_{70} ions. This indicates that the sputtering yield by C_{60} and C_{70} ions is 60 and 70 times as high as that by monatomic C ions, respectively, *i.e.*, nonlinear effect on the sputtering yield was not observed.

The measured sputtering yields were compared with those obtained with Monte Carlo simulation using the

SRIM2008 code [6]. In the simulation, the target was assumed to be graphite: the lattice binding energy, the surface binding energy and the displacement energy were 3.0 eV, 7.41 eV and 28.0 eV, respectively. The measured sputtering yields are much higher than those obtained with the simulation. In addition, energy dependence of the measured sputtering yield is different from that of the simulation. As known well, the SRIM2008 code takes only the contribution of nuclear collisions into account; thus, the obtained sputtering yields are induced by collisional sputtering. Therefore, the obvious difference between the measured and simulated sputtering yields indicates that the measured sputtering yields are not attributed to collisional sputtering. It should be noted that this is not the case only for C_{60} and C_{70} ions, but also for C ions. Further investigation is necessary for discussion on the origin of carbon sputtering.

Acknowledgments

The authors are grateful to Dr. Hiroshi Amekura for the preparation of carbon films. This work was supported in part by JSPS KAKENHI Grant Number JP18K05005.

References

- [1] K. Narumi *et al.*, QST Takasaki Annu. Rep. 2022, **QST-M-47** 95 (2024).
- [2] K. Narumi *et al.*, Quantum Beam Science, **6** 12 (2022). DOI: 10.3390/qubs6010012
- [3] K. Narumi *et al.*, QST Takasaki Annu. Rep. 2021, **QST-M-39** 106 (2022).
- [4] H.H. Andersen and H.L. Bay, Radiat. Effects, **19** 139 (1973). DOI: 10.1080/00337577308232233
- [5] A. Chiba *et al.*, Quantum Beam Science, **4** 13 (2020). DOI: 10.3390/qubs4010013
- [6] Available online: <http://www.srim.org>.

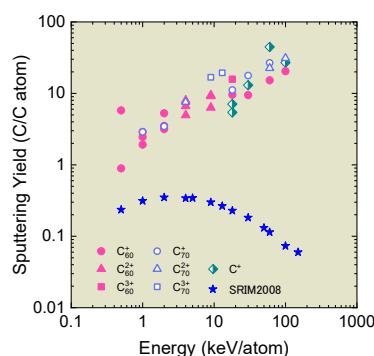


Fig. 1 Dependence of the sputtering yield per atom on energy per atom. Results by the SRIM2008 code are also shown.

4 - 07

Study of radiation resistance of Coal Ash Fiber (BASHFIBER®) using Positron Annihilation method, etc.

Y. Murakami ^{a)}, K. Sekine ^{a)} H. Fukazawa ^{a)}, M. Maekawa ^{b)} and A. Kawasuso ^{b)}

^{a)}Nippon Fiber Corporation

^{b)} Department of Advanced Quantum Beam Technology, QST

Introduction

Nippon Fiber Co. has succeeded in multi-winding of continuous long fiber BASHFIBER®, which is mainly made from coal ash (fly ash) exhausted from thermal power plants. Major advantages of BASHFIBER® are its superior heat and radiation resistance in compared with the conventional glass fiber. Utilizing these characteristics, we invented BASHFIBER US® as a novel shielding material for thermal neutrons with a Gd solid solution. Moreover, we also succeeded in its multi-winding (Fig.1) using a spinning equipment built at the QST Takasaki institute.



Fig. 1 BASHFIBER® and BASHFIBER US®

To produce higher performance fibers, we have investigated the physical properties of BASHFIBER® and BASHFIBER US® using several spectroscopic methods, such as the positron annihilation techniques. In addition, from a fundamental viewpoint, we have also studied simple silicate glasses containing Fe, Gd, and other metallic elements in solid solution. This report presents our recent findings for the Fe addition to E-glass, which is the most common composition of glass fiber.

Experimental

The composition of E-glass was simplified to a four-component system (SiO_2 , Al_2O_3 , CaO , B_2O_3), and samples were prepared by adding 0, 5, 10, 15, or 20 wt% Fe_2O_3 to the composition. The reagent mixture was placed in an alumina crucible, held at 1500°C for 2 hours in an electric furnace, and poured out onto a carbon table for rapid cooling to obtain the amorphous material. Although a wide range of concentrations was tested, the sample with 20 wt% Fe_2O_3 was excluded due to the detection of phase separation via X-ray diffraction measurements.

These samples were irradiated with 500 MGy of 2 MeV electrons using the electron accelerator at the QST Takasaki institute. Subsequently, these samples were subjected to positron annihilation lifetime measurements employing the anti-coincidence method [1] with a $^{22}\text{NaCl}$ source. Raman spectroscopy measurements were also performed using a micro-Raman spectrometer with a 448 nm laser at a power of 0.5 mW.

Results and Discussion

[Positron annihilation lifetime spectroscopy (PALS)]

As shown in Fig.2., in the low Fe_2O_3 concentration region, the intensity of the long-lived component originating from the microvoids is reduced by the electron irradiation. This suggests that new types of the positron trapping site are generated by the electron irradiation and act as the competing centers for the microvoids.

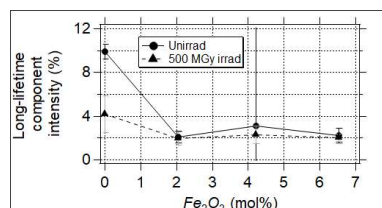


Fig. 2 Comparison of PALS long-time component intensities

[Raman spectroscopy]

By the Gaussian function fitting, the 700 cm^{-1} peak and the $900\sim 950\text{ cm}^{-1}$ peak are identified, which are attributed to the Fe_3O_4 microcrystalline and the Fe-O bonding incorporated into the SiO_2 network, respectively [2].

Figure 3 shows the Fe_2O_3 concentration dependence of the area intensity of the Raman shifts. This result suggests that Fe atoms preferentially penetrate the SiO_2 network at the lower Fe_2O_3 concentrations, however, as increasing the concentration, they gradually grow into Fe_3O_4 microcrystals. Before and after electron irradiation, the Raman spectra were rarely changed unlike the positron measurements.

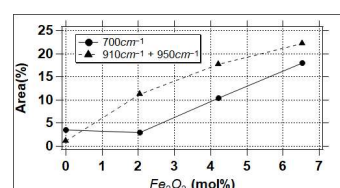


Fig. 3 Comparison of Raman shift peaks

We have just started the detailed study to clarify this difference focusing on this lower concentration region.

Acknowledgments

We would like to express our gratitude to Dr. Sakai in QST Takasaki for kindly lending us the Raman spectrometer.

References

- [1] M. Yamawaki *et al.*, Jpn. J. Appl. Phys. 50, 086301 (2011). DOI:10.1143/JJAP.50.086301
- [2] M. T. Nayak *et al.*, Journal of Raman spectroscopy Vol.49, 1507 (2018). DOI: 10.1002/jrs.5397

K. Enomoto ^{a)}, Y. Nagao ^{a,b)}, T. Yabe ^{a)}, M. Tsuda ^{a)}, M. Yamaguchi ^{a)}, S. Yamasaki ^{b)}, S. Kano ^{c)}, N. Nagasawa ^{b)} and N. Kawachi ^{a)}

^{a)} Department of Quantum-Applied Biosciences, QST

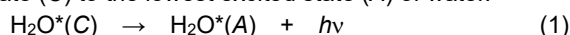
^{b)} Department of Advanced Quantum Beam Technology, QST

^{c)} Takasaki Establishment, Radiation Application Development Association

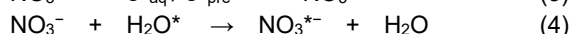
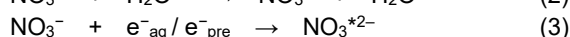
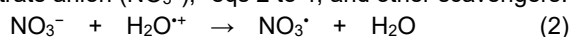
Introduction

Charged particles (electrons, protons, and carbon ions, etc.) traveling through liquid water at speeds below the velocity of light in the medium induce weak luminescence.¹ The mechanism of this luminescence would involve both chemical and physical processes corresponding to incident energies ranging from eV to MeV; however, it remains unclear. Herein, we reveal the source of the luminescence through chemical processes at 245 keV electrons, below the Cherenkov light threshold (261 keV) in the liquid water.

The radiolysis of liquid water generates several excited and ionized states of the water, such as excited states (H_2O^*), radical cation ($\text{H}_2\text{O}^{+\bullet}$), hydrated electron (e^-_{aq}) and its precursor (e^-_{pre}). The luminescence source is tentatively associated with a radiative transition from a superexcited state (C) to the lowest excited state (A) of water.²



However, the quenching of the excited state responsible for the luminescence is not verified experimentally. The H_2O^* is expected to be the source of luminescence by eq 1; therefore, a decrease in luminescence intensity would be observed if the H_2O^* and its precursor are quenched by nitrate anion (NO_3^-),³ eqs 2 to 4, and other scavengers.



To identify the source, we examine the scavenging of the precursors to luminescence in liquid water in the presence of sodium nitrate (NaNO_3) at 245 keV electrons.

Experimental

Electron-beam irradiation (0.5 MeV, 0.1 mA) of the water phantom was carried out using an electron accelerator at QST Takasaki (Fig. 1a). Previous studies have shown that luminescence from water with an irradiation of 245 keV electrons is not detectable with a CCD camera, likely due to the camera's low sensitivity to wavelengths below 400 nm. We therefore detected visible fluorescence via

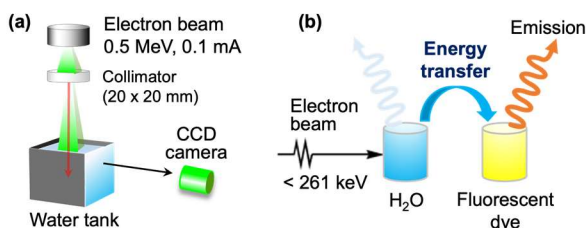


Fig. 1 (a) Experimental setup, and the CCD detection system; (b) Schematic image of a luminescence energy transfer to an acceptor dye under electron-beam irradiation.

luminescence energy transfer to an acceptor dye used as wavelength shifter (Fig. 1b). The water phantom was used to the aqueous NaNO_3 solutions in the concentration range 0.1 to 500 mM, with 50 μM of uranine or rhodamine B as the dye. During electron beam irradiation of the phantom, fluorescence imaging was performed with the CCD camera for 60 seconds and subsequently analyzed by ImageJ.

Results and Discussion

Use of 50 μM of aqueous rhodamine B without NaNO_3 quencher enabled a clear fluorescence image around the water surface, corresponding to the energy deposition by the electrons (Fig. 2a). A similar result was obtained with uranine dye. In addition to the NaNO_3 quencher and dyes, the fluorescence was quenched with increasing of NO_3^- concentration (Fig. 2b). This decrease suggests that the existence of H_2O^* production contributes to the fluorescence through a chemical process. However, fluorescence intensity was not completely suppressed even at very high NO_3^- concentration, ignoring any scavenging of H_2O^* , $\text{H}_2\text{O}^{+\bullet}$, e^-_{aq} , and e^-_{pre} . The remaining fluorescence may arise from a physical process, such as polariton-assisted phase matching.¹

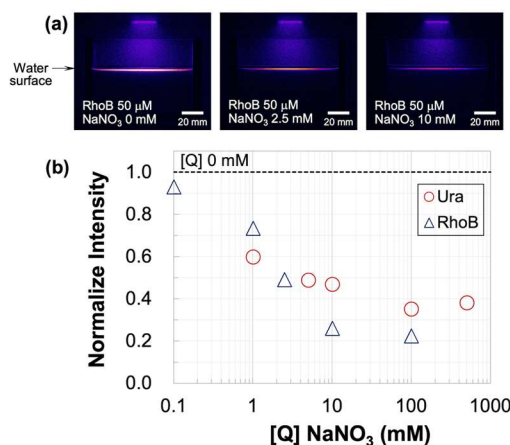


Fig. 2 (a) Electron-stimulated luminescence images of the water phantom with an irradiation of 245 keV electrons for 60 s; (b) The luminescence intensity as a function of NaNO_3 concentration: 50 μM uranine (\circ), 50 μM rhodamine B (\triangle).

References

- [1] S. Yamamoto, Radiol. Phys. Technol. **14**, 16 (2021). DOI: 10.1007/s12194-020-00588-x
- [2] V. Engel *et al.*, J. Chem. Phys. **87**, 4310 (1987). DOI: 10.1063/1.452889
- [3] G. P. Horne *et al.*, J. Phys. Chem. B **121** 5385 (2017). DOI: 10.1021/acs.jpcc.7b02775

4 - 09 ESR measurement of carbonated hydroxyapatite for dosimeter

H. Seito ^{a)}, E. Yokozuka ^{a)}, T. Oka ^{b)}, Y. Kitatsuji ^{b)} and N. Nagasawa ^{a)}

^{a)} Department of Advanced Quantum Beam Technology, QST

^{b)} Nuclear Science and Engineering Center, JAEA

Introduction

Radiation dosimeters are devices used to measure exposure to ionizing radiation such as X-rays, gamma-rays, and electron beams. However existing dosimeters have limited measurement dose ranges, must be periodically calibrated, and require expensive processing. Consequently, more than one device type may need to be used together. To address these issues, we have examined dosimetric characteristics of carbonate hydroxyapatite (CO₃HAp), which is a dental bone graft material. The irradiation of tooth generates stable radicals in the enamel, which is useful for measuring irradiation dose in calcified tissues like tooth enamel by detecting the concentration of radiation-induced stable carbonate radicals in the enamel [1]. The purpose of this work is to investigate the reproducibility and stability of radiation-induced radicals on CO₃HAp samples and assess the feasibility of using these materials as dosimeters.

Experimental

CO₃HAp samples were exposed to gamma-rays with radiation doses ranging from 10 Gy to 1000 Gy at room temperature. Irradiation was performed using ⁶⁰Co gamma-ray field which provides a dose rate of 4.15 Gy/min at the Takasaki Institute for Advanced Quantum Science, QST. Each group of CO₃HAp samples was irradiated, being placed into plastic tube. A 3-mm-thick polymethylmethacrylate plate was placed in front of the samples to provide the buildup of secondary electrons. The electron spin resonance (ESR) spectra for irradiated samples were measured by a model ESR spectrometer (JES-FA200, JEOL, Tokyo, Japan) under the conditions of a microwave power of 2 mW, a sweep width of ± 5 mT, a modulation width of 0.2 mT, a time constant of 0.03 seconds, and a sweep time of 30 seconds. The samples were measured immediately after irradiation at room temperature and subsequently measured at time of 1, 2, 3, 4, 7, 8, 15 and 40 days after irradiation. The ESR signal of dose determinations for this study was obtained by measurement of the peak-to-peak intensities.

Results and Discussion

Figure 1 shows the changing of ESR signal intensity in different time repeatedly. The ESR intensity decreases enormously with aging time in any dose, and the intensity approached a constant after 15 days. This quantitative changes in speed differs between different doses. The absorbed dose value is higher, the intensity decreases more sharply. The changes decreased 18 ± 5 % for dose

less than 300 Gy, whereas the changes decreased 25 ± 5 % for dose more than 500 Gy. These results suggest that the time of 15 days after irradiation or later is recommended for the standard storage time for the measurement of ESR signal intensity of CO₃HAp from the practical point of view.

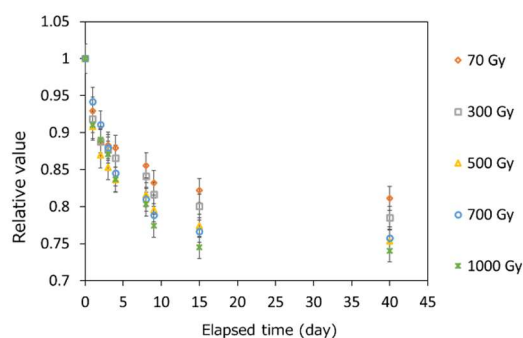


Fig. 1 Stability of ESR intensity of CO₃HAp irradiated at 70, 300, 500, 700 and 1000 Gy.

Figure 2 shows the signal intensity variation of the CO₃HAp samples compared to alanine dosimeter samples as functions of absorbed dose values. Both of dose response curves have a linear ESR signal intensity with dose up to ~ 10000 Gy. The slope of dose response curve for CO₃HAp is 5.0, which is almost comparable to that for alanine of 5.1. As shown in Figure 2, variation in ESR intensity of CO₃HAp relative to the absorbed dose closely resembles that of the alanine dosimeter [2]. These results reinforce the CO₃HAp may be a base material for chemical dosimeters.

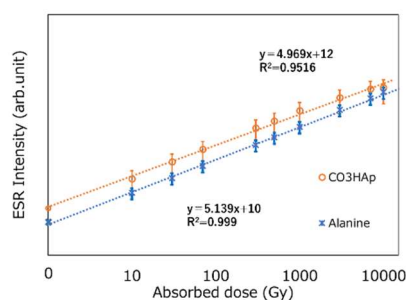


Fig. 2 Dose response curves for CO₃HAp (orange dashed line) and alanine (blue dashed line).

Acknowledgments

We would like to express our gratitude to Mr. Yamanaka (GC Corporation) for providing samples.

References

- [1] T. Oka *et al.*, Radiat. Meas. 134, 106315 (2020). DOI: 10.1016/j.radmeas.2020.106315
- [2] H. Seito *et al.*, Radiat. Prot. Dosim. accepted, (2024).

Effect of polyacrylic acid on remineralization of demineralized dentin

Y. Matsuda ^{a)}, K. Okuyama ^{b)}, H. Yamamoto ^{c)}, M. Sakurai ^{b)}, K. Naito ^{c)}, H. Kanda ^{c)}, T. Saito ^{b)}, M. Hayashi ^{c)}, Y. Tamaki ^{a)}, T. Sato ^{d)}, N. Yamada ^{d)} and R. Yamagata ^{d)}

^{a)} School of Dentistry, Health Sciences University of Hokkaido,

^{b)} Asahi University School of Dentistry,

^{c)} Graduate School of Dentistry, Osaka University,

^{d)} Department of Advanced Quantum Beam Technology, QST

Introduction

Remineralisation in dentin involves not only the classical pathway with hydroxyapatite (HAP) crystals as nuclei, but also collagen-centred interfibrillar calcification. Some organic acids promote not only demineralization but also crystallization [1]. We discovered that polyacrylic acid (PAA) plays a crucial role in regulating interfibrillar calcification, and its ability to protect collagen fibers and suppress HAP demineralization is vital in preventing dentin caries. Similarly, zinc's role in inhibiting MMPs, protecting collagen, and promoting calcification is not to be overlooked. Our investigation into the remineralization of collagen in PAA-decalcified dentin using the in-air microbeam proton-induced X-ray/ γ -ray emission (PIXE/PIGE) method, which allows elemental analysis in air, has shed new light on this complex process.

MATERIALS AND METHODS

Bovine extracted from mandibular premolars (n=5) was cut into 300 μ m thick specimens perpendicular to the tooth axis using a low-speed rotary cutter (IsoMet, Buehler; diamond blade). The specimens were then immersed in a solution of 10% polyacrylic acid (polyacrylic acid 2500, Fujifilm Wako Pure Chemicals) (PAA) and 10% lactic acid (special grade lactic acid, Fujifilm Wako Pure Chemicals) (Lac) for 72 hours at 37°C to prepare demineralized bovine tooth dentin samples. The dentin samples were pre-mineralized by immersion in 1% zinc chloride solution (ZnCl) as the material group and deionized distilled water (DDW) as the control group for 24 hours at 37°C. The specimens were then remineralized by immersion in the solution for one week at 37°C. Samples were prepared by the above method for each material group (PAA-DDW-DDW group, Lac-DDW-DDW group, PAA-DDW-Re group, Lac-DDW-Re group, PAA-ZnCl-Re group, and Lac-ZnCl-Re group) by the combination of demineralization, pretreatment, and remineralization treatments. Each sample's calcium and zinc uptake was analyzed for elemental abundance using the In-air Micro PIXE/PIGE method. Statistical analysis of elemental concentrations in the samples was performed using SPSS Statistics version 29 (IBM et al., USA) with one-way ANOVA and Tukey HSD at a significance level of 5%.

Results and Discussion

Fig.1 and Fig.2 show Calcium and Zinc intake in demineralized dentin. The Lac-ZnCl-Re group was not significantly different from the control group (PAA-DDW-DDW, Lac-DDW-DDW) in the amount of calcium in demineralized dentin by the in-air micro PIXE/PIGE method. The PAA-DDW-Re and Lac-DDW-Re groups showed a significant increase in calcium compared to the control group. In contrast, the PAA-ZnCl-Re group showed a significant increase in calcium compared to the PAA-DDW-Re and Lac-DDW-Re groups. In addition, the PAA-ZnCl-Re group showed a higher uptake of zinc than the PAA-DDW-Re and Lac-DDW-Re groups in terms of the uptake of each element.

These results suggest that polyacrylic acid promotes zinc uptake, calcium uptake, and remineralization in demineralized dentin.

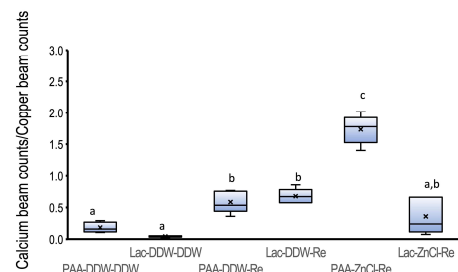


Fig. 1. Calcium beam count in demineralized dentin. Same letters indicate no significant differences ($p > 0.05$).

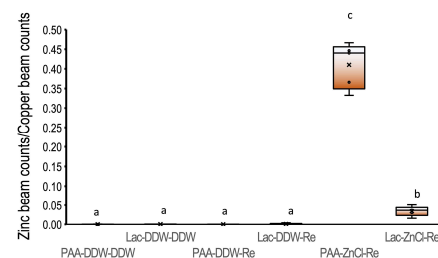


Fig. 2. Zinc beam count in demineralized dentin. Same letters indicate no significant differences ($p > 0.05$).

Reference

[1] Oguma, H.; Matsuda, Y.; et al. *Materials* **2023**, *16*, 1454. <https://doi.org/10.3390/ma16041454>

Part II

5. Status of Quantum-Beam Facilities

5-01	Utilization status at the TIARA facility	77
	H. Hanaya, I. Ishibori, S. Watanabe, N. Kubota, T. Shimizu and S. Kaneya	
5-02	Operation of the AVF cyclotron	78
	K. Yoshida, T. Yuyama, T. Ishizaka, S. Hosoya, I. Ishibori, N. Miyawaki, H. Kashiwagi, Y. Yuri, T. Nara, K. Takano H. Saitoh and S. Kurashima	
5-03	Operation of electrostatic accelerators in TIARA	79
	A. Chiba, K. Yamada, Y. Hirano, R. Suganuma, S. Kanai, Y. Aoki, M. Hashizume and S. Kurashima	
5-04	Operation, maintenance and utilization status of the gamma-ray irradiation facilities	80
	Y. Nagao, E. Yokozuka, H. Seito, M. Takagi, N. Yagi, T. Agematsu, S. Yamasaki and N. Nagasawa	
5-05	Operation, maintenance and utilization status of the electron accelerator	81
	S. Yamasaki, E. Yokozuka, S. Kano, M. Takagi, N. Yagi, T. Agematsu, Y. Nagao, H. Seito and N. Nagasawa	
5-06	Radiation monitoring in QST Takasaki.....	82
	Department of Administrative Services, QST	
5-07	Radioactive waste management in TIARA	83
	N. Higuchi, K. Iida, H. Hanaya and S. Watanabe	
5-08	The Shared Use Program of QST facilities in Takasaki	84
	S. Nozawa, H. Hanaya and A. Shimada	

5-01

Utilization status at the TIARA facility

H. Hanaya^{a)}, I. Ishibori^{a)}, S. Watanabe^{a)}
 N. Kubota^{a)}, T. Shimizu^{b)} and S. Kaneya^{c)}

^{a)}Department of Advanced Quantum Beam Technology, QST,

^{b)}Takasaki Establishment, Radiation Application Development Association

^{c)}Beam Operation Co., Ltd.

Four kinds of accelerators, a cyclotron and three electrostatic accelerators (tandem accelerator, single-ended accelerator and an ion implanter), are used at the TIARA facility to meet various researchers' needs. The activities of research fields that the cyclotron was used for the past 5 fiscal years are shown in Fig. 1. Total utilization time of each fiscal year (FY) was in the range of 379 to 1,280 hours. The utilization time of FY 2021 and FY 2022 was lower than FY 2019 and FY 2020 because of changing of the cyclotron daily operating time from 24 hours to 14 hours. And also, the utilization time of FY 2023 was lower than the other fiscal years because the operation time was decreased under the influence of the rising energy costs. The utilization time of "Life Science" and "Material Science" accounted for more than about 70% of the total time.

On the other hand, for the three electrostatic accelerators, as shown in Fig. 2, the utilization time of "Material Science" and "Basic Technology of Quantum Beam" accounted for more than about 60% of the total time. Total utilization time of each fiscal year was in the range of 330 to 430 days.

The trend of the number of project category (Internal use, Joint research, Cooperation priority research, and Facility use program) for the past 5 years is shown in Fig. 3. The total number of projects was in the range of 59 to 73 per year.

The trend of the number of users in the past 5 years is shown in Fig. 4. The total number of users was in the range of 286 to 665 per year.

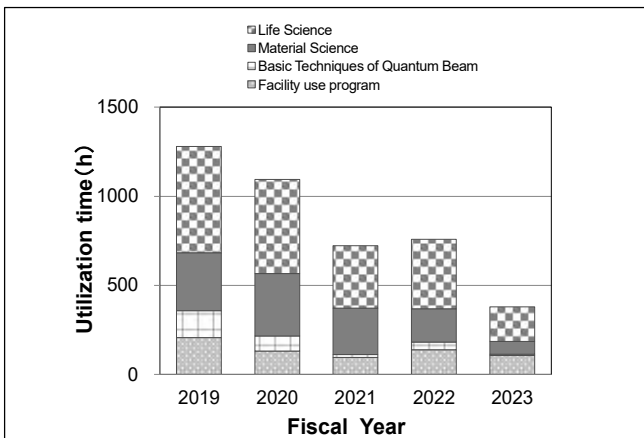


Fig. 1. Research activities for the cyclotron for the past 5 years.

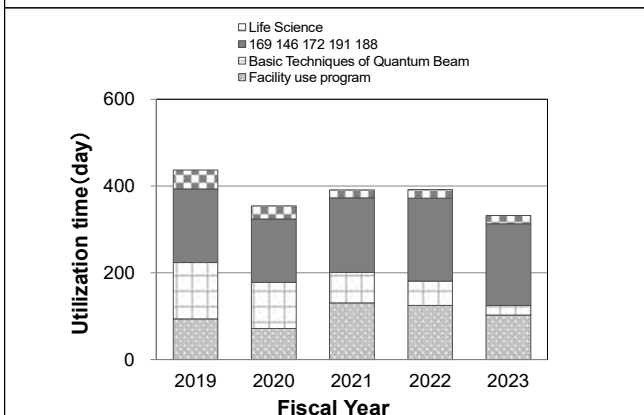


Fig. 2. Research activities for the three electrostatic accelerators for the past 5 years.

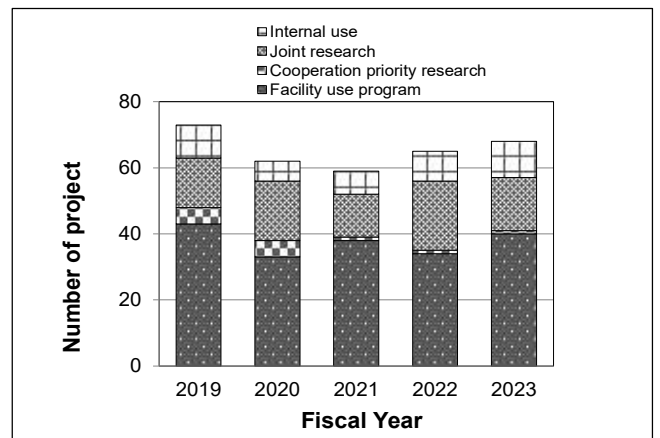


Fig. 3. The number of projects for the past 5 years.

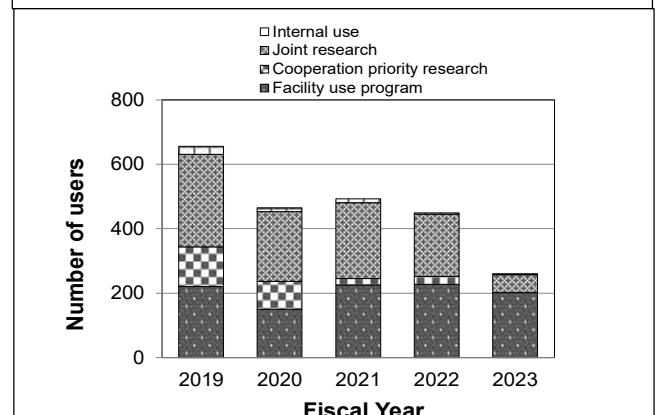


Fig. 4. The number of users for the past 5 years.

5-02

Operation of the AVF cyclotron

K. Yoshida, T. Yuyama, T. Ishizaka, S. Hosoya, I. Ishibori, N. Miyawaki,
H. Kashiwagi, Y. Yuri, T. Nara, K. Takano, H. Saitoh, S. Kurashima

Department of Advanced Quantum Beam Technology, QST

Operation

In fiscal 2023, The operation time of the AVF cyclotron was considerably reduced due to the high electricity costs since last year. The initial operation period was only one month, avoiding summer and winter seasons that require a lot of electricity for air conditioning. However, the operation period was extended to four months because an additional budget was approved and some users paid all the cost for cyclotron operation.

The total operation time of the AVF cyclotron eventually limited to 656h, and the number of experiments of the year was 86. The accumulative operation time was 90715h and the total number of experiments was 12933 from the first beam extraction in 1991 to March, 2024

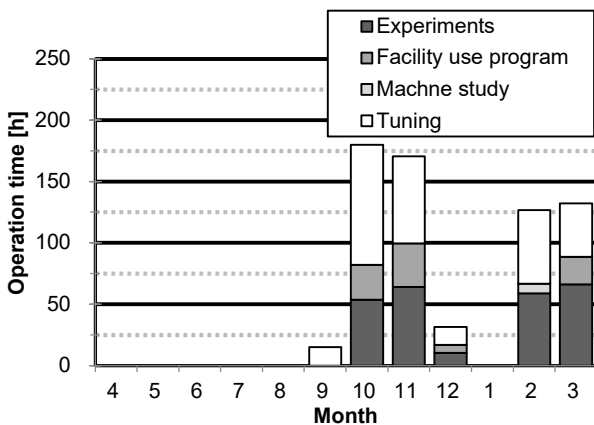


Fig. 1. Monthly operation times in fiscal 2023

Table 1

Statistics for cyclotron operation.

Fiscal year	2022	2023
Beam service time	640 h	346 h
Beam tuning	586 h	302 h
Machine study	42 h	8 h
Total operation time	1269 h	656 h
Change of particle and/or energy	140 times	77 times
Change of beam course	129 times	47 times
Change of harmonic number	57 times	28 times
The number of experiments	168	86
Cancellation due to machine trouble	0	0

Monthly operation times are shown in Fig. 1. Table 1 shows the statistics of the cyclotron operation of fiscal 2023, with the data of fiscal 2022 for comparison. The percentages of operation time of the year used for regular experiments, facility use program and promotion of shared use program, beam tuning, and beam development are 38.6%, 14.1%, 46.0%, and 1.2%, respectively. Table 2 shows the operation time of each ion source. NANOGAN ion source is used to produce H, D, and He ions. For

production of ions heavier than He, HYPERNANOGAN ion source is used. OCTOPUS ion source which has been used as backup ion source for HYPERNANOGAN. However, OCTOPUS ion source is not available except for periodic inspection owing to a trouble of the remote-control system. Therefore, the operation time of OCTOPUS was only 5 hours. Fractional distribution of major ions used for experiments is shown in Fig. 2.

Table 2

Operation times of ion sources.

ECR Ion source	2022	2023
NANOGAN	635 h (47.1%)	305 h (43.4%)
OCTOPUS	13 h (1.0%)	5 h (0.7%)
HYPERNANOGAN	699 h (51.9%)	393 h (55.9%)

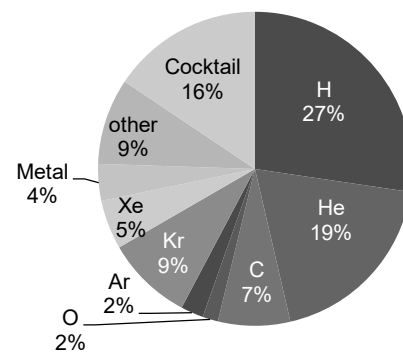


Fig. 2 Ion species used for experiments in fiscal 2023

Machine trouble and maintenance

The scheduled maintenances were carried out from the end of August to September. The major items of the maintenance were replacements of the contact fingers (CH1) and the main amplifiers of the cyclotron RF system, and the water pump for vacuum cooling system that was making abnormal noise.

Because of long time shutdown for six months since April, there were many troubles when the cyclotron operation resumed at the end of September. The failures of devices were as follows: 1) Semiconductor elements in the power supplies of the mirror coil (EML1) and the steering magnet (MST). 2) Motor driver of the outside position of the magnetic channel. 3) Programmable logic controller of the beam scanner (LD1). 4) Controllers of the turbo molecular pump (TTP1 & TTPHD1). 5) Transistor bank in the power supply (TDQ1). The number of machine troubles and maintenances of the year were 109 and 59, respectively.

5-03

Operation of electrostatic accelerators in TIARA

A. Chiba, K. Yamada, Y. Hirano, R. Suganuma,
S. Kanai, Y. Aoki, M. Hashizume and S. Kurashima

Department of Advanced Quantum Beam Technology, QST

The operating times of three electrostatic accelerators (the 3-MV tandem accelerator, the 3-MV single-ended accelerator and the 400-kV ion implanter) in FY2023 had been reduced compared to the previous fiscal year. The annual operating times including conditioning operations of the tandem accelerator, the single-ended accelerator and the ion implanter were 1012 h, 1088 h and 853 h, respectively. The accumulated operating time of the ion implanter reached 50000 hours. The transitions of the annual operating times of each electrostatic accelerator since the start of operation and the operating times for use patterns over the past three years are shown in Fig. 1 and Fig. 2, respectively. While the number of experimental uses of the tandem accelerator and the ion implanter were roughly the same as last year, the significant decrease in those of the single-ended accelerator was noticeable. Recently, the number of experimental uses has been gradually decreasing, but the significant decrease of more than 30% compared to the previous year should be perceived as a serious problem. One of the reasons for the decrease may be that the several collaborative research projects had to be terminated due to a lack of manpower to support the experiments. Figure 3 shows the utilization rates of ion species in each electrostatic accelerator. In recent years, the use of Sn⁺ and Ni⁺ in the tandem

accelerator, and Si⁺, Ge⁺, and Pr⁺ in the ion implanter, has increased. These ions were mainly used in fundamental research for the development of quantum devices and quantum sensing technologies. In the single-ended accelerator, H⁺ were used for μ PIXE and PBW, and He⁺ were mainly used for RBS. Table 1 shows the number of troubles and maintenances in FY2023. The number of machine troubles at electrostatic accelerators was about the same as the previous year. Serious troubles that required repairs by the product manufacturer occurred in the power supplies for focusing lenses, and in the accelerator control applications. Furthermore, there were a number of breakdowns of the bending magnet power supplies due to initial defects. Maintenance was mainly carried out, such as the renewal of the cooling system of the tandem accelerator. There was one case where an experiment was postponed due to a malfunction in the ion source of the tandem accelerator that caused significant reduction in the Zr ion beam. Even though the tandem accelerator is equipped with two ion sources for producing heavy ions to reduce the risk of canceling the experiments, in this rare case, it was postponed due to an unexpected trouble with both ion sources. Since operating times were shortened to 5 p.m., the risk of a minor trouble causing the experiment to be canceled has increased.

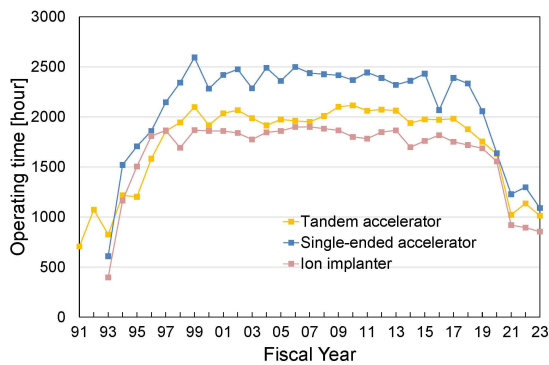


Fig. 1 Transitions of annual operating times.

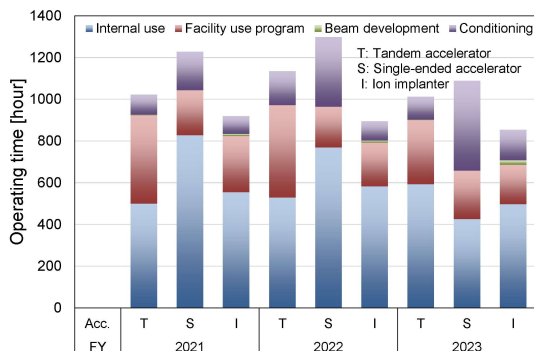


Fig. 2 Operating times for use patterns over the past three years.

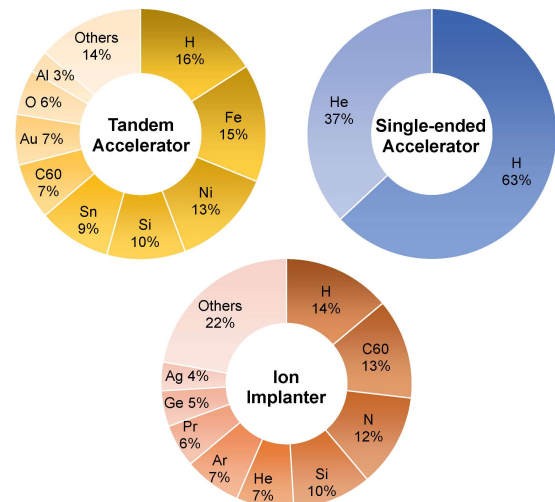


Fig. 3 Utilization rates of ion species.

Table 1

Number of machine troubles and maintenances.

	Tandem Accelerator	Single-ended Accelerator	Ion Implanter
Minor trouble	20	9	10
Serious trouble	8	1	3
Maintenance	27	17	11
Cancellation or Postponement	1	0	0

5-04

Operation, maintenance and utilization status of the gamma-ray irradiation facilities

Y. Nagao^{a)}, E. Yokozuka^{a)}, H. Seito^{a)}, M. Takagi^{b)}, N. Yagi^{b)},
T. Agematsu^{a)}, S. Yamasaki^{a)}, and N. Nagasawa^{a)}

^{a)}Department of Advanced Quantum Beam Technology, QST

^{b)}Takasaki Establishment, Radiation Application Development Association

Operation

The ⁶⁰Co gamma-ray irradiation facilities in Takasaki Institute for Advanced Quantum Science were operated almost smoothly in fiscal year (FY) 2023. The food irradiation facility closed at the end of February 2022.

The ⁶⁰Co gamma-ray irradiation facilities consisting of two buildings with six irradiation rooms cover a wide dose-rate range from 2×10^{-1} Gy/h to 8×10^3 Gy/h as of March 2024. The annual operation times of the first and the second ⁶⁰Co gamma-ray irradiation facilities were 25,133 h and 21,937 h, respectively, as shown in Fig. 1. Due to seismic retrofitting works on the buildings, the annual operation times of the first and the second ⁶⁰Co gamma-ray irradiation facilities have been reduced in FY 2021. The annual operation times of the first and the second ⁶⁰Co gamma-ray irradiation facilities in FYs 2022–2023 increased from that in FY 2021. However, the total annual operation time was lower than that in FY 2020 due to the closure of the food irradiation facility. Additionally, the annual operation time of the second ⁶⁰Co gamma-ray irradiation facility did not increase significantly due to long-term maintenance.

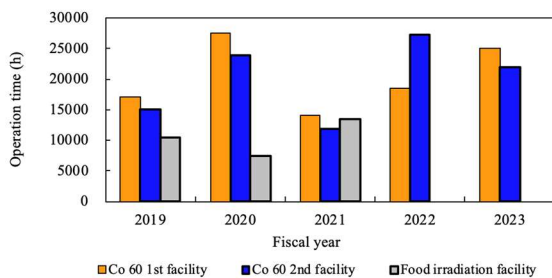


Fig. 1 Annual operation time of the gamma-ray irradiation facilities in the period from FY 2019 to FY 2023.

Maintenance

In order to manipulate the ⁶⁰Co sources safely, the master-slave manipulators at the first and the second ⁶⁰Co gamma-ray irradiation facilities have been replaced, as well as polishing the shielding window on each irradiation room. In addition, the inside of the irradiation rooms of the second ⁶⁰Co gamma-ray irradiation facilities was repainted for protection of concrete walls. In August 2023, some electrical devices in the first ⁶⁰Co gamma-ray irradiation facility were broken by a thunderbolt. The broken devices were replaced in December 2023 and in January 2024.

The periodical maintenance check mainly on mechanical systems for radiation source transportation is performed

every year at one of the gamma-ray irradiation facilities in turn. The maintenance check of the second ⁶⁰Co gamma-ray irradiation facility was done from September to November 2023 with suspension of operation for 44 days.

Utilization

The two facilities were operated for various research subjects according to the operation plans of the FY 2023. Figure 2 shows the irradiation time and the number of experiments in each research field in FY 2023. The facilities were mainly used in the materials science field such as research on metal absorbent, biocompatible protein hydrogels, polymer membrane for fuel cell and radiation-resistant materials and parts of the International Thermonuclear Experimental Reactor (ITER). Furthermore, radiation effects tests on microorganisms and plants in the life science field were conducted.

In the field of materials science, long-term radiation resistance evaluation of fusion reactor equipment and materials are being conducted. On the other hand, in the life science field such as research on the effects of irradiation on animal and plant cells, irradiation time is often short (e.g. the order of a few minutes) and experiments are conducted frequently.

The facility use program is often used to evaluate the radiation resistance of space electronic equipment and nuclear reactor materials.

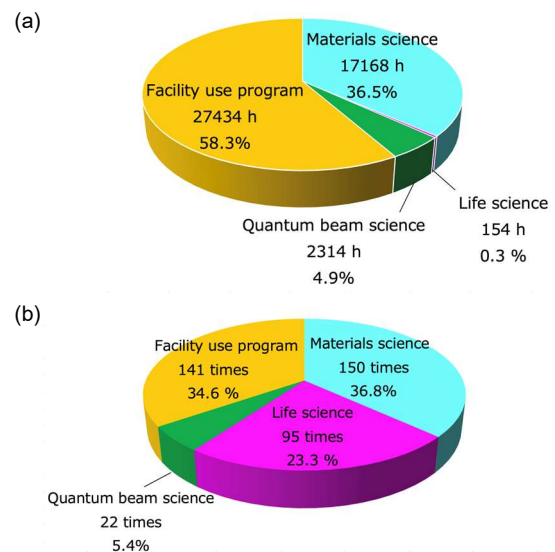


Fig. 2 The irradiation time (a) and the number of experiments (b) in each research field in FY 2023.

5-05

Operation, maintenance and utilization status of the electron accelerator

S. Yamasaki^{a)}, E. Yokozuka^{a)}, S. Kano^{b)}, M. Takagi^{b)}, N. Yagi^{b)},
T. Agematsu^{a)}, Y. Nagao^{a)}, H. Seito^{a)} and N. Nagasawa^{a)}

^{a)}Department of Advanced Quantum Beam Technology, QST,

^{b)}Takasaki Establishment, Radiation Application Development Association

Operation

The electron accelerator in Takasaki Institute for Advanced Quantum Science was operated almost smoothly in fiscal year (FY) 2023. The electron accelerator operates from 9:30 to 12:00 and from 13:00 to 17:00 on weekdays, for a maximum of 6.5 hours a day. The accumulated operation time from the installation to the end of FY2023 reached more 30,000 hours.

Maintenance

The main failure cases and maintenance details for the electron accelerator were (1) broken trolley of the conveyor system, (2) capacity dropout of the capacitor in the boost circuit and (3) maintenance of beam shutter drive unit in FY2023. (1) Due to an operational error by the experimenter, the two trolleys were not connected properly, resulting in collision between the trolleys and breaking two trolleys. (2) There are 12 stages of capacitor counts used in the boost circuit, with each stage consisting of two 60 nF capacitors connected in series for a total of 30 nF. One capacitor on the high potential side has a capacitance dropout, with the other capacitor measuring 61.8 nF. Since the other capacitor functions as the boost circuit, we decided to continue accelerator operations as they are. (3) The beam shutter is driven by compressed air, and the solenoid valve, air cylinder and air tube were damaged due to deterioration caused by exposure to X-rays and ozone were replaced.

Utilization

The electron accelerator was operated for various research subjects according to the operation plans of the FY2023. Figure 1 shows annual operation time in the period from FY2019 to FY2023. In FY2020, the facility use program decreased significantly due to the COVID-19 pandemic, but the QST use increased, resulting in approximately 1,000 hours of operation as in usual years. In FY2021, there was a long shutdown of about 10 months due to seismic retrofitting works and electronic flow control system update works, etc., therefore, it was reduced to about 300 hours, which is 30% of that in usual years. Except for FY2021, the annual operation time was about 1000 hours and almost reached the upper limit in the current operation plan. Figure 2 shows the operation time in each experimental field in FY2023. The electron accelerator was used by QST users in materials science for the experiments of quantum materials such as diamond for

quantum sensors, catalysts for fuel cell and modification of polymers (grafting polymerization, crosslinking and degradation) for biodevices. It was also used by the facility use program for radiation resistance effect studies on satellites materials and parts. Approximately 60% of the operation time was used for the development of quantum materials, which has more demand for operation time than actual use. Therefore, to satisfy users' requirements, it is necessary to increase the upper limit by changing the operation plan.

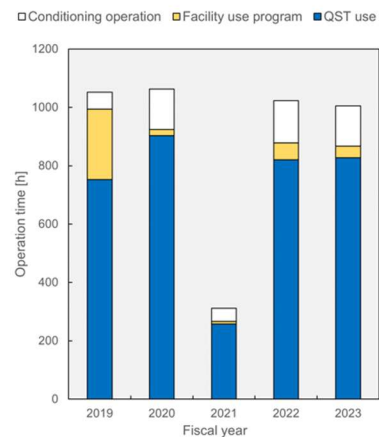


Fig. 1 Annual operation time in the period from FY2019 to FY2023.

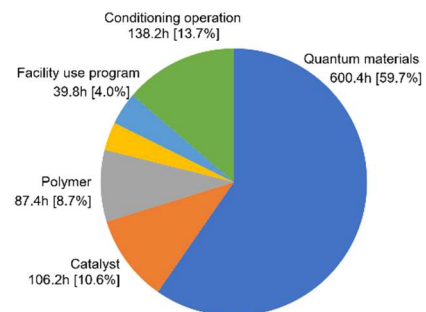


Fig. 2 The operation time in each experimental field in FY2023.

Individual monitoring

(1) Individual monitoring for radiation workers

Table 1 shows the distribution of effective doses among radiation workers in FY 2023. The effective dose values for almost all radiation workers were below the detection limit of 0.1 mSv. However, two workers had effective doses from external exposure that exceeded this detection limit.

The maximum effective dose from external exposure received by one worker was 0.2 mSv/y, resulting from experiments with unsealed radioisotopes at TIARA.

Table 1

Distribution of effective doses among radiation workers in FY 2023.

Items	Quarterly totals and annual unique count					
	1st quarter	2nd quarter	3rd quarter	4th quarter	Annual	
Distribution of people by effective dose range	HE < 0.1	390	445	509	518	689
	0.1 ≤ HE ≤ 1.0	0	0	2	1	2
	1.0 < HE ≤ 5.0	0	0	0	0	0
	5.0 < HE ≤ 15.0	0	0	0	0	0
HE: Effective dose*1 (mSv)	15.0 < HE	0	0	0	0	0
Total number of people (A)		390	445	511	519	691
Exposure above 1mSv	Number of people (B)	0	0	0	0	0
	(B)/(A)×100(%)	0	0	0	0	0
Collective dose (Person·mSv)		0.0	0.0	0.2	0.1	0.3
Mean effective dose (mSv)		0.00	0.00	0.00	0.00	0.00
Maximum effective dose (mSv)		0.0	0.0	0.1	0.1	0.2

*1 The effective dose from internal exposure was not detected.

(2) Individual monitoring for visitors and others

Table 2 shows the number of people who temporarily entered the radiation-controlled areas. The effective doses for all people were less than 0.1 mSv.

Table 2

Number of people who temporarily entered the radiation-controlled areas in FY 2023.

Quarters	1st quarter	2nd quarter	3rd quarter	4th quarter	Total
Number of people	318	458	1,349	362	2,487

Monitoring of radioactive gases and dust at TIARA

Table 3 shows the maximum radioactive concentrations and total activities for radioactive gases released from the stack of TIARA during each quarter of FY 2023.

Small amounts of ¹¹C, ¹⁸F, ⁴¹Ar, and ⁷⁷Br were occasionally detected during the operation of the cyclotron or experiments, but the particulate radioactive substances (e.g., ⁶⁵Zn) were not detected.

Table 3

Monitoring results of released radioactive gases and dust in FY 2023.

Nuclide	Quarters Items	1st quarter	2nd quarter	3rd quarter	4th quarter	Total
		⁴¹ Ar	Maximum concentration	<1.1×10 ⁻⁴	<1.1×10 ⁻⁴	
	Activity	0	0	2.0×10 ⁷	0	2.0×10 ⁷
¹¹ C	Maximum concentration	—	—	<1.1×10 ⁻⁴	<1.1×10 ⁻⁴	
	Activity	—	—	2.8×10 ⁸	5.2×10 ⁸	8.0×10 ⁸
¹⁸ F	Maximum concentration	—	—	<1.1×10 ⁻⁴	—	
	Activity	—	—	3.2×10 ⁷	—	3.2×10 ⁷
⁷⁷ Br	Maximum concentration	—	—	—	4.8×10 ⁻⁹	
	Activity	—	—	—	8.1×10 ⁴	8.1×10 ⁴
⁶⁵ Zn	Maximum concentration	<6.6×10 ⁻¹⁰	<6.0×10 ⁻¹⁰	<7.1×10 ⁻¹⁰	<6.8×10 ⁻¹⁰	
	Activity	0	0	0	0	0

Unit : Bq/cm³ for Maximum concentration, Bq for Activity.

Monitoring of external radiation and surface contamination at TIARA

The monitoring for external radiation and surface contamination was routinely performed in/around the radiation-controlled areas. Neither anomalous value of dose equivalent rate nor surface contamination was detected.

Figure 1 shows a typical example of the distribution of the γ-ray dose equivalent rate in the radiation-controlled area of the cyclotron building.

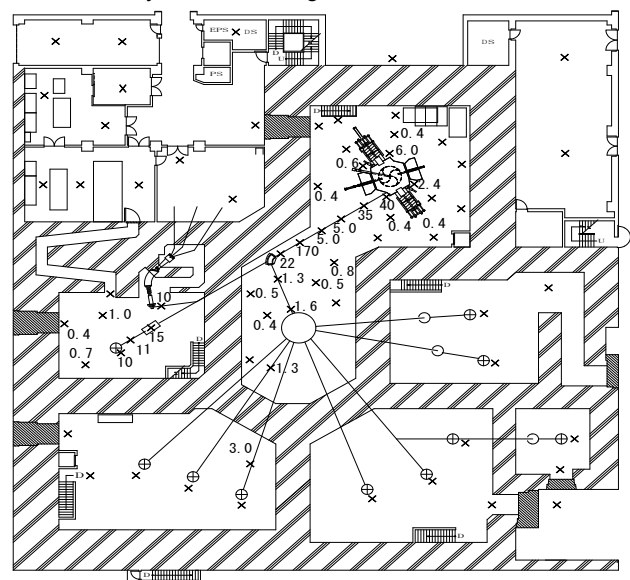


Fig. 1. Distribution of the γ-ray dose equivalent rate in the radiation-controlled area of the cyclotron building.

Measurement date : March 18 and 27, 2024.

Measuring position : Indicated with × (1 meter above floor).

Unit : μSv/h (Values below 0.2 μSv/h are not displayed.)

5-07

Radioactive waste management in TIARA

N. Higuchi ^{a)}, K. Iida ^{a, b)}, H. Hanaya ^{b)} and S. Watanabe ^{b)}

^{a)}Department of Administrative Services, QST

^{b)}Department of Advanced Quantum Beam Technology, QST

Radioactive waste management

The radioactive waste generated in TIARA is managed by Utilization and Coordination Section. The main radioactive waste is the solid waste generated from research experiments and the maintenance of the cyclotron. Other radioactive waste is the liquid waste such as inorganic waste fluids generated from research experiments and the air-conditioning machines in the radiation controlled area. These wastes are managed according to their properties. Radioactive waste is stored in a storage facility and handed over to the Japan Radioisotope Association for disposal.

Solid radioactive waste

Table 1 shows the amounts of various types of solid waste generated in each quarter of FY 2023. Combustible waste consists of papers and clothes, and so on. Flame-retardant waste consists of rubber gloves, plastic articles, and polyethylene articles. Incombustible waste consists of

metal pieces and the glasses, and so on. Solid waste emitting α , β , and γ is classified according to the properties.

Liquid radioactive waste

Table 2 shows the amounts of liquid waste generated in each quarter of FY 2023. The main liquid waste is inorganic water, which consists of condensed water generated from the air-conditioner installed in the radiation controlled area and waste water generated from chemical experiments. In Table 2, large amount of inorganic waste water is generated in 2nd quarter. It is due to the condensed water generated from the air-conditioner. To reduce the inorganic waste water, distillation of the inorganic waste water is carried out. After the distillation, small amount of distillation residual liquid remains, and that is discarded for liquid waste. On the other hand, the purified water prepared by distillation is reused in the radiation controlled area.

Table 1
Radioactive solid waste generated in FY 2023.

Items	Amounts	Amounts of generation in each period (m ³)					Number of package /drum
		1st quarter	2nd quarter	3rd quarter	4th quarter	Total	
Category β, γ^*		0	0	0.26	0.20	0.46	15 **
Combustible		0	0	0.04	0.06	0.10	3 **
Flame-retardant		0	0	0.08	0.08	0.16	4 **
Incombustible(Compressible)		0	0	0.02	0.04	0.06	5 **
" (Incompressible)		0	0	0	0	0	3
Laboratory animal		0	0	0	0.02	0.02	0
Filters		0	0	0	0	0	-
Category α^*		0	0	0	0.12	0.12	4
Combustible		0	0	0	0.02	0.02	0
Flame-retardant		0	0	0	0.06	0.06	0
Incombustible(Compressible)		0	0	0	0.00	0.00	4
" (Incompressible)		0	0	0	0	0	0
Laboratory animal		0	0	0	0.04	0.04	0
Filters		0	0	0	0	0	-

* defined by amount in Bq (β, γ): < 2 GBq, (α): < 37 MBq,

** 50-liter drum.

Table 2
Radioactive liquid waste generated in FY 2023.

Items	Amounts	Amounts of generation in each period (m ³)					Number of package /drum
		1st quarter	2nd quarter	3rd quarter	4th quarter	Total	
Category β, γ^*		4.34	20.43	4.02	0.82	29.61	-
1)Inorganic		4.34	20.43	4.02	0.82	29.61	-
Inorganic		4.34	20.43	4.02	0.82	29.61	0
Distillation residual liquid, Sludge		0.00	0.00	0.00	0.00	0.00	0
2)Organic		0.00	0.00	0.00	0.00	0.00	0
Organic		0.00	0.00	0.00	0.00	0.00	0
Oil		0.00	0.00	0.00	0.00	0.00	0
Category α^*		0.00	0.00	0.00	0.00	0.00	0

* defined by concentrations in Bq/mL (β, γ Inorganic): < 200 kBq, (Organic): < 2 kBq, (α): \leq 1.85 kBq,

5-08 The Shared Use Program of QST Facilities in Takasaki

S. Nozawa, H. Hanaya and A. Shimada

The First Office of Research Planning and Promotion,
Department of Management and Planning, QST

Introduction

Irradiation facilities in the Takasaki Institute for Advanced Quantum Science have been opened to many researchers who belongs to universities, public institutes, and R&D divisions of private companies (hereafter 'external users').

Under the Shared Use Program of QST Facilities (hereafter 'Shared Use Program'), external users can conduct irradiation experiments by using gamma-rays, electron beams, and ion beams, these were provided from the irradiation facilities of Co-60 gamma-ray, the electron accelerator, and the TIARA's four ion accelerators. When using these facilities, external users are required to bear the operating costs of irradiation equipment.

Pricing system of the Shared Use Program

In the Shared Use Program, experimental charges have been calculated from total amount of the service charge, the irradiation charge, and extra-costs (e.g., additional consumable goods and human support).

Research-and-development's users, who disclose results of studies by publication, have been partially discounted for the irradiation charge. To receive this discount, users were required to submit a research proposal, which will be considered by the expert committee members, in terms of effectiveness of experimental plans. The approved proposals are implemented with the partially discounted charges. This partial discount is not applied to the gamma-ray irradiation facilities and the electron accelerator.

Number of irradiation experiments under the Shared Use Program in FY2023

Number of irradiation experiments under the Shared Use Program in FY2023 were shown in Table 1. Number of experiments in the Co-60 gamma-ray irradiation facilities was much higher than other irradiation facilities.

Number of experiments classified by user's affiliation were shown in Table 2. The four accelerators in the TIARA facilities and the Electron accelerator were mainly used by researchers who belonging to the Academia such as universities and public institutes. On the other hand, many users of the Co-60 gamma ray irradiation facilities were belonging to private companies.

Additional information about this program is available at the following QST website:

<https://www.qst.go.jp/site/shisetsukyoyo-takasaki/>

Table 1

Number of irradiation experiments under the Shared Use Program of QST Facilities in FY2023

Irradiation facility		Pricing system		
		Public disclosure	Non-disclosure	Total
TIARA	AVF cyclotron	2	14	16
	3 MV tandem accelerator	15	17	32
	3 MV single-ended accelerator	17	4	21
	400 kV ion implanter	9	13	22
Co-60 gamma-ray irradiation facilities		-*	155	155
Electron accelerator		-*	17	17
Total		43	220	263

*: Discounting was not applied

Table 2

Number of irradiation experiments classified by user's affiliations.

Irradiation Facility		User's affiliation			Total
		University	Public institute	Private company	
TIARA	AVF cyclotron	8	3	5	16
	3 MV tandem accelerator	20	6	6	32
	3 MV single-ended accelerator	13	8	0	21
	400 kV ion implanter	17	4	1	22
Co-60 gamma-ray irradiation facilities		34	15	106	155
Electron accelerator		9	4	4	17
Total		101	40	122	263

Appendix

Appendix: Publication List

P1-1 Quantum Sensing Project

Papers

- 1. Quantum circuit distillation and compression.**
Daimon Shunsuke, Tsunekawa Kakeru, Takeuchi Ryoto, Sagawa Takahiro, Yamamoto Naoki, Saitoh Eiji, JAPANESE JOURNAL OF APPLIED PHYSICS, 63, 032003, 2024. DOI:10.35848/1347-4065/ad29d8
- 2. Enhancement in photoluminescence from GaPAsN/GaP alloys by 6-MeV electrons irradiation and rapid thermal annealing.**
E.-M. Pavelescu, D. Ticos, O. Ligor, C. Romanitan, A. Matei, F. Comanescu, V. Tucureanu, S.I. Spanulescu, C. Ticos, Ohshima Takeshi, T. Nakamura, M. Imaizumi, R. S. Goldman, A. Wakahara, K. Yamane, Optical Materials, 149, 115075-1 - 115075-5, 2024.
DOI:10.1016/j.optmat.2024.115075
- 3. Spin-State Control of Shallow Single NV Centers in Hydrogen-Terminated Diamond.**
Taisuke Kageura, Yosuke Sasama, Tokuyuki Teraji, Kenji Watanabe, Takashi Taniguchi, Yamada Keisuke, Kimura Kosuke, Onoda Shinobu, Yamaguchi Takahide, ACS Applied Materials & Interfaces, 2024.
DOI:10.1021/acsami.3c17544
- 4. Development of a SiC semiconductor-based dosimeter for evaluating clinical dose distribution in carbon ion cancer therapy fields.**
Takumi Matsumoto, Kohei Yamaguchi, Yanagisawa Rio, Kei Kubodera, Arai Yudai, Makino Takahiro, Ohshima Takeshi, Sakai Makoto, Matsumura Akihiko, Nuclear Instruments & Methods B, 542, 151 - 157, 2024.
DOI:10.1016/j.nimb.2023.06.013
- 5. Transform-limited photon emission from a lead-vacancy center in diamond above 10 K.**
Peng Wang, Lev Kazak, Katharina Senkalla, Petr Siyushev, Ryotaro Abe, Takashi Taniguchi, Onoda Shinobu, Hiromitsu Kato, Toshiharu Makino, Mutsuko Hatano, Fedor Jelezko, Takayuki Iwasaki, Physical Review Letters, (132), 073601-1 - 073601-7, 2024.
DOI:10.1103/PhysRevLett.132.073601
- 6. Cathodoluminescence spectral and lifetime mappings of Cs₄PbBr₆: fast lifetime and its scintillator application.**
Tetsuya Kubota, Sotatsu Yanagimoto, Hikaru Saito, Keiichirou Akiba, Ayumi Ishii, Takumi Sannomiya, Applied Physics Express, 2024. DOI:10.35848/1882-0786/ad1bc4
- 7. All-optical determination of one or two emitters using quantum polarization with nitrogen-vacancy centers in diamond.**
Davin Yue Ming Peng, Josef G. Worboys, Qiang Sun, Shuo Li, Marco Capelli, Onoda Shinobu, Ohshima Takeshi, Philipp Reineck, Brant C. Gibson, Andrew D. Greentree, Physical Review A, 109(2), 023723, 2024.
DOI:10.1103/PhysRevA.109.023723
- 8. Fast coherent control of nitrogen-14 spins associated with nitrogen-vacancy centers in diamonds using dynamical decoupling.**
Kosuke Mizuno, Ikuya Fujisaki, Hiroyoshi Tomioka, Ishiwata, Hitoshi, Onoda Shinobu, Takayuki Iwasaki, Keigo Arai, Mutsuko Hatano, Journal of physics communications, 8(3), 035002, 2024.
DOI:10.1088/2399-6528/ad2b8b
- 9. Competitive coexistence of ferromagnetism and metal-insulator transition of VO₂ nanoparticles.**
Tsuyoshi Hatano, Akihiro Fukawa, Hiroki Yamamoto, Keiichirou Akiba, Satoshi Demura, Kouichi Takase, Japanese Journal of Applied Physics, 2024.
DOI:10.35848/1347-4065/ad2d04
- 10. Detection of temporal fluctuation in superconducting qubits for quantum error mitigation.**
Hirasaki Yuta, Daimon Shunsuke, Itoko Toshinari, Kanazawa Naoki, Saitoh Eiji, Applied Physics Letters, 123(18), 184002, 2023. DOI:10.1063/5.0166739
- 11. Change in charge state of NV center caused by monovacancy formation.**
Chikara Shinei, Abe Hiroshi, Ohshima Takeshi, Tokuyuki Teraji, Diamond & Related Materials, 140(Part B), 110523-1 - 110523-6, 2023.
DOI: 10.1016/j.diamond.2023.110523
- 12. Quantum sensing and light guiding with fluorescent nanodiamond-doped PVA fibers.**
Roy Styles, Andrea Candini, Vincenzo Guarino, Islay Robertson, Priya Singh, Valentina Benfenati, Abe Hiroshi, Ohshima Takeshi, Andrew D. Greentree, Brant C. Gibson, Luigi Ambrosio, Jean-Philippe Tetienne, Philipp Reineck, ADVANCED OPTICAL MATERIALS, ,2302940-1 - 2302940-9, 2023.
DOI: 10.1002/adom.20230294
- 13. Highly Dispersed 3C Silicon Carbide Nanoparticles with a Polydopamine/Polyglycerol Shell for Versatile Functionalization.**
Shingo Sotoma, Abe Hiroshi, Yohei Miyanoiri, Ohshima Takeshi, Yoshie Harada, ACS APPLIED MATERIALS & INTERFACES, 15, 21413 - 21424, 2023.
DOI: 10.1021/acsami.3c00194
- 14. Radiation Response of Large-Area 4H-SiC Schottky Barrier Diodes.**
Robert Bernat, Tihomir Knežević, Vladimir Radulović, Luka Snoj, Makino Takahiro, Ohshima Takeshi, Ivana Capan, Materials, 16, 2202, 2023.
DOI:10.3390/ma16062202
- 15. Measurement of radiation-induced current through a SiC Schottky barrier diode in a clinical carbon beam cancer therapy field.**
Kei Kubodera, Takumi Matsumoto, Kohei Yamaguchi, Ryo Yokota, Yudai Arai, Takahiro Makino, Takeshi Ohshima, Makoto Sakai, Akihiko Matsumura, Wataru Kada, Nuclear Inst. and Methods in Physics Research, B, 540, 80 - 84, 2023. DOI:10.1016/j.nimb.2023.04.009

- 16. Absorption and birefringence study for reduced optical losses in diamond with high nitrogen-vacancy concentration.**
Tingpeng Luo, Felix A. Hahl, Julia Langer, Volker Cimalla, Lukas Lindner, Xavier Vidal, Marko Haertelt, Remi Blinder, Onoda Shinobu, Ohshima Takeshi, Jan Jeske, Philosophical Transactions A, 2023.
DOI:10.1098/rsta.2022.0314
- 17. A wide dynamic range diamond quantum sensor as an electric vehicle battery monitor.**
Yuji Hatano, Junya Tanigawa, Akimichi Nakazono, Takeharu Sekiguchi, Onoda Shinobu, Ohshima Takeshi, Takayuki Iwasaki, Mutsuko Hatano, Philosophical Transactions A, 2023. DOI:10.1098/rsta.2022.0312
- 18. Influence of Gate Depletion Layer Width on Radiation Resistance of Silicon Carbide Junction Field-Effect Transistors.**
Takeyama Akinori, Makino Takahiro, Yasunori Tanaka, Shin-Ichiro Kuroki, Ohshima Takeshi, Quantum Beam Science, 7(4), 31-1 - 31-10, 2023.
DOI:10.3390/qbs7040031
- 19. Time-correlated electron and photon counting microscopy.**
Sotatsu Yanagimoto, Naoki Yamamoto, Tatsuro Yuge, Hikaru Saito, Keiichiro Akiba, Takumi Sannoimya, Communications Physics, 6, 260, 2023.
DOI:10.1038/s42005-023-01371-1
- 20. Charge pumping electrically detected magnetic resonance of silicon carbide power transistors.**
C. T.-K. Lew, V. K. Sewani, Ohshima Takeshi, J. C. McCallum, B. C. Johnson, Journal of Applied Physics, 134, 055703-1 - 055703-7, 2023.
DOI:10.1063/5.0167650
- 21. Enhanced magnetometry with an electrically detected spin defect ensemble in silicon carbide.**
C. T.-K. Lew, V. K. Sewani, N. Iwamoto, Ohshima Takeshi, J. C. McCallum, B. C. Johnson, Applied Physics Letters, 122, 234001-1 - 234001-6, 2023.
DOI:10.1063/5.0154382
- 22. Enhancing photon collection from single shallow nitrogen-vacancy centers in diamond nanopillars for quantum heterodyne measurements.**
Akirabha Chanuntranont, Kazuki Otani, Daiki Saito, Yuki Ueda, Masato Tsugawa, Shuntaro Usui, Yuto Miyake, Tokuyuki Teraji, Onoda Shinobu, Takahiro Shinada, Hiroshi Kawarada, Takashi Tani, Applied Physics Express, 16(8), 082006-1 - 082006-5, 2023.
DOI:10.35848/1882-0786/acede9
- 23. Voltage Dependence of Single-Event Cross Sections of FinFET SRAMs for Low LET Condition.**
Kozo Takeuchi, Keita Sakamoto, Kazuki Yukumatsu, Takashi Kato, Hideya Matsuyama, Takeyama Akinori, Makino Takahiro, Ohshima Takeshi, Hiroyuki Shindou, IEEE Transactions on Nuclear Science, 70(8), 1755 - 1759, 2023. DOI:10.1109/TNS.2023.3295340
- 24. Optically detected magnetic resonance of silicon vacancies in 4H-SiC at elevated temperatures toward magnetic sensing under harsh environments.**
Motoki Shu, Sato Shinichiro, Saiki Seiichi, Masuyama Yuta, Yamazaki Yuichi, Ohshima Takeshi, Koichi Murata, Hidekazu Tsuchida, Yasuto Hijikata, Journal of Applied Physics, 133(15), 154402, 2023.
DOI:10.1063/5.0139801
- 25. Nitrogen Concentration Control during Diamond Growth for NV- Center Formation.**
T. Teraji, C. Shinei, Masuyama Yuta, M. Miyakawa, T. Taniguchi, Philosophical Transactions of the Royal Society A, 382(2265), 20220322., 2023.
DOI:10.1098/rsta.2022.0322
- 26. Myosin and tropomyosin-troponin complementarily regulate thermal activation of muscles.**
Ishii Shuya, Oyama Kotaro, Fuyu Kobirumaki-Shimozawa, Tomohiro Nakanishi, Naoya Nakahara, Madoka Suzuki, Shin'ichi Ishiwata, Norio Fukuda, The Journal of General Physiology, 155(12), e202313414, 2023. DOI:10.1085/jgp.202313414
- 27. High-resolution nanoscale NMR for arbitrary magnetic fields.**
Jonas Meinel, Minsik Kwon, Durga Dasari, Hitoshi Sumiya, Onoda Shinobu, Junichi Isoya, Vadim Vorobyov, Jörg Wrachtrup, Communications Physics, 6(302), 01419-2-1 - 01419-2-7, 2023. DOI:10.1038/s42005-023-01419-2
- 28. Transition from quantum to classical dynamics in weak measurements and reconstruction of quantum correlation.**
Vadim Vorobyov, Jonas Meinel, Hitoshi Sumiya, Onoda Shinobu, Junichi Isoya, Oleg Gulinsky, Jörg Wrachtrup, Physical Review A, 107(4), 042212-1 - 04221-31, 2023.
DOI:10.1103/PhysRevA.107.042212
- 29. Extension of spin dephasing time of continuously excited ensemble NV centres by double-quantum Ramsey magnetometry with spin bath driving.**
Ikuya Fujisaki, Yuta Araki, Yuji Hatano, Takeharu Sekiguchi, Hiromitsu Kato, Onoda Shinobu, Ohshima Takeshi, Takayuki Shibata, Takayuki Iwasaki, Hatano Mutsuko, Physica Status Solidi A: Applications and Materials Science, 221(8), 2300333, 2023.
DOI:10.1002/pssa.202300333
- 30. Wide temperature operation of diamond quantum sensor for electric vehicle battery monitoring.**
Keisuke Kubota, Yuji Hatano, Yuta Kainuma, Jaewon Shin, Daisuke Nishitani, Takashi Taniguchi, Tokuyuki Teraji, Onoda Shinobu, Ohshima Takeshi, Takayuki Iwasaki, Mutsuko Hatano, Diamond & Related Materials, 135, 10953-1 - 10953-8, 2023.
DOI:10.1016/j.diamond.2023.109853
- 31. Detecting nuclear spins in an organosilane monolayer using nitrogen-vacancy centers for analysis of precursor self-assembly on diamond surface.**
Yuki Ueda, Yuto Miyake, Akirabha Chanuntranont, Kazuki Otani, Masato Tsugawa, Daiki Saito, Shuntaro Usui, Tokuyuki Teraji, Onoda Shinobu, Takahiro Shinada, Hiroshi Kawarada, Takashi Tani, Japanese Journal of Applied Physics, 62, SG1049-1 - SG1049-5, 2023.
DOI:10.35848/1347-4065/accc91
- 32. Superbunching in cathodoluminescence: A master**

equation approach.

Tatsuro Yuge, Naoki Yamamoto, Takumi Sannomiya, Keiichirou Akiba, Physical Review B, 107, 165303, 2023. DOI:10.1103/PhysRevB.107.165303

33. Two-Emitter Multimode Cavity Quantum Electrodynamics in Thin-Film Silicon Carbide Photonics.

Daniil M. Lukin, Melissa A. Guidry, Joshua Yang, Misagh Ghezellou, Sattwik Deb Mishra, Abe Hiroshi, Ohshima Takeshi, Jawad Ul-Hassan, Jelena Vučković, Physical Review X, , 2023. DOI: 10.1103/PhysRevX.13.011005

Patents

1. I V 族 – 空孔センターの生成方法、及び、I V 族 – 空孔センターを有するダイヤモンド結晶の製造方法

小野田 忍, 馬場 智也, 木村 晃介, 飯澤 正登実, 加田 渉, 宮川仁, 特願2023-143180 (2023-09-04).

2. センサ及び発光素子

村田晃一, 浅田聡志, 佐藤 真一郎, 増山 雄太, 特願2023-36789 (2023-03-09).

3. デバイス及びデバイスの製造方法

村田晃一, 浅田聡志, 坂本邦博, 佐藤 真一郎, 増山 雄太, 特願2023-036316 (2023-03-09).

Press

1. 重い IV 族元素からなるダイヤモンド量子光源からの 自然幅の発光を観測 – 量子ネットワークの実現に前進 –

東京工業大学、物材機構、産総研・QST, 2024-02-15 プレス発表。

2. 加速電子と光子の時間相関電子顕微鏡を実現～個々の加速電子を利用してナノスケール発光寿命を計測～

東京工業大学・静岡大学・九州大学・QST, 2023-10-17 プレス発表。

P1-2 Spin-photonics in 2D Materials Project

Papers

1. Reversible structure change in graphene/metal interface by intercalation and deintercalation.

Yuki Fukaya, Entani Shiro, Sakai Seiji, Physical Review B, 108, 155422, 2023.

DOI: 10.1103/PhysRevB.108.155422

2. Cubic-type Heusler compound Mn_2FeGa thin film with strain-induced large perpendicular magnetic anisotropy.

Phillip david Bentley, Li Songtian, Keisuke Masuda, Yoshio Miura, Du Ye, Mitsui Takaya, Fujiwara Kosuke,

Yasuhiro Kobayashi, Tengyu Guo, Guoqiang Yu, Suzuki Chihiro, Yamamoto Shunya, Fu Zheng, Yuya Sakuraba, Sakai Seiji, Physical Review Materials, 7, 064404, 2023. DOI: 10.1103/PhysRevMaterials.7.064404

Patent

1. 高記録密度磁性層用材料、磁気抵抗記憶素子、及び高記録密度磁性層用材料の製造方法

境 誠司, Bentley Phillip David, 李 松田, 三井 隆也, 藤原 孝将, PCT/JP2024/5076 (2024-02-14).

P1-3 Laser-cooled Ion Research Project

Papers

1. Design of an apertureless two-stage acceleration lens for a single-ion implantation system.

Ishii Yasuyuki, Okubo Takeru, Miyawaki Nobumasa, Yuri Yosuke, Onoda Shinobu, Narumi Kazumasa, Nuclear Instruments and Methods in Physics Research B, 541, 200 - 204, 2024. DOI: 10.1016/j.nimb.2023.05.021

2. Simulation study of ultrahigh-precision single-ion extraction from a linear Paul trap.

Muroo Kento, Okamoto Hiromi, Miyawaki Nobumasa, Yuri Yosuke, Progress of Theoretical and Experimental Physics, 2023, 063G1, 2023. DOI:10.1093/ptep/ptad071

3. Calculation study of selective ion extraction from ion

source with Paul-trap-type laser cooling device.

Miyawaki Nobumasa, Ishii Yasuyuki, Yuri Yosuke, Narumi Kazumasa, Kento Muroo, Ito Kiyokazu, Okamoto Hiromi, Nuclear Inst. and Methods in Physics Research, B, 542, 183 - 187, 2023.

DOI:10.1016/j.nimb.2023.06.015

4. Label-free mid-infrared photothermal live-cell imaging beyond video rate.

Genki Ishigane, Keiichiro Toda, Miu Tamamitsu, Hiroyuki Shimada, Venkata Ramaiah Badarla, Takuro Ideguchi, Light, science & applications, 12(1), 174, 2023.

DOI:10.1038/s41377-023-01214-2

P1-4 Quantum Optical and Spin State Control Project

Papers

- 1. Highly Sensitive Temperature Sensing Using the Silicon Vacancy in Silicon Carbide by Simultaneously Resonated Optically Detected Magnetic Resonance.**
Yamazaki Yuichi, Masuyama Yuta, Kojima Kazutoshi, Ohshima Takeshi, PHYSICAL REVIEW APPLIED, 20(3), L031001-1 - L031001-6, 2024.
DOI:10.1103/PhysRevApplied.20.L031001
- 2. Spin property improvement of boron vacancy defect in hexagonal boron nitride by thermal treatment.**
Tetta Suzuki, Yamazaki Yuichi, Takashi Taniguchi, Kenji Watanabe, Yusuke Nishiya, Matsushita Yuichiro, Harii Kazuya, Masuyama Yuta, Yasuto Hijikata, Ohshima Takeshi, Applied Physics Express, 16(3), 032006, 2023.
DOI:10.35848/1882-0786/acc442
- 3. Deterministic Current-Induced Perpendicular Switching in Epitaxial Co/Pt Layers without an External Field.**
Kohda Makoto, Advanced Functional Materials, 35(33), 2209693 - 2209693, 2023.
DOI: 10.1002/adfm.202209693
- 4. Perspective on spin-based wave-parallel computing.**
Kohda Makoto, Applied Physics Letters, (123), 190502 - 190502, 2023. DOI: 10.1063/5.0168083
- 5. Amorphous ferromagnetic metal in van der Waals materials.**
Siyue Zhang, Harii Kazuya, Yokouchi Tomiyuki, Okayasu Satoru, Yuki Shiomi, Advanced Electronic Materials, , 2300609, 2023. DOI: 10.1002/aelm.202300609
- 6. Magnetic hysteresis induction with nanocolumnar defects in magnetic insulators.**
Harii Kazuya, Maki Umeda, Hiroki Arisawa, Tomosato Hioki, Nana Sato, Satoru Okayasu, Jun'ichi Ieda, Journal of the physical society of japan, 92(7), 073701, 2023.
DOI:10.7566/JPSJ.92.073701

Press

- 1. シリコンカーバイド (SiC) 量子センサーの高感度化を実現！～次世代パワー半導体の信頼性向上へ～**
QST, 2023-09-06 プレス発表.
- 2. 光と電気どちらでも書き込める不揮発性磁気メモリ材料を開発 – シンプルなデバイス構造で外部磁場不要の磁化反転を実現 –**
東北大学・QST・韓国科学技術院・マサチューセッツ工科大学, 2023-07-06 プレス発表.

P1-5 Quantum Materials Theory Project

Papers

- 1. Temperature and size dependence of energy barrier for magnetic flips in $L1_0$ FePt nanoparticles: A theoretical study.**
Hung Ba Tran, Matsushita Yuichiro, Scripta Materialia, 242(15), 115947, 2024.
DOI: 10.1016/j.scriptamat.2023.115947
- 2. Skyrmions in van der Waals centrosymmetric materials with Dzyaloshinskii–Moriya interactions.**
Hung Ba Tran, Matsushita Yuichiro, Scripta Materialia, 239(15), 115799, 2024.
DOI: 10.1016/j.scriptamat.2023.115799
- 3. Quantum circuit distillation and compression.**
Daimon Shunsuke, Tsunekawa Kakeru, Takeuchi Ryoto, Sagawa Takahiro, Yamamoto Naoki, Saitoh Eiji, JAPANESE JOURNAL OF APPLIED PHYSICS, 63, 032003, 2024. DOI:10.35848/1347-4065/ad29d8
- 4. Illuminating the Bragg intersections as roots of Dirac nodal lines and high-order van Hove singularities.**
Akashi Ryosuke, Physical Review Research, 6(3), 033012, 2024.
DOI:10.1103/PhysRevResearch.6.033012
- 5. Exhaustive search for optimal molecular geometries using imaginary-time evolution on a quantum computer.**
Taichi Kosugi, Hirofumi Nishi, Matsushita Yuichiro, npj quantum information, 9, 112, 2023.
DOI: 10.1038/s41534-023-00778-6
- 6. Energy levels of carbon dangling-bond center (P_{bc} center) at 4H-SiC(0001)/SiO₂ interface.**
Mitsuru Sometani, Yusuke Nishiya, Ren Kondo, Rei Inohana, Hongyu Zeng, Hirohisa Hirai, Dai Okamoto, Matsushita Yuichiro, Takahide Umeda, APL Materials, 11(11), 111119-1 - 111119-5, 2023.
- 7. Optimal scheduling in probabilistic imaginary-time evolution on a quantum computer.**
Hirofumi Nishi, Koki Hamada, Yusuke Nishiya, Taichi Kosugi, Matsushita Yuichiro, Physical Review Research, 5, 043048-1 - 043048-14, 2023.
DOI: 10.1103/PhysRevResearch.5.043048
- 8. Effect of nitrogen introduced at the SiC/SiO₂ interface and SiC side on the electronic states by first-principles calculation.**
Keita Tachiki, Yusuke Nishiya, Jun-Ichi Iwata, Matsushita Yuichiro, Japanese Journal of Applied Physics, 62, 061005-1 - 061005-7, 2023.
DOI:10.35848/1347-4065/acd9ff
- 9. Dzyaloshinskii–Moriya interactions in Nd₂Fe₁₄B as the origin of spin reorientation and the rotating magnetocaloric effect.**
Hung Ba Tran, Matsushita Yuichiro, Applied Materials Today, 32, 101825, 2023.
DOI: 10.1016/j.apmt.2023.101825
- 10. Atomic scale localization of Kohn–Sham wavefunction at SiO₂/4H–SiC interface under electric field, deviating from envelope function by effective mass approximation.**
Hironori Yoshioka, Jun-Ichi Iwata, Matsushita Yuichiro,

Applied Physics Letters, 122(22), 222104-1 - 222104-6, 2023. DOI: 10.1063/5.0151547

11. Detection of temporal fluctuation in superconducting qubits for quantum error mitigation.

Hirasaki Yuta, Daimon Shunsuke, Itoko Toshinari, Kanazawa Naoki, Saitoh Eiji, Applied Physics Letters ,

123(18), 184002 , 2023. DOI:10.1063/5.0166739

Press

1. 固体中のワイル粒子」が現れるか？現れないか？ ～精密な実験と計算の組み合わせにより10年以上の謎を解決～
東京大学・広島大学・QST, 2023-05-09プレス発表.

P1-6 Rare-earth Quantum Device Project

Papers

1. Investigating a Pb-free n-i-p perovskite solar cell with BFCO absorber using SCAPS-1D.

Nassim Ahmed Mahammed, Afif Benameur, Hamza Gueffaf, Boualem Merabet, Osman Murat Ozkendir, Sato Shinichiro, Optik, 302(171659), 1 - 19, 2024.

DOI: 10.1016/j.ijleo.2024.171659

2. Optical activation of implanted lanthanoid ions in aluminum nitride semiconductors by high temperature annealing.

Sato Shinichiro, Kanako Shojiki, Ken-ichi Yoshida, Hideaki Minagawa, Hideto Miyake, Optical Materials Express, 14(2), 340 - 355, 2024.

DOI:10.1364/OME.507312

3. Optical activation of praseodymium ions implanted

in gallium nitride after ultra-high pressure annealing.

Ito Shin, Sato Shinichiro, Michal Bockowski, Manato Deki, Hiroataka Watanabe, Shugo Nitta, Yoshio Honda, Hiroshi Amano, Ken-ichi Yoshida, Hideaki Minagawa, Naoto Hagura, Nuclear Instruments and Methods in Physics Research B, 547(165181), 1 - 7, 2024.

4. Enhancing Room-temperature Photoluminescence from Erbium-doped Silicon by Fabricating Nanopillars in a Silicon-on-Insulator Layer.

Yuma Takahashi, Tomoki Ishii, Kaisei Uchida, Takumi Zushi, Lindsay Coe, Sato Shinichiro, Enrico Prati, Takahiro Shinada, Takashi Tanii, e-Journal of Surface Science and Nanotechnology, 21(4), 262 - 266, 2023.

DOI:10.1380/ejsnt.2023-041

P1-7 Quantum Materials Ultrafine Fabrication Project

Papers

1. Competitive coexistence of ferromagnetism and metal-insulator transition of VO₂ nanoparticles.

Tsuyoshi Hatano, Akihiro Fukawa, Hiroki Yamamoto , Keiichirou Akiba , Satoshi Demura, Kouichi Takase, Japanese Journal of Applied Physics, 2024.

DOI:10.35848/1347-4065/ad2d04

2. Design of High-sensitive Resist Materials Based on Polyacetals.

Maekawa Hiroyuki, Iwashige Yutaro, Yamamoto Hiroki, Kazumasa Okamoto, Takahiro Koazawa, Hiroto Kudo, J.

Photopolymer Science and Technology, 36(1), 31 - 39, 2023.

Patents

1. 感光性組成物及びパターン形成方法

服部繁樹, 山本 洋揮, 特願2023- 091341 (2023-06-02).

2. 金属化合物、感光性組成物、パターン形成方法、基板の製造方法

服部繁樹, 長山和弘, 加藤茜, 山本 洋揮, 特願2023-169294 (2023-09-29).

P2-1 Hydrogen Energy Conversion Device Project

Papers

1. Ion Tracks and Nanohillocks Created in Natural Zirconia Irradiated with Swift Heavy Ions.

Ishikawa Norito, Fukuda Shoma, Nakajima Toru, Ogawa Hiroaki, Fujimura Yuki, Taguchi Tomitsugu, materials, 17(3), 547-1 - 547-21, 2024. DOI:10.3390/ma17030547

2. Effect of Ion Irradiation After Platinum Deposition onto Carbon Substrates on Oxygen Reduction Reaction Activity of Electrocatalysts.

Taguchi Tomitsugu, Yamamoto Shunya, Koshikawa Hiroshi, Okazaki Hiroyuki, Idesaki Akira, Yamaki Tetsuya, Nuclear

Instruments and Methods in Physics Research Section B, 549(165286-1), 549 - 165286-6, 2024.

DOI:10.1016/j.nimb.2024.165286

3. Latent ion tracks were finally observed in diamond.

Amekura Hiroshi, Abdelhak Chettah, Narumi Kazumasa, Chiba Atsuya, Hirano Yoshimi, Yamada Keisuke, Yamamoto Shunya, Aleks Leino, Flyura Djurabekova, Kai Nordlund, Ishikawa Norito, Okubo Nariaki, Saito Yuuichi, Nature Communications, 2024.

4. Development of a radiation tolerant laser-induced breakdown spectroscopy system using a single crystal

micro-chip laser for remote elemental analysis.

Tamura Koji, Nakanishi Ryuzo, Oba Hironori, 狩野 貴宏, 柴田 卓弥, 平等拓範, 若井田育夫, Journal of Nuclear Science and Technology, 61(8), 1109 - 1116, 2024.

DOI:10.1080/00223131.2023.2298485

5. Dependence of radiation-induced conductivity and electrical degradation of silicon carbides on ionizing dose rates.

Tsuchiya Bun, Kataoka Keisuke, Terasawa Ryosuke, Yamamoto Shunya, Ito Shun, Nuclear Instruments and Methods in Physics Research B, 2024.

DOI:10.1016/j.nimb.2024.165284

6. A DFT study on photodissociation of the palladium tetrachloride anion PdCl₄²⁻ in solution.

Anzai Aiko, Kurosaki Yuzuru, Saeki Morihisa, Muraoka Azusa, Chemical Physics, 579, 112182, 2024.

DOI:doi.org/10.1016/j.chemphys.2024.112182

7. Weakened Oxygen Adsorbing the Pt-O Bond of the Pt Catalyst Induced by Vacancy Introduction into Carbon Support.

Okazaki Hirofumi, Idesaki Akira, Koshikawa Hiroshi, Ikeda Takashi, Yamamoto Shunya, Yamaki Tetsuya, Daiju Matsumura, The Journal of Physical Chemistry C, 127(49), 23628 - 23633, 2023. DOI:10.1021/acs.jpcc.3c04117

8. Robustness of semimetallic transport properties of TaAs against off-stoichiometric disorder.

Kawasuso Atsuo, Suda Masayuki, Murakawa Hiroshi, Komada M., Suzuki Chihiro, Amada Haruyo, Michishio Koji, Maekawa Masaki, Miyashita Atsumi, Seko Noriaki, Yamamoto Shunya, Oshima Nagayasu, Seki Shuhei, Hanasaki N., Journal of Applied Physics, 133(22), 223903-1 - 223903-6, 2023. DOI:10.1063/5.0147663

9. Platinum nanoparticles prepared by ion implantation

exhibit high durability for fuel cell applications.

Kimata Tetsuya, Kato Sho, Kobayashi Tomohiro, Yamamoto Shunya, Yamaki Tetsuya, Terai Takayuki, APL Materials, 11(6), 061115, 2023. DOI:10.1063/5.0148263

10. Two-dimensional elemental mapping of simulated fuel debris using laser-induced breakdown spectroscopy.

Munkhbat Batsaikhan, Katsuaki Akaoka, Saeki Morihisa, Takahiro Karino, Hironori Ohba, Ikuo Wakaida, JOURNAL OF NUCLEAR SCIENCE AND TECHNOLOGY, 61(5), 658 - 670, 2023. DOI:10.1080/00223131.2023.2255186

11. Mechanism of Au nanowire growth by Au evaporation on Si substrates irradiated with Ar ions.

Mizutani Hitomi, Yamamoto Shunya, Takahiro Katsumi, Applied Surface Science, 638, 158063, 2023.

DOI:10.1016/j.apsusc.2023.158063

12. Cubic-type Heusler compound Mn₂FeGa thin film with strain-induced large perpendicular magnetic anisotropy.

Phillip david Bentley, Li Songtian, Keisuke Masuda, Yoshio Miura, Du Ye, Mitsui Takaya, Fujiwara Kosuke, Yasuhiro Kobayashi, Tengyu Guo, Guoqiang Yu, Suzuki Chihiro, Yamamoto Shunya, Fu Zheng, Yuya Sakuraba, Sakai Seiji, Physical Review Materials, 7, 064404, 2023.

DOI: 10.1103/PhysRevMaterials.7.064404

13. 可視光を99.98%以上吸収する至高の暗黒シート。

雨宮 邦昭, 清水 雄平, 越川 博, 八巻 徹也, 放射線化学, (116), 21 - 25, 2023.

14. 原子層堆積法で成膜したTiO₂薄膜の酸性溶液中での電気化学特性とそのPEFCカソードへの適用可能性。

渡辺 友理, 松澤 幸一, 永井 崇昭, 池上 芳, 門田 隆二, 今西 哲士, 山本 春也, 石原 顕光, 燃料電池, 23(1), 69 - 78, 2023.

P2-2 Nanostructured Polymer Materials Project

Papers

1. Effects of functional graft polymers on phase separation and ion-channel structures in anion exchange membranes analyzed by SANS partial scattering function.

Yoshimura Kimio, Hiroki Akihiro, Aurel Radulescu, Yohei Noda, Satoshi Koizumi, Yue Zhao, Maekawa Yasunari, Macromolecules, 57, 1998 - 2007, 2024.

2. Toward the design of graft-type proton exchange membranes with high proton conductivity and low water uptake: A machine learning study.

Sawada Shinichi, Maekawa Yasunari, Sakamoto Yukiko, Funatsu Kimito, Journal of Membrane Science, 692, 2024.

3. Extended Q-range small-angle-neutron scattering to understand the morphology of proton-exchange membranes: the case of the functionalized syndiotactic-polystyrene model system.

Maria-Maddalena Schiavone, David Hermann Lamparelli, Christophe Daniel, Yue Zhao, Hiroki Iwase, Hiroshi Arima-Osonoi, Shin-ichi Takata, Laszlo Szentmiklosi,

Aurel Radulescu, Journal of Applied Crystallography, 56(4), 947 - 960, 2023.

DOI:10.1107/S1600576723005496

4. Microscopic Determination of the Local Hydration Number of Polymer Electrolyte Membranes Using SANS Partial Scattering Function Analysis.

Yue Zhao, Yoshimura Kimio, Sawada Shinichi, Hiroki Akihiro, Aurel Radulescu, Maekawa Yasunari, ACS Macro Letters, 12(4), 481 - 486, 2023.

DOI:10.1021/acsmacrolett.3c00019

5. Effect of High-Dose Electron Beam Irradiation on Thermal Decomposition Behavior of Polytetrafluoroethylene (PTFE).

Hao Yu, Maekawa Yasunari, Idesaki Akira, Hiroki Akihiro, Hirota Koichi, Hasegawa Shin, Radiation Physics and Chemistry, 2023.

6. Direct observation of radiation-induced graft polymerization on a polyethylene film.

Motegi Toshinori, Omichi Masaaki, Maekawa Yasunari, Seko Noriaki, radiation physics and chemistry, 214, 111281, 2023.

Patents

1. **樹脂組成物、樹脂組成物の製造方法、及び電気化学デバイス**
長谷川 伸, 吉村 公男, ザオ ユ工, 廣木 章博, 前川 康成,
特願2023-161783 (2023-09-25).

2. **高分子材料の分解方法及び分解装置、高分子材料の構成単位化合物の製造方法及び製造装置**
出崎 亮, 前川 康成, Y U H a o, 廣木 章博, 広田 耕一,
長谷川 伸, 特願2023-117122 (2023-07-18).

P2-3 Energy Regeneration Materials Project

Papers

1. **GFN-xTB Based Computations Provide Comprehensive Insights into Emulsion Radiation-Induced Graft Polymerization.**
Matsubara Kiho, Takahashi Kei, Takeshi Matsuda, Ueki Yuuji, Seko Noriaki, Ryohei Kakuchi, ChemPlusChem, 89(4), e202300480, 2023. DOI:10.1002/cplu.202300480
2. **Modified abaca fiber prepared by radiation-induced graft polymerization as reinforcement for unsaturated polyester resin composites.**
Bin Jeremiah D. Barba, Seko Noriaki, Jordan F. Madrid, David P. Penaloza, Jr., Polymer Journal, 56, 97 - 105, 2023. DOI:10.1038/s41428-023-00851-z
3. **Robustness of semimetallic transport properties of**

TaAs against off-stoichiometric disorder.

- Kawasuso Atsuo, Suda Masayuki, Murakawa Hiroshi, Komada M., Suzuki Chihiro, Amada Haruyo, Michishio Koji, Maekawa Masaki, Miyashita Atsumi, Seko Noriaki, Yamamoto Shunya, Oshima Nagayasu, Seki Shuhei, Hanasaki N., Journal of Applied Physics, 133(22), 223903-1 - 223903-6, 2023. DOI:10.1063/5.0147663
4. **Direct observation of radiation-induced graft polymerization on a polyethylene film.**
Moteji Toshinori, Omichi Masaaki, Maekawa Yasunari, Seko Noriaki, radiation physics and chemistry, 214, 111281, 2023.
DOI:10.1016/j.radphyschem.2023.111281

P2-4 Advanced Biodevice Project

Papers

1. **Linear Energy Transfer Dependence of Scintillation Properties of CeFs.**
Koshimizu Masanori, Kurashima Satoshi, Kimura Atsushi, Taguchi Mitsumasa, Nuclear Inst. and Methods in Physics Research, B, 546, 165158, 2023.
DOI:10.1016/j.nimb.2023.165158
2. **Myosin and tropomyosin-troponin complementarily regulate thermal activation of muscles.**
Ishii Shuya, Oyama Kotaro, Fuyu Kobirumaki-Shimozawa, Tomohiro Nakanishi, Naoya Nakahara, Madoka Suzuki, Shin'ichi Ishiwata, Norio Fukuda, The Journal of General Physiology, 155(12), e202313414, 2023. DOI:10.1085/jgp.202313414
3. **Hybrid Biophysics: Interdisciplinary approaches for trans-scale analysis of organism-environment interactions.**
Madoka Suzuki, Oyama Kotaro, Toshiko Yamazawa, Biophysics and Physicobiology, 20(4), e200043, 2023.
DOI:10.2142/biophysico.bppb-v20.0043
4. **Development of environmentally friendly soft contact lenses made from cellulose-derived hydrogel materials.**
Hiroki Akihiro, Kimura Atsushi, Taguchi Mitsumasa, Radiation Physics and Chemistry, 213, 111257, 2023.
DOI:10.1016/j.radphyschem.2023.111257
5. **Development of Non-Electrically Controlled SalivaDirect LAMP (NEC-SD-LAMP), a New Nonelectrical Infectious Disease Testing Method.**

- Kimura Yusuke, Masashi Ikeuchi, scientific reports, 13, 11791, 2023. DOI:10.1038/s41598-023-38800-8
6. **Trans-scale thermal signaling in biological systems.**
Madoka Suzuki, Chujie Liu, Oyama Kotaro, Toshiko Yamazawa, The Journal of Biochemistry, 174(3), 217 - 225, 2023. DOI:10.1093/jb/mvad053
 7. **Radiolysis of water at the surface of ZrO₂ nanoparticles.**
John McGrady, Shinichi Yamashita, Sho Kano, Huilong Yang, Atsushi Kimura, Mitsumasa Taguchi, Hiroaki Abe, Radiation Physics and Chemistry, 209, 110970, 2023.
DOI:10.1016/j.radphyschem.2023.110970
 8. **An In Vivo Dual-Observation Method to Monitor Tumor Mass and Tumor-Surface Blood Vessels for Developing Anti-Angiogenesis Agents against Submillimeter Tumors.**
Tomoko Tachibana, Tomoko Oyama, Yukie Yoshii, Fukiko Hihara, Chika Igarashi, Mitsuhiro Shinada, Hiroki Matsumoto, Tatsuya Higashi, Toshihiko Kishimoto, Mitsumasa Taguchi, International journal of molecular sciences, 24(24), 2023. DOI:10.3390/ijms242417234

Patents

1. **細胞判定方法、スクリーニング方法、細胞分離方法及びゲル**
三好 洋美, 山本 翔太郎, 田口 光正, 大山 智子, 大山 廣太郎, 特願2024-032003 (2024-03-04).
2. **細胞培養用ハイドロゲル、ゲルキット、細胞培養物の製造方法、及び細胞培養用ハイドロゲルの製造方法**
田口 光正, 大山 智子, 木村 敦, 大山 廣太郎, 石原 弘, 下川 卓志, 特許第7414224号 (2024-01-05).

3. **ハイドロゲル、細胞培養物の製造方法、およびハイドロゲルの製造方法**
田口 光正, 大山 智子, 大山 廣太郎, 特願2023-216124 (2023-12-21).
4. **細胞培養用ハイドロゲル、ゲルキット、細胞培養物の製造方法、及び細胞培養用ハイドロゲルの製造方法**
田口 光正, 大山 智子, 木村 敦, 大山 廣太郎, 石原 弘, 下川 卓志, 特願2023-166391 (2023-09-27).
5. **色素沈着を調節された皮膚モデル、皮膚モデルの製造方法、シミ色素沈着予防、軽減、改善又は治療剤のスクリーニング方法、ケラチノサイト培養用の細胞外マトリクスタンパク質ゲル及びその製造方法**
井上 大悟, アリフミーム ヌラニ, 前野 克行, 田口 光正, 大

- 山 智子, 大山 廣太郎, 特願2023-116222 (2023-07-14).
6. **臓器モデルおよびその製造方法並びに焼灼治療トレーニング用キット**
今西彩花, 宮本久生, 吉井 文男, 田口 光正, 木村 敦, 特許第7246638号 (2023-03-17).

Press

1. **骨格筋はわずかな温度の変化を敏感に感じてパフォーマンスを向上させる！～ウォーミングアップの効果をタンパク質レベルで解明～**
東京慈恵会医科大学・QST・大阪大学, 2023-10-24プレス発表.

P3-1 Radiotracer Imaging Project

Papers

1. **Construction and initial performance evaluation of a newly developed plant PET system.**
Yamamoto Seiichi, Watabe Hiroshi, Yamaguchi Mitsutaka, Suzui Nobuo, Kawachi Naoki, Kataoka Jun, Journal of Instrumentation, 19, T04002, 2024.
DOI:10.1088/1748-0221/19/04/T04002
2. **A triple-imaging-modality system for simultaneous measurements of prompt gamma photons, prompt x-rays, and induced positrons during proton beam irradiation.**
Yamamoto Seiichi, Watabe Hiroshi, Nakanishi Kohei, Yabe Takuya, Yamaguchi Mitsutaka, Kawachi Naoki, Kamada Kei, Yoshikawa Akira, Miyake Masayasu, Tanaka S. Kazuo, Kataoka Jun, Phys. Med. Biol., 69, 055012, 2024. DOI:10.1088/1361-6560/ad25c6
3. **A large field-of-view angled panel detector for the development of a plant PET system.**
Yamamoto Seiichi, Watabe Hiroshi, Yamaguchi Mitsutaka, Suzui Nobuo, Kawachi Naoki, Kataoka Jun, Journal of Instrumentation, 19, T01002, 2024.
DOI:10.1088/1748-0221/19/01/T01002
4. **Optimization of a YAP(Ce) prompt X-ray camera for imaging with spot scanning proton beams at clinical dose levels.**
Yamamoto Seiichi, Yamashita Tomohiro, Kobayashi Yusuke, Yabe Takuya, Akagi Takashi, Yamaguchi Mitsutaka, Kawachi Naoki, Kamada Kei, Yoshikawa Akira, Kataoka Jun, Journal of Instrumentation (JINST), 18, T12005, 2023.
DOI:10.1088/1748-0221/18/12/T12005
5. **Predicting blurless and noise-free Ir-192 source images from gamma camera images for high-dose-rate brachytherapy using a deep-learning approach.**
Kohei Nakanishi, Seiichi Yamamoto, Yabe Takuya, Katsunori Yogo, Yumiko Noguchi, Kuniyasu Okudaira, Kawachi Naoki, Jun Kataoka, Biomedical Physics & Engineering Express, 10(1), 015006, 2023.
DOI:10.1088/2057-1976/ad0bb2
6. **Development of DynamicMC for PHITS Monte Carlo package.**
Watabe Hiroshi, Sato Tatsuhiko, Kwan Ngok Yu, Milena Zivkovic, Dragoslav Nikezic, Kyeong Min Kim, Yamaya Taiga, Kawachi Naoki, Tanaka Hiroki, A.K.F. Haque, M. Rafiqul Islam, Mehrdad S. Beni, Radiation Protection Dosimetry, 200(2), 130 - 142, 2023.
DOI:10.1093/rpd/ncad278
7. **Simultaneous imaging of prompt gamma photons and prompt X-rays during irradiation of proton beams to human torso phantom at clinical dose level.**
Yamamoto Seiichi, Yamashita Tomohiro, Kobashi Yusuke, Yabe Takuya, Akagi Takashi, Yamaguchi Mitsutaka, Kawachi Naoki, Kamada Kei, Yoshikawa Akira, Yokokawa Hiromu, Sagisaka Mayu, Kataoka Jun, Journal of Instrumentation, 18, P07046, 2023.
DOI:10.1088/1748-0221/18/07/P07046
8. **Simultaneous imaging of luminescence and prompt X-rays during irradiation with spot-scanning proton beams at clinical dose level.**
Yamamoto Seiichi, Yamashita Tomohiro, Kobashi Yusuke, Yabe Takuya, Takashi Akagi, Yamaguchi Mitsutaka, Kawachi Naoki, Kamada Kei, Kataoka Jun, Biomedical Physics & Engineering Express, 9(4), 045301, 2023. DOI:10.1088/2057-1976/acdf61
9. **Hybrid imaging of prompt x-rays and induced positrons using a pinhole gamma camera during and after irradiation of protons.**
Yamamoto Seiichi, Watabe Hiroshi, Nakanishi Kohei, Yabe Takuya, Yamaguchi Mitsutaka, Kawachi Naoki, Kamada Kei, Yoshikawa Akira, Islam Md Rafiqul, Miyake Masayasu, S Kazuo Tanaka, Kataoka Jun, Physics in Medicine & Biology, 68(11), 115015, 2023.
DOI:10.1088/1361-6560/acd2a2
10. **Prompt X-ray imaging during irradiation with spread-out Bragg peak (SOBP) beams of carbon ions.**
Yamamoto Seiichi, Yabe Takuya, Akagi Takashi, Yamaguchi Mitsutaka, Kawachi Naoki, Kamada Kei, Yoshikawa Akira, Kataoka Jun, Physica Medica, 109, 102592, 2023. DOI:10.1016/j.ejmp.2023.102592
11. **Development of a list-mode data acquisition system for prompt X-ray imaging during irradiation with carbon-ions.**

- Yamamoto Seiichi, Yabe Takuya, Akagi Takashi, Yamaguchi Mitsutaka, Kawachi Naoki, Kamada Kei, Yoshikawa Akira, Kataoka Jun, Journal of Instrumentation, 18, P04025, 2023.
DOI:10.1088/1748-0221/18/04/P04025
- 12. Translocation of ¹¹C-labelled photosynthates to strawberry fruits depends on leaf transpiration during twilight.**
Miyoshi Yuta, Jens Mincke, Jonathan Vermeiren, Jan Courtyn, Christian Vanhove, Stefaan Vandenberghe, Kawachi Naoki, Kathy Steppe, Environmental and Experimental Botany, 211, 105353, 2023.
DOI:10.1016/j.envexpbot.2023.105353
- 13. Non-invasive range-shift measurement for therapeutic carbon-ion beams by detecting SEB with a CdTe imager.**
Tsuda Michiko, Yamaguchi Mitsutaka, Toyokawa Hidenori, Yabe Takuya, Nagao Yuuto, Kawachi Naoki, Satori Ryota, Sakai Makoto, Kada Wataru, Kamiya Tomihiro, Journal of Instrumentation, 18, C04008, 2023.
DOI:10.1088/1748-0221/18/04/C04008
- 14. Non-invasive ¹¹C-imaging revealed no change in the dynamics of photosynthates translocation of strawberry in response to increasing daylight integrals under low light conditions.**
Miyoshi Yuta, Kota Hidaka, Yonggen Yin, Suzui Nobuo, Kurita Keisuke, Kawachi Naoki, Acta Horticulturae, 1381(12), 89 - 96, 2023.
DOI:10.17660/ActaHortic.2023.1381.12
- 15. Starch-dependent sodium accumulation in the leaves of *Vigna riukiensis*.**
Noda Yusaku, Atsushi Hirose, Mayumi Wakazaki, Mayuko Sato, Kiminori Toyooka, Kawachi Naoki, Jun Furukawa, Keitaro Tanoi, Ken Naito, Journal of Plant Research, 136, 705 - 714, 2023.
DOI:10.1007/s10265-023-01470-8
- 16. ADP-glucose pyrophosphorylase genes are differentially regulated in sugar-dependent or -independent manners in tomato (*Solanum lycopersicum L.*) fruit.**
Yong-Gen Yin, Atsuko Sanuki, Yukihisa Goto, Suzui Nobuo, Kawachi Naoki, Chiaki Matsukura, plant biotechnology, 40(4), 345 - 351, 2023.
DOI:10.5511/plantbiotechnology.23.1004a
- 17. Visualization of the initial radiocesium dynamics after penetration in living apple trees with bark removal using a positron-emitting ¹²⁷Cs tracer.**
Noda Yusaku, Toshihiro Yoshihara, Suzui Nobuo, Yonggen Yin, Miyoshi Yuta, Enomoto Kazuyuki, Kawachi Naoki, Applied Radiation and Isotopes, 198, 110859, 2023. DOI:10.1016/j.apradiso.2023.110859
- 18. Lattice strain visualization inside a 400-nm single grain of BaTiO₃ in polycrystalline ceramics by Bragg coherent X-ray diffraction imaging.**
Oshime Norihiro, Ohwada Kenji, Machida Akihiko, Fukushima Nagise, Kosuke Shirakawa, Ueno Shintaro, Fujii Ichiro, Wada Satoshi, Sugawara Kento, Shimada Ayumu, Ueno Tetsuro, Watanuki Tetsu, Ishii Kenji, Toyokawa Hidenori, Momma Koichi, Kim Sangwook, Tsukada Shinya, Kuroiwa Yoshihiro, Japanese Journal of Applied Physics (Special Issues: Ferroelectric Materials and Their Applications), 62, SM1022, 2023.
DOI:10.35848/1347-4065/ace832

Press

1. 特殊なデンブでナトリウムを吸着・無害化するヒナアズキ - ナトリウム蓄積の害から葉を守る特殊な耐塩性機構の正体 - 農研機構・QST・筑波大学・東京大学・理研, 2023-07-06プレス発表.

P3-2 Environmental-Stress Tolerance Genes Project

Papers

1. **イオンビーム照射による清酒酵母育種技術の基礎検討.**
渡部貴志, 佐藤 勝也, 大野 豊, 吉野功, 田島創, 日本醸造協会誌, 119(6), 323, 2024
2. **Lethal and mutagenic effects of different LET radiations in *Bacillus subtilis* spore.**
Sato Katsuya, Wataru Hoshino, Hase Yoshihiro, Kitamura Satoshi, Hidenori Hayashi, Masakazu Furuta, Ono Yutaka, Mutation Research - Fundamental and Molecular Mechanisms of Mutagenesis, 827, 111835, 2023. DOI:10.1016/j.mrfmmm.2023.111835
3. **Physiological Importance and Role of Mg²⁺ in Improving Bacterial Resistance to Cesium.**
Yoshiki Ishida, Chongkai Zhang, Sato Katsuya, Masahiro Ito, Frontiers in Microbiology, 14, 1201121, 2023.
DOI:10.3389/fmicb.2023.1201121

Patents

- 1 **はまごころ7号**
山口絵梨香, 長谷 純宏, 野澤 樹, 大野 豊, 品種登録第29714 (2024-06-08)
- 2 **はまごころ6号**
山口絵梨香, 長谷 純宏, 野澤 樹, 大野 豊, 品種登録第29713 (2024-06-08)
3. **窒素源存在条件下オイル高蓄積藻類株の育種方法、窒素源存在条件下オイル高蓄積藻類株及びそれを用いた油脂製造方法**
蓮沼誠久, 加藤悠一, 小山智己, 近藤昭彦, 佐藤 勝也, 大野 豊, 特許第7402447号 (2023-12-13).
4. **きく品種「舞夢黄」**
長谷川徹, 伊藤健二, 新井和俊, 渡邊孝政, 遠山宏和, 平松裕邦, 鈴木良地, 二村幹雄, 奥村義秀, 辻孝子, 近藤満治, 石川高史, 青木献, 竹内良彦, 野村浩二, 小久保恭明, 山本雅春, 西尾讓一, 加藤博美, 鬼頭温文, 浅見逸夫, Hase Yoshihiro, Nozawa Shigeki, 品種登録 (中国) 第2023027048号2023027048 (2023-05-24).
5. **きく品種「舞夢紫」**
長谷川徹, 伊藤健二, 新井和俊, 渡邊孝政, 遠山宏和, 平松裕邦, 鈴木良地, 二村幹雄, 奥村義秀, 辻孝子, 近藤満治,

石川高史, 青木献, 竹内良彦, 野村浩二, 小久保恭明, 山本雅春, 西尾讓一, 加藤博美, 浅見逸夫, Hase Yoshihiro, Nozawa Shigeki, 品種登録 (中国) 2023027047号 (2023-05-24).

6. さく品種「舞夢白」

長谷川徹, 伊藤健二, 新井和俊, 渡邊孝政, 遠山宏和, 平松

裕邦, 鈴木良地, 二村幹雄, 奥村義秀, 辻孝子, 近藤満治, 石川高史, 青木献, 竹内良彦, 野村浩二, 小久保恭明, 山本雅春, 西尾讓一, 加藤博美, 浅見逸夫, Hase Yoshihiro, Nozawa Shigeki, 品種登録 (中国) 2023027046号 (2023-05-24).

P3-3 Medical Radioisotope Application Project

Papers

1. Copper-mediated astatination of ²¹¹At-labelled prostate-specific membrane antigen probes in the presence of basic salts.

Watanabe Shigeki, Yuto Kondo, Sasaki Ichiro, Oshima Yasuhiro, Hiroyuki Kimura, Ishioka Noriko, Tetrahedron, 2024.

2. モンテカルロシミュレーションを用いた¹⁷⁷Luイメージングにおける定量的精度と再現性の検証.

久保田 千裕, 石川 一磨, 佐藤 充, 安本 佳章, 深井 翔平, 坂下 哲哉, 大崎 洋充, 日本放射線技術学会雑誌, 2024.

3. 1-(N,N-Dialkylcarbamoyl)-1,1-difluoromethane-sulfonyl ester as a stable and effective precursor for a neopentyl labeling group with astatine-211.

Sasaki Ichiro, Tada Masatoshi, Liu Ziyun, Tatsuta Maho, Okura Takeru, Aoki Miho, Takahashi Kazuhiro, Ishioka Noriko, Watanabe Shigeki, Tanaka Hiroshi, Organic & Biomolecular Chemistry, 21(36), 7467 - 7472, 2023. DOI:10.1039/D3OB00944K

4. Short-term γ -ray Irradiation with Hyperoxia Induces Lifespan Extension in *C. elegans*.

Sumino Yanase, Michiyo Suzuki, Qui-Mei Zhang-Akiyama, Tetsuya Sakashita, Biological Sciences in Space, 37, 12 - 19, 2023. DOI:10.2187/bss.37.12

5. Production of Auger-electron-emitting ^{103m}Rh via a ¹⁰³Pd/^{103m}Rh generator using an anion-exchange

resin.

Ohya Tomoyuki, Ichinose Jun, Nagatsu Kotaro, Sugo Yumi, Ishioka Noriko, Watabe Hiroshi, Ito Masatoshi, Minegishi Katsuyuki, Zhang Ming-Rong, Radiochimica Acta, 2023. DOI:10.1515/ract-2023-0238/html

6. Solvent extraction following oxidation of astatine for the use of a ²¹¹Rn-²¹¹At generator.

Shin Yuki, Maruyama Shunpei, Kawasaki Kohei, Aoi Keito, Washiyama Kohshin, Nishinaka Ichiro, Yano Shinya, Haba Hiromitsu, Yokoyama Akihiko, Journal of Radioanalytical and Nuclear Chemistry, 2023. DOI:10.1007/s10967-023-09282-9

Patents

1. ウイルスを不活化する方法、薬剤、およびウイルス不活化用組成物

大島 康宏, 佐々木 一郎, 石岡 典子, 特願2023-191082 (2023-11-08).

2. 放射性標識化合物の製造方法及び製造装置

石岡 典子, 近藤 浩夫, 渡辺 茂樹, 特許第7339692号 (2023-08-29).

3. 分離装置、分離方法、R I 分離精製システムおよびR I 分離精製方法

森 勝伸, 大平 慎一, 戸田 敬, 須郷 由美, 渡辺 茂樹, 石岡 典子, 特許第7288261号 (2023-05-30).

P3-4 Quantum-Applied Biotechnology Project

Papers

1. A Method for Locally Irradiate Specific Tissue of Model Organisms using Focused Heavy-Ion Microbeam.

Tomoo Funayama, Michiyo Suzuki, Nobumasa Miyawaki, Hirotsugu Kashiwagi, Biology, 12(12), 1524, 2023. DOI:10.3390/biology12121524

2. Short-term γ -ray Irradiation with Hyperoxia Induces Lifespan Extension in *C. elegans*.

Sumino Yanase, Michiyo Suzuki, Qui-Mei Zhang-Akiyama, Tetsuya Sakashita, Biological Sciences in

Space, 37, 12 - 19, 2023. DOI:10.2187/bss.37.12

3. Radiation-quality-dependent bystander cellular effects induced by heavy-ion microbeams through different pathways.

Suzuki Masao, Funayama Tomoo, Suzuki Michiyo, Kobayashi Yasuhiko, Journal of Radiation Research, 64(5), 824 - 832, 2023. DOI:10.1093/jrr/rrad059

Patent

1. 試験方法および線虫試験用プレート

鈴木 芳代, 特許第7301436号 (2023-06-23).

P4-1 Beam Engineering Section

Papers

- 1. Latent ion tracks were finally observed in diamond.**
Amekura Hiroshi, Abdelhak Chettah, Narumi Kazumasa, Chiba Atsuya, Hirano Yoshimi, Yamada Keisuke, Yamamoto Shunya, Aleksii Leino, Flyura Djurabekova, Kai Nordlund, Ishikawa Norito, Okubo Nariaki, Saito Yuuichi, Nature Communications, 2024.
- 2. Design of an apertureless two-stage acceleration lens for a single-ion implantation system.**
Ishii Yasuyuki, Okubo Takeru, Miyawaki Nobumasa, Yuri Yosuke, Onoda Shinobu, Narumi Kazumasa, Nuclear Instruments and Methods in Physics Research B, 541, 200 - 204, 2024.
DOI: <https://doi.org/10.1016/j.nimb.2023.05.021>
- 3. Robustness of semimetallic transport properties of TaAs against off-stoichiometric disorder.**
Kawasuso Atsuo, Suda Masayuki, Murakawa Hiroshi, Komada M., Suzuki Chihiro, Amada Haruyo, Michishio Koji, Maekawa Masaki, Miyashita Atsumi, Seko Noriaki, Yamamoto Shunya, Oshima Nagayasu, Seki Shuhei, Hanasaki N., Journal of Applied Physics, 133(22), 223903-1 - 223903-6, 2023. DOI:10.1063/5.0147663
- 4. Modification of Hardness and Electrical Conductivity of Copper-Titanium Alloy by Energetic Electron Irradiation.**
Akihiro Iwase, Yuki Fujimura, Satoshi Semboshi, Saito Yuuichi, Fuminobu Hori, Materials Transactions, 64(9), 2232 - 2236, 2023.
DOI:10.2320/matertrans.MT-M2023061
- 5. Linear Energy Transfer Dependence of Scintillation Properties of CeF₃.**
Koshimizu Masanori, Kurashima Satoshi, Kimura Atsushi, Taguchi Mitsumasa, Nuclear Inst. and Methods in Physics Research, B, 546, 165158, 2023.
DOI: <https://doi.org/10.1016/j.nimb.2023.165158>
- 6. Ion beam induced luminescence analysis of europium complexes in styrene-divinylbenzene copolymer-coated spherical silica by proton and argon ion beams irradiation.**
Masaumi Nakahara, Sou Watanabe, Masayuki Takeuchi, Yuyama Takahiro, Ishizaka Tomohisa, Ishii Yasuyuki, Yamagata Ryohei, Naoto Yamada, Masashi Koka, Wataru Kada, Naoto Hagura, Nuclear Instruments and Methods in Physics Research B, 542, 144 - 150, 2023.
DOI:10.1016/j.nimb.2023.06.012
- 7. Current status of the Tohoku microbeam system at Tohoku University and other facilities.**
Shigeo Matsuyama, Misako Miwa, Sho Toyama, Tomihiro Kamiya, Ishii Yasuyuki, Satoh Takahiro, Nuclear Instruments & Methods in Physics Research Section B, 539, 79 - 88, 2023.
DOI:10.1016/j.nimb.2023.03.023

Press

- 1. 元素比率がそろっていない量子材料でも高い電子移動度が発現することを実証—超省エネ・高速化の次世代デバイスと期待される量子デバイスの開発促進—**
QST・大阪大学・京都大学, 2024-02-21プレス発表.

QST Takasaki Annual Report 2023
(Ed) YAMAMOTO Hiroyuki

Date of Publishing : March 2025

Editorial committee : YAMAMOTO Hiroyuki, OHSHIMA Takeshi, ISHIOKA Noriko S.,
NARUMI Kazumasa and TAGUCHI Mitsumasa

Publication : Takasaki Institute for Advanced Quantum Science
National Institutes for Quantum Science and Technology
1233 Watanuki, Takasaki, Gunma 370-1292, Japan

Tel : +81-27-346-9232

E-mail : taka-annualrep@qst.go.jp

Homepage : <https://www.qst.go.jp/site/taka/>

©2025 National Institutes for Quantum Science and Technology

QST-M-52

<https://www.qst.go.jp>